

The unexpected health toll of  
Japan's nuclear disaster p. 978

Indie science films to  
watch in 2021 p. 984

A rocky exoplanet orbiting a  
nearby red dwarf star p. 1038

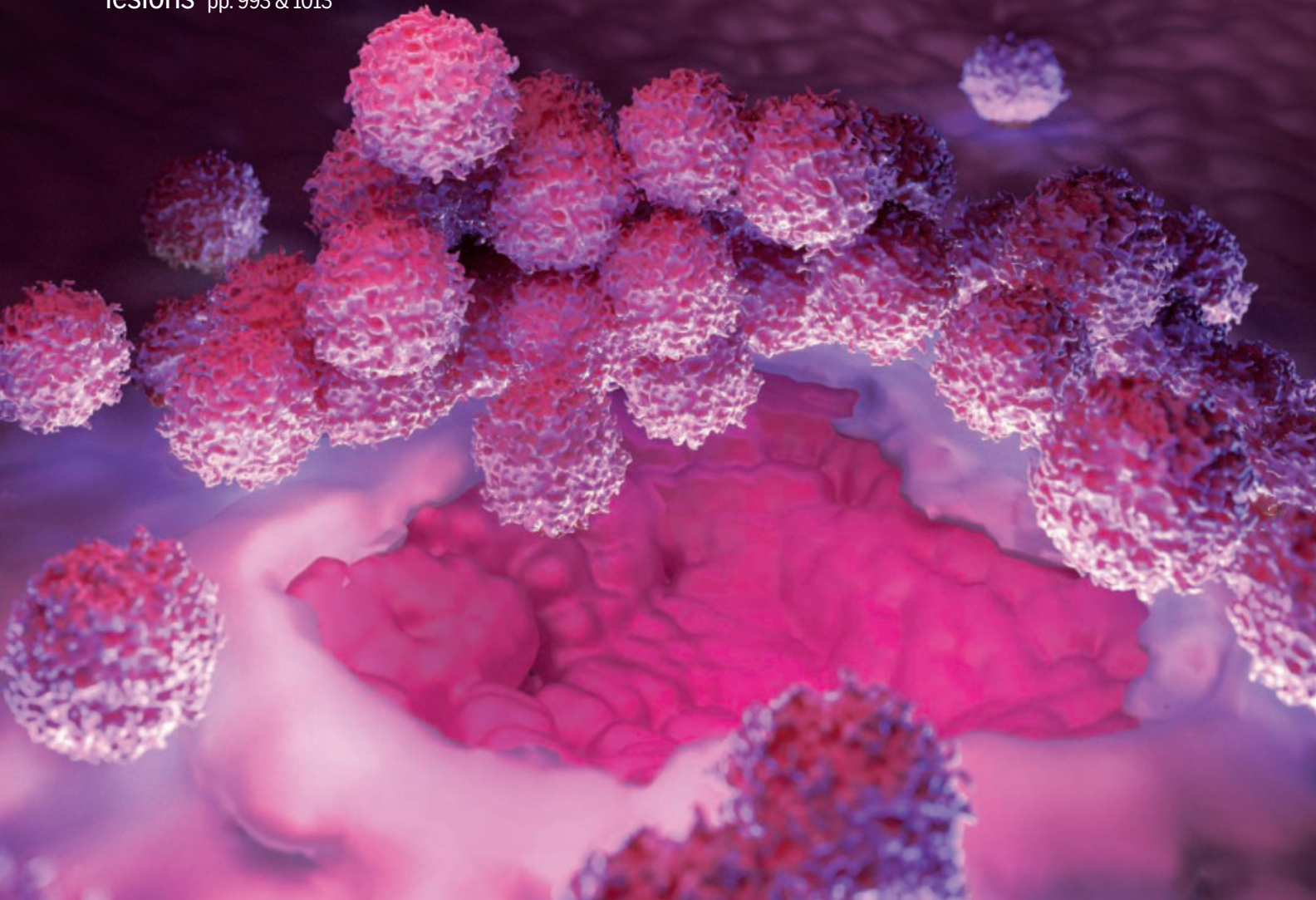
# Science

\$15  
5 MARCH 2021  
[sciencemag.org](http://sciencemag.org)

 AAAS

## MIGRATING MACROPHAGES

Repair clusters help seal peritoneal  
lesions pp. 993 & 1013





# EMPOWER WITH EVIDENCE

 AAAS | ANNUAL MEETING

Knowledge based on well-validated scientific discovery gives us the ability to transform our world. Over the last half-century, new discoveries from many different areas of science, technology, engineering, mathematics, and medicine have provided solutions to seemingly intractable problems. Research provides an unparalleled opportunity to explore and transform our world in all its complexity and mechanistic detail. It enables us to uncover fundamental aspects of how we relate to our world and to one another.

And yet, while the trajectory of the future will be defined by both the predictable and unexpected consequences of current scientific endeavors, the value of and trust in science have diminished. Science literacy, evidence-based decision making, science-based planning, and the use of validated knowledge to drive public policy are no longer universal societal aspirations. Engagement and communication must ensure that the value of science becomes accessible to all.

The 2022 AAAS Annual Meeting will feature groundbreaking trans- and multi-disciplinary research – not only to advance knowledge, but to understand and ultimately resolve many of the problems we face. The meeting will also highlight new initiatives in advocacy, education, and policy to address the challenges of rebuilding the public's trust and appreciation of science.

[aaas.org/meetings](https://aaas.org/meetings) | [#AAASmtg](https://twitter.com/AAASmtg)



## Pushing the Boundaries of Knowledge

As AAAS's first multidisciplinary, open access journal, *Science Advances* publishes research that reflects the selectivity of high impact, innovative research you expect from the *Science* family of journals, published in an open access format to serve a vast and growing global audience. Check out the latest findings or learn how to submit your research: [ScienceAdvances.org](https://www.scienceadvances.org)

Science  
Advances  
AAAS

---

**GOLD OPEN ACCESS, DIGITAL, AND FREE TO ALL READERS**

---



# CONTENTS

5 MARCH 2021 • VOLUME 371 • ISSUE 6533

978

After Japan's Fukushima region was devastated by the 11 March 2011 earthquake and tsunami, thousands fled radiation from a damaged nuclear power plant.

## NEWS

### IN BRIEF

**968** News at a glance

### IN DEPTH

#### **972** WHO's treatment megatrial is at a standstill

Unique international trial has struggled to build on its first batch of results  
By K. Kupferschmidt

#### **973** Data in paper about Swedish schoolchildren come under fire

Critics question *NEJM* letter that downplayed the risks of keeping schools open with few precautions  
By G. Vogel

#### **974** Life could use oxygen long before it was abundant

"Major innovation" emerged more than 3 billion years ago but was slow to catch on, study says  
By R. F. Service

#### **975** First Brazilian-made satellite watches the Amazon

Launch promises more deforestation data, but researchers fear government obstruction  
By S. Moutinho

#### **976** The genes behind the sexiest birds on the planet

Genomes from the tropical performers called manakins reveal the power of sexual selection  
By E. Pennisi

#### **977** NIH apologizes for 'structural racism,' pledges change

Activists fault agency for not directly addressing funding disparity between white and Black grant applicants  
By J. Kaiser

### FEATURES

#### **978** Nuclear medicine

After 10 years advising survivors of the Fukushima disaster about radiation, Masaharu Tsubokura thinks the evacuations posed a far bigger health risk  
By D. Normile

#### **983** Endless cleanup

By D. Normile

## INSIGHTS

### BOOKS ET AL.

#### **984** Science at Sundance 2021



### PERSPECTIVES

#### **990** Deforestation, forestation, and water supply

A systematic approach helps to illuminate the complex forest-water nexus  
By M. Zhang and X. Wei

#### **992** Whirls and swirls of polarization

Exotic toroidal polarization textures in a polymer ferroelectric interact with terahertz radiation  
By L. W. Martin  
REPORT p. 1050

#### **993** Surgical adhesions: A sticky macrophage problem

Body-cavity macrophages superaggregate in a platelet-like response to wounding  
By S. E. Herrick and J. E. Allen  
RESEARCH ARTICLE p. 1013

#### **995** Eyeless worms detect color

Roundworms discriminate color of toxic food despite a lack of eyes and opsin photoreceptor genes  
By L. A. Neal and L. B. Vosshall  
REPORT p. 1059

#### **996** Targeting cancer with bispecific antibodies

Bispecific antibodies might provide off-the-shelf immunotherapeutics for treating cancer  
By J. Weidanz  
RESEARCH ARTICLE P. 1009; *SCI. TRANSL. MED.* BY S. PAUL ET AL. 10.1126/SCITRANSLMED.ABD3595; *SCIENCE IMMUNOLOGY* BY J. DOUGLASS ET AL. 10.1126/SCIIMMUNOL.ABD5515



## POLICY FORUM

### 998 Human embryo research beyond the primitive streak

It is time to revisit the “14-day limit”  
By I. Hyun et al.

## LETTERS

### 1002 Editorial Expression of Concern

By H. Holden Thorp

### 1002 China's new laws overlook native herpetofauna

By K. Wang et al.

### 1003 Protecting China's finless porpoise

By Q. Yan and Y. Hu

### 1003 Technical Comment abstracts

# RESEARCH

## IN BRIEF

1004 From *Science* and other journals

## REVIEW

### 1007 Infectious disease

Infectious diseases and social distancing in nature S. Stockmaier et al.

REVIEW SUMMARY; FOR FULL TEXT:  
DOI.ORG/10.1126/SCIENCE.ABC8881

## RESEARCH ARTICLES

### 1008 Sperm genomics

Widespread haploid-biased gene expression enables sperm-level natural selection  
K. Bhutani et al.

RESEARCH ARTICLE SUMMARY; FOR FULL TEXT:  
DOI.ORG/10.1126/SCIENCE.ABB1723

### 1009 Cancer

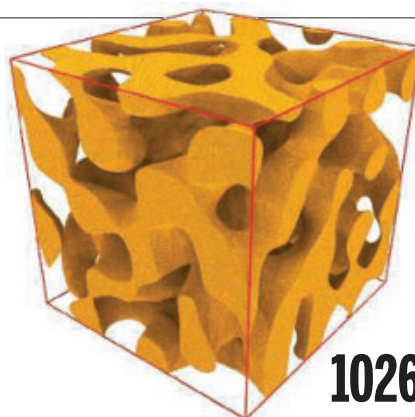
Targeting a neoantigen derived from a common TP53 mutation E. H. Hsiue et al.

RESEARCH ARTICLE SUMMARY; FOR FULL TEXT:  
DOI.ORG/10.1126/SCIENCE.ABC8697  
PERSPECTIVE P. 996; *SCI. TRANSL. MED.* BY  
S. PAUL ET AL. 10.1126/SCITRANSLMED.  
ABD3595; *SCIENCE IMMUNOLOGY* BY  
J. DOUGLASS ET AL. 10.1126/SCIMMUNOL.  
ABD5515

### 1010 Enzyme evolution

Parallel molecular mechanisms for enzyme temperature adaptation M. M. Pinney et al.

RESEARCH ARTICLE SUMMARY; FOR FULL TEXT:  
DOI.ORG/10.1126/SCIENCE.AAY2784



### 1011 Heart development

Characterization of a common progenitor pool of the epicardium and myocardium  
R. C. V. Tyser et al.

RESEARCH ARTICLE SUMMARY; FOR FULL TEXT:  
DOI.ORG/10.1126/SCIENCE.ABB2986

### 1012 Structural biology

A structure of human Scap bound to Insig-2 suggests how their interaction is regulated by sterols R. Yan et al.

RESEARCH ARTICLE SUMMARY; FOR FULL TEXT:  
DOI.ORG/10.1126/SCIENCE.ABB2224

### 1013 Immunology

Primordial GATA6 macrophages function as extravascular platelets in sterile injury  
J. Zindel et al.

RESEARCH ARTICLE SUMMARY; FOR FULL TEXT:  
DOI.ORG/10.1126/SCIENCE.ABE0595  
PERSPECTIVE p. 993

### 1014 Climate variability

Multidecadal climate oscillations during the past millennium driven by volcanic forcing  
M. E. Mann et al.

### 1019 Hematology

Combined liver–cytokine humanization comes to the rescue of circulating human red blood cells Y. Song et al.

### 1026 Metallurgy

Scaling behavior of stiffness and strength of hierarchical network nanomaterials  
S. Shi et al.

## REPORTS

### 1033 Microbiology

Redox-active antibiotics enhance phosphorus bioavailability D. L. McRose and D. K. Newman

### 1038 Exoplanets

A nearby transiting rocky exoplanet that is suitable for atmospheric investigation  
T. Trifonov et al.

### 1042 Insect declines

Fewer butterflies seen by community scientists across the warming and drying landscapes of the American West M. L. Forister et al.

### 1046 Black holes

Cygnus X-1 contains a 21-solar mass black hole—Implications for massive star winds J. C. A. Miller-Jones et al.

### 1050 Ferroelectrics

Toroidal polar topology in strained ferroelectric polymer  
M. Guo et al.

PERSPECTIVE P. 992

### 1056 Spectroscopy

Tracing orbital images on ultrafast time scales  
R. Wallauer et al.

### 1059 Sensory perception

*C. elegans* discriminates colors to guide foraging  
D. D. Ghosh et al.

PERSPECTIVE P. 995; PODCAST

## DEPARTMENTS

### 967 Editorial

Science's new frontier

By Aaron F. Mertz and Abhilash Mishra

### 1070 Working Life

Leadership challenges defused

By Samuel Peña-Llopis

## ON THE COVER

Illustration of macrophages infiltrating a wound in the peritoneal cavity. Multicellular organisms as primitive as sea urchins harbor their organs in body cavities surrounded by macrophages—cells that fight infections and repair tissue. In mammals, macrophages assemble into thrombus-like structures to rapidly seal



injuries. This activity has unintended consequences, such as undesirable growth of scar tissue after surgery, which can now be therapeutically targeted. See pages 993 and 1013.  
Illustration:  
C. Bickel/Science

Science Staff ..... 966  
New Products ..... 1064  
Science Careers ..... 1065

Editor-in-Chief Holden Thorp, hthorp@aaas.org

Executive Editor Monica M. Bradford

Editors, Research Valda Vinson, Jake S. Yeston Editor, Insights Lisa D. Chong

DEPUTY EDITORS Julia Fahrenkamp-Uppenbrink (UK), Stella M. Hurlley (UK), Phillip D. Szurmi, Sacha Vignieri SR. EDITORIAL FELLOW Andrew M. Sugden (UK) SR. EDITORS Gemma Alderton (UK), Caroline Ash (UK), Brent Grocholski, Pamela J. Hines, Di Jiang, Marc S. Lavine (Canada), Yevgeniya Nusinovich, Ian S. Osborne (UK), Beverly A. Purnell, L. Bryan Ray, H. Jesse Smith, Keith T. Smith (UK), Jelena Stajic, Peter Stern (UK), Valerie B. Thompson, Brad Wible, Laura M. Zahn ASSOCIATE EDITORS Michael A. Funk, Priscilla N. Kelly, Tage S. Rai, Seth Thomas Scanlon (UK), Yury V. Suleymanov LETTERS EDITOR Jennifer Sills LEAD CONTENT PRODUCTION EDITORS Harry Jach, Lauren Kmec CONTENT PRODUCTION EDITORS Amelia Beyna, Jeffrey E. Cook, Chris Filiatreau, Julia Katris, Nida Masiulis, Suzanne M. White SR. EDITORIAL COORDINATORS Carolyn Kyle, Beverly Shields EDITORIAL COORDINATORS Aneera Dobbins, Joi S. Granger, Jeffrey Hearn, Lisa Johnson, Maryrose Madrid, Ope Martins, Shannon McMahon, Jerry Richardson, Hilary Stewart (UK), Alana Warnke, Alice Whaley (UK), Anita Wynn PUBLICATIONS ASSISTANTS Jeremy Dow, Alexander Kief, Ronnel Navas, Brian White EXECUTIVE ASSISTANT Jessica Slater ASI DIRECTOR, OPERATIONS Janet Clements (UK) ASI SR. OFFICE ADMINISTRATOR Jessica Waldo (UK)

News Editor Tim Appenzeller

NEWS MANAGING EDITOR John Travis INTERNATIONAL EDITOR Martin Enserink DEPUTY NEWS EDITORS Elizabeth Culotta, Lila Guterman, David Grimm, Eric Hand (Europe), David Malakoff SR. CORRESPONDENTS Daniel Cley (UK), Jon Cohen, Jeffrey Mervis, Elizabeth Pennisi ASSOCIATE EDITORS Jeffrey Brainard, Catherine Maticic NEWS REPORTERS Adrian Cho, Jennifer Couzin-Frankel, Jocelyn Kaiser, Kelly Servick, Robert F. Service, Erik Stokstad, Paul Voosen, Meredith Wadman INTERNS Lucy Hicks, Cathleen O'Grady CONTRIBUTING CORRESPONDENTS Warren Cornwall, Andrew Curry (Berlin), Ann Gibbons, Sam Kean, Eli Kintisch, Kai Kupferschmidt (Berlin), Andrew Lawler, Mitch Leslie, Eliot Marshall, Virginia Morell, Dennis Normile (Shanghai), Elisabeth Pain (Careers), Charles Piller, Michael Price, Tania Rabesandratana (Barcelona), Joshua Sokol, Emily Underwood, Gretchen Vogel (Berlin), Lizzie Wade (Mexico City) CAREERS Donisha Adams, Rachel Bernstein (Editor), Katie Langin (Associate Editor) COPY EDITORS Julia Cole (Senior Copy Editor), Cyra Master (Copy Chief) ADMINISTRATIVE SUPPORT Meagan Weiland

Creative Director Beth Rakouskas

DESIGN MANAGING EDITOR Marcy Atarod GRAPHICS MANAGING EDITOR Alberto Cuadra PHOTOGRAPHY MANAGING EDITOR William Douthitt WEB CONTENT STRATEGY MANAGER Kara Estelle-Powers DESIGN EDITOR Chrystal Smith DESIGNER Christina Aycock GRAPHICS EDITOR Nirja Desai INTERACTIVE GRAPHICS EDITOR Kelly Franklin SENIOR SCIENTIFIC ILLUSTRATORS Valerie Altounian, Chris Bickel SCIENTIFIC ILLUSTRATOR Alice Kitterman SENIOR GRAPHICS SPECIALISTS Holly Bishop, Nathalie Cary SENIOR PHOTO EDITOR Emily Petersen PHOTO EDITOR Kaitlyn Dolan WEB DESIGNER Jennie Pajeroski

## Chief Executive Officer and Executive Publisher Sudip Parikh

Publisher, Science Family of Journals Bill Moran

DIRECTOR, BUSINESS SYSTEMS AND FINANCIAL ANALYSIS Randy Yi DIRECTOR, BUSINESS OPERATIONS & ANALYSIS Eric Knott DIRECTOR OF ANALYTICS Enrique Gonzales MANAGER, BUSINESS OPERATIONS Jessica Tierney SENIOR BUSINESS ANALYST Cory Lipman, Meron Kebede FINANCIAL ANALYST Alexander Lee ADVERTISING SYSTEM ADMINISTRATOR Tina Burks SENIOR SALES COORDINATOR Shirley Young DIGITAL/PRINT STRATEGY MANAGER Jason Hillman QUALITY TECHNICAL MANAGER Marcus Spiegler ASSISTANT MANAGER DIGITAL/PRINT Rebecca Doshi SENIOR CONTENT SPECIALISTS Steve Forrester, Jacob Hedrick, Antoinette Hodal, Lori Murphy PRODUCTION SPECIALIST Kristin Wolk DIGITAL PRODUCTION MANAGER Lisa Stanford CONTENT SPECIALIST Kimberley Oster ADVERTISING PRODUCTION OPERATIONS MANAGER Deborah Tompkins DESIGNER, CUSTOM PUBLISHING Jeremy Hunsinger SR. TRAFFIC ASSOCIATE Christine Hall SPECIAL PROJECTS ASSOCIATE Sarah Dhere

ASSOCIATE DIRECTOR, BUSINESS DEVELOPMENT Justin Sawyers GLOBAL MARKETING MANAGER Allison Pritchard DIGITAL MARKETING MANAGER Aimee Aponte JOURNALS MARKETING MANAGER Shawana Arnold MARKETING ASSOCIATES Tori Velasquez, Mike Romano, Ashley Hylton DIGITAL MARKETING SPECIALIST Asleigh Rojanavongse SENIOR DESIGNER Kim Huynh

DIRECTOR AND SENIOR EDITOR, CUSTOM PUBLISHING Sean Sanders ASSISTANT EDITOR, CUSTOM PUBLISHING Jackie Oberst

DIRECTOR, PRODUCT & PUBLISHING DEVELOPMENT Chris Reid DIRECTOR, BUSINESS STRATEGY AND PORTFOLIO MANAGEMENT Sarah Whalen ASSOCIATE DIRECTOR, PRODUCT MANAGEMENT Kris Bishop PRODUCT DEVELOPMENT MANAGER Scott Chernoff PUBLISHING TECHNOLOGY MANAGER Michael Di Natale SR. PRODUCT ASSOCIATE Robert Koepke SPJ ASSOCIATE Samantha Bruno Fuller

DIRECTOR, INSTITUTIONAL LICENSING Iquo Edim ASSOCIATE DIRECTOR, RESEARCH & DEVELOPMENT Elisabeth Leonard MARKETING MANAGER Kess Knight SENIOR INSTITUTIONAL LICENSING MANAGER Ryan Rexroth INSTITUTIONAL LICENSING MANAGER Marco Castellani MANAGER, AGENT RELATIONS & CUSTOMER SUCCESS Judy Lillibridge SENIOR OPERATIONS ANALYST Lana Guz FULFILLMENT COORDINATOR Melody Stringer SALES COORDINATOR Josh Haverlock

DIRECTOR, GLOBAL SALES Tracy Holmes US EAST COAST AND MID WEST SALES Stephanie O'Connor US WEST COAST SALES Lynne Stickrod US SALES MANAGER, SCIENCE CAREERS Claudia Paulsen-Young US SALES REP, SCIENCE CAREERS Tracy Anderson ASSOCIATE DIRECTOR, ROW ROWR Gonçalves SALES REP, ROW Sarah Lelarge SALES ADMIN ASSISTANT, ROW Bryony Cousins DIRECTOR OF GLOBAL COLLABORATION AND ACADEMIC PUBLISHING RELATIONS, ASIA Xiaoying Chu ASSOCIATE DIRECTOR, INTERNATIONAL COLLABORATION Grace Yao SALES MANAGER Danny Zhao MARKETING MANAGER Kilo Lan ASCA CORPORATION, JAPAN Kaoru Sasaki (Tokyo), Miyuki Tani (Osaka) COLLABORATION/CUSTOM PUBLICATIONS/JAPAN Adarsh Sandhu

DIRECTOR, COPYRIGHT, LICENSING AND SPECIAL PROJECTS Emilie David RIGHTS AND LICENSING COORDINATOR Jessica Adams RIGHTS AND PERMISSIONS ASSOCIATE Elizabeth Sandler CONTRACTS AND LICENSING ASSOCIATE Lili Catlett

### MAIN HEADQUARTERS

Science/AAAS  
1200 New York Ave. NW  
Washington, DC 20005

### SCIENCE INTERNATIONAL

Clarendon House  
Clarendon Road  
Cambridge, CB2 8FH, UK

### SCIENCE CHINA

Room 1004, Culture Square  
No. 59 Zhongguancun St.  
Haidian District, Beijing, 100872

### SCIENCE JAPAN

ASCA Corporation  
Sibaura TY Bldg. 4F, 1-14-5  
Shibaura Minato-ku  
Tokyo, 108-0073 Japan

### EDITORIAL

science\_editors@aaas.org

### NEWS

science\_news@aaas.org

### INFORMATION FOR AUTHORS

sciencemag.org/authors/

science-information-authors

### REPRINTS AND PERMISSIONS

sciencemag.org/help/

reprints-and-permissions

### MEDIA CONTACTS

scipak@aaas.org

### MULTIMEDIA CONTACTS

SciencePodcast@aaas.org

ScienceVideo@aaas.org

### INSTITUTIONAL SALES

AND SITE LICENSES

sciencemag.org/librarian

### PRODUCT ADVERTISING

& CUSTOM PUBLISHING  
advertising.sciencemag.org/  
products-services

science\_advertising@aaas.org

### CLASSIFIED ADVERTISING

advertising.sciencemag.org/

science-careers

advertise@sciencecareers.org

### JOB POSTING CUSTOMER SERVICE

employers.sciencemag.org

support@sciencecareers.org

### MEMBERSHIP AND INDIVIDUAL

SUBSCRIPTIONS

sciencemag.org/subscriptions

### MEMBER BENEFITS

aaas.org/membercentral

### AAAS BOARD OF DIRECTORS

CHAIR Steven Chu

PRESIDENT Claire M. Fraser

PRESIDENT-ELECT Susan G. Amara

TREASURER Carolyn N. Ainslie

CHIEF EXECUTIVE OFFICER

Sudip Parikh

BOARD Cynthia M. Beall

Rosina M. Bierbaum

Ann Bostrom

Stephen P.A. Fodor

S. James Gates, Jr.

Laura H. Greene

Kaye Husbands Fealing

Maria M. Klawe

Robert B. Millard

Alondra Nelson

William D. Provine

### BOARD OF REVIEWING EDITORS (Statistics board members indicated with \$)

Takuzo Aida, U. of Tokyo

Leslie Aiello,

Wenner-Gren Foundation

Deji Akinwande, UT Austin

Judith Allen, U. of Manchester

Marcella Alsan, Harvard U.

Sebastian Amigorena,

Institut Curie

James Analytis, UC Berkeley

Trevor Archer, NIEHS, NIH

Paola Arlotto, Harvard U.

David Awschalom, U. of Chicago

Clare Baker, U. of Cambridge

Delia Baldassarri, NYU

Nenad Ban, ETH Zürich

Franz Bauer,

Pontificia U. Católica de Chile

Ray H. Baughman,

IST Dallas

Carlo Beenakker, Leiden U.

Yasmine Belkaid, NIAID, NIH

Philip Benfey, Duke U.

Kiros T. Berhane, Columbia U.

Bradley Bernstein,

Mass. General Hospital

Joseph J. Berry, NREL

Alessandra Biffi,

Harvard Med.

Chris Bowler,

École Normale Supérieure

Ian Boyd, U. of St. Andrews

Emily Brodsky, UC Santa Cruz

Ron Brookmeyer, UCLA (\$)

Christian Büchel, UKE Hamburg

Dennis Burton, Scripps Res.

Carter Tribble Butts, UC Irvine

György Buzsáki,

NYU School of Med.

Mariana Byndloss,

Vanderbilt U. Med. Ctr

Annmarie Carlton, UC Irvine

Nick Chater, U. of Warwick

Ling-Ling Chen, SIBCB, CAS

M. Keith Chen, UCLA

Zhijian Chen,

UT Southwestern Med. Ctr.

Ib Chorkendorff, Denmark TU

James J. Collins, MIT

Robert Cook-Deegan,

Arizona State U.

Virginia Cornish, Columbia U.

Carolyn Coyne, U. of Pitt.

Roberta Croce, VU Amsterdam

Ismail Dabo, Penn State U.

Jeff L. Dangl, UNC

Chiara Daraio, Caltech

Nicolas Dauphas, U. of Chicago

Christian Davenport,

U. of Michigan

Frans de Waal, Emory U.

Claude Desplan, NYU

Sandra Díaz,

U. Nacional de Córdoba

Ulrike Diebold, TU Wien

Stefanie Dimpfeler,

Goethe-U. Frankfurt

Hong Ding, Inst. of Physics, CAS

Dennis Discher, UPenn

Jennifer A. Doudna,

UC Berkeley

Ruth Drdla-Schutting,

Med. U. Vienna

Raissa M. D'Souza, UC Davis

Bruce Dunn, UCLA

William Dunphy, Caltech

Scott Edwards, Harvard U.

Todd Ehlers, U. of Tübingen

Jennifer Eliseeff,

Johns Hopkins U.

Andrea Encalada,

U. San Francisco de Quito

Nader Engheta, U. of Penn.

Karen Ersche, U. of Cambridge

Beate Escher,

UFZ & U. of Tübingen

Barry Everitt, U. of Cambridge

Vanessa Ezenwa, U. of Georgia

Michael Feuer, GWU

Toren Finkel,

U. of Pitt. Med. Ctr.

Gwenn Flowers, Simon Fraser U.

Peter Fratzi,

Max Planck Inst. Potsdam

Elaine Fuchs, Rockefeller U.

Jay Gallagher, U. of Wisconsin

Daniel Gerschwind, UCLA

Ramon Gonzalez,

U. of South Florida

Sandra González-Bailón,

UPenn

Elizabeth Grove, U. of Chicago

Nicolas Gruber, ETH Zürich

Hua Guo, U. of New Mexico

Taekjip Ha, Johns Hopkins U.

Sharon Hammes-Schiffer,

Yale U.

Wolf-Dietrich Hardt, ETH Zürich

Louise Harra, U. Coll. London

Jian He, Clemson U.

Carl-Philipp Heisenberg,

IST Austria

Ykä Helariutta, U. of Cambridge

Janet G. Hering, Eawag

Heather Hickman, NIAID, NIH

Hans Hilgenkamp, U. of Twente

Kai-Uwe Hinrichs, U. of Bremen

Deirdre Hollingsworth,

U. of Oxford

Randall Hulet, Rice U.

Auke Ijspeert, EPFL

Akiko Iwaseki, Yale U.

Stephen Jackson,

USGS & U. of Arizona

Erich Jarvis, Rockefeller U.

Peter Jonas, IST Austria

Matt Kaerberlein,

U. of Wash.

William Kaelin Jr.,

Dana-Farber Cancer Inst.

Daniel Kammen, UC Berkeley

V. Narry Kim, Seoul Nat. U.

Robert Kingston,

Harvard Med.

Nancy Knowlton,

Smithsonian Institution

Etienne Koehlin,

École Normale Supérieure

Alex L. Kolodkin,

Johns Hopkins U.

Julia Krupic, U. of Cambridge

Gabriel Lander, Scripps Res. (\$)

Mitchell A. Lazar, UPenn

Wendell Lim, UCSF

Luis Liz-Marzán, CIC bioGUNE

Omar Lizardo, UCLA

Jonathan Losos,

Wash. U. in St. Louis

Ke Lu, Inst. of Metal Res., CAS

Christian Lüscher, U. of Geneva

Jan Lynch-Stieglitz,

Georgia Inst. of Tech.

David Lyons, U. of Edinburgh

Fabienne Mackay,

QIMR Berghofer

Anne Magurran, U. of St. Andrews

Asifa Majid, U. of York

Oscar Marin, King's Coll. London

Charles Marshall, UC Berkeley

Christopher Marx, U. of Idaho

David Masopust, U. of Minnesota

Geraldine Masson, CNRS

Jason Matheny, Georgetown U.

Heidi McBride, McGill U.

C. Robertson McClung,

Dartmouth

Rodrigo Medellín,

U. Nacional Autónoma de México

Jane Memmott, U. of Bristol

C. Jessica Metcalf, Princeton U.



# Science's new frontier

**T**he year 2020 saw a reusable rocket launch two astronauts into space, multiple COVID-19 vaccines developed in record time, and a robot that could write a persuasive op-ed. In the United States, the year also saw public distrust of science contribute to the worst health crisis in modern history. This contrast highlights a sharp dichotomy in the role of science in American public life: breathtaking discovery and innovation alongside growing distrust of scientific evidence and recommendations. How can the country reconcile this dissociation?

The problem is that few Americans have access to scientific institutions, to the process of research and discovery, and to scientists themselves. Elite American universities lead in scientific R&D, but low-income and even middle-class students are underrepresented. Clinical trials, a core part of medical research, often do not reflect America's demographic and socioeconomic diversity. A recent poll reported that more than 80% of Americans could not name a living scientist. If most Americans are not scientifically knowledgeable or engaged, they are less likely to trust scientific evidence and rally together to tackle future pandemics, confront climate change, or adopt new technologies.

To bridge this disconnect, the Biden administration could launch an "American Science Corps" (ASC) to elevate science as a central part of American culture. Such a nonpartisan agency, federally funded and administered, would employ early-career scientists in underserved urban and rural communities to fulfill the goal expressed by Alondra Nelson, the Office of Science and Technology Policy's newly appointed deputy director for science and society: "to situate [scientific] development in our values of equality, accountability, justice, and trustworthiness." Eventually placing 20,000 full-time ASC service members across the country, each serving roughly 16,500 Americans, would create a cooperative extension service—for science.

The ASC is inspired by the Agricultural Extension Service, which, for over a century, has employed county agents at land-grant universities. The agents serve as a conduit between academic researchers and farmers, designing educational programs that respond to local needs and communicating farmers' problems back to researchers. Equally ambitious, the ASC would administer civic science workshops, public events, and train-

ing programs to engage Americans on the nuances and assumptions associated with scientific research and discovery. The ASC would enable dialogue that redirects science toward problems that plague local communities but often remain blind spots for academic researchers.

ASC service members would receive training from communications experts and behavioral and social scientists. Training would include learning how to listen to community needs and engage in forums that scientists have traditionally avoided, such as places of worship, state and county fairs, farmers' markets, town halls, local theaters, libraries, community colleges, and sporting events. To attract talent, the ASC needs to become a viable career option. The scientific enterprise incentivizes research careers, but full-time jobs in public engagement are often considered fringe, alternative, or second-rate choices. Potential ASC service members exist among the Ph.D. students and postdocs whose academic job prospects have been diminished by the pandemic. Elevating ASC service members to the same prestige and compensation as those of researchers would attract highly qualified scientists committed to pursuing this new career, giving them time to build trust and carry out long-term programs that can lead to lasting change.

We estimate that deployment of 7000 ASC service members for a pilot year would cost \$500 million—a mere 0.4% of annual federal R&D spending across the Departments of Defense and Energy, National Science Foundation, National Institutes of Health, and National Aeronautics and Space Administration. This relatively small investment would bolster the missions of these departments and agencies, ensure a stronger workforce, and encourage greater public support for their work while benefiting public health, economic justice, and national security. As the economy adapts to new technologies, ASC service members could help retrain and bring new skills to American adults. The ASC would also counter misinformation and conspiracy theories arising from gaps in trust in science.

Uniting the country around the conviction that science can improve the life of every American would be one of the most important public investments of the century. Without such an effort, vast swaths of Americans may not benefit from, or participate in, "the endless frontier" of scientific progress.

—Aaron F. Mertz and Abhilash Mishra

## Aaron F. Mertz

is the director of the Aspen Institute Science & Society Program, New York, NY, USA. [aaron.mertz@aspeninstitute.org](mailto:aaron.mertz@aspeninstitute.org)

## Abhilash Mishra

is the director of the Xu Initiative on Science, Technology, and Public Policy at the University of Chicago Harris School of Public Policy and the founder of EquiTech Futures, Chicago, IL, USA. [abhilashmishra@uchicago.edu](mailto:abhilashmishra@uchicago.edu)

"...pursuing this new career...to build trust...can lead to lasting change."

# NEWS

## IN BRIEF

Edited by Jeffrey Brainard



A worker at drug wholesaler McKesson Corp. in Shepherdsville, Kentucky, prepares a shipment of Johnson & Johnson's COVID-19 vaccine.

### COVID-19

## United States authorizes first single-shot vaccine

**J**ohnson & Johnson (J&J) last week became the third COVID-19 vaccinemaker to receive emergency use authorization for its product from the U.S. Food and Drug Administration. In contrast to the two-dose vaccines from Moderna and Pfizer authorized earlier, the J&J vaccine—a harmless virus delivering the gene for the spike protein from SARS-CoV-2—proved safe and effective with a single dose. The company intends to deliver 20 million doses to the United States this month, 80 million more by the end of June, and more than 1 billion doses worldwide this year. A placebo-controlled trial that took place in eight countries and involved more than 43,000 participants found that the single shot had 66% efficacy against moderate to

severe COVID-19 after 28 days and 85% protection against severe disease. This is below the approximately 95% efficacy against mild disease achieved by the Pfizer and Moderna vaccines, which produce the spike protein using messenger RNA (mRNA)—but the J&J trial included locations in South Africa and Brazil where SARS-CoV-2 variants that may escape vaccine-induced antibodies are now common. (The mRNA vaccine results came before their spread.) No one who received the J&J vaccine in any country was hospitalized or died from COVID-19. The White House also brokered a deal with Merck, a major vaccine producer that dropped its own COVID-19 candidates because of poor performance, to help make the J&J product.

## NIH eyes lasting virus symptoms

**COVID-19** | The U.S. National Institutes of Health (NIH) last week announced a multipronged research effort to better understand and treat Long COVID, in which people suffer lingering effects after infection by the pandemic coronavirus. Symptoms include lung problems, heart abnormalities, and enduring fatigue. In December 2020, Congress gave NIH \$1.15 billion over 4 years to study the perplexing condition. The agency is inviting applications for research on its natural history, prevalence,

and underlying biology and plans an expansive biorepository for samples from volunteers. Last week, the World Health Organization released a policy document estimating 10% of patients remain unwell 12 weeks after being infected. Explanations for the lasting effects have been elusive (*Science*, 7 August 2020, p. 614).

## Carbon dioxide cuts lag badly

**CLIMATE CHANGE** | Countries are drastically lagging in the fossil fuel cuts needed to reach the goals of the Paris climate

agreement, a new analysis suggests. Globally, emissions were up by an average of 0.21 billion tons of carbon dioxide (CO<sub>2</sub>) per year from 2016 to 2019 compared with 2011–15, the Global Carbon Project reported this week in *Nature Climate Change*. Although 64 countries—most of them wealthy ones that have contributed the most to climate change—cut their CO<sub>2</sub> emissions by a collective 0.16 billion tons per year during this time, their reductions must increase 10-fold, to some 1 billion tons annually, to meet the Paris goal of limiting global warming to 2°C. Although



the pandemic caused a 7% drop in emissions in 2020, the report says, evidence from previous economic crises suggests emissions will rebound to previous levels unless recovery plans aggressively push decarbonization.

## Biden relaxes immigration bans

**IMMIGRATION** | U.S. President Joe Biden last week ended a policy, imposed last year by then-President Donald Trump, that had barred most noncitizens not already in the United States from seeking permanent residency and work permits, or green cards. Trump had said issuing new green cards didn't make sense given unemployment caused by the COVID-19 pandemic. But industry groups had challenged the policy, in part because they said it prevented companies from hiring needed scientists and skilled technical workers. In revoking the ban, Biden said it had harmed U.S. businesses "that utilize talent from around the world." A Trump ban on temporary work permits remains in place but is set to expire on 31 March.

## Biden ups carbon's social cost

**CLIMATE POLICY** | U.S. President Joe Biden's administration last week raised the government's benchmark for the "social cost of carbon," the estimate it uses in cost-benefit analyses of regulations and other policies to represent the burden that global warming places on present and future generations. The figure will rise to \$51 per ton on an interim basis; former President Donald Trump's administration had set it as low as \$1. The revised standard restores the level set under former President Barack Obama, adjusted for inflation. The Biden administration may further increase the figure in an update due in January 2022 to reflect increased damages from heat waves and other disasters made worse by global warming.

## 'Nepotistic' journals examined

**PUBLISHING** | A study of more than 5000 biomedical journals found a pattern of apparent favoritism: In 206 journals, a single author was responsible for between

## IN OTHER NEWS

**DINO TRACKS IN PERIL** Ongoing mining threatens to destroy China's largest site of dinosaur tracks, researchers reported online on 27 February in *Geoscience Frontiers*. In 1994, the first of the tracks, 145 million to 120 million years old, were uncovered in a copper mine in China's southwestern Sichuan province. Paleontologists have identified 1928 individual footprints from dozens of individuals, representing ornithomimids, theropods, sauropods, and pterosaurs. By 2012, mining had led one of the track-bearing rock faces to collapse, before it was fully studied.

**NEW MINE HELD UP** The Biden administration has delayed a huge Arizona copper mine opposed by archaeologists and Native tribes, who say it will destroy cultural treasures. In 2014 Congress approved giving 970 hectares of federal land at Oak Flat to a mining firm. But this week officials said they want to review an environmental study needed for the transfer. Mine opponents have asked Congress and the courts to kill the project.

**A WIN AGAINST MALARIA** El Salvador last week became the first country in Central America to be certified free of malaria by the World Health Organization. The country became eligible after recording no home-grown cases of the mosquito-borne disease since 2017. Globally, 38 countries and territories have reached this milestone.

**BIG CANCER FUND** A new foundation will provide \$250 million for cancer research, one of the largest such gifts ever. Break Through Cancer was financed by a Richmond, Virginia, businessperson whose son died of cancer in 2020. The funding will support research teams drawn from five prominent U.S. university cancer centers that will study cancer types that are difficult to treat and have high mortality rates, including pancreatic and ovarian cancer, glioblastomas, and acute myelogenous leukemia.

**NO PLACE LIKE HOME** Americans value space research aimed at protecting Earth over sending astronauts to other bodies, a survey by Morning Consult says. Sixty-three percent of respondents called monitoring Earth's climate a top or important priority. Just 33% voiced that level of backing for launching astronauts to Mars or the Moon.



A dog buried at Berenice was protected with a piece of pottery.

## ARCHAEOLOGY

### Burials 2000 years ago show humans' bonds with pets

**A** detailed excavation in what was once a Roman port city has helped archaeologists identify what may be the oldest known pet cemetery. The remains of nearly 600 cats and dogs had been laid in prepared pits and covered with pieces of pottery and textiles, and some wore collars and other adornments. Researchers discovered the graveyard in 2011 outside the ancient city of Berenice, which today lies in Egypt. Features of some skeletons indicated the animals had lived with debilitating injuries and illnesses and survived into old age, indicating the animals were cared for, the researchers reported recently in *World Archaeology*.

PHOTO: M. OŚPIŃSKA

## UP FOR DEBATE

## Should peer reviewers be paid?

Reviewing journal articles can seem a thankless task. Scientists do the work for free, even as journals publish ever more papers and some publishers make sizable profits. Even before the COVID-19 pandemic led to a blizzard of submissions, journal editors were reporting that "reviewer fatigue" was making it harder to find volunteers. At the Researcher to Reader conference on scholarly publishing last week, two teams debated a provocative question: Should peer reviewers be paid? Here are some of their arguments. (See a fuller version at <http://scim.ag/PayPeerReview>.)

**YES:** "There is no downward pressure on the endless use of academic labor. And the easiest way to exert that pressure is to value the task not [only] with recognition, but with the traditional way to support skilled labor in every other industry, which is money." *James Heathers, a former research scientist, now chief scientist at a technology startup*

**NO:** "A 2018 survey found that only 17% of respondents selected cash or in-kind payment as something that would make them more likely to accept review requests." (Nearly half said more explicit recognition of reviewing work from their universities or employers would inspire them to do it.) *Alison Mudditt, CEO of PLOS, a nonprofit publisher of open-access articles*

**NO:** It could cost \$3960 per accepted paper to cover the cost of reviewing, if each reviewer was paid \$450, each manuscript received 2.2 reviews, and the journal accepted 25% of submissions. "Surely that money would better spent on the research itself and on solving our most pressing global challenges." *Tim Vines, a publishing consultant*

**YES:** "What might very well happen is fewer papers get submitted, because the costs go up. ... A contract provides much needed certainty around the time frame, the quality, and the predictability of the review received." *Brad Fenwick, senior vice president at Taylor & Francis, a for-profit publisher*

**NO:** "It's completely unrealistic to expect that anybody is going to have either the time or the expertise or the scale to be able to manage and monitor hundreds of thousands of additional new contracts across the publishing system. Just not gonna happen." *A.M.*



## ART AND SCIENCE

## 'Dance Your Ph.D.' winner uses rap to explain clouds

**"**'m the first author, you're just *et al.*," raps this year's winner of *Science*'s annual "Dance Your Ph.D.," a contest that challenges scientists to explain their research through dance. The first place video by Jakub Kubečka, a doctoral student at the University of Helsinki, features an original rap song and choreography, performed by him and two friends (above), explaining the search for atmospheric molecular clusters—groups of atoms that stick together and encourage water vapor to condense into clouds. Kubečka beat out 39 competitors for the \$2000 top prize, sponsored by the artificial intelligence firm Primer. The winning entry is at <http://scim.ag/DancePhD2021>.

11% and 40% of the papers published between 2015 and 2019. Of 100 of these "nepotistic" journals given closer scrutiny, the prolific author was the editor-in-chief for about one-quarter and on the editorial board for more than 60%. Prolific authors also enjoyed faster peer reviews, according to a preprint of the study posted last month on the bioRxiv server. A research team did the analysis after scrutinizing publications by microbiologist Didier Raoult of Aix-Marseilles University, who has promoted hydroxychloroquine as a COVID-19 treatment, although most other studies have found no evidence of benefit. Raoult, who now faces disciplinary action by a French medical regulator, appears as an author on one-third of the 728 papers at the journal *New Microbes and New Infections*, where some of his collaborators serve as editors.

## For AI bard, this play's the thing

**SCIENCE AND ART** | An artificial intelligence (AI) program for the first time has written a play, which was staged by actors in Prague's Švanda Theater and premiered online last week. The script, depicting a robot's journey trying to understand

humans, was generated by a widely available AI system called GPT-2. Researchers at Charles University helped it start to write the play by feeding it two sentences of dialogue about human experiences, and the software generated more, using related information drawn from the internet. Dramatist David Košťák, who tweaked about 10% of the resulting script to ensure it followed a coherent storyline, called its style "abstract." But *AI: When a robot writes a play* showcases what the evolving technology can now do, specialists say. Judge the 60-minute play for yourself at <http://scim.ag/AIplay>.

## Monarch population falls again

**CONSERVATION** | The population of monarch butterflies overwintering in Mexico showed another big drop this year. Researchers counted 2.1 hectares of occupied habitat, down 26% from last year and more than 80% from 2 decades ago, the Center for Biological Diversity said. Six hectares is the minimum considered necessary to avoid a risk of extinction.

**S** **SCIENCEMAG.ORG/NEWS**  
Read more news from *Science* online.




CALL FOR PAPERS

[spj.sciencemag.org/bmef](http://spj.sciencemag.org/bmef)



# BME Frontiers

 OPEN ACCESS

*Biomedical Engineering (BME) Frontiers* is a **Science Partner Journal** distributed by the **American Association for the Advancement of Science (AAAS)** in collaboration with the **Suzhou Institute of Biomedical Engineering and Technology, Chinese Academy of Sciences (SIBET CAS)**. *BME Frontiers* aims to serve as an effective platform for the multidisciplinary community of biomedical engineering. The journal will publish breakthrough research in the fields of pathogenic mechanisms as well as disease prevention, diagnosis, treatment, and assessment.

The Science Partner Journals (SPJ) program was established by the American Association for the Advancement of Science (AAAS), the nonprofit publisher of the *Science* family of journals. The SPJ program features high-quality, online-only, open access publications produced in collaboration with international research institutions, foundations, funders and societies. Through these collaborations, AAAS expands its efforts to communicate science broadly and for the benefit of all people by providing top-tier international research organizations with the technology, visibility and publishing expertise that AAAS is uniquely positioned to **offer as the world's largest general science membership society**.

**Submit your research to *Biomedical Engineering Frontiers* today!**

Learn more at: [spj.sciencemag.org/bmef](http://spj.sciencemag.org/bmef)

ARTICLE PROCESSING CHARGES WAIVED UNTIL 2021



Clinicians care for a COVID-19 patient in Tehran. Iran is one of more than 40 countries taking part in the Solidarity trial testing coronavirus treatments.

## COVID-19

# WHO's treatment megatrial is at a standstill

Unique international trial has struggled to build on its first batch of results

By Kai Kupferschmidt

**T**he only global trial of potential COVID-19 treatments is languishing. The World Health Organization's (WHO's) Solidarity trial, set up last year to quickly test potential COVID-19 therapies with tens of thousands of patients, produced headlines in October 2020 when it showed that four candidate treatments offer little benefit. But since then, it hasn't launched any new tests. On 27 January, John-Arne Røttingen, who works at Norway's foreign ministry and chairs the trial's executive group, pulled the plug on the study's only remaining arm, which tested the antiviral remdesivir. "The Solidarity trial is now on pause," he says.

The executive group discussed potential new targets at a meeting on 24 February, and Røttingen hopes to restart the trial in a few weeks. But observers are dismayed at the pause in the challenging but important trial. "It would be such a shame for this extraordinary network of clinical researchers to not maintain their momentum of discovery," says Eric Topol, director of the Scripps Research Translational Institute. "They have had a strong influence on global patient care during the pandemic."

Solidarity and the United Kingdom's Re-

covery trial, which both launched in March 2020, are the largest COVID-19 treatment trials worldwide. Hundreds of smaller studies of experimental COVID-19 therapies have not included enough patients to convincingly rule in or out any drugs. "We're trying to distinguish reliably between a moderate but worthwhile effect, and no worthwhile effect. And for that, you need big numbers," says Richard Peto, a University of Oxford epidemiologist who helped design Solidarity and analyze the data.

Solidarity was set up to make it easy for doctors around the world to take part, by randomizing patients to one of the study treatments and recording minimal data. It quickly launched tests of four treatments: remdesivir, hydroxychloroquine (a drug touted by former U.S. President Donald Trump and others), interferon beta, and the HIV drug combination lopinavir and ritonavir. Results published from more than 11,000 patients in 400 hospitals showed none of the therapies led to a significant reduction in deaths (*Science*, 23 October 2020, p. 388). A smaller U.S. trial had shown remdesivir reduced the time patients needed to recover. So Solidarity continued to randomize patients to receive remdesivir or standard of care, to hunt for

any small effect, particularly in patients who need little or no supplemental oxygen. When the arm finally stopped, about 4500 patients had received the drug. "We believe that we will have solid data that should convincingly demonstrate whether remdesivir has any value," Røttingen says.

The Recovery trial also produced important results, including showing in June 2020 that the cheap steroid dexamethasone could cut deaths from COVID-19 by one-third (*Science*, 10 July 2020, p. 124). And unlike Solidarity, it has continued to add patients and test new candidate drugs. The trial has randomized more than 38,000 participants and is testing five drugs: aspirin; colchicine, a gout treatment; a COVID-19-targeted antibody cocktail made by Regeneron Pharmaceuticals; baricitinib, which treats rheumatoid arthritis; and dimethyl fumarate, a treatment for multiple sclerosis. With about 7000 patients treated with aspirin and 5500 with colchicine, results could come soon, says Martin Landray, a principal investigator of Recovery at the University of Oxford.

The United States has tried to create a similar clinical trial program, but its efforts have been "slow moving, cumbersome, and basically not ... simple like Recovery and

*Science's*  
COVID-19  
reporting is  
supported  
by the  
Heising-Simons  
Foundation.



Solidarity,” Topol says. Meanwhile, Recovery has recently expanded to include patients in Indonesia and Nepal, a move to build capacity to run clinical trials in those countries.

Solidarity, spread across dozens of countries, has been harder to manage than Recovery and has had some bad luck. Immediately after the results on the first four drugs were published, Solidarity negotiated with AstraZeneca to test its cancer drug acalabrutinib, which dampens the immune system. Investigators changed treatment protocols to include the medicine, but then the company decided not to give the green light. Solidarity was also hoping to test monoclonal antibodies, but it became clear that the patients most likely to benefit are those with early stage infections, and Solidarity was designed to test drugs in hospitalized patients. So the companies that make the antibodies pulled back, says Soumya Swaminathan, chief scientist at WHO. “Some of those things fell through, and we did lose some time.”

And there was no real plan B or C. “In retrospect, we should have had a pipeline of other drugs that we could add,” Swaminathan says. One problem was that the ad hoc group set up to choose the first batch of drugs for testing was not a permanent body. Only in November 2020 did WHO set up a permanent drug-selecting group.

Another mistake was waiting for a particularly promising drug after the first four all disappointed, Røttingen says. “We maybe were too cautious,” he says. “I think we should have rather started with some cheap generic product while waiting for potentially stronger candidates to come.”

Among the new candidates the executive group discussed last week is the malaria drug artesunate, which has both an anti-inflammatory and an antiviral effect. The researchers also hope to test an inhibitor of tumor necrosis factor, which is involved in inflammation, and another drug that inhibits the complement system, an arm of the immune system. But other parties also need to sign on. “Timing depends on agreements with companies [that make the drugs] and approvals in countries,” Røttingen says.

In future emergencies, Swaminathan says, the process for prioritizing drugs to be tested should be streamlined. “Some kind of global coordination, where you also then make decisions as to which trials are going to look at what, would make sense,” she says.

Despite its doldrums, Solidarity is still a success story, Peto argues. “We are talking about the second most successful trial in the world in terms of recruitment,” he says. “We’ve got 38,000 randomized in Recovery; we’ve got 15,000 randomized in Solidarity. And the next biggest one that I know of is about 1000.” ■

## COVID-19

# Data in paper about Swedish schoolchildren come under fire

Critics question *NEJM* letter that downplayed the risks of keeping schools open with few precautions

By Gretchen Vogel

**P**ediatrician and epidemiologist Jonas Ludvigsson of Sweden’s Karolinska Institute has been a staunch defender of his country’s unorthodox coronavirus policies. Among them was the decision in the spring of 2020 to keep preschools and schools open for children through grade nine, despite limited understanding of the virus and with few precautions to prevent school outbreaks. But Ludvigsson’s research, which suggested that policy was relatively safe—and has been widely cited in arguments against school closures—has repeatedly come under fire from critics of Sweden’s approach.

The latest example is a research letter, published online by *The New England Journal of Medicine* (*NEJM*) on 6 January, that looked at severe disease and deaths among children and teachers in Sweden between March and June 2020. Critics—including the authors of two letters *NEJM* published on 1 March—have said the study was beside the point and a distraction. It’s well known that children are less likely to be hospitalized or die from COVID-19; instead schools worldwide have shut down to slow the spread of the virus in the wider community.

But *Science* has learned that another complaint sent to *NEJM* makes a more serious allegation: that the authors deliberately left out key data that contradicted their conclusion.

The complaint comes from Bodil Malmberg, a private citizen in Vårgårda, Sweden. She used the country’s open records law to obtain email correspondence between Ludvigsson and Swedish chief epidemiologist Anders Tegnell, the architect of the country’s pandemic policies, that shed light on how the paper came about. Malmberg says she requested the emails because the data in the

*NEJM* paper “did not add up.” Ludvigsson does not dispute the content of the emails, but stands by the study’s conclusions. However, he says the barrage of criticism and personal attacks has made him decide to quit COVID-19 research.

Ludvigsson, whose prepandemic research focused on gastroenterology, was one of the 47 original signers of the Great Barrington Declaration, a controversial document published in October 2020 that argued that pandemic policies should focus on protecting the vulnerable while the rest of the population builds up immunity through natural infection.

Ludvigsson’s research seemed to support those ideas. In a review about children’s role in the pandemic, published in *Acta Paediatrica* in May 2020, he reported there had been “no major school outbreaks in Sweden,” which he attributed to “personal communication” from Tegnell. But as critics noted, Swedish media had reported several school outbreaks by then, including one in which at least 18 of 76 staff were infected and one teacher died. (Children were not tested.)

His *NEJM* letter sounded another reassuring note. It reported that in all of Sweden, only 15 children, 10 preschool teachers, and 20 school teachers were admitted to intensive care units for COVID-19 complications between March and June 2020. The authors noted that 69 children ages 1 to 16 died of any cause in Sweden during that same period, compared with 65 between November 2019 and February 2020, suggesting the pandemic had not led to an increase in child deaths.

But the emails obtained by Malmberg show that in July 2020, Ludvigsson wrote to Tegnell that “unfortunately we see a clear indication of excess mortality among children ages 7-16 old, the ages where ‘kids



A barrage of criticism led Jonas Ludvigsson of the Karolinska Institute to quit COVID-19 research.

went to school.” For the years 2015 through 2019, an average of 30.4 children in that age group died in the four spring months; in 2020, 51 children in that age group died, “= excess mortality +68%,” Ludvigsson wrote. The increase could be a fluke, he wrote, especially because the numbers are small. Deaths in 1- to 6-year-olds were below average during the same period, so combining the age groups helped even out the increase, he noted.

The emails “cast a serious shadow” on the research letter, Malmberg wrote in an email to *NEJM*. (The journal declined to comment on her complaint.) Epidemiologist Jonas Björk of Lund University agrees that the time comparison used in the paper was unusual. “I can see no good reason to compare with previous months,” he says. “It is standard to compare with the same period in previous years” to account for seasonality and to decrease statistical uncertainty.

Ludvigsson told *Science* a peer reviewer for *NEJM* suggested the comparison to deaths in November through February, and that he combined the numbers for preschool and school children because of *NEJM*’s length requirements. As part of his 1 March response to the published critiques, he updated the paper’s supplementary data with the monthly deaths from 2015 through 2020, but did not flag the 68% increase in school-aged children.

The rise in mortality is unlikely to be due solely to COVID-19, Björk notes. Although Sweden tested very few children in the early months of the pandemic, fatal cases of COVID-19 would have likely shown up somewhere in the health care system. “This of course must be ruled out by looking at causes of death and medical records in more detail,” he says. And Björk agrees that the increase could be due to chance.

The mortality questions aside, critics say the *NEJM* letter just wasn’t very helpful in the heated debate over school closures. The main concern is not that children may end up in intensive care, but that schools may accelerate community spread, says Antoine Flahault, a global health expert at the University of Geneva and a co-author on one of the critiques in *NEJM*. Nisha Thampi, a pediatric infectious disease physician at the CHEO pediatric health and research center in Ottawa, Canada, agrees. The paper “doesn’t really tell me much about what’s happening to kids in schools,” she says.

Arguing about whether schools are “safe” has slowed down efforts to find ways to reduce the risk of viral spread in classrooms and hallways, Flahault says—which is key to keeping schools open and the virus under control. ■

## EVOLUTION

# Life could use oxygen long before it was abundant

“Major innovation” emerged more than 3 billion years ago but was slow to catch on, study says

By Robert F. Service

**T**he first organisms to “breathe” oxygen—or at least use it—appeared 3.1 billion years ago, according to a new genetic analysis of dozens of families of microbes. The find is surprising because the Great Oxidation Event, which filled Earth’s atmosphere with the precious gas, didn’t occur until some 500 million years later.

“I was pretty thrilled to see this paper,” says Patrick Shih, an evolutionary biologist at the University of California (UC), Davis, because by tracking protein evolution, it offers a new way to reconstruct some of life’s most consequential transformations. “The transition from a world that was mostly anaerobic to one that was mostly aerobic was one of the major innovations in life,” says Tim Lyons, a biogeochemist at UC Riverside.

Scientists broadly agree that Earth’s early atmosphere and oceans were largely devoid of oxygen gas—but perhaps not completely. Geochemists, for example, have found mineral deposits dated to about 3 billion years ago that they argue could only have formed in the presence of oxygen. And genetic analyses of photosynthetic cyanobacteria, which release oxygen gas as a waste product, suggest they may have arisen as early as 3.5 billion years ago.

Yet skeptics have argued that if oxygen producers and users came along that early, they would have spread quickly across the globe. That’s because using oxygen allows organisms to extract more energy from their food. But the Great Oxidation Event, which left sediments around the world filled with red bands of iron oxides, didn’t occur until about 2.4 billion years ago.

In the new study, Dan Tawfik, a biological chemist at the Weizmann Institute of Science, and his Ph.D. student Jagoda Jabłońska decided to look for clues in present-day microbes. They analyzed the genomes of hundreds of organisms thought to be descendants of Earth’s earliest bacte-

ria and archaea. That allowed them to create an evolutionary family tree from the genes for some 700 enzymes that either use or generate oxygen, which they divided into 134 protein families based on structural similarities.

Then, they turned to a long-used approach that tracks the likely mutation rate of proteins to construct a “molecular clock.” The clock enabled them to pin down when the protein families likely evolved, dating 36 with high confidence.

“We saw something quite striking,” Tawfik says: a “clear burst” of microbes using and producing oxygen between 3 billion and 3.1 billion years ago. Twenty-two of the 36 families appear to have emerged

at that time, the team reported last week in *Nature Ecology & Evolution*. Overall, the analysis suggests that about 3.1 billion years ago, an organism (or more likely a collection of organisms) they dub the last universal oxygen ancestor emerged. Ultimately, the ability to use oxygen gave rise to aerobes that could take advantage of the increased energy output that oxygen use enabled. Eventually, those pioneers with their

innovative way of life led to eukaryotic microbes that have a cell nucleus, multicellular organisms, animals, and us.

The new timeline suggests early oxygen producers and users didn’t immediately sweep the planet, the researchers say. Rather, they likely evolved in small pockets that slowly spread over hundreds of millions of years. Only when they became abundant enough did these organisms modify Earth’s environment enough to lead to the Great Oxidation Event. “I feel like an archaeologist that is opening a grave for the first time,” Tawfik says.

Still, Shih and others caution that the team’s dating could be off, because molecular clocks are still an evolving science. “The order of events is almost certainly robust,” says Roger Buick, an astrobiologist at the University of Washington, Seattle. “But the timing of the events may not be.” ■

**“I feel like an archaeologist that is opening a grave for the first time.”**

**Dan Tawfik,**  
Weizmann  
Institute of Science





Images from a new satellite will provide near-real-time monitoring of dwindling Amazon forests.

## ENVIRONMENT

# First Brazilian-made satellite watches the Amazon

Launch promises more deforestation data, but researchers fear government obstruction

By **Sofia Moutinho**

**B**razil's first entirely home-built satellite has joined the fleet of spacecraft monitoring threats to the country's tropical rainforest, the world's largest. With the 28 February launch of Amazonia-1 from a base in India, Brazil now ranks with more than 20 other countries that have managed satellite design, production, and operation. The satellite enables near-daily updates on Amazonian deforestation. But researchers face an unsupportive government that has repeatedly cut budgets for Amazon monitoring and rejected unwelcome findings.

A 2.5-meter-long metallic cuboid, Amazonia-1 carries three wide-angle cameras that can detect any area of deforestation bigger than four soccer fields. Its development, begun in 2008, involved more than a dozen Brazilian companies and an investment of 360 million reais (\$60 million)—about one-sixth the cost to import ready-to-use equipment, says Adenilson Silva, an engineer at Brazil's National Institute for Space Research (INPE) who led the project. Funding and supply shortages postponed the original launch, slated for 2018.

With Amazonia-1, INPE aims to leave behind a disastrous history. In 2003, a satellite exploded during launch from the Brazilian base in Alcântara, killing 21 people. The base hasn't launched a satellite since. It's now operational again, but it's not equipped for craft as big as Amazonia-1, which ranks as a midweight satellite at 640 kilograms.

Now in orbit 752 kilometers above Earth, Amazonia-1 will spend 6 months in tests of its data transmission, sensors and solar

panels, and other systems. Its images, sent to INPE's processing center in Campinas, Brazil, will be freely available to researchers. They'll be integrated into the country's Amazon monitoring programs later this year.

Amazonia-1 will track a rainforest in crisis because of record-breaking clear-cutting and burning, mostly for agriculture and cattle farming. INPE reports 20% of areas officially designated as protected have already been destroyed. Combining data from Amazonia-1 and existing satellites offers a more accurate picture of burned areas and crop and pasture productivity, says landscape ecologist Marcia Macedo of the Woodwell Climate Research Center. "We can now create composite data sets that address new research questions," she says.

Until now, Brazil's Amazon monitoring program has relied primarily on the U.S. satellite Landsat, which provides high-definition images every 16 days, and on two satellites codeveloped by Brazil and China, CBERS-4 and CBERS-4A, which together provide images every 3 to 4 days.

Amazonia-1's cameras, which capture an 850-kilometer-wide strip of Earth at 65-meter resolution, are no sharper than those on the existing satellites. But its addition to the fleet shortens the gap between flyovers to generate new images every day or two. That increases the chances of getting clear pictures without cloud cover and gives authorities faster alerts about new deforestation.

"A day can make all the difference," says Cláudio Almeida, who coordinates INPE's Amazonian monitoring program. Near-real-time alerts mean that "enforcement teams can go to the right place at the right time."

INPE plans to build two more Amazon-monitoring satellites with the infrastructure developed for Amazonia-1. The fleet will give the country technological autonomy it has long desired, Almeida says. He recalls a problem with Landsat in 2012 that forced INPE to buy satellite data with poorer image quality from the U.K. government.

Yet lack of support from the Brazilian government may limit INPE's ability to process a new surge of data, says environmental modeling expert Britaldo Soares Filho of the Federal University of Minas Gerais. "It is not enough to invest in technology without investing in research and people," he says. INPE's budget and staff have been cut repeatedly since 2019, when President Jair Bolsonaro denied the agency's alarming data on deforestation and ousted its director, physicist Ricardo Galvão.

Brazil's proposed 2021 budget includes a new 15% cut to INPE that has already prompted the cancellation of 100 fellowships, which supported nearly one-quarter of the agency's technical staff. Amazonia-1's launch was at risk after seven researchers lost their grants. They were temporarily reinstated with Brazilian Space Agency funds.

The Brazilian Ministry of Defense has meanwhile invested in a parallel remote sensing strategy, allocating 145 million reais in June 2020 for an undisclosed satellite imaging system for Amazon monitoring. The move undermines INPE's goal of relying on its own satellite infrastructure, Galvão says.

But his bigger worry is that new evidence of deforestation will be met with inaction. "I am sure INPE's scientists will provide the data without bowing to any pressure," he says, "but I have doubts that the current government will value this data." ■



Rapid wing movements mark the courtship display of Ecuador's club-winged manakin (*Machaeropterus deliciosus*) and its relatives.

## EVOLUTION

# The genes behind the sexiest birds on the planet

Genomes from the tropical performers called manakins reveal the power of sexual selection

By Elizabeth Pennisi

For a glimpse of the power of sexual selection, the dance of the golden-collared manakin is hard to beat. Each June in the rainforests of Panama, the sparrow-size male birds gather to fluff their brilliant yellow throats, lift their wings, and clap them together in rapid fire, up to 60 times a second. When a female favors a male with her attention, he follows up with acrobatic leaps, more wing snaps, and perhaps a split-second, twisting backflip. “If manakins were human, they would be among the greatest artists, athletes, and socialites in our society,” says Ignacio Moore, an integrative organismal biologist at Virginia Polytechnic Institute and State University.

As biologists have understood since Charles Darwin, such exhibitionism evolves

when females choose to mate with males that have the most extravagant appearances and displays—a proxy for fitness. And now, by studying the genomes of the golden-collared manakin (*Manacus vitellinus*) and its relatives, researchers are exploring the genes that drive these elaborate behaviors and traits. Last month at the virtual meeting of the Society for Integrative and Comparative Biology, Moore and other researchers introduced four manakin genomes, adding to two already published, and singled out genes at work in the birds’ muscles and brains that may make the displays possible.

The work offers “a better understanding of why manakins do all the amazing things that they do,” says Emily DuVal, a behavioral ecologist at Florida State University. Over the past decade, researchers have learned much about how natural selection

affects genomes. “In contrast, we know very little about the underlying basis of sexually selected traits,” says Christopher Balakrishnan, an evolutionary biologist at East Carolina University (ECU). By mapping traits and genes onto the manakin family tree, researchers are beginning to trace the stepwise genetic changes that led to the most elaborate displays and determine whether sexual selection works differently from natural selection.

Other species—birds of paradise and bowerbirds, in particular—also mount impressive sexual displays. But manakins have a greater variety of such traits and, being more abundant and more accessible, are easier to study in-depth. We can “assess the genomic basis for these behaviors in a way that isn’t possible for many other complex behavioral traits in vertebrates,” says Morgan Wirthlin, an evolutionary neurobiologist at Carnegie Mellon University.

As Balakrishnan and his colleagues reported at the meeting, a sweet tooth—or beak—may have set the stage for sexual selection in manakins. Their ancestors are known to have switched their diet from insects to fruit, and researchers suspected the change to a more available and abundant food source gave males extra energy for procuring mates.

By comparing genomes of manakin relatives that continue to eat insects with those of fruit-eating manakins, Balakrishnan, Maude Baldwin from the Max Planck Institute for Ornithology, and colleagues found evidence that fruit eating and elaborate male displays evolved in steps. The researchers learned that the genes coding for a savory taste receptor began to change even before manakins became fruit eaters. By the time the saffron-crested tyrant-manakin (*Neopelma chryscephalum*) evolved, Baldwin reported at the meeting, the receptor had become sensitive to the sweetness of ripe fruits—a trait rare among birds. That species courts with simple hops—partway to the elaborate displays of the fruit-eating species that evolved later.

Wirthlin and others explored the DNA that changed to make those behaviors possible. In her analysis of five manakin genomes, she focused on ultraconserved noncoding elements, segments of DNA that have stayed almost exactly the same across animals ranging from chickens to humans and are thought to play a crucial role in regulating other genes. Given this conservation, she thought they’d be a good place to look for possible fingerprints of sexual selection.

PHOTO: MURRAY COOPER/MINDEN PICTURES



In the manakin genomes, 57 elements showed slight differences from the matching sequences in other species; those changes might alter the activity of the genes they regulate. Some of those elements are clustered around genes for muscle proteins and hormone receptors and some are near genes expressed in the brain, including two, *TLE4* and *MEIS2*, active in a region needed for fast visual processing. Both genes are less active in manakins than in zebra finches, Wirthlin reported—a change that might help male manakins cope with the visual demands of their frenetic dances.

Matthew Fuxjager, an integrative biologist at Brown University, is excited about Wirthlin's finding that evolution may have revved up the activity of genes for the birds' hormone receptors. The high-speed wing clapping in some species requires extra fast and powerful wing pectoral muscles—which are highly sensitive to the male hormone androgen. “Androgens are what dial up the speed,” by changing the activity of muscle performance genes, Fuxjager says.

At the meeting, Balakrishnan reported pinpointing other genes that may also have supercharged those crucial muscles. His genomic analysis suggested that the activity of genes involved in muscle metabolism and growth changed early in manakin evolution, yielding more powerful muscles. He has not looked in females, but he and Fuxjager think the demands of flight, not mating, may have driven those early changes. Then, as sexual selection began to act on later-evolving species, changes in the androgen receptors and other signaling paths made the flight muscles in males capable of the very fast movements needed for the courtship displays. (Other research shows female muscles are not as sensitive to androgens.)

The manakins' performance involves more than sound and movement—in some species it's a social act as well, coordinated among as many as 20 males. In all vertebrates, a network of brain “nuclei”—clusters of similar nerve cells—helps control social behavior, and studies presented at the meeting show the pattern of gene activity in those nuclei varies with testosterone levels. The work, by evolutionary biologist Peri Bolton at ECU and ecologists Brent Horton at Millersville University and Brent Ryder at the Smithsonian National Zoological Park, suggests changes in androgen receptors could have aided the birds' social sophistication as well as their athleticism.

Dazzling as the manakins' displays are, researchers are just as awed by their intricate genetic underpinnings. “Our studies are teaching us that beauty is more than skin deep,” Moore says. ■

## BIOMEDICAL RESEARCH

# NIH apologizes for ‘structural racism,’ pledges change

Activists fault agency for not directly addressing funding disparity between white and Black grant applicants

By Jocelyn Kaiser

National Institutes of Health (NIH) Director Francis Collins this week issued a public apology for what he called “structural racism in biomedical research” and pledged to address it with sweeping actions.

NIH's long-running efforts to expand opportunities for minority researchers “have not been sufficient,” Collins wrote in the statement. “To those individuals in the biomedical research enterprise who have endured disadvantages due to structural racism, I am truly sorry.” The agency plans “new ways to support diversity, equity, and inclusion,” and will also correct policies within the agency “that may harm our workforce and our science,” he added.

NIH's move is, in part, a response to last year's incidents of police brutality as well as the disproportionate impact of the coronavirus pandemic on Black people. At a meeting last week of NIH's Advisory Committee to the Director, a working group on diversity released a report that calls for NIH to “acknowledge the prevalence of racism and anti-Blackness in the scientific workforce.” The group focused on Black people because of the country's 300-year legacy of slavery and segregation, said co-chair Roy Wilson, president of Wayne State University.

NIH has faced long-standing concerns about racial bias in its funding patterns. A 2011 study known as the Ginther report found funding rates for Black researchers were 10 percentage points lower than rates for white researchers. The latest data show improvement: From 2003 to 2020, the number of basic R01 grants awarded to Black investigators rose from 52 to 166, and the success rate of Black applicants doubled to 24%, compared with 31% for white investigators. Still, that is only “incremental improvement,” said Marie Bernard, NIH acting chief officer for scientific workforce diversity.

In a bid to move faster, NIH has launched an initiative called UNITE. Five internal committees leading UNITE have issued a long list of recommendations, including that NIH make public more data about the demographics of its staff and extramural grantees, appoint a diversity officer at each of its 27 institutes and centers, and improve outreach about NIH's diversity training programs. NIH is also seeking suggestions from the public for promoting racial equity.

The agency also plans to spend \$60 million over 5 years from the Common Fund, a pot of money in the director's office, for an initiative focused on health disparities and equity. Some awards will be reserved for minority-serving institutions.

The announcements have drawn a mixed response. “Our group was very excited” by Collins's statement, says Lola Eniola-Adefeso, a chemical and biomedical engineer at the University of Michigan, Ann Arbor. “It's the first time we're seeing that kind of language from the NIH director and NIH.”

But many of the planned steps were presented “in a passive, noncommittal way,”

says Eniola-Adefeso, who with 18 other women biomedical engineers wrote a recent commentary in *Cell* urging NIH to fund more Black scientists. Her group was disappointed that NIH has not agreed to fund Black scientists seeking R01s at the same rate as white scientists. Some observers have argued NIH could narrow the gap by funding Black scientists whose proposals receive peer-review scores that fall just outside the cutoff for funding.

“That is the immediate action that is needed,” Eniola-Adefeso says. “We cannot wait for more studies. We will lose [investigators] from the pipeline which then propagates this vicious cycle.” But NIH's diversity working group noted that Supreme Court decisions make it difficult for the agency to make funding decisions based on race or ethnicity. ■

**“It's the first time we're seeing that kind of language from the NIH director and NIH.”**

**Lola Eniola-Adefeso,**  
University of Michigan,  
Ann Arbor

## FEATURES

# NUCLEAR MEDICINE

After 10 years advising survivors of the Fukushima disaster about radiation, Masaharu Tsubokura thinks the evacuations posed a far bigger health risk

By **Dennis Normile**

**O**ne evening in June 2011, Masaharu Tsubokura went to bed and found he couldn't close his left eye. His face was paralyzed, and for a few weeks the doctor who had spent months counseling residents displaced by a massive nuclear disaster was himself a patient.

The paralysis was temporary. But the stress that caused it has been a constant in Tsubokura's life since he volunteered in Japan's Fukushima prefecture, days after the triple catastrophe that rocked it on 11 March 2011: a magnitude 9 earthquake, a tsunami that rose up to 40 meters, and multiple meltdowns and explosions at the Fukushima Daiichi Nuclear Power Plant. What was meant to be a short volunteer stint giving health checks to evacuees became a career that has lasted 10 years and counting.

In the months after the disaster, Tsubokura moved from routine medicine to measuring radiation exposure. He became adept at explaining radiation basics and risks to residents and officials. "He spent a huge amount of time in town hall meetings, lectures, and dialogues with local people, which made him respected and trusted," says Kenji Shibuya, a global health scholar at King's College London who collaborated with him. And Tsubokura soon reached a controversial conclusion:

The evacuation had a far bigger impact on health than the radiation. "No one died of radiation," he says, whereas uprooting tens of thousands of people caused clear social and health problems.

Early on, Tsubokura did his best to allay fears among evacuees and residents living just outside the evacuation zone. Many people welcomed his reassurances, though some accused him of being an apologist for the power company and the government. But the physician, now 39, persisted.

"Many people would have left and said, 'OK, I tried my best,'" says Gilles Hériard-Dubreuil, a Paris-based consultant involved in community rehabilitation in Belarus after the Chernobyl nuclear plant accident in Ukraine in 1986. It's a sign of Tsubokura's courage and humanity, he says, "that he maintained his presence and he faced the adversity."

Splitting his time between jobs at hospitals in Tokyo and Fukushima, Tsubokura accumulated data that would put the risks in perspective. In more than 140 papers, he and colleagues have documented the relatively low radiation exposure of Fukushima residents and the health impacts of the evacuation—a high death toll among the elderly, increases in chronic diseases, and a decline in general well-being. That perspective is likely to be valuable in the future, says Masahiro Kami, a physician who

was Tsubokura's medicine Ph.D. adviser and heads a nonprofit that strives to improve medical practice in Japan. "A Fukushima-like accident will happen again in China or somewhere in the world," Kami says.

Tsubokura seized "a unique opportunity to study health effects following a nuclear accident," adds Mikhail Balonov, a radiation health specialist at the Research Institute of Radiation Hygiene in St. Petersburg, Russia. High radiation after the Chernobyl accident made its health effects hard to separate from the social and psychological impacts of displacement. But the lower radiation levels at Fukushima allowed Tsubokura to isolate the impacts of the evacuation in his studies, which he mostly financed himself.



PHOTO: MASAHARU TSUBOKURA





Masaharu Tsubokura went from providing routine health care to giving lectures and visiting classrooms.

“My goal was to help the local people, not as a researcher but as a local physician,” Tsubokura says. He wrote papers “to share the knowledge with the scientific community.” But another motivation, he says, “was to record how the disaster affected people [as a way to] give my condolences.”

**TSUBOKURA'S FUKUSHIMA ODYSSEY** began, improbably, in Paris, where he attended a medical meeting in April 2011, less than 1 month after the disaster.

He and his girlfriend were aboard one of the iconic sightseeing barges that ply the Seine, gliding past the stately Parisian facades, when his cellphone rang. Kami was calling from Tokyo, explaining

that physicians were urgently needed. He asked whether Tsubokura could volunteer in Hamadōri—a local name for Fukushima prefecture's coastal region.

Kami says he had confidence Tsubokura was a good fit. The region needed hands-on clinicians, preferably young and adaptable, who could work well with the overwhelmed local physicians struggling to provide basic care. Even while he was a medical undergraduate student, Tsubokura's focus on patients had impressed Kami, one of his professors. Many medical scientists “treat patients as if they are material for research,” Kami says; but for Tsubokura, patients came first and research followed.

An Osaka native, Tsubokura had never

been to Fukushima. “My first reaction was, ‘What's Hamadōri?’” he says. An internet search back at the hotel set him straight: Kami was summoning him to the heart of the disaster. Tsubokura's girlfriend was furious that he might put himself in danger. It would be just a couple of weeks, he recalls promising.

When Tsubokura arrived in the Fukushima city of Minamisōma in late April 2011, Japan was still counting the victims. The earthquake and tsunami had devastated more than 800 kilometers of coastline, leaving 15,899 dead, 2527 missing, and 500,000 homeless. And a nebulous peril had been unleashed: Swamped by the tsunami, the Fukushima Daiichi plant had suffered

explosions and meltdowns that released an estimated 538.1 petabecquerels of radioactivity into the atmosphere.

That amount was about one-tenth of the estimated radiation release in Chernobyl. But it inflicted further trauma on the people of the region. Fearing more radiation releases, the government ordered the evacuation of everyone within 20 kilometers of the plant and under a plume of radiation that poked like a finger toward the northwest. Many more people, living beyond the 20-kilometer line, left voluntarily. Eventually more than 160,000 fled, most within a week or two of the accident.

people outside the evacuation zone that their radiation exposure was likely very low. Although Tsubokura explained the risks and urged residents to make their own decisions, some people accused him of being a government agent intent on minimizing the hazards. The stress and grueling schedule likely contributed to his temporary facial paralysis.

Eventually Tsubokura learned to take hostile questions in stride. At one meeting in Sendai in 2015, Hériard-Dubreuil recalls some audience members grilling Tsubokura, asking: “Are you on the side of the NGOs [nongovernmental organiza-

Tsubokura went back to his lectures better equipped to answer specific questions.

Demand for his presentations picked up in late 2011 and early 2012 as families with children considered returning to the voluntarily evacuated areas ahead of the 1 April start of the new school year. “It was crazy; he was giving lectures day and night,” says Sachiko Bamba, a Minamisōma resident whose Veteran Mothers Society support group arranged venues and printed flyers.

With his boyish demeanor and unruly mop of tousled hair, Tsubokura had a particular rapport with children. “Instead of a one-way presentation of information, he started by asking the children to tell him what they were worried about,” Bamba says. Questions centered on such daily conundrums as whether laundry hung out to dry would get contaminated and the safety of well water. One student asked whether hugging a cat that had played outside carried a risk of radiation exposure. Bamba recalls Tsubokura making a humorous nod to the Japanese custom of removing shoes at the door and saying, “Cats don’t wear shoes, so it may be a good idea to wipe its paws when you bring a cat into the house.”

The Veteran Mothers gathered the material from Tsubokura’s lectures to create an illustrated pamphlet; the 10,000 copies sold out in the blink of an eye, Bamba says. There were two more printings, and volunteers even created an English version so residents could reassure overseas friends. Tsubokura convinced many “that it is OK for us to live here,” Bamba says.

Takako Watanabe was among the believers. Her Minamisōma home was outside the mandatory evacuation zone, but concerns for her then-9-year-old daughter, Misaki, led them to move in with Watanabe’s uncle in neighboring Ibaraki prefecture. She took Misaki back to Minamisōma when schools reopened in late April 2011. But alarmed by “talk of radiation making young girls unable to bear children,” the two evacuated again during the school’s summer break. As the 2012 school year approached, Misaki increasingly missed her Minamisōma classmates. Watanabe attended several of Tsubokura’s presentations. “His easy-to-follow explanations were a relief to hear,” she says, and she and Misaki returned to Minamisōma for good.

Not everyone was convinced. Mizue Kanno, an evacuee from the town of Namie, still doubts that the whole-body counters accurately measured internal exposure. Tsubokura “seems to have worked on behalf of the country and TEPCO,” she says, referring to the Tokyo Electric Power Co., owner of Fukushima Daiichi. Kanno, who cannot return home because of lingering



Fearing radiation from the damaged reactors, masked residents evacuate nearby Minamisōma on 17 March 2011.

Evacuees crammed into schools, gyms, and other public buildings in cities outside the evacuation zones for several months until emergency housing was built. Some people chose to bunk with relatives.

As Tsubokura visited evacuation centers scattered across Fukushima, checking on residents’ health, he heard one overriding concern: “What is radiation?” he was asked. “Is it OK for me to stay here? Is it OK for my children to go outside?” At first he explained radiation basics one on one, drawing on his experience in using radiation to treat leukemia. In early May, one mother asked him to talk to a group of her friends. Tsubokura worked up a PowerPoint presentation, explaining radiation basics and exposure levels in the region. Word got around, and he was soon giving public lectures in Minamisōma and nearby towns.

“Many, many people came to the seminars and asked a lot of questions,” he says. His message was often reassuring, telling

tions]? Are you on the side of the government?” He says Tsubokura answered, “I’m on the side of the people.”

**HARD DATA ON THE RADIATION** risks were scarce, however, so Tsubokura and colleagues set out to change that. Fukushima residents feared they were breathing in radioactive particles and eating contaminated food, major sources of internal radiation exposure after the Chernobyl accident. Minamisōma General Hospital acquired a whole-body radiation counter and launched Fukushima’s first radiation screening program in early July 2011. “The phone rang all day” when the hospital started to take reservations, Tsubokura says. Soon, every time slot available for months was filled.

To his relief, “the numbers were really low,” he says. Meanwhile, authorities bolstered radiation monitoring of the environment and gave residents dosimeters.





Evacuations driven by radiation concerns added to the thousands of people who packed into temporary shelters after the Fukushima earthquake and tsunami.

radiation in Namie, had a friend who died of leukemia, one of five leukemia victims from the same village. And despite official assurances to the contrary, she believes the incidence of cancer has risen in the Fukushima region. “Did the nuclear accident really cause no health damage?” she asks.

**TSUBOKURA HAS COME TO BELIEVE** it did—but indirectly. Scores of the region’s medical personnel—doctors, nurses, technicians, and clerical and support staff—evacuated either under order or voluntarily, often fearing how radiation would affect their young children. In a retrospective study, Tsubokura and colleagues found that hospitals in Minamisōma were working with just half their normal staff during the first month after the disaster, when they were still dealing with earthquake and tsunami injuries and trying to evacuate bedridden patients. Even after 18 months, staffing was 15% less than before the accident, and Tsubokura believes the weakened health care system had grim consequences.

In that first month, “the risk of death rose in both genders and every age group,” Tsubokura wrote in a 2018 review article in the *Journal of the National Institute of Public Health*. The impact was most notable among the elderly living in long-term care facilities. Tsubokura and colleagues found

that among 715 residents of five evacuated Minamisōma nursing homes, the relative risk of death was 2.7 times higher than before the disaster. At one facility, 25% of residents evacuated died within 90 days. The most common cause of death was pneumonia, suggesting “they died as a re-

sult of weakness, a decrease in care, and the general deterioration of their physical condition, and not from the onset of any particular disease,” Tsubokura wrote.

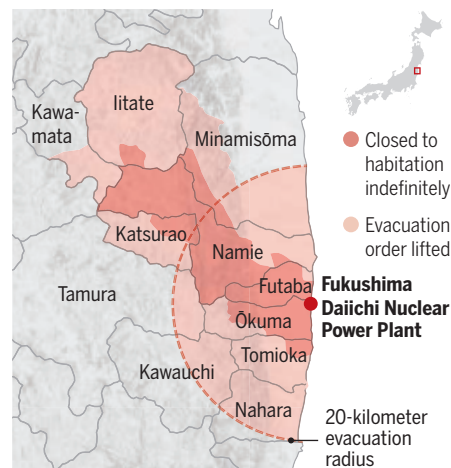
Other health impacts emerged. Akihiko Ozaki, a breast cancer surgeon and frequent Tsubokura collaborator, found that after the disaster the lag between when women recognized possible breast cancer symptoms and when they saw a doctor grew, resulting in more advanced cancer and more difficult treatment. And Tsubokura found that the incidence of diabetes in Minamisōma and nearby Sōma increased by 5% over 3 years, and diabetes-related complications such as stroke became more common and severe. Tsubokura and colleagues blame changes in exercise habits and diet, as well as disrupted familial and community ties. The social stresses “led people to pay less attention to their own health,” Ozaki says.

The findings all suggest that, in Fukushima, those stresses were the real health threat. Evacuation after a nuclear accident may be unavoidable, Tsubokura says. Still, he believes waiting until temporary housing and other facilities are ready could sometimes save lives. “Tsubokura’s findings can be, to some extent, used for the modification of evacuation paradigms,” Balonov says.

Some experts think the hazards of ra-

## Under a cloud

More than 160,000 people were initially evacuated within a 20-kilometer radius of the damaged power station and to the northwest of Fukushima. Many have returned.







Yuji Onuma visits his hometown of Futaba in 2020, nearly 10 years after evacuating. The town, 4 kilometers from the Fukushima nuclear plant, is still off-limits for habitation.

radiation are too poorly understood to warrant a less cautious approach. “Radiation exposure from this accident was not at a level that would cause acute injury,” says Hideyuki Ban, secretary-general of the anti-nuclear Citizens’ Nuclear Information Center in Tokyo. But low-level exposure could still lead to a cancer increase years later, he says. “Delayed effects of radiation exposure should be avoided, and evacuation orders are put in place for that purpose.”

Hériard-Dubreuil says Tsubokura’s more important lesson may be for communities recovering from disruptions of all kinds. Tsubokura’s efforts to give the public reliable information and explain risks empowered people “to become, again, the actors in their own lives,” Hériard-Dubreuil says.

Tsubokura’s Fukushima work teaches other kinds of lessons, his admirers say. His studies there have ranged far beyond his hematology background, something “very unusual for Japanese M.D.s,” who tend to stick to the clinical specialty they studied in medical school, says Shibuya, formerly on the faculty of the University of Tokyo. He adds that Tsubokura “had a broader social perspective from the beginning.”

He has become a mentor for younger doctors and researchers who share his social concerns. Ozaki is one example. He landed at Minamisōma General a few years out of

medical school. Working with Tsubokura allowed him to explore “the role medical care plays in the bigger framework of society,” he says. Toyoaki Sawano, another surgeon, also moved to Minamisōma General in part to study the bullying of schoolchildren who evacuated to other prefectures and the health issues facing the legions of workers who decontaminated Fukushima’s landscape. “I don’t think I would have been on this path through life without meeting professor Tsubokura,” Sawano says.

U.S. student Claire Leppold was pursuing a master’s in public health at the University of Edinburgh when Tsubokura gave a presentation there in early 2015. “I was just blown away” by his research on indirect health impacts, she says. Leppold won a grant from Edinburgh to join the Minamisōma group studying a cohort of evacuees with diabetes. “I have been profoundly lucky to meet him,” says Leppold, now at the University of Melbourne.

Every Monday evening, Tsubokura and younger doctors from the region gather in a “Tsubokura study session” to discuss their research and trade tips on writing papers. Tsubokura says he is out to show his younger colleagues that those working in a rural area can still publish papers garnering international attention. When he thinks of his hematology colleagues from

medical school, he says, “No one has published as many papers as I have; no one has been involved with public health issues like I have been.”

Today, evacuation orders have been lifted for many towns in the disaster region, and residents are returning. But there is more to do in Fukushima, Tsubokura says. In June 2020, he joined the faculty of Fukushima Medical University and became eligible for grants. With funding from Japan’s Nuclear Regulation Authority, he is pursuing several research efforts, including studying how medical and nursing care facilities within the evacuation zone handled bedridden patients. He is also discussing with local authorities how to stave off lifestyle diseases among the 37,000 Fukushima evacuees who still cannot return to their homes and communities. They remain off-limits because annual radiation doses remain at more than 50 millisieverts—more than 10 times the typical annual background radiation.

Tsubokura is well aware of how much of his life he has spent working near ground zero. The woman who objected to his initial sojourn in Fukushima married him despite his disregard for her concerns. But she often reminds him, he says, that “you said you will go to Minamisōma for a week, but it’s been 10 years.” ■



# Endless cleanup

**M**uch of northeastern Japan is well along in recovering from the magnitude 9 earthquake and 40-meter tsunami of 11 March 2011. However, at the Fukushima Daiichi Nuclear Power Plant, “We’re still just very near the starting line” for cleaning up after the meltdowns and explosions triggered by the natural disasters, Fukushima prefecture Governor Masao Uchibori said at a 17 February press briefing.

The plant owner, Tokyo Electric Power Co. (TEPCO), envisions roughly 30 more years of work to retrieve undamaged fuel, remove resolidified melted fuel debris, disassemble the reactors, and dispose of contaminated cooling water. The fuel debris and contaminated water pose especially thorny problems that could threaten that timetable. The government puts the cost of decommissioning the four reactors at 8 trillion yen (\$76 billion); but the Japan Center for Economic Research, a think tank, estimates the bill could be much more.

The earthquake cut the plant’s electrical lines, moving it to emergency generators, which the tsunami swamped 50 minutes later. The power failures disabled pumps that circulate cooling water. As the reactor cores overheated and melted, radioactive steam and hydrogen escaped from the reactor pressure vessels, accumulated in the upper floors of three of the buildings, and then exploded, blowing out roofs and wall panels and spewing fallout over nearby communities (see main story, p. 978).

Though the four reactors are similar, the meltdowns and explosions damaged them differently. So, four unique structures (see graphic, right) have been or will be built to support cranes needed to safely retrieve undamaged fuel stored on upper floors of the units. Removing the fuel is expected to take until 2031.

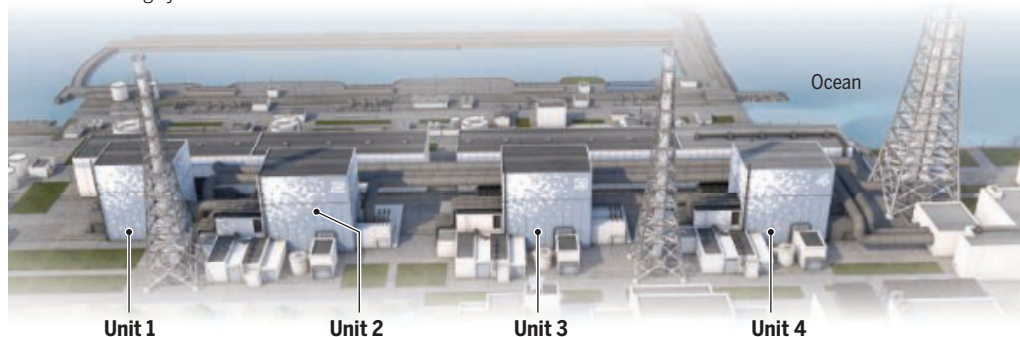
Removing the fuel debris is a tougher task, with no target completion date yet. TEPCO believes some of the debris is still in the reactor cores; some dropped to the bottoms of the reactor pressure vessels, which surround the cores; and some burned through the vessels and landed on the concrete at the base of the reactors. Remote-control devices have been used to try to verify the location and condition of the fuel within the highly contaminated reactors. But, “We do not yet have an accurate grasp of what has happened to the molten fuel,” Uchibori said. In 2022, workers will test a remotely operated mechanical arm to retrieve small amounts of fuel debris believed to be at the bottom of the Unit 2 reactor.

The other major challenge is disposing of water that gets contaminated as it circulates through the reactors to remove residual heat from the fuel debris. Initial treatment removes many radioactive elements but not tritium, an isotope of hydrogen that is extremely difficult to

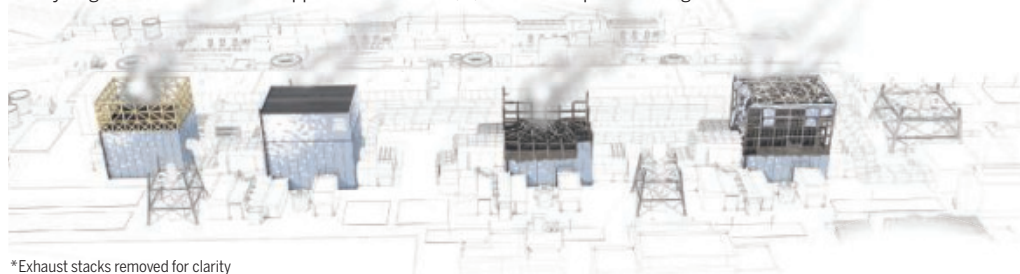
## Past, present, future

It took 237 billion yen (\$2.2 billion) and 10 years to construct the four units damaged in the Fukushima Daiichi Nuclear Power Plant accident. It’s going to take roughly 30 more years and \$76 billion to remove intact nuclear fuel, recover resolidified melted fuel debris, dismantle the reactors, and dispose of contaminated water.

**11 MARCH 2011** At the time of the magnitude 9 earthquake, units 1, 2, and 3 were in operation. When the earthquake hit, the fission reaction automatically shut down in all three reactors, but the tsunami cut off power to reactor cooling systems.

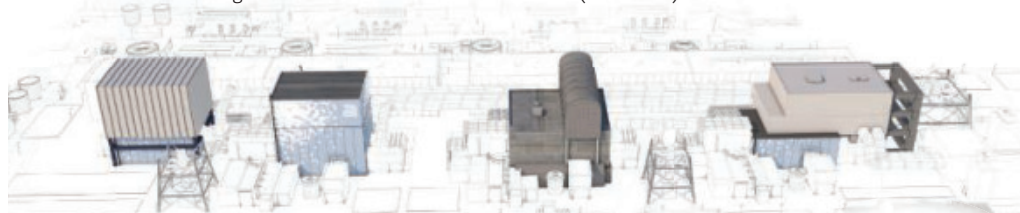


**15 MARCH 2011** With cooling systems disabled, heat built up until nuclear fuel in units 1, 2, and 3 melted. Steam and hydrogen accumulated in the upper floors of units 1, 3, and 4 and exploded. The gas in Unit 2 was vented.



\*Exhaust stacks removed for clarity

**MARCH 2021** Because of differing damage and site conditions, each unit requires a unique structure and strategy to retrieve undamaged fuel and fuel debris. Trial fuel debris removal is expected to start in Unit 2 in 2022. Contaminated cooling water is stored in more than 1000 tanks (not shown).



**Unit 1**  
A planned cover, to be completed by 2023, will contain dust while rubble is removed. Fuel removal will start in 2027.

**Unit 2**  
A structure behind the building in this view will be used to retrieve 615 fuel assemblies—bundles of rods holding fuel—starting in 2024.

**Unit 3**  
A steel framework supports a barrel-shaped roof and fuel-handling equipment. Removal of 566 fuel assemblies should be completed this month.

**Unit 4**  
A structure cantilevered over Unit 4 holds a crane that had removed 1535 fuel assemblies by December 2014. No fuel debris is present.

capture. Over the past decade, more than 1.24 million tons of tritium-contaminated water have accumulated, filling more than 1000 tanks that occupy nearly every available nook on the Fukushima Daiichi campus.

Because it gives off only low-energy beta particles, tritium poses a modest health risk. It is also present in seawater and the atmosphere, something Japan’s Ministry of Economy, Trade and Industry points out in defense of proposals to gradually discharge the accumulated water into the ocean or

atmosphere. But neighboring nations, environmental groups, and the fishing industry fiercely oppose both options. Government officials say no final decision has been made.

Traces of ruthenium, cobalt, strontium, and plutonium isotopes in the treated water also raise concerns, says Ken Buesseler, a marine chemist at the Woods Hole Oceanographic Institution. TEPCO says it will reduce such material “as much as possible.” A reckoning approaches: TEPCO says it will run out of room for water by summer 2022. —D.N.

# INSIGHTS

BOOKS *et al.*

## FILM

### Science at Sundance 2021

Like most events that have taken place since March of last year, the Sundance Film Festival—normally hosted in the cozy ski town of Park City, Utah—was held virtually in 2021. But what it lacked in celebrity sightings and snowy ambiance was more than made up for in the festival's assortment of provocative and timely offerings—from gripping accounts of the COVID-19 pandemic and California's wildfire crisis to mind-bending meditations on the limits of perception and the nature of reality. Read on to see what our reviewers thought of nine of the films that featured strong science and technology themes. —Valerie Thompson

### Son of Monarchs

Reviewed by **Nia Imara**<sup>1</sup>

Science and spirituality unite in *Son of Monarchs*, a new semi-autobiographical film by director Alexis Gambis that tells the story of Mendel, played by Tenoch Huerta

Mejía, a butterfly scientist from the small mining town of Angangueo in Michoacán, Mexico. Since childhood, Mendel has been enthralled by monarch butterflies, which arrive in Angangueo by the millions each year. An endangered insect that crosses two national borders during its annual 3000-mile migration from Canada, the monarch

leads Mendel to fantasize about a world in which humans can fly—across borders, for instance—while also imagining that the ethereal creatures are the souls of relatives who have passed on from this world.

Mendel and his older brother Simon were raised by their grandmother, who encouraged Mendel's curiosity about nature by sharing her own deep knowledge of the natural and nonmaterial worlds. Years later, her death brings Mendel home from New York, where he has spent the past several years working as a postdoctoral researcher in a biology lab. The occasion instigates the spiritual journey that drives the action of the film.

"This land belongs to no one," observes Mendel's uncle Don Gabino as he drives his nephew through town on the day of his return. Deforestation and the adverse environmental impacts of mining and climate change have compounded to wreak havoc on Angangueo. Simon's work in the mines drives an ongoing tension between the two brothers, leading Mendel to remark that these could be the last days of the butterfly, one of many allusions in the film to the mon-

ILLUSTRATION: BENEDETTO CRISTOFANI/SALZMANART





arch as both a political and a spiritual symbol.

The film's cinematography is beautiful, alternating between flashbacks of Mendel's childhood—enchanted scenes of him and his brother playing in a forest filled with butterflies—and his life in New York, where we see him in the lab, peering through a microscope at the magnified scales of a multi-colored wing as he endeavors to understand why the monarch is so colorful. Like his namesake, Mendel is fascinated by the macroscopic consequences of the “invisible” genes. He has developed a technique that uses the gene-editing technique CRISPR to turn on and off the colors of the butterfly wing, one gene at a time.

Seeing a Mexican man portrayed as an innovative, intuitive scientist drawing inspiration from people in his life—women, in particular—who connect with the physical world in a metaphysical way drives home one of the most poignant themes of the film: Science is as diverse and connected with the spiritual as the people who practice it.

**Son of Monarchs**, Alexis Gambis, director, Imaginal Disc, 2020, 97 minutes.

## A Glitch in the Matrix

Reviewed by Valerie Thompson<sup>2</sup>

*A Glitch in the Matrix*, a new film ostensibly about simulation theory—the notion that what we perceive as reality is nothing more than a convincing computer simulation—features no scientific experts. If it had, such individuals might have offered counterarguments to the testimony of the film's “eyewitnesses,” whose ardent belief that they are living in a simulation is generally accepted at face value. But like director Rodney Ascher's 2012 film *Room 237*, which centered on far-out fan theories advanced by obsessive viewers of Stanley Kubrick's 1980 film *The Shining*, *A Glitch in the Matrix* is not necessarily concerned with the veracity of the topic under consideration. It is, instead, a portrait of a particular subculture of people with a provocative worldview.

Featuring archival footage of a speech given by Philip K. Dick in 1977 in which the science fiction author revealed his belief that he was living in a constructed reality and clips of contemporary public fig-

ures who have either expressed support for (Elon Musk) or not ruled out (Neil deGrasse Tyson) the possibility that we are living in a simulation, *A Glitch in the Matrix* leans heavily into quasi-reality with vivid video-game-like animations and scenes from pop culture touchpoints including *The Truman Show* and, of course, *The Matrix*. Cleverly rendered avatars transform the film's main subjects into fantastical creatures—a decision that preserves their anonymity but does little to instill confidence in their assertions—while experts, including University of Oxford philosopher Nick Bostrom, whose 2003 article “Are We Living in a Simulation” compellingly argued in favor of simulation theory, appear unaltered, offering context to the increasingly sinister beliefs toyed with by some of the theory's advocates. (The notion embraced by some believers that other humans might be “nonplayer characters”—computer-generated avatars rather than fellow sentient beings—is “such a school shooter fantasy,” notes cultural critic Emily Pothast, foreshadowing the film's harrowing retelling of one *Matrix* enthusiast's gruesome 2003 killing spree.)

Leaving aside the flawed evidence for simulation theory offered by the film's subjects—the instances of déjà vu and coincidence that they interpret as “glitches” and “synchronicities” but that are better understood as artifacts of our imperfect nervous systems—*A Glitch in the Matrix* lacks a cultural foil that might have placed the ideas presented in the film into broader perspective. Although their physical features are hidden behind avatars, one can infer that the simulation theory proponents that appear in the film are native English-speaking men with Western worldviews. It is perhaps not surprising that such individuals might come to believe that reality has been constructed especially for them. In a very real way, it has.

**A Glitch in the Matrix.** Rodney Ascher, director. Campfire, 2021, 108 minutes.

## Taming the Garden

Reviewed by **Amit Chandra**<sup>3</sup>

In *Taming the Garden*, a surreal documentary from director Salomé Jashi, the evocative images speak for themselves. Colossal trees uprooted from rural communities in the Republic of Georgia creep down narrow village lanes and float across the open sea. But as work crews labor around the clock to remove, transport, and transplant the region's most beautiful trees, environmental concerns yield to larger themes of inequity and political influence.

The film begins with the technical dimensions of this herculean project. Heavy bulldozers and excavators rip into the earth to

tear the giant trees from their homes. Roads must be widened and reinforced to transport them through remote villages, which often requires the felling of more trees along the path. At the edge of the Black Sea, the trees are loaded onto barges and drift mutely along their journey.

Gradually, the communities from which the trees are sourced enter the frame. The film captures families in conflict as they decide whether to sell. The trees in question loom large in many owners' family histories and, in many cases, are now their most valuable economic asset. Once removed, they leave behind a scarred landscape and an emotional void. In one scene, a laborer argues with an elderly woman, suggesting that she plant a new tree, which will be just as tall in a few years. “Will I be alive in two years?” she replies.

The oligarch behind this project is not featured in the documentary, but his presence looms large behind every scene. His purpose is never articulated, although the conversations captured between villagers and work crews allude to his political and economic influence.

In the final scenes, we get a glimpse of the ultimate destination for the ancient trees, the Shekvetili Dendrological Park, a lush tourist destination owned by the oligarch's family. Giant steel cables anchor the transplanted trees to the ground as their root systems take hold, almost as if they are being held against their will. The gratuitous resources consumed to maintain the perfectly manicured grounds and whirring irrigation systems reveal the pathos behind the film's title.

The story told in *Taming the Garden* is ultimately a dystopian one. It reveals how a

community's natural wealth can be mined on the whim of a powerful individual and how impoverished people have little economic agency to push back against those who believe they can tame nature.

**Taming the Garden.** Salomé Jashi, director. Syndicado Film Sales, 2021, 91 minutes.

## All Light, Everywhere

Reviewed by **Nia Imara**<sup>1</sup>

The ideal of achieving complete observational objectivity seems to have been around for at least as long as the idea that such a feat might be possible to achieve. But both the idea and the ideal are dismantled in Theo Anthony's new documentary, *All Light, Everywhere*, a film about human perception and its limits, police surveillance, and, ultimately, power.

The film begins with a history lesson. A few years before the 1874 transit of Venus across the Sun, an astronomer named Pierre Jules César Janssen invented a device intended to record this elusive astronomical event with unprecedented fidelity. Étienne-Jules Marey would later improve upon Janssen's design, creating a “photographic rifle”—the first portable movie camera. Marey redirected his invention from the heavens and pointed it toward his fellow man with the firm conviction that it would uncover an entirely objective truth about the nature of reality. The film follows this fascinating history—science's attempt to capture objective images—uncovering the roots of the surveillance technology central to law enforcement today.

In one scene, a spokesperson for Axon International, a manufacturer of bodycams used by military and police departments around the world, demonstrates how to use the company's most popular “smart weapon,” the Taser. He shows the sharp prongs attached to the ends of long coils of wire, explaining in a breezy manner how they have to stick to “clothes or skin.” The link between cameras, surveillance, and weapons is clear.

Later, a police trainer who is teaching officers in the Baltimore Police Department how to use a bodycam tells his audience, “Cameras don't take sides.” The film's narrator, however, reminds viewers that “there's always a body behind the body camera.” Alluding metaphorically to the blind spot in the human eye, she declares: “At the exact point where the world meets the seeing of the world, we're blind.”

What I appreciate about this film is how it challenges underlying assumptions about the ideal of objectivity and clearly shows how attempts to control the framing of an image—whether scientific, social, or political—are at the heart of power dynamics. *All*



A mature tree uprooted from a rural Georgian community floats along the Black Sea in *Taming the Garden*.





Vivid footage from California's 2018 Camp Fire and Woolsey Fire drives home the devastation wrought during the state's deadliest fire season in *Bring Your Own Brigade*.

*Light, Everywhere* reveals how on many levels, throughout history, attempts to achieve objectivity have frequently resulted in failure and how such efforts have also been harmful to vulnerable, criminalized groups. As Anthony suggested in the Q&A following the Sundance screening of the film, perhaps rather than focusing on this unachievable goal, the more honest and just thing would be to “include ourselves in the act of telling the story.”

**All Light, Everywhere**, Theo Anthony, director, MEMORY, 2021, 105 minutes.

## Bring Your Own Brigade

Reviewed by Mike Gil<sup>4</sup>

In 2018, California experienced the deadliest and most destructive wildfire season on record. The most devastating of the fires that year was the Camp Fire, which took an unexpected turn when it rapidly engulfed the working-class town of Paradise. Residents had little to no warning, and those lucky enough to escape their properties by car found themselves in gridlock on two-lane roads, surrounded on both sides by an inferno. Videos recorded by those inside these vehicles gripped the attention of the world. By its conclusion, the Camp Fire had claimed 85 lives and reduced most of Paradise to ashes. *Bring Your Own Brigade* is a documentary film that draws its audience into the

midst of these events as they unfolded, with first-hand footage and audio recordings as well as gut-wrenching interviews with rescue personnel and citizens who lived through the experience. But that is just the beginning.

The film brilliantly interweaves the timelines of devastation wrought not only by the Camp Fire but also the Woolsey Fire, which began on the same day and ravaged the wealthy enclave of Malibu. Juxtaposing the experience of disaster from both ends of the socioeconomic spectrum, the film paints a biting dichotomy. The role played by wealth inequality in shaping both the immediate and downstream effects of corporate-driven environmental calamities provides a powerful subtext throughout the film.

Following the play-by-play of the harrowing events of that day is a rigorous, systematic foray into how these kinds of wildfires originate, in an attempt to reconcile their unparalleled devastation with their apparent frequency and pervasive causes. It turns out that conventional wisdom about wildfires, their origin, and their role in our environment may be at the root of the problem. According to the film, Western wildfire troubles began with colonialism, as European settlers, many from regions lacking natural fire cycles, failed to anticipate the long-term consequences of building dense structural developments in fire-prone areas in western North America. And although touted by timber lobbyists as a critical service that reduces fuel for wildfires, industrial clear-cutting actually creates fields of debris and early-growth grasses, shrubs, and trees that serve

as fire corridors, spreading devastation to residential areas that may have been spared if old-growth forests had remained.

Although fire takes center stage in the film, *Bring Your Own Brigade* is ultimately about humanity, boldly shining a spotlight on aspects of human psychology and behavior that we rarely face and that, as the film unapologetically showcases, are likely to increasingly threaten our existence in a human-altered landscape.

**Bring Your Own Brigade**, Lucy Walker, director, Good 'n Proper, 2021, 127 minutes.

## Luzzu

Reviewed by Mike Gil<sup>4</sup>

*Luzzu*, directed by Alex Camilleri (*Fahrenheit 451*, *Icarus*), is the first film from Malta to be screened at Sundance and is among only a handful of films that have been made on the Mediterranean island. Local fishermen, most with no previous acting experience, make up the majority of the cast. The scripted film takes a narrative-driven approach to communicating how climate change and ocean overharvesting affect the economically disadvantaged, who bear the brunt of these global problems, combining documentary-like interactions and cinematography in a way that makes it difficult to remember that the film is a work of fiction.

*Luzzu* takes viewers into the lives of Jesmark, played by real-life fisherman and



In *Luzzu*, fisherman and first-time actor Jesmark Scicluna embodies the frustrations of artisanal fishermen grappling with reduced yields and increased bureaucracy.

first-time actor Jesmark Scicluna, and his partner Denise, played by Michela Farrugia. When the couple's baby is diagnosed with a costly health condition, Jesmark faces a harsh reality: Diminishing returns from a sea overexploited by industrial fishing have rendered traditional fishing methods aboard his heirloom luzzu fishing boat increasingly impractical as a means for supporting his family. We follow Jesmark as he struggles to maintain a grip on both his fishing legacy—which spans at least four generations—and the financial needs of his young family, ultimately giving up his beloved luzzu and finding employment with an illegal fishing enterprise that sidesteps fisheries regulations that he sees as punishing small-scale fishermen for the sins of industrial fishing operations.

Jesmark's story of navigating uncharted waters highlights multiple paradoxes. Viewers learn, for example, about a program sponsored by the European Union that offers financial compensation to fishermen who decommission their vessels. The program, intended to facilitate sustainable ocean harvesting practices, appears to have had little effect on commercial fishing operations. By paying independent fishermen to give up their livelihoods, it has instead diminished small-scale, artisanal fishing. Meanwhile, Jesmark's interactions with Uday, a migrant worker whose

financial plight and murky residence status force him to engage in various illegal activities to get by, place the story in a broader, global context.

The film's power lies in the empathy it engenders for the characters it portrays, especially for Jesmark, who feels like the underdog fighting against a system that disenfranchises familial custom in favor of profit. The narrative impressively interweaves relatable dichotomies of various flavors: tradition versus modernity, family obligation versus personal aspiration, financial stability versus career fulfillment, and nature versus industry. But, at its core, *Luzzu* provides a distinctive, personal glimpse into the human experience at the front lines of a major sustainability crisis that extends far beyond the shores of Malta.

**Luzzu**, Alex Camilleri, director, Memento Films International, 2021, 94 minutes.

## In the Earth

Reviewed by **Lindsey Brown**<sup>5</sup>

Against the backdrop of a raging pandemic, scientist Martin Lowery (Joel Fry) sets out for a remote research site to join a colleague who is studying a complex root system deep

in the forest. While being led to the site by park guide Alma (Ellora Torchia), the pair are brutally attacked and robbed. They continue their trek through the woods shoeless and without their gear, before encountering Zach (Reece Shearsmith), who lives in the woods and offers them food and shelter and bandages their wounds. The film shifts from unease to a tense fight for survival, as the pair are forced to join in Zach's arcane rituals by which he worships and seeks to gain the favor of the forest spirit Parnag Fegg.

Part thriller, part horror film, *In the Earth* offers viewers a thought-provoking comparison of the varied methodologies we use to understand and interact with nature as scientific inquiry and ancient tribal ritual begin to blur. In one scene, riffing on Arthur C. Clarke's famous law ("Any sufficiently advanced technology is indistinguishable from magic"), Zach comments that "photography is like magic—then again so is all technology if you don't know how it works." The line between ancient alchemy and modern-day science becomes even thinner after Martin and Alma find Martin's colleague Olivia (Hayley Squires) and discover that her work is more similar to Zach's than it first appears.

Although the pandemic is not the main focus of the story, *In the Earth* was filmed over 15 days during the height of the

<sup>1</sup>Department of Astronomy and Astrophysics, University of California, Santa Cruz, Santa Cruz, CA 95064, USA. Email: nia@ucsc.edu <sup>2</sup>Science, Washington, DC 20005, USA. Email: vthompson@aaas.org <sup>3</sup>Department of International Health, Georgetown University, Washington, DC 20057, USA. Email: amit.chandra@georgetown.edu <sup>4</sup>Department of Ecology and Evolutionary Biology, University of Colorado Boulder, Boulder, CO 80309, USA. Email: mikegil@sciall.org <sup>5</sup>Division of Biotechnology Manufacturing, U.S. Food and Drug Administration (FDA), Silver Spring, MD 20993, USA. Email: lindsey.james.brown@gmail.com



COVID-19 pandemic and it aims to capture the zeitgeist of our current era, even as its vivid forest setting offers a brief respite for those of us who find ourselves stuck inside for days on end. The film's main characters are thrust into extraordinary circumstances controlled by forces they do not fully comprehend, individuals manipulate science and myth to advance their own aims, and seemingly disparate people must work together to survive.

"I wanted to make a film that contextualized the moment," explained director Ben Wheatley in the press notes accompanying the film. To ignore the pandemic would have been "like making a film in 1946 and not referencing the fact that everyone had just gone through the second world war."

**Editor's note:** The content of this review is solely the responsibility of the author and does not necessarily represent the views of the U.S. FDA.

**In the Earth**, Ben Wheatley, director, Neon, 2020, 107 minutes.

## Fire in the Mountains

Reviewed by **Amit Chandra**<sup>3</sup>

Amid breathtaking mountain views of the Himalayan foothills in Northern India, hardworking Chandra (Vinamrata Rai) manages her own household alongside a homestay for visiting tourists. When necessary, she carries her preteen son, Prakash (Mayank Singh Jaira), up and down the steep trail that serves as the remote village's only means of access. Prakash remains wheelchair-bound following a recent injury, despite his physician's insistence that there is no medical reason preventing the boy from walking.

Chandra carefully hides her earnings from her frequently intoxicated husband, Dharam (Chandan Bisht), so that she can pay for Prakash's medical appointments. Dharam, meanwhile, spends his time searching for the hidden cash in order to finance a religious ceremony that an eccentric faith healer has promised will cure his son.

Chandra's daydreaming daughter Seema (Harshita Tewari) and a lecherous local politician round out *Fire in the Mountain's* cast of complex characters. Seema is a top student at the local high school, but her attention is increasingly diverted toward romantic interests and the seduction of social media. Meanwhile, the politician offers his support to ensure that a road is built to Chandra's village, although his offer comes at a steep price.

*Fire in the Mountains* is a tale of contemporary India that treads familiar yet fertile storytelling themes: urban versus rural, ambition versus apathy, and modernity versus tradition. These tensions are further underscored by optimistic radio reports on the country's progress that appear throughout the film and visuals that convey the harsh realities of village life.

Writer and director Ajitpal Singh was inspired to make this film after the untimely passing of a female cousin, who died after a brief illness when her in-laws took her to a faith healer rather than a hospital. Given his cousin's high level of education, Singh was convinced that she would not have



Chandra struggles to reconcile modern medicine with traditional healing practices in *Fire in the Mountains*.

made that choice on her own, that someone else made that choice for her. In the film, Chandra wrestles back her agency from family, community, and state.

The film's tension builds toward an explosive and chaotic climax, shaking loose each character from their self-possessed roles: Chandra from her restraint, Dharam from his indifference, and even Prakash, whose affliction proves to be beyond the reach of either parent's cure.

**Fire in the Mountains**, Ajitpal Singh, director, Jar Pictures, 2020, 83 minutes.

## In the Same Breath

Reviewed by **Lindsey Brown**<sup>5</sup>

On 1 January 2020, the Chinese state news reported that eight doctors had been arrested for spreading rumors about a new form of pneumonia. This brief report

would inadvertently become the first official acknowledgment of COVID-19. *In the Same Breath*, by filmmaker Nanfu Wang (*One Child Nation*), examines the impact that misinformation about the coronavirus has had on people in China and the United States.

As the documentary begins, Wang recounts how she was returning to the United States from China on 23 January 2020, the same day that the lockdown in Wuhan was announced. After chest x-rays started flooding Chinese social media platforms because the hospitals were overwhelmed, she assembled a team of 10 camera people who risked arrest as they documented life under lockdown and captured the drama that was unfolding.

"When the government is telling us where to look, they're also telling us where not to look," advises Wang. Footage from Chinese New Year celebrations and large government meetings where Communist Party leaders assured the Chinese public and the rest of the world that everything was under control is juxtaposed with contemporaneous social media posts, footage of busy hospital wards, off-camera interviews with scared patients and frustrated hospital staff, and closed-circuit camera footage of patients with respiratory symptoms seeking care in December 2019 at a clinic located near the market where the virus is thought to have originated.

Turning the lens from China to the United States, Wang's U.S. camera team captured footage documenting how misinformation likewise wreaked havoc on the U.S. health care system, as evidenced by the number of deaths witnessed by traumatized health care workers and by the emergence of large groups of pandemic-denying protesters. Even as both countries' leadership cited the other as a foil to extol their own virtues, the film reveals how citizens in China and the United States became casualties in what would ultimately become a futile quest to maintain appearances.

The film ends with scenes from Wuhan's eerily "normal" 2020 New Year's Eve celebrations. As fireworks explode over packed city streets, Wang reminds us that normality has led to our current circumstances. Insisting on rushing back to normal, she cautions, is not the answer.

**Editor's note:** The content of this review is solely the responsibility of the author and does not necessarily represent the views of the U.S. FDA.

**In the Same Breath**, Nanfu Wang, director, Stay At Home Production Inc., 2021, 95 minutes.

10.1126/science.abg9908



## HYDROLOGY

# Deforestation, forestation, and water supply

A systematic approach helps to illuminate the complex forest-water nexus

By **Mingfang Zhang**<sup>1</sup> and **Xiaohua Wei**<sup>2</sup>

**F**orests as natural reservoirs and filters can store, release, and purify water through their interactions with hydrological processes. For humans, a clean, stable, and predictable water supply is one of the most valuable ecosystem services provided by forests. Yet, globally, forests have undergone many changes driven by human activities (logging, reforestation, afforestation, agriculture, and urbanization) and natural disturbances (wildfires and insect infestations). From 2010 to 2015, tropical forests declined by 5.5 million ha year<sup>-1</sup>, whereas temperate forests expanded by 2.2 million ha year<sup>-1</sup> (1). The effects of both deforestation and forestation (reforestation and afforestation) on water supply have generated serious

concerns and debates (2, 3), particularly after recent catastrophic fires in Australia and the western United States. However, hydrological consequences of forest changes are never simple, and future research and watershed management require a systematic approach that considers key contributing factors and a broad spectrum of response variables related to hydrological services.

Zhang *et al.* showed the consistent tendency of deforestation to increase annual streamflow (4). More than 80% of deforested watersheds had annual streamflow increases ranging from 0.4 to 599.1%, mainly owing to reduced evapotranspiration after 1.7 to 100% forest cover loss (4). The large variations in the magnitude of changes depend on the scale, type, and severity of forest disturbance, climate, and watershed properties (4, 5). Larger-scale disturbance tends to cause greater increase in annual streamflow. Hydrological response to fire is similar to the response to logging, but the severity of the impact varies with climate, fuel accumulation, fire intensity, overstory tree mortality,

Large-scale deforestation and plantation threaten the water supply for local and regional communities in Indonesia by altering streamflow conditions.

and climate. Fires often cause hydrophobic soils, with reduced soil infiltration and acceleration of surface runoff and soil erosion. In a recent national assessment of the contiguous United States, forest fires had the greatest increase in annual streamflow in semiarid regions, followed by warm temperate and humid continental climate regions, with insignificant responses in the subtropical Southeast (6). The hydrological impact of insect infestation is likely less pronounced than those of other disturbances. Large-scale beetle outbreaks in the western United States and British Columbia, Canada, over recent decades were predicted to increase streamflow, with reduced evapotranspiration because of the death of infested trees (5). However, further evidence showed negligible impacts of beetle infestation on annual streamflow, owing to increased evapotranspiration of surviving trees and understory vegetation (7).

Forestation can either reduce annual streamflow or increase it (4, 8). Zhang *et al.* (4) found that 60% of the forestation watersheds had annual streamflow reduced by 0.7 to 65.1% with 0.7 to 100% forest cover gain, whereas 30% of them (mostly small watersheds) had annual streamflow increased by 7 to 167.7% with 12 to 100% forest cover gain. Variations in annual streamflow response to forestation are even greater than those caused by deforestation, possibly owing to site conditions prior to forestation and tree species selected. Planting with a single fast-growing exotic species can have greater reduction in annual streamflow than with native species (8). Streamflow reductions after forestation are more common in semiarid and arid regions than in the humid subtropics and tropics (4, 5). Large-scale reforestation programs in the semiarid Loess Plateau in China caused substantial streamflow reductions that consequently approached water resource limits (9).

Dry-season low flow is critical for water supply, particularly in the face of more severe droughts under climate change. Low-flow response to forest change can be positive, neutral, or negative (5, 10). The variable low-flow responses are mainly attributed to low-flow generation processes, forest characteristics (age, species, and regeneration), forestry practices (retention of riparian buffers, logging methods, and silviculture), changes in soil conditions, and choice of low-flow metrics (daily or 7-day minimum flow). Nevertheless, negative low-flow response is commonly expected if soil water storage and infiltration capacities are impaired by forest disturbances (soil compaction and erosion

<sup>1</sup>School of Resources and Environment, University of Electronic Science and Technology of China, Chengdu 611731, China. <sup>2</sup>Department of Earth, Environmental and Geographic Sciences, University of British Columbia (Okanagan), Kelowna, British Columbia, V1V 1V7, Canada. Email: mingfangzhang@uestc.edu.cn



from logging, and soil water repellency following severe fires), and their recovery through reforestation could take much longer, because of the difficulty in restoring damaged soils (10).

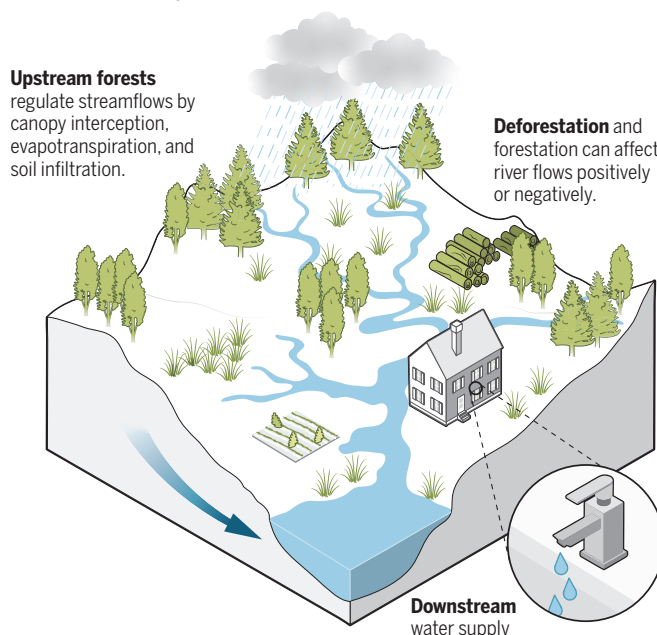
Generally, climate, watershed properties, forest characteristics, and their interactions are the major drivers for large variations in hydrological responses to forest change (2, 4). Zhou *et al.* assessed global land-cover effects on annual streamflow, based on a general theoretical framework (11). They found that hydrological sensitivity to land-cover change was determined by watershed properties (watershed size, slope, configuration, and soil), climate (precipitation or potential evaporation), and their interactions, where land cover and watershed properties jointly indicate water retention ability. Land cover or forest change can cause greater hydrological responses in drier watersheds or those with low water retention capacity. Similarly, McDonnell *et al.* (12) recommended studying watershed storages and water movements in the vertical zone that includes forest canopy, soil, fresh bedrock, and the bottom of groundwater (13), to further reveal the mechanisms for variable hydrological response to forest change.

The feedback between forests and climate may also introduce complexity. Forests can supply atmospheric moisture through evapotranspiration and potentially increase precipitation (precipitation recycling) locally and in downwind directions. Therefore, forest change affects not only downstream river flow, but also precipitation and water supply downwind (5). Lawrence and Vandecar revealed variable rainfall responses to tropical deforestation across landscapes, depending on deforestation thresholds, such as reduced rainfall by large-scale deforestation and increased rainfall by small clearings (14). The effects of forest change on precipitation are likely related to topography, prevailing wind, and climate, because they affect moisture residence time, moisture transportation, and precipitation generation. The lack of observational evidence highlights the need for research on the feedback between climate and forest change at regional or continental scales.

Time scale is important for understanding these variations. Hydrological effects of forest change can vary with time as forests regrow. Coble *et al.* reviewed long-term responses of low flows to logging in 25 small catchments in North America (10). They identified dynamic

## The complex influence of forests on water supply

Forests in watersheds play a critical role in regulating downstream water supply and associated ecosystem services.



low-flow responses over three distinct time periods associated with the development of forest canopy leaf area index and corresponding evapotranspiration: consistent increase in the first 5 to 10 years, variable responses (increase, no change, or decline) during the next 10 to 20 years, and substantial decline in some (16 out of 25) watersheds multiple decades later. However, no decline in low flows was found in nine watersheds during the third period—likely dependent on similar factors previously identified for variations in low-flow response. The dynamic hydrological responses suggest that long-term studies are critical for fully capturing possible trends and variations in the effects of forest change on water supply (5).

The consistencies and large variations over space and time in streamflow responses to forest change call for a systematic perspective to elucidate both explanatory (factors affecting hydrological functions) and response (hydrological functions) variables in future studies (see the figure). In the systematic context, explanatory variables, including climate, forest, watershed properties, and their interactions and feedback across multiple spatial-temporal scales that jointly control streamflow responses, should all be assessed. To better clarify the response, a more complete spectrum of hydrological variables, including the magnitude, duration, timing, frequency, and variability of flows, which collectively determine river flow conditions, aquatic functions, and thus ecosystem services such as water supply, should be included in an assessment (15). Nonetheless, water-supply

assessments often use limited hydrological variables (such as annual mean flows), which could underestimate total hydrological functions or even produce misleading conclusions resulting from different or contrasting responses of various flow variables.

A systematic assessment of the effects of deforestation and forestation on water supply requires multidisciplinary collaborations. The classic paired watershed experiment (PWE: one watershed as a control and the others as the treatment) (12), mainly designed to assess streamflow response to forest change, has limitations to evaluate interactions and feedback among water, forests, climate, and watershed properties. Future PWEs should systematically consider more variables and processes (flow pathways, water storage and retention, and hydrological sensitivity) with various approaches (isotopic

tracing, telemetering, and modeling). With long-term in situ monitoring and growing remote-sensing data, the forest-water nexus at larger spatial scales should be explored using advanced analytical tools (machine learning, and coupled climatic-ecohydrological modeling) within a systematic context. Future assessment should also focus on watershed management tools such as payments for ecosystem services, with the inclusion of more representative water variables to support synergies or trade-offs between hydrological and other ecosystem services provided by forests in a changing environment. ■

### REFERENCES AND NOTES

1. R. J. Keenan *et al.*, *For. Ecol. Manage.* **352**, 9 (2015).
2. X. Wei *et al.*, *Glob. Change Biol.* **24**, 786 (2018).
3. K. D. Holl, P. H. S. Brancalion, *Science* **368**, 580 (2020).
4. M. Zhang *et al.*, *J. Hydrol. (Amst.)* **546**, 44 (2017).
5. I. F. Creed *et al.*, in *Forest and Water on a Changing Planet: Vulnerability, Adaptation and Governance Opportunities. A Global Assessment Report*, I. F. Creed, M. van Noordwijk, Eds. (International Union of Forest Research Organizations, 2018).
6. D. W. Hallema *et al.*, *Nat. Commun.* **9**, 1307 (2018).
7. K. M. Sliniski, T. S. Hogue, A. T. Porter, J. E. McCray, *Environ. Res. Lett.* **11**, 074010 (2016).
8. S. Filoso, M. O. Bezerra, K. C. B. Weiss, M. A. Palmer, *PLOS ONE* **12**, e0183210 (2017).
9. X. Feng *et al.*, *Nat. Clim. Chang.* **6**, 1019 (2016).
10. A. A. Coble *et al.*, *Sci. Total Environ.* **730**, 138926 (2020).
11. G. Zhou *et al.*, *Nat. Commun.* **6**, 5918 (2015).
12. J. McDonnell *et al.*, *Nat. Sustain.* **1**, 378 (2018).
13. G. Grant, W. Dietrich, *Water Resour. Res.* **53**, 2605 (2017).
14. D. Lawrence, K. Vandecar, *Nat. Clim. Chang.* **5**, 27 (2015).
15. N. L. Poff, J. K. H. Zimmerman, *Freshw. Biol.* **55**, 194 (2010).

### ACKNOWLEDGMENTS

This paper was supported by China National Science Foundation (no. 31770759).

10.1126/science.abe7821

## FERROELECTRICS

# Whirls and swirls of polarization

Exotic toroidal polarization textures in a polymer ferroelectric interact with terahertz radiation

By Lane W. Martin<sup>1,2</sup>

In Greek mythology, sailors feared the perils of getting near the whirlpool said to be created by the sea monster Charybdis, who created turbulence by swallowing huge amounts of water. Today, researchers are creating whirlpools in materials at the nano- and microscale, not from water but from magnetic spins or electric dipoles. In return, they have observed exotic phenomena and physics. On page 1050 of this issue, Guo *et al.* (1) provide another example of how the exacting control of materials is producing effects one thought impossible to achieve. They created self-assembled topological and toroidal polarization textures—that is, a toroidal polarization arrangement in which the polar toroidal dipole configuration corresponds to the field of a solenoid bent into a torus (see the figure, bottom) in ferroelectric polymers. Because of the exotic structure, this material exhibits properties not observed in its native state.

For some time, similar whirling structures were observed in the spins of magnetic materials. Such features include vortex structures that act as domain walls and so-called skyrmions, nanoscale whirls of smoothly evolving spin that are robust because of their topological nature (2). Such emergent-spin topologies have been widely studied and are currently being considered for high-density, ultrafast memory applications (3). In ferroelectrics (materials that have a spontaneous polarization instead of magnetization), it was not expected that such smoothly evolving, topologically protected structures would be possible because the primary order parameter (polarization) is strongly coupled to the lattice. Thus, continuous evolution of the order parameter would result in a large cost in elastic energy.

Despite this limitation, theoretical predictions provided clues for overcoming these limitations to realize vortex structures (4). In turn, as experimental approaches both for synthesizing and characterizing materials and order-parameter structures at the nanoscale matured, such continuous-symmetry

structures were realized in the form of polarization vortices and skyrmions in  $(\text{PbTiO}_3)_m/(\text{SrTiO}_3)_n$  superlattices (5–7), where  $m$  and  $n$  are the respective number of repeated layers in artificial stacks of different materials created with unit cell-level control. Researchers found that they could create vortices and skyrmions in superlattices by manipulating various energy scales.

By controlling the electric, elastic, and gradient energies, a material could effectively occupy a state in which no single energy dominated. Nanoscale features (with typical

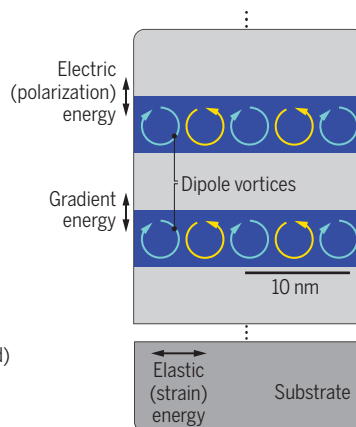
## Emergent polar textures

In ferroelectrics (materials that have a spontaneous polarization), creating smoothly evolving, topologically protected dipole vortices must overcome large elastic energy costs.

### Complex oxides

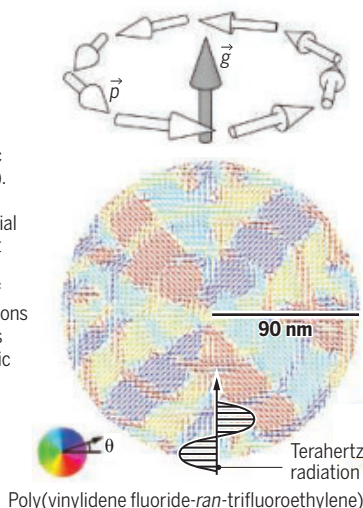
Superlattice heterostructures put electrical polarization, gradient, and strain energies in competition. The emergent and exotic dipole structures form on a 10-nm scale.

- $\text{SrTiO}_3$  (not polarized)
- $\text{PbTiO}_3$  (polarized)



### Ferroelectric polymers

Guo *et al.* showed that similar structures can form in toroidally structured ferroelectric polymer films (bottom). The circle of electric dipoles  $\vec{p}$  induces an axial toroidal dipole moment  $\vec{g}$  (top). The intrinsic polarization plays off of periodic strain modulations and electrostatic forces to produce similar exotic polarization structures. These structures can interact with terahertz radiation.



length scales of ~10 nm) once thought impossible were observed (see the figure, top) that had merely been hidden until the appropriate energy competitions could be produced. It was quickly realized that emergent properties and function also followed. These effects included emergent chirality (8), an exotic capacitive response (9, 10), and an emergent order parameter—a so-called electric toroidal moment (4, 11) that can also give rise to a range of phenomena, such as pyrotoroidic and piezotoroidic effects, in response to thermodynamic stimuli.

Guo *et al.* have now extended this exciting direction in ferroelectrics to a new class of materials based on the ferroelectric polymer poly(vinylidene fluoride-*ran*-trifluoroethylene), or P(VDF-TrFE). Instead of heterostructured complex oxides, they formed exotic polar structures with toroidal-polar topology in a single-layer film of the polymer through self-organized alignment of the polymer chains (see the figure, bottom). This material was purposefully chosen to provide the most robust polarization. The authors used a creative melt-recrystallization process formed ring-shaped bands and a periodically undulating surface topography (which could be described as “wrinkled”).

This structure produces substantial strain in a periodic fashion that ultimately provides the appropriate competition between the same electric, elastic, and gradient energies to drive the formation of a concentric, continuously rotating polar structure. It has a net axial moment that makes it toroidal. What is perhaps most unexpected is that whereas the complex-oxide superlattices produce exotic-polar topologies at the ~10-nm length scale, Guo *et al.* created features at the 100- to 1000-nm length scale. This observation suggests that there are multiple length scales across which similar energy competition might produce exotic structures, and also that mesoscopic hierarchical-polarization textures (unit cell-level structures inside of domain-level structures) could enable exotic function.

In that regard, when Guo *et al.* probed the properties of the system, they found that it exhibited unexpected responses. Perpendicular to the polymer chains, there is continuous rotation and the formation of a toroidal structure, but parallel to the polymer chains, unexpected relaxor-

<sup>1</sup>Department of Materials Science and Engineering, University of California, Berkeley, Berkeley, CA 94720, USA. <sup>2</sup>Materials Sciences Division, Lawrence Berkeley National Laboratory, Berkeley, CA 94720, USA. Email: lwmartin@berkeley.edu



like response is observed. Relaxors are characterized by diffuse-phase transitions and frequency dispersion of dielectric response arising from the complex-polar structure and fluctuations of that structure with applied field and temperature (12). Chemical disorder, random electric fields, and coexisting local dynamics are all sources of such fluctuations in complex materials. The periodic strain on the material likely induces this range of responses to applied stimuli and the observed relaxor-like response.

The authors also recognized that strong coupling between ferroelectric polarization and light should occur at the length scale of the emergent toroidal-polar topology, which would be in the terahertz range. They manipulated terahertz radiation with this material in a way that the parent material normally could not. This result could find application in terahertz optics for rastering and light modulation and motivates further design of such mesoscopic polar structures to address important needs in applications.

What this study by Guo *et al.* and other studies in recent years have shown is that advances in our ability to make and probe materials can potentially rewrite what we think is possible. The current work shows the universality of the power of manipulating energy scales—be it in unit cell-sized superlattices or micrometer-sized polymer crystals—to carefully control the pertinent energies that can produce unexpected features. The observation of toroidal order may not only lead to exotic optical responses but could also provide for exotic electric field-induced function and the potential for new types of thermal and electromechanical responses. Also, because of the intrinsically mesoscopic nature of the polymer systems, the study by Guo *et al.* represents just the beginning of what could be a large design landscape in which exotic dielectric, optical, and other properties could be coaxed from these complex materials. ■

#### REFERENCES AND NOTES

1. M. Guo *et al.*, *Science* **371**, 1050 (2021).
2. A. Fert, N. Reyren, V. Cros, *Nat. Rev. Mater.* **2**, 17031 (2017).
3. N. Nagaosa, Y. Tokura, *Nat. Nanotechnol.* **8**, 899 (2013).
4. I. I. Naumov, L. Bellaiche, H. Fu, *Nature* **432**, 737 (2004).
5. A. K. Yadav *et al.*, *Nature* **530**, 198 (2016).
6. A. R. Damodaran *et al.*, *Nat. Mater.* **16**, 1003 (2017).
7. S. Das *et al.*, *Nature* **568**, 368 (2019).
8. P. Shafer *et al.*, *Proc. Natl. Acad. Sci. U.S.A.* **115**, 915 (2018).
9. A. K. Yadav *et al.*, *Nature* **565**, 468 (2019).
10. S. Das *et al.*, *Nat. Mater.* **20**, 194 (2020).
11. H. Schmid, *J. Phys. Condens. Matter* **20**, 434201 (2008).
12. R. A. Cowley, S. N. Gvasaliya, S. G. Lushnikov, B. Roessli, G. M. Rotaru, *Adv. Phys.* **60**, 229 (2011).

#### ACKNOWLEDGMENTS

L.W.M. acknowledges support from the National Science Foundation under grant DMR-1708615.

10.1126/science.abg4477

#### IMMUNOLOGY

# Surgical adhesions: A sticky macrophage problem

Body-cavity macrophages superaggregate in a platelet-like response to wounding

By Sarah E. Herrick and Judith E. Allen

It is estimated that ~66% of patients who have gastrointestinal surgery will develop adhesions (1). These bands of scar tissue arise in the abdominal cavity and can lead to small bowel obstruction and infertility in women as well as severe chronic abdominal pain. Unfortunately, there are no satisfactory ways to prevent adhesions, and once formed, surgery is often required to lyse them, which predisposes to further adhesions. Thus, there is an urgent need to develop more effective means to prevent them from forming or to minimize their growth. On page 1013 of this issue, Zindel *et al.* (2) demonstrate that macrophages in the peritoneal cavity home to sites of damage, forming an immediate protective wound covering. In response to surgical insult, these macrophages act like platelets to form superaggregates, which then develop into adhesions. A fascinating parallel exists with invertebrates whereby body-cavity macrophages express evolutionarily ancient receptors, which may be potential targets for adhesion prevention.

The peritoneum is a gliding interface that lines the fluid-filled body cavity and internal organs. It comprises a surface monolayer of mesothelial cells adherent to a basement membrane, overlying a submesothelial connective tissue rich in capillaries and lymphatics. Surgical adhesions are proposed to evolve from initial fibrin clots spanning between internal organs and/or the cavity wall (3). Critically, reduced fibrinolysis after surgery and subsequent collagen production stabilizes these initial connections and stimulates the formation of mature myofibroblast-rich fibrous bands. Indeed, experimental animal studies and clinical trials investigating the

prevention of surgical adhesions have been based on the idea of regulating coagulation and fibrinolytic pathways (4).

More recently, attention has shifted to identifying the source of myofibroblasts that stabilize early adhesions. In addition to tissue-resident fibroblasts (5), mesothelial cells have been shown to participate in the generation of fibroblasts and adhesion development (6, 7) by undergoing a phenotypic switch, called mesothelial-to-mesenchymal transition (MMT). Anti-adhesion strategies are exploring ways to reduce MMT and hence prevent adhesions from forming (8).

Although reduced fibrinolysis and MMT are recognized events in the biology of surgical adhesions, data on the contribution of macrophages are inconclusive. Rigorous ex-

ploration of the heterogeneity and functional diversity of serous-cavity macrophage subpopulations during adhesion formation is needed to resolve this uncertainty (9). Macrophages that are free-floating in peritoneal fluid include monocyte-derived cells as well as resident macrophages that rely on the transcription factor GATA-binding protein 6 (GATA6) for their differ-

entiation and survival (10, 11). A previous study had demonstrated that GATA6<sup>+</sup> cavity macrophages are rapidly recruited, via a nonvascular route, to an injury site on the liver of mice where they assisted tissue repair (12).

Building on these observations, Zindel *et al.* showed that within minutes of laser-induced wounding of the cavity wall in mice, GATA6<sup>+</sup> macrophages provide a protective wound covering (see the figure). Although it remains unclear exactly how serous-cavity macrophages recognize sites of injury, recruitment was by passive transport, relying on the natural movement of peritoneal fluid. Free-floating macrophages became adherent only after injury. Within several hours, macrophages formed cell-to-cell aggregates with secondary tethers to the initially adherent cells. Notably, GATA6<sup>+</sup> mac-

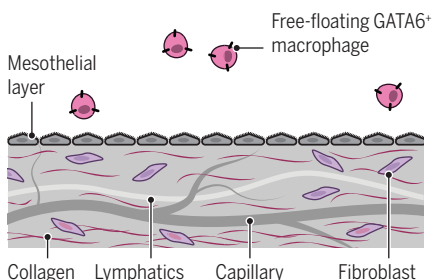
**“...body-cavity macrophages express evolutionarily ancient receptors, which may be potential targets for adhesion prevention.”**

School of Biological Sciences, Faculty of Biology, Medicine and Health, The University of Manchester, Manchester, UK.  
Email: sarah.herrick@manchester.ac.uk

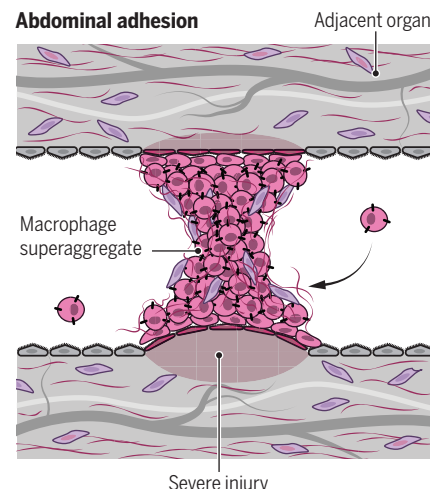
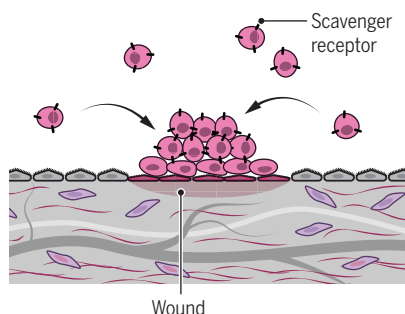
## Macrophages as precursors to adhesions

Free-floating GATA-binding protein 6 (GATA6)-expressing macrophages in the abdominal cavity are recruited to wound sites and form aggregates using scavenger receptors. In response to more severe injury, such as abdominal surgery, they form superaggregates that evolve into mature collagen-rich adhesions.

### Healthy peritoneum



### Damaged peritoneum



rophages have been found to also aggregate around bacteria introduced into the body cavities of mice (13). Zindel *et al.* showed that cavity macrophage aggregation was calcium dependent and strongly resembled intravascular platelet aggregation.

An important connection was made to repair processes in invertebrates, such as the purple sea urchin, that also have a body cavity. Macrophage equivalents, known as coelomocytes, also repair internal wounds by initial adherence and then aggregation. As such, Zindel *et al.* concluded that both coelomocytes and GATA6<sup>+</sup> macrophages have conserved evolutionarily ancient roles, functioning as platelets as well as phagocytes after injury. The corollaries with invertebrates also helped to identify the way in which macrophages formed aggregates. The authors ruled out many traditional cell-to-cell adhesion molecules that they had expected to be involved but found that heparin prevented macrophage aggregation. Coelomocytes aggregate using a type of scavenger receptor that contains conserved scavenger receptor cysteine-rich (SRCR) domains, which recognize negatively charged ligands such as heparin. Zindel *et al.* identified two scavenger receptors with SRCR domains, MARCO (macrophage receptor with collagenous structure) and MSR1 (macrophage scavenger receptor 1), which were highly expressed on peritoneal-cavity macrophages in mice. Inhibition of these receptors did not prevent initial cavity macrophage adherence but did prevent secondary tethering and aggregation. Furthermore, evidence of delayed serosal healing with specific receptor inhibitors highlighted that aggregate formation was integral to the repair process.

To investigate the effect of surgery on macrophage aggregation, Zindel *et al.* made an incisional wound into the abdominal cavity of mice and imaged GATA6<sup>+</sup>

macrophages over time. As before, initial adherence to the wound and aggregation occurred, but now tethering continued, with macrophages forming superaggregates a hundred times greater in size than those made after a simple laser injury in the closed abdomen. Notably, these superaggregates evolved into collagen-rich adhesions covered with mesothelial cells within 7 days. Switching to a more clinically relevant mouse model of ischaemia-induced adhesions (7, 8), the authors found that, again, extensive GATA6<sup>+</sup> macrophage superaggregates formed that acted as precursors for adhesion development. Depleting these macrophages or blocking receptor-mediated aggregation resulted in reduced adhesions, and those that did form were not as strong. Of note, cavity macrophage number dropped significantly in peritoneal lavage after surgery, indicating that a large quantity participated in this process.

How do these new findings connect with our current understanding of adhesion formation involving reduced fibrinolysis and MMT? Although the extent of injury may determine if GATA6<sup>+</sup> macrophages form superaggregates, this process alone is unlikely to drive adhesion formation, which also involves coagulation and fibrin deposition. Indeed, GATA6<sup>+</sup> cavity macrophages in mice express coagulation cascade factors and promote macrophage-rich fibrin-containing clots, which are largely responsible for macrophage disappearance after insult to the cavity (13). Together, these studies strongly implicate resident macrophages in adhesion development, but much remains to be discovered. For example, it is unclear whether specific GATA6<sup>+</sup> macrophage subpopulations are responsible for superaggregation and/or clot formation and whether these “platelet-like” properties can be promoted or inhibited by the immune environment or prior activation history.

Although the study of Zindel *et al.* is perhaps most immediately relevant to adhesions, it would be fascinating to know if SRCR domain-mediated macrophage aggregation contributes to other poorly understood processes, such as the initiation of macrophage-rich granulomas, which encase many pathogens. A critical question is whether macrophages retain extravascular platelet-like functions in the other two body cavities that contain the lung (pleural cavity) and the heart (pericardial cavity), where adhesions can also be a major problem after surgery. In this respect, Wilms-tumor-1 (WT1)-expressing mesothelial and fibroblastic stromal cells that are present in all three serosal cavities provide precise signals that instruct the tissue-specific GATA6<sup>+</sup> transcriptional program of cavity macrophages (14). It is highly likely that there is a reciprocal dialogue whereby cavity resident macrophages regulate stromal cell behavior. The high conservation between mouse and human scavenger receptors with SRCR domains (15) presents an exciting opportunity to inhibit these receptors as a potential therapeutic strategy to prevent adhesion formation. ■

### REFERENCES AND NOTES

1. K. Okabayashi *et al.*, *Surg. Today* **44**, 405 (2014).
2. J. Zindel *et al.*, *Science* **371**, eaabe0595 (2021).
3. G. B. Ryan, J. Grobety, G. Majno, *Am. J. Pathol.* **65**, 117 (1971).
4. J. Tang, Z. Xiang, M. T. Bernards, S. Chen, *Acta Biomater.* **116**, 84 (2020).
5. D. S. Foster *et al.*, *Nat. Commun.* **11**, 4061 (2020).
6. S. Namvar *et al.*, *J. Pathol.* **245**, 491 (2018).
7. P. Sandoval *et al.*, *J. Pathol.* **239**, 48 (2016).
8. J. M. Tsai *et al.*, *Sci. Transl. Med.* **10**, eaan6735 (2018).
9. C. C. Bain, S. J. Jenkins, *Cell. Immunol.* **330**, 126 (2018).
10. E. L. Gautier *et al.*, *J. Exp. Med.* **211**, 1525 (2014).
11. M. Rosas *et al.*, *Science* **344**, 645 (2014).
12. J. Wang, P. Kubes, *Cell* **165**, 668 (2016).
13. N. Zhang *et al.*, *J. Exp. Med.* **216**, 1291 (2019).
14. M. B. Buechler *et al.*, *Immunity* **51**, 119 (2019).
15. D. M. E. Bowdish, S. Gordon, *Immunol. Rev.* **227**, 19 (2009).

10.1126/science.abg5416



# Eyeless worms detect color

Roundworms discriminate color of toxic food despite a lack of eyes and opsin photoreceptor genes

By Lauren A. Neal<sup>1</sup> and Leslie B. Vosshall<sup>1,2,3</sup>

**A**nimals use color vision to explore their environment, recognize mates, avoid predators, and guide feeding decisions. Color vision across the tree of life relies on specialized retinal photoreceptor cells and light-sensitive opsins with different spectral sensitivities. *Caenorhabditis elegans* are eyeless roundworms that dwell in rotting vegetation and compost heaps, feeding on a rich diversity of microbes (1). In its natural environment, *C. elegans* must traverse a complex microbial terrain while determining which food is safe for consumption. Some bacteria produce colorful toxins (2), making color discrimination a potentially life-or-death decision for the worm. On page 1059 of this issue, Ghosh *et al.* (3) demonstrate that *C. elegans*, despite lacking eyes and opsin genes, can discriminate between colors to guide foraging decisions. They identify two conserved stress-response genes that are required for color discrimination, revealing a new biology of color vision.

An estimated 80% of the bacteria naturally found in the *C. elegans* environment are beneficial to the organism, but the worm can encounter potentially harmful microorganisms while foraging for food (1). Pyocyanin, a blue-pigmented toxin secreted by the bacterium *Pseudomonas aeruginosa*, is known to generate tissue-damaging reactive oxygen species. This pigment is a major cause of pathogenicity because mutant *P. aeruginosa* that do not produce pyocyanin are less pathogenic to humans (2). When *C. elegans* encounters this colorful and toxic microbe, how does it recognize and avoid it?

Previous work demonstrated that *C. elegans* is sensitive to visible and ultraviolet light. *lite-1* (high-energy light unresponsive protein 1) and *gur-3* (gustatory receptor family protein 3) were identified as two components of a non-opsin phototransduction pathway that contributes to light-avoidance behavior (4–7). Ghosh *et al.* demonstrated that avoidance of toxic blue *P. aeruginosa* bacterial lawns by *C. elegans* on a Petri dish is enhanced in the presence of white

light and requires the *lite-1-gur-3* pathway. Adding pyocyanin to a culture of beneficial bacteria triggered repulsion by *C. elegans* in white light, yet solely illuminating beneficial bacteria with blue light in the absence of pyocyanin did not. The authors triggered avoidance of beneficial bacteria by adding a colorless chemical that produces reactive oxygen species and illuminating the environment with precise blue-amber wavelengths to mimic the color of pyocyanin. Moreover, this blue-amber light enhanced avoidance of nonpathogenic bacteria scented with an odor that worms find repellent. Therefore, pathogen avoidance is a multisensory experience that relies on both visual and chemical cues.

Ghosh *et al.* uncovered pronounced behavioral variation under blue or amber illumination in 59 wild strains of *C. elegans*. Some

**“...bacteria produce colorful toxins, making color discrimination a... life-or-death decision...”**

strains avoided pathogens only in blue light, and others were sensitive only to amber light. Several strains avoided these colors even without a repellent odor—a compelling demonstration that *C. elegans* detects and discriminates colors. The authors identified two genes that together strongly influenced color-dependent foraging, *jdk-1* (dual specificity mitogen-activated protein kinase kinase) and *lec-3* (32-kDa  $\beta$ -galactoside-binding lectin). Both are conserved in mammals and function as a kinase activator and a sugar-binding protein, respectively, but how they contribute to color discrimination is unknown.

The work of Ghosh *et al.* suggests that *C. elegans* integrate multiple chemosensory and visual inputs to create a “view” of their environment, allowing them to identify toxic bacteria by both their spectral and chemical properties. *P. aeruginosa* advertises its presence not only with pyocyanin, the bifunctional toxin that induces the generation of reactive oxygen species and is blue, but also with a characteristic smell. It was previously shown that *C. elegans* can learn to avoid *P. aeruginosa* by pairing this bacterial odor with the aversive memories associated with

encountering the pathogen (8, 9). It is possible that all three types of sensory cues are integrated to trigger an avoidance response. Although high concentrations of pyocyanin are naturally toxic to *C. elegans* and are avoided in the absence of light, at lower pyocyanin concentrations, blue light illumination seemingly intensifies the behavioral response, providing sensory circuits in the worm with additional input to influence their movement away from the potentially toxic food source. Where in the *C. elegans* nervous system these disparate sensory cues are integrated remains an important topic for future investigation (10).

The discovery that *C. elegans* can detect and discriminate different wavelengths of light raises many additional questions. How *jdk-1* and *lec-3* participate in color vision is unknown: These proteins might directly detect light or indirectly transduce a signal from unidentified non-opsin photoreceptors. It is possible that the *jdk-1-lec-3* pathway interacts with the previously described *lite-1-gur-3* pathway, or it may function independently. It is also unknown what cells are required for the detection of colorful toxins: Are there dedicated sensory structures, or is worm color vision distributed across many cells and tissues?

The work by Ghosh *et al.* additionally raises the question of what evolutionary path led to *C. elegans* color discrimination. The development of colorful toxins could enhance the survival of a bacterial species and may serve as a warning to potential predators. It would be highly advantageous for roundworms to discriminate pathogenic and nonpathogenic bacteria by color. Indeed, Ghosh *et al.* reported that color discrimination varies widely in natural populations, suggesting that genetic variation of pigmented toxins in the local microbial community may coevolve with noncanonical *C. elegans* color vision. How ambient light filtered through decomposing vegetation in the local microenvironment enables color discrimination by *C. elegans* would also be interesting to understand. This study will inspire the search for unconventional mechanisms of color vision in other eyeless invertebrates, as well as the evolution of the *jdk-1* and *lec-3* pathway as a mediator of color discrimination across species. ■

## REFERENCES AND NOTES

1. B. S. Samuel, H. Rowedder, C. Braendle, M.-A. Félix, G. Ruvkun, *Proc. Natl. Acad. Sci. U.S.A.* **113**, E3941 (2016).
2. G. Y. Liu, V. Nizet, *Trends Microbiol.* **17**, 406 (2009).
3. D. D. Ghosh *et al.*, *Science* **371**, 1059 (2021).
4. A. Ward *et al.*, *Nat. Neurosci.* **11**, 916 (2008).
5. J. Gong *et al.*, *Cell* **167**, 1252 (2016).
6. S. L. Edwards *et al.*, *PLoS Biol.* **6**, e198 (2008).
7. N. Bhatla, H. R. Horvitz, *Neuron* **85**, 804 (2015).
8. Y. Zhang, H. Lu, C. I. Bargmann, *Nature* **438**, 179 (2005).
9. K. Lee, E. Mylonakis, *Cell Rep.* **20**, 2501 (2017).
10. G. Harris *et al.*, *PLoS Genet.* **15**, e1007706 (2019).

<sup>1</sup>Laboratory of Neurogenetics and Behavior, The Rockefeller University, New York, NY, USA. <sup>2</sup>Howard Hughes Medical Institute, New York, NY, USA. <sup>3</sup>Kavli Neural Systems Institute, New York, NY, USA. Email: lneal@rockefeller.edu; leslie@rockefeller.edu

## IMMUNOTHERAPY

# Targeting cancer with bispecific antibodies

Bispecific antibodies might provide off-the-shelf immunotherapeutics for treating cancer

By Jon Weidanz

**P**rotein-based immunotherapies offer the possibility of generic or “off-the-shelf” immunotherapies, different from the highly personalized approach of engineered immune cell therapies.

For example, T cell-engaging bispecific antibodies (CD3 BsAbs) trigger signaling of the CD3 surface receptor on T cells and also bind to a second target protein on tumor cells, thereby activating cytotoxic T cells to eliminate cancer cells with one antibody molecule. But this approach has challenges, including identifying shared cancer-selective targets and protein engineering to redirect T cells. A study by Hsiue *et al.* (1) on page 1009 of this issue and a study by Douglass *et al.* (2) describe the development of CD3 BsAbs that recognize mutation-associated neoantigens (MANAs). Additionally, Paul *et al.* (3) describe a CD3 BsAb that uses T cell receptor (TCR)-specific antibodies to selectively eliminate T cell malignancies. In the future, these immunotherapeutic agents could be used to treat diverse cancers with specific mutations.

Tumor antigens are classified as either tumor-associated antigens (TAAs) or tumor-specific antigens (TSAs). TAAs are aberrantly expressed by, but are not specific to, cancer cells. Because normal tissue also expresses TAAs, albeit at lower levels, on-target off-tumor toxicities of immunotherapies that target TAAs are a concern. Conversely, TSAs are found only on cancer cells. MANAs are a subclass of TSAs and are derived from the expression of common hotspot mutations in cancer genes. Next-generation sequencing combined with proteomics and bioinformatic tools have accelerated the discovery of MANAs, with particular focus on those derived from cancer-driver genes (which give a selective growth advantage to cells when mutated), such as the tumor suppressor gene *TP53* (which encodes p53) and the RAS family of oncogenes (*KRAS*, *HRAS*, and *NRAS*) (4, 5).

MANAs, like other cellular proteins, are processed by the proteasome, and the peptides that are generated are transported into the lumen of the endoplasmic reticulum (ER) by the heterodimeric transporter

associated with antigen processing (TAP1-TAP2) complex before being trimmed by ER aminopeptidases into 8 to 10 amino acid peptides. These mutated peptides (neopeptides) are loaded onto classical human leukocyte antigen (HLA) class I molecules that present MANAs on the cell surface as neoantigens (pHLA).

Finding neopeptides that bind to HLA molecules can be assisted by using in silico prediction software. Hsiue *et al.* and Douglass *et al.* provide a roadmap to discover and quantify neoantigens. Each group used computer modeling to predict binding of commonly mutated proteins in cancer—p53<sup>R175H</sup>, KRAS<sup>G12V</sup>, HRAS<sup>G12V</sup>, NRAS<sup>G12V</sup>, NRAS<sup>Q61L</sup>, and HRAS<sup>Q61L</sup>—to different HLA class I molecules. For example, p53<sup>R175H</sup> binds to HLA-A2, KRAS<sup>G12V</sup> binds to HLA-A3, and NRAS<sup>Q61L</sup> binds to HLA-A1. To confirm in silico predictions, both teams used a highly sensitive mass spectrometry (MS)-based approach

**“The studies...offer a potential avenue to achieve off-the-shelf, protein-based immunotherapeutics...”**

[MANA-selective reaction monitoring (SRM)] to analyze HLA-bound peptides. Hsiue *et al.* estimated on average that there are only 2.4 copies of p53<sup>R175H</sup>/HLA-A2 expressed per cell by a human multiple-myeloma cell line. Douglass *et al.* showed that both the 9- and 10-amino-acid-long peptides from KRAS<sup>G12V</sup> are processed and presented by HLA-A3. However, only the 10-amino-acid-long KRAS<sup>G12V</sup> peptide is presented by HLA-A3 on human lung papillary adenocarcinoma and pancreatic ductal adenocarcinoma cell lines at nine and three copies per cell, respectively. Although adoptive T cell therapies have been used to target mutant oncogenes and tumor suppressor genes (6), the findings from these studies directly confirm that MANA pHLAs are present but at very low amounts on human cancer cells.

TCR-mimic (TCRm) antibodies are a class of biologics that recognize pHLA derived from intracellular proteins (7). CD3 bispecifics that include a TCRm were previously described and shown to mediate T cell cytotoxicity of human colorectal adenocarcinoma

cells in vitro and elimination of human transformed B cells in mice (8, 9). Hsiue *et al.* and Douglass *et al.* used phage display to screen naïve human antibody libraries to discover TCRms specific to their MANA pHLA of interest. Both groups then made CD3 BsAbs by using a single-chain diabody (scDb) format, comprising a single-chain TCRm antibody fragment (Fv) specific for MANA pHLA fused to an scFv CD3 antibody. The CD3 scFv moiety binds CD3 and activates a polyclonal T cell response when targeted to cancer cells expressing the MANA pHLA antigen.

As with any immunotherapy, safety and toxicity issues are a potential concern. Creation of scDbs with affinity for mutated residue(s) in the neopeptide could reduce the possibility for cross-reactivity and hence the risk for off-target toxicity. Characterization of the binding selectivity of TCRm from both studies revealed that scDbs could specifically recognize mutated peptides and not the corresponding wild-type or related mutated peptides. Hsiue *et al.* used x-ray crystallography to provide a structural basis for scDb binding only to mutated p53<sup>R175H</sup>/HLA-A2 and more broadly support the use of structural data to predict cross-reactivity of scDbs.

Hsiue *et al.* and Douglass *et al.* describe scDbs with high sensitivity that can activate T cells in vitro to lyse human myeloma cells and lung papillary adenocarcinoma cells expressing less than 10 copies of neoantigen pHLAs. Moreover, Hsiue *et al.* show that immunodeficient mice engrafted with human T cells suppressed growth of a human multiple-myeloma cell line expressing an average of 2.4 copies of p53<sup>R175H</sup>/HLA-A2 per cell after treatment with the H2-scDb. These studies provide the first evidence for CD3 BsAbs to eliminate cancer cells by activating polyfunctional T cell responses against previously nondruggable intracellular targets presented by tumor cells at very low density.

To date, more than 100 different CD3 BsAb formats have been developed for therapeutic use (10). Hsiue *et al.* and Douglass *et al.* created multiple formats of CD3 BsAbs, including using different CD3 antibodies, to identify scDb as the optimal format. It might be the small, compact, and rigid nature of the scDb structure that is responsible for the observed enhancement in antitumor activity over other bispecific formats. This is especially true when it comes to tumor targets expressed at low densities such as described

College of Nursing and Health Innovation, University of Texas at Arlington, Arlington, TX 76019, USA.  
Email: weidanz@uta.edu



by Hsiue *et al.* and Douglass *et al.* Perhaps the more potent antitumor activity reported for the scDb is related to establishing an optimized immunological synapse between tumor cells and T cells. Or possibly, the affinity of the CD3 antibody or its binding epitope are important. Regardless, these findings will likely foster rapid development of scDb CD3 BsAbs that target MANA pHLA and other TAAs and TSAs on cancer cells.

Paul *et al.* describe an approach to deplete T cell malignancies (T cell leukemias and lymphomas) while preserving healthy T cells by using scDb molecules. To establish proof of concept, the authors took advantage of previously identified antibodies to TCR  $\beta$ -chain variable regions, TRBV5-5 and TRBV12, which are two of 30 possible TRBV family members that form a functional  $\alpha\beta$  TCR expressed by T cells (see the figure). Because T cell malignancies are clonal and express only one TRBV family member on their surface, targeting a single TRBV type represents an ideal TAA for selectively treating with CD3 BsAbs. Paul *et al.* show that scDb composed of an antibody to TRBV5-5 or TRBV12 and tethered to a CD3 antibody can selectively eliminate malignant human T cells that express TRBV5-5 or TRBV12 in mouse models while preserving the majority of healthy human T cells not expressing the targeted TRBV.

Although the studies of Hsiue *et al.*, Douglass *et al.*, and Paul *et al.* are promising for advancing scDbs into the clinic, there are other factors to consider before therapeutic efficacy can be fully realized. scDbs are small molecules that are rapidly cleared from the blood in humans and mice, which will likely make it necessary to continuously infuse scDb drugs with an implanted pump. The addition of an immunoglobulin G (IgG) fragment crystallizable (Fc) domain to the scDb molecule would be expected to increase its plasma half-life. However, the addition of an Fc domain would also create a bulkier molecule that could sterically hinder epitope binding and result in reduced antitumor potency. Although further identification of commonly shared MANA pHLA will expand the

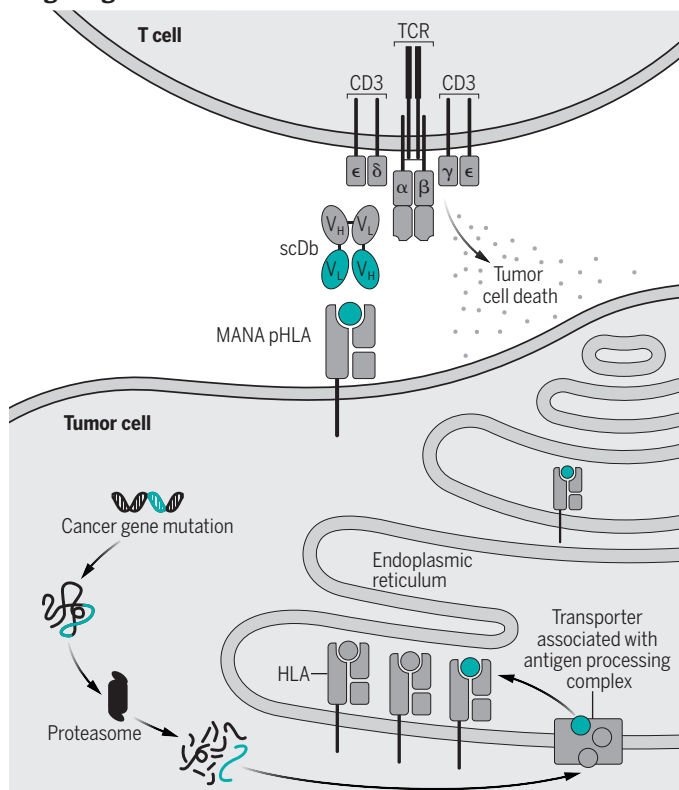
targets available on solid tumors for CD3 BsAbs, the polymorphic nature of classical HLA class I limits the individuals who can be targeted with these agents. To broaden population coverage, an alternative may be to find MANA-derived peptides presented by non-classical HLA (that is, HLA-E and HLA-G). Unlike classical HLA, HLA-E and HLA-G are essentially monomorphic, and their activity is up-regulated on cancer cells. Whether HLA-E and HLA-G present peptides from MANAs may be worth investigating.

There are potential issues related to the tumor microenvironment that might limit the effectiveness of CD3 BsAbs, including scDb against both hematological malignancies and solid tumors. For example, in cases in which limited T cell activation has been observed, combination with agonist antibodies to activate costimulatory receptors such as CD137 is being pursued (11). Both hematological and solid tumors actively evade immune cell responses through the expression of inhibitory immune checkpoints that would negatively affect T cell activation by CD3 BsAbs. Potential solutions include combination with immune checkpoint blockers, such as antibodies that block cytotoxic T lymphocyte-associated protein 4 (CTLA-4) and programmed cell death protein 1 (PD-1) and thereby allow T cell activation (12). Additionally, some solid tumors lack T cell infiltration, and the combination of BsAbs with oncolytic viruses and cancer vaccines is being evaluated to encourage T cell trafficking to tumors (10, 13). The studies by Hsiue *et al.*, Douglass *et al.*, and Paul *et al.* offer a potential avenue to achieve off-the-shelf, protein-based immunotherapeutics for treating cancers with specific TAAs or mutations that are expressed as MANAs. However, much more work will be required before this ambitious goal can be achieved. ■

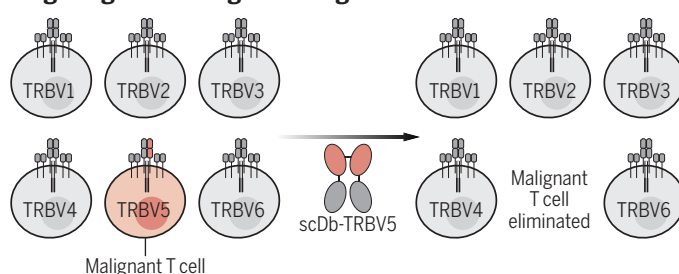
## Single-chain diabetides for cancer immunotherapy

Commonly shared mutations in tumor suppressor genes and oncogenes in different solid tumors lead to mutation-associated neoantigens (MANAs), which are presented by human leukocyte antigens (MANA pHLA) on cancer cells. These can be targeted by CD3 bispecific antibodies, such as single-chain diabetides (scDb), which redirect T cells to target tumor cells. Clonal malignant T cells that express tumor-associated antigens, such as T cell receptor (TCR)  $\beta$ -chain variable region 5 (TRBV5), can also be selectively targeted by scDbs.

### Targeting solid tumor cells



### Targeting hematological malignancies



## REFERENCES AND NOTES

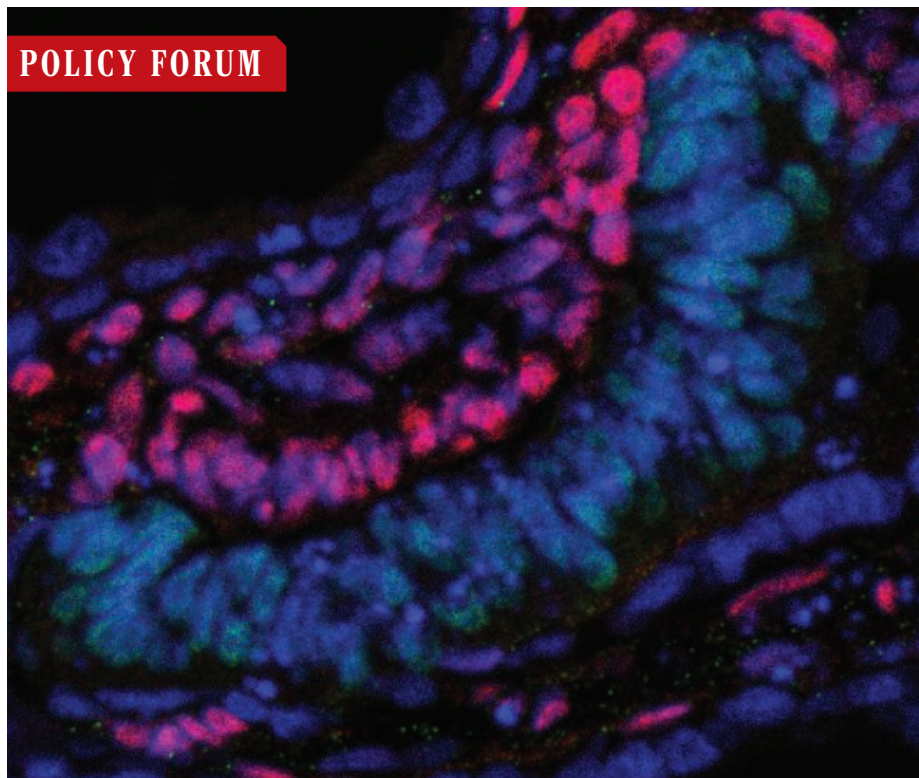
1. E. H.-C. Hsiue *et al.*, *Science* **371**, eabc8697 (2021).
2. J. Douglass *et al.*, *Sci. Immunol.* **6**, eabd5515 (2021).
3. S. Paul *et al.*, *Sci. Transl. Med.* (2021). 10.1126/scitranslmed.abd3595
4. A. Levine, *Nat. Rev. Cancer* **20**, 471 (2020).
5. M. H. Bailey *et al.*, *Cell* **174**, 1034 (2018).
6. W. Lo *et al.*, *Cancer Immunol. Res.* **7**, 534 (2019).
7. J. A. Weidanz *et al.*, *J. Immunol.* **177**, 5088 (2006).
8. N. Kurosawa, Y. Wakata, K. Ida, A. Midorikawa, M. Isobe, *Sci. Rep.* **9**, 9827 (2019).
9. M. Ahmed *et al.*, *JCI Insight* **3**, 97805 (2018).
10. J. Middelburg *et al.*, *Cancers (Basel)* **13**, 287 (2021).
11. X. Han, M. D. Vesely, *Int. Rev. Cell Mol. Biol.* **342**, 1 (2019).
12. S. Kobold, S. Pantelyushin, F. Rataj, J. Vom Berg, *Front. Oncol.* **8**, 285 (2018).
13. C. Groeneveld *et al.*, *J. Immunother. Cancer* **8**, 1 (2020).

## ACKNOWLEDGMENTS

J.W. is a cofounder of and chief scientist at Abexa Biologics.

Published online 1 March 2021  
10.1126/science.abg5568

## POLICY FORUM



Epiblast cells (green in this cryosection of a cultured 16-day monkey embryo) will migrate and differentiate to form the primitive streak and start gastrulation.

## RESEARCH ETHICS

# Human embryo research beyond the primitive streak

It is time to revisit the “14-day limit”

By Insoo Hyun<sup>1,2</sup>, Annelien L. Bredenoord<sup>3</sup>, James Briscoe<sup>4,5</sup>, Sigal Klipstein<sup>6,7</sup>, Tao Tan<sup>8</sup>

Since the first successful birth resulting from in vitro fertilization (IVF) in the late 1970s, human embryo research has been subject to limits of time and developmental benchmarks. National guidelines, laws, and international norms have prohibited scientists from culturing embryos for research beyond 14 consecutive days, or beyond the appearance of a structure called the “primitive streak,” which defines the beginning of the formation of the principal tissues of the body and the end of the period when an embryo can divide into identical twins (1). At the time this limit was put in place 40 years ago, there were no methods to culture embryos in a dish for anywhere close to 14 days. But research since 2016 (2, 3) shows

that it is likely possible to culture human research embryos past the 2-week limit and suggests that doing so will yield scientific insights that could prove important for human health and fertility (4). We thus urge policy-makers and the International Society for Stem Cell Research (ISSCR), which will soon release updated guidelines for stem cell and embryo research, to consider a cautious, stepwise approach to scientific exploration beyond the 14-day limit.

## THE 14-DAY LIMIT EMERGES IN POLICY

The first articulation of the 14-day limit appeared in the Ethics Advisory Board's report for the U.S. Department of Health, Education, and Welfare in 1979. It was popularized by the United Kingdom's Warnock Committee in 1984 and was echoed in the Human Embryo Research Panel's report for the U.S. National Institutes of Health (NIH)

in 1994 (5–7). Each of these committees advocated that, although embryos in vitro warrant special consideration by virtue of their human developmental potential, they lack the full moral status accorded to persons. As such, it was deemed acceptable to use embryos for scientifically meritorious research whose goal was to benefit human health and improve reproduction.

Having made these key ethical determinations, the committees' remaining task was to provide recommendations for national governance, which the United Kingdom succeeded in doing. Seen in its original light, the 14-day limit is best viewed as a policy decision for science regulation in a pluralistic society, not as a rigid moral principle. The 14-day limit never stood as a philosophical position that the embryo gained an inviolable degree of moral status at that developmental point.

History supports this interpretation. The U.S. Ethics Advisory Board recommended the 14-day limit as part of a national policy for the acceptable uses of IVF-derived embryos. It was important for this policy not to clash with 16 state laws that based fetal research restrictions in utero upon a definition of the fetus as a product of conception that has implanted in the womb. To avoid possible conflict between their recommendations and state laws, the Board declared that in vitro research should conclude 14 days after fertilization, around the time that implantation in the womb would normally be completed.

The NIH Human Embryo Research Panel had a similar policy consideration to weigh. U.S. Federal regulations, based on the recommendations of the National Commission for the Protection of Human Subjects of Biomedical and Behavioral Research, set requirements for federal research funding involving post-implantation embryos and fetuses. The Panel wanted to draft guidelines that would allow federal funding for embryo research in vitro. But they realized that this could trigger extant funding constraints around post-implantation embryos, so setting the limit at 14 days made good policy sense. The Panel also said that in vitro research should be limited to the shortest time period consistent with the goals of each research proposal and “for the present” should not go past primitive streak formation. Thus, the Panel's 14-day limit was not offered as

<sup>1</sup>Department of Bioethics, Case Western Reserve University School of Medicine, Cleveland, OH, USA. <sup>2</sup>Center for Bioethics, Harvard Medical School, Boston, MA, USA. <sup>3</sup>Department of Medical Humanities, University Medical Center Utrecht, Utrecht University, Utrecht, Netherlands. <sup>4</sup>The Francis Crick Institute, London, UK. <sup>5</sup>Development, The Company of Biologists, Cambridge, UK. <sup>6</sup>InVia Fertility Specialists, Hoffman Estates, IL, USA. <sup>7</sup>Department of Obstetrics and Gynecology, University of Chicago Pritzker School of Medicine, Chicago, IL, USA. <sup>8</sup>Yunnan Key Laboratory of Primate Biomedical Research, Institute of Primate Translational Medicine, Kunming University of Science and Technology, Kunming, Yunnan, China. Email: insoo.hyun@case.edu; insoo\_hyun@hms.harvard.edu



an immutable stopping point, as further evidenced by their suggestion that the study of embryos slightly longer than 14 days would be permissible if the goal of the research was to study the primitive streak itself.

Recently, Mary Warnock, who chaired the United Kingdom's Warnock Committee, has acknowledged that the 14-day limit was a somewhat arbitrary number that helped get the bill through Parliament (8). In light of these original rationales, we believe it is time to reevaluate the 14-day limit and offer recommendations for a cautious path forward. But first, one must appreciate the scientific reasons for doing so.

## LOOKING BEYOND THE PRIMITIVE STREAK

Researchers' access to early-stage embryos from natural pregnancy losses is extremely limited. Most women do not know that they are pregnant in the first weeks after implantation, such that the acquisition of embryonic tissue from this early stage of development is extremely difficult. Thus, many scientific questions of both fundamental and practical importance can be answered only by studying IVF-derived human embryos in culture beyond primitive streak formation (see the box).

The difficulty of accessing embryos means that the 2 weeks between the 14th and 28th day after fertilization have been called the "black box" of human development. It covers gastrulation (around days 13 to 20), when cells are allocated into the principal tissues and the body plan is developed. Most of what researchers now know comes from the Carnegie Embryo Series (9) and the Kyoto Collection (10). The descriptions of these embryos, which were collected over a long span of time, have been limited to histology, and no modern methods of analysis have been possible. Consequently, researchers have little if any direct molecular, cellular, or other data about dynamics or cell fate relationships during this crucial black box period. Yet, it is during this window of development that many congenital anomalies arise, implantations fail, and miscarriages occur. Together, these affect many women and their families. For example, in one study of women presenting for delivery, 43% reported having had at least one early spontaneous abortion (11).

People may wonder if there are alternative ways to study these questions. One of us (T.T.) has demonstrated that monkey embryos can be cultured past 14 days, which allows monkey embryos in extended culture to be compared point by point with monkey embryos in utero (12, 13). But, although there are many advantages to using monkey embryos in lieu of human embryos, differences between early human and monkey

development should not be ignored. For example, monkey embryos implant on the surface of the endometrium, whereas human embryos (as well as those of apes) implant within the endometrium, and this process might be relevant for disorders such as intrauterine growth restriction, which keeps babies from reaching a healthy birth weight. Only through the direct study of human embryos in extended culture systems can researchers fully understand the mechanisms underpinning human development. Rather than monkey embryo culture standing as an alternative, it is likely to fuel the feasibility of, and further scientific interest in, extended human embryo culture.

Another technique for studying human embryo development involves constructing three-dimensional embryo-like models from pluripotent stem cells rather than using actual human embryos (14). But to know whether observations from such models are meaningful, it is essential to compare in vitro embryo model systems with IVF-derived embryos. Indeed, comparisons could provide a benchmark to calibrate and validate these new approaches, making stem cell-based human embryo model systems more

useful and allowing them to answer questions that currently could only be addressed with IVF-derived human embryos. Once such validation and benchmarking are done, researchers might be able to use embryo model systems more broadly, thereby reducing the number of IVF-derived embryos needed in the future.

## AN INCREMENTAL WAY FORWARD

If research on human embryos is to be permitted beyond the primitive streak, it should proceed in incremental, measured steps. Here we propose six principles that can be used to weigh whether these extensions are permissible. These apply for extending the 14-day limit, as well as for other complex research, and show how regulations can be shaped to support and promote good scientific practice and beneficial research, not just limit harmful or unethical research.

### Scientific justification

Researchers should adhere to the 14-day limit, unless a strong scientific justification can be offered to culture human embryos longer in locales where it would be legally

## Scientific goals

There are five categories of questions to be addressed by studies of human embryos beyond primitive streak formation.

### FUNDAMENTAL KNOWLEDGE

What are the similarities and differences between development in humans and other mammals?

### UNDERSTANDING DISEASE

What are the origins and mechanisms of developmental disorders that arise early in development?

### CLINICAL UTILITY

Can we develop therapeutic interventions that address causes of infertility, developmental disorders, and failed pregnancy?

### SCIENTIFIC VALIDATION

How closely do nonhuman primate and stem cell–derived embryo models of human development compare to IVF-derived embryos?

### PRECLINICAL SAFETY ASSESSMENT

If human sperm and eggs are derived from stem cells or are genetically edited, will embryos created from them develop normally? Will mitochondrial transfer (a process already under consideration for clinical use) affect embryo development?

Perhaps the most compelling questions fall into the category of understanding disease. For example, around 3% of births show some form of congenital anomaly, and many pregnancies fail prior to birth. For instance, approximately 1 in 250 conceptions result in holoprosencephaly, a defect in the formation of the embryonic midline that affects the development of the brain and face. It can be mild or severe and can cause miscarriage or early death. Genetic mutations that contribute to the disease have been identified, but predicting their exact effects—and disease severity—has been elusive. Embryo research might provide answers. Embryo research past 14 days might also explain why many embryos fail to implant and others subsequently spontaneously abort. It might help identify ways to distinguish between viable and nonviable IVF embryos and so might lead to fewer lost pregnancies and implantation failures—and the concomitant suffering and health risks—in fertility patients. It might also help evaluate whether other cutting-edge infertility treatments can produce viable embryos, including gene editing or mitochondrial replacement, and also assess whether embryos made using sperm or egg derived from stem cells develop normally.

permissible to do so. Any such proposed research must serve important goals that cannot be adequately met by other means.

### Well-defined increments

Extended embryo culture should commence in small steps, with frequent interim evaluations and reassessments by regulators. For instance, it would first be necessary to assess feasibility of culture past 14 days and, if so, to assess whether those newly permitted experiments were informative enough to justify the use of human embryos. Any research teams proposing to move beyond the 14-day mark would need to seek regulatory permission for each subsequent experiment. Even if the 14-day limit were lifted today, technical limitations mean that experiments could not go far beyond it.

### Independent peer review

Research proposals should be peer reviewed by qualified science and ethics committees that are independent of the researchers. Some countries, such as the United Kingdom, have a robust national system in place for such review. For countries that lack a centralized and consistent system for embryo research review, the ISSCR should provide an ad hoc review panel composed of independent scientific and ethics experts to provide advice for local review committees.

### Public dialogue

Any incremental step in embryo culture should be preceded by public dialogue at the local institutional level and, if feasible, more broadly. Responsible embryo research can only take place if scientific, ethical, and societal concerns and opportunities are explored and discussed in inclusive and deliberative forums hosted by regulators who are empowered to approve the research. Through such forums, researchers involved in these studies should be actively engaged in dialogues with the broader public, which should include nonscientific forms of knowledge, drawing on culture, philosophy, and experience. These should follow what science communicators call a “dialogue model” rather than the “deficit model” (15). That is, conversations should be interactive, not instructive, and aim for a bilateral exchange of ideas, such that science-based societal questions benefit from broad input.

### Informed consent

Anyone with dispositional authority over IVF embryos, and any donors whose gametes are used to create embryos that are donated, must give specific consent for extended embryo culture and research. Given people’s diverse views around human embryo research, including the views of gamete

donors recruited in assisted reproductive contexts, broad consent for any unspecified embryo research would not be ethically acceptable. Those donating embryos or gametes should be told the purpose and length of time that embryos will be studied and whether embryos will be preserved or discarded once the study is concluded. Donors should be informed that the embryos will not be used for reproduction.

### Separation of clinical care and research

The process of obtaining consent for embryo research must be kept separate from any clinical decisions for fertility treatments. Physicians who are treating patients or gamete donors should not be involved in informed consent interviews, nor should people who are involved in the research program. To avoid undue incentives or coercion of embryo donors, nondirective counseling should be provided to donors by people independent of both the research and clinical teams.

Each of these principles will be familiar to many scientists, ethicists, and policy-makers. With singular emphasis, or in combination, they are widely called into action in many other contexts where unconventional research is proposed and weighed. Taken together, this principled approach allows room for collaborative deliberation and compromise between researchers and citizens about what experiments are acceptable or which merit being prioritized.

Allowing some exceptions to the 14-day limit will depend on the technical feasibility of being able to culture embryos beyond this point, a process that will take time and deliberate study. Both scientific and regulatory considerations will prevent the science from advancing too far, too fast. First, a few progressive steps would be necessary to optimize culture conditions to see if human embryos can be sustained a day or two past the 14-day period. Next, one would have to see what data can be collected at these new time points and whether the experiments are informative. Concretely, increments of 2 or 3 days linked to defined developmental milestones seem appropriate.

For example, if reliable conditions for the culture of embryos beyond the 14-day time point are established, the next permissible endpoint could be day 16 to 17 (Carnegie stage 7) with morphological and molecular evidence of the extension of the primitive streak. If achieved, it would then be possible to propose extending culture an additional ~2 days until the equivalent of day 18 (Carnegie stage 8) corresponding to the formation of the neural groove. Stipulating both a time and an embryological constraint for each increment ensures

that limits agreed through debate and public dialogue are not inadvertently breached because of our relatively scant knowledge of exact developmental timing at these stages of human development in vitro or because there is a mismatch between the tempo of in vitro and in vivo development.

The process also makes clear the rationale for an incremental approach. Each increment can be viewed as a hypothesis of the developmental progress expected in a particular time frame. If an experiment fails to support the hypothesis, it will help revise our understanding of human development. If it holds, the next increment may be proposed. Unlike the 14-day limit, this approach can accommodate the possibility that days in culture may not always match up to milestones in embryonic development.

Together with scientists, ethicists, patient groups, and policy-makers, public input will help inform decisions regarding the relative merits of continuing down this path and trying to culture a few days beyond this new point. Many countries have their own national traditions for dealing with difficult discussions like these, for example, in allowing preimplantation genetic testing or mitochondrial replacement strategies. We believe the pace of human embryo culture research should be determined by measured scientific progress and societal openness to moving forward. Realistically, an incremental approach seems to be our only path forward, both from a scientific and a policy standpoint. ■

### REFERENCES AND NOTES

1. J. B. Appleby, A. L. Bredenoord, *EMBO Mol. Med.* **10**, e9437 (2018).
2. M. N. Shahbazi et al., *Nat. Cell Biol.* **18**, 700 (2016).
3. A. Deglincerti et al., *Nature* **533**, 251 (2016).
4. I. Hyun, A. Wilkerson, J. Johnston, *Nature* **533**, 169 (2016).
5. Ethics Advisory Board, Department of Health, Education, and Welfare, *HEW Support of Research Involving Human In Vitro Fertilization and Embryo Transfer* (U.S. Government Printing Office, 1979).
6. UK Department of Health and Social Security, *Report of the Committee of Inquiry into Human Fertilisation and Embryology* (Her Majesty’s Stationary Office, 1984).
7. Ad Hoc Group of Consultants to the Advisory Committee to the Director, NIH, *Report of the Human Embryo Research Panel* (U.S. Government Printing Office, 1994).
8. J. B. Hurlbut et al., *Nat. Biotechnol.* **35**, 1029 (2017).
9. Carnegie Collection, [https://embryology.med.unsw.edu.au/embryology/index.php/Carnegie\\_Collection](https://embryology.med.unsw.edu.au/embryology/index.php/Carnegie_Collection).
10. Kyoto Human Embryo Visualization Project, [http://bird.cac.med.kyoto-u.ac.jp/index\\_e.html](http://bird.cac.med.kyoto-u.ac.jp/index_e.html).
11. J. S. Cohain, R. E. Buxbaum, D. Mankuta, *BMC Pregnancy Childbirth* **17**, 437 (2017).
12. Y. Niu et al., *Science* **366**, eaaw5754 (2019).
13. H. Ma et al., *Science* **366**, eaaw7890 (2019).
14. N. Moris et al., *Nature* **582**, 410 (2020).
15. C. M. Reincke, A. L. Bredenoord, M. H. W. van Mil, *EMBO Rep.* **21**, e51278 (2020).

### ACKNOWLEDGMENTS

A.L.B. is a member of the Dutch Senate and a member of the Ethics Advisory Panel of IQVIA.

10.1126/science.abf3751





## Get answers. Keep moving.

From the leader in COVID-19 testing—solutions you can trust for the information you need

In a time when getting answers quickly is critical, we've responded with solutions to help keep the world moving forward. We deliver:

- **Proven COVID-19 testing solutions for accurate, trusted results**
- **Reliable supply from a single source for uninterrupted testing**
- **Worldwide service and support to get—and keep—testing up and running**

And we'll continue to anticipate evolving testing needs and proactively developing innovative solutions to address future challenges.

Thermo Fisher Scientific is involved in more than 50% of global COVID-19 testing, helping to enable greater access to fast, reliable, trusted answers. So the world can keep moving.



**ThermoFisher**  
SCIENTIFIC

Find out more at [thermofisher.com/covid19science](https://thermofisher.com/covid19science)

For Emergency Use Only. For prescription use only. For *in vitro* diagnostic use. Intended use of the products mentioned may vary. For specific intended use statements please refer to the instructions for use. © 2020, 2021 Thermo Fisher Scientific Inc. All rights reserved. All trademarks are the property of Thermo Fisher Scientific and its subsidiaries unless otherwise specified. COL014596 0221

ScienceTranslationalMedicine.org

# PUT HUMAN HEALTH AT THE HEART OF YOUR RESEARCH

Submit your research at: [cts.ScienceMag.org](https://cts.ScienceMag.org)

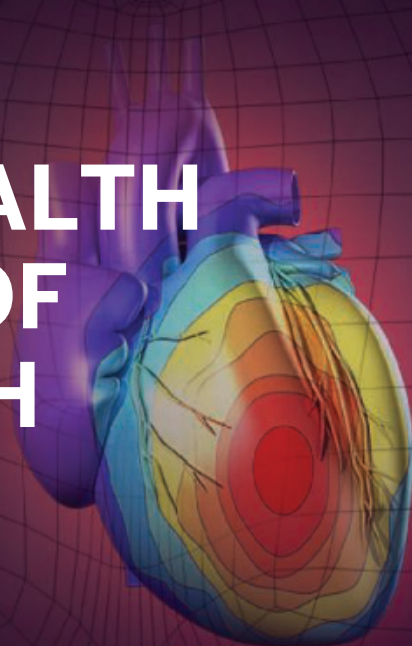
Science Translational Medicine



Twitter: @ScienceTM



Facebook: @ScienceTranslationalMedicine



## LETTERS

Edited by Jennifer Sills

## Editorial Expression of Concern

On 24 February 2006, *Science* published the Report “Molecular linkage between the kinase ATM and NF- $\kappa$ B signaling in response to genotoxic stimuli” by Z.-H. Wu *et al.* (1). Concerns about Figs. 4E and 4F and fig. S2A were posted to PubPeer in 2020 (2). Because of the age of the paper, we no longer had original files to examine. We have now learned that relevant institutions have completed investigations and have concluded that there was figure manipulation. We are contacting the institutions to obtain further clarification but in the meantime are notifying readers of our concern about the paper's data integrity.

H. Holden Thorp  
Editor-in-Chief

### REFERENCES AND NOTES

1. Z.-H. Wu, Y. Shi, R. S. Tibbets, S. Miyamoto, *Science* **311**, 1141 (2006).
2. E. M. Bik, Comment on “Molecular linkage between the kinase ATM and NF- $\kappa$ B signaling in response to genotoxic stimuli,” PubPeer (2020); <https://pubpeer.com/publications/7D3169F9D6FD50088CCC35361A4E4>.

10.1126/science.abh1300

## China's new laws overlook native herpetofauna

After revising the China Wildlife Protection Law in 2018 (1), China released an updated version of the accompanying List of Wild Animals under Special State Protection in China (2) on 5 February. Although these long-awaited changes are progress, they continue to inadequately protect the country's diverse herpetofauna (3), which represents more than 4% of global reptile species [511 (3) out of 11,341 (4) global species] and more than 6% of global amphibian diversity [515 species (3) out of 8294 globally (5)].

The revised List remains biased toward megafauna. The percentage of threatened species compared with the percentage of protected species in each group shows that herpetofauna are less represented than birds and mammals (2, 3, 6–8). For example, about 30% and 43% of China's reptile and amphibian species, respectively, are threatened, according to China's Red List (6), but only about 18% and 20% of each group's respective total diversity is protected by the revised List (2, 3). Meanwhile,



China's new wildlife legislation protects *Paramesotriton labiatus* but overlooks the similarly vulnerable *Pachytriton inexpectatus* (shown here).

11% of China's bird species are threatened (6), but about 27% of China's bird species are given protected status (2, 8).

Furthermore, decisions about whether to include a given species on the List do not follow the set criteria (9). For example, 77 reptile species that are designated as Vulnerable or higher in China's Red List Assessment (6)—representing about 56% of China's total threatened reptile diversity—are excluded from the List (2), with no justifications to explain why. Likewise, 110 threatened amphibians—63% of China's total threatened amphibian diversity—were omitted without specific explanations (2, 6). Species with similar ecology and conservation threats seem to have been selected or excluded randomly (e.g., inclusion of *Paramesotriton* spp. but omission of *Pachytriton* spp.) (10).

The protection classifications in the List also fail to distinguish between Critically Endangered species and those with a less urgent conservation status. Critically Endangered species, based on China's Red List (6) (such as *Cuora* spp. and *Platyisternon megacephalum*), are prescribed the same protection level as species that are classified as Least Concern (such as *Laticauda colubrina* and *Salamandrella keyserlingii*) (2, 6). If the protection level is not prescribed properly, these Critically Endangered species may soon be extinct from the wild.

Finally, the List's species-specific approach to listing is vulnerable to unstable taxonomy. All species that are newly discovered or recorded or have experienced recent changes in species-level taxonomy are excluded from protection until the next revisionary cycle. However, there has been a continuous influx of new species and new national records in China, and the current taxonomy is far from stable (3). Given that many new species are already threatened

at the time of discovery (11, 12), the time lag in extending protective coverage has substantial conservation implications.

The next revision of this legislation should include unbiased coverage of all vertebrate groups in China, particularly herpetofauna. It should be based on set criteria that best reflect the true conservation needs of species, and any adjustment to the List should be accompanied by publicly available justifications. We also recommend that the current legislation be amended to grant temporary protection to all new species, newly recorded species, and species with recent changes at species-level taxonomy until the next revisionary cycle.

Kai Wang<sup>1</sup>, Yunke Wu<sup>2</sup>, Zhiyong Yuan<sup>3\*</sup>

<sup>1</sup>Sam Noble Oklahoma Museum of Natural History and Department of Biology, University of Oklahoma, Norman, OK 73072, USA. <sup>2</sup>Department of Ecology and Evolutionary Biology, Cornell University, Ithaca, NY 14853, USA. <sup>3</sup>Key Laboratory for Conserving Wildlife with Small Populations in Yunnan, Southwest Forestry University, Kunming, 650024, China.

\*Corresponding author. Email: [yuanzhiyongkiz@126.com](mailto:yuanzhiyongkiz@126.com)

### REFERENCES AND NOTES

1. National Forestry and Grassland Administration of China, “Wildlife Protection Law of China” (2018); [www.forestry.gov.cn/main/3949/20170314/204777.html](http://www.forestry.gov.cn/main/3949/20170314/204777.html) [in Chinese].
2. National Forestry and Grassland Administration of China, “Official release of the updated List of Wild Animals under Special State Protection in China” (2021); [www.forestry.gov.cn/main/586/20210208/095403793167571.html](http://www.forestry.gov.cn/main/586/20210208/095403793167571.html) [in Chinese].
3. K. Wang *et al.*, *Biodivers. Sci.* **28**, 189 (2020).
4. P. F. Uetz, P. Freed, J. Hošek, “Species numbers by higher taxa,” The Reptile Database (2021); [www.reptile-database.org/db-info/SpeciesStat.html](http://www.reptile-database.org/db-info/SpeciesStat.html).
5. D. R. Frost, *Amphibian Species of the World* (2021); <https://amphibiansoftheworld.amnh.org>.
6. Z. Jiang *et al.*, *Biodivers. Sci.* **24**, 500 (2016).
7. Z. Jiang *et al.*, *Biodivers. Sci.* **23**, 351 (2015).
8. G. Zheng, Ed., *A Checklist on the Classification and Distribution of the Birds of China* (Science Press, Beijing, ed. 3, 2017).
9. National Forestry and Grassland Administration of China, “Explanations of the solicitation of comments for the List of Wild Animals under Special State Protection in China” (2020); [www.forestry.gov.cn/html/main/main\\_153/20200619092731170435586/file/20200619110013939647622.pdf](http://www.forestry.gov.cn/html/main/main_153/20200619092731170435586/file/20200619110013939647622.pdf) [in Chinese].



10. J. J. L. Rowley *et al.*, *Biol. Conserv.* **199**, 96 (2016).
11. M. Hou *et al.*, *Zootaxa* **3895**, 89 (2014).
12. B. L. Stuart *et al.*, *Science* **312**, 1137 (2006).

10.1126/science.abg9978

## Protecting China's finless porpoise

The Yangtze finless porpoise (*Neophocaena asiaeorientalis*), one of the 13 flagship global species recognized by the World Wildlife Fund (1), has been officially upgraded to first-class status under the framework of the National Wildlife Protection Act in China (2). This action, coupled with a series of initiatives to protect the environment of the Yangtze River (3), will hopefully help double the current wild population within a decade (4). However, the funding and penalties provided by protected status are not enough. China must take further action to make protection a reality.

The 1000 finless porpoises alive today are the last of a species that has existed in the middle and lower reaches of the Yangtze River for over 2.5 million years (4). The only *Neophocaena* species living in fresh water and endemic to that river, the Yangtze finless porpoise—whose close kin, the baiji (*Lipotes vexillifer*), has been extinct since 2007 (5)—is Critically Endangered as a result of changes to their natural habitat and foraging areas by industrialization and human activities along the Yangtze River (6, 7). Finless porpoises have suffered lasting damages to their immune and reproduction systems by eating fish that have eaten plankton polluted by industrial chemicals and sewage (8). Because the habitat and foraging areas of the finless porpoises are close to riverbanks and estuary regions, the porpoises often compete directly with shipping, industrial, and agricultural activities, complicating efforts to preserve their habitat (9, 10). In riverside metropolises like Wuhan, the Yangtze finless porpoises share urban waters with the city's residents.

The promotion of this scientifically, ecologically, and culturally valuable species to first-class endangered status is a step forward, but additional action must follow. The porpoise's water quality and sound environment should be improved (11). Comprehensive deterrents and penalties should be put in place for polluting or degrading their habitat. Conservation of the Yangtze finless porpoise should include policies similar to China's recently implemented 10-year fishing ban on the Yangtze River: Preservation areas should be established, and fishermen should be directed to avoid fishing in the porpoise's habitat

(12). Given the traditional proximity of the Yangtze finless porpoise's habitat to human activities, innovative programs should incentivize local residents to observe and protect the species, especially in the urban watersheds of the Yangtze River.

Qi Yan<sup>1\*</sup> and Yunhong Hu<sup>2,3</sup>

<sup>1</sup>School of Tourism and Social Administration, Nanjing Xiaozhuang University, Nanjing, China.

<sup>2</sup>School of Landscape Architecture, Nanjing Forestry University, Nanjing, China. <sup>3</sup>Research Center on Forestry Legacy and Environmental History of China National Forestry and Grassland Administration, Nanjing, China.

\*Corresponding author. Email: yorknrcn@msn.com

### REFERENCES AND NOTES

1. World Wildlife Fund, "WWF annual marine flagship species highlights" (2021): <http://marine-flagships.panda.org/>.
2. "Yangtze finless porpoise, etc. are promoted to national first-class protected wildlife," *Teller Report* (2021).
3. "China races to rescue rare Yangtze finless porpoise," *Xinhuanet* (2020).
4. F. Wu, *Guide on Fishery Guide to Be Rich* **20**, 1 (2020) [in Chinese].
5. Y. Liu, *World Environ.* **5**, 1 (2019) [in Chinese].
6. M. Chen *et al.*, *Aquatic Conserv. Mar. Freshw. Ecosyst.* **30**, 6 (2020).
7. H. Yang *et al.*, *Science* **337**, 410 (2012).
8. P. D. Jepson, R. J. Law, *Science* **352**, 1388 (2016).
9. B. Wu *et al.*, *Bull. Biol.* **55**, 19 (2020).
10. Y. Han *et al.*, *Ecol. Model.* **424**, 1 (2020).
11. Z. Wang *et al.*, *Environ. Pollut.* **262**, 1 (2020).
12. Z. Mei *et al.*, *Science* **367**, 1314 (2020).

10.1126/science.abg9955

### TECHNICAL COMMENT ABSTRACTS

**Comment on "Increased growing-season productivity drives earlier autumn leaf senescence in temperate trees"**

Richard J. Norby

Zani *et al.* (Research Articles, 27 November 2020, p. 1066) propose that enhancement of deciduous tree photosynthesis in a CO<sub>2</sub>-enriched atmosphere will advance autumn leaf senescence. This premise is not supported by consistent observations from free-air CO<sub>2</sub> enrichment (FACE) experiments. In most FACE experiments, leaf senescence or abscission was not altered or was delayed in trees exposed to elevated CO<sub>2</sub>.

**Full text:** [dx.doi.org/10.1126/science.abg1438](https://doi.org/10.1126/science.abg1438)

**Response to Comment on "Increased growing-season productivity drives earlier autumn leaf senescence in temperate trees"**

Deborah Zani, Thomas W. Crowther, Lidong Mo, Susanne S. Renner, Constantin M. Zohner

Our study showed that increases in seasonal productivity drive earlier autumn senescence of temperate trees. Norby argues that this finding is contradicted by observations from free-air CO<sub>2</sub> enrichment (FACE) experiments, where elevated CO<sub>2</sub> has been found to delay senescence in some cases. We provide a detailed answer showing that the results from FACE studies are in agreement with our conclusions.

**Full text:** [dx.doi.org/10.1126/science.abg2679](https://doi.org/10.1126/science.abg2679)



Share  
Your  
Robotics  
Research  
with the  
World.

Submit your research today.

Learn more at:  
[robotics.sciencemag.org](https://robotics.sciencemag.org)

Twitter: @SciRobotics

Facebook: @ScienceRobotics

ScienceRobotics

AAAS

# RESEARCH

## IN SCIENCE JOURNALS

Edited by Michael Funk

### INSECT DECLINES

#### Warming autumns, fewer butterflies

**M**any recent studies have revealed sweeping declines in insects over the past few decades. Butterflies are no exception. Forister *et al.* used three different datasets, collected by both experts and community scientists, and found that the number of butterflies has declined over the past 40 years. Although the drivers of decline are complex, the authors found that climate change—in particular, warmer months in the autumn—explain a large portion, even as warming summers actually lead to increases. This work shows that climate change impacts may be insidious and unexpected in their effects. —SNV *Science*, this issue p. 1042

Butterflies such as the great purple hairstreak, *Atlides halesus*, are in decline in the warming American West according to community surveys.



### METALLURGY

#### A two-stage lightweighting

Dealloying allows voids to be created in metals, decreasing the weight of the material. However, when the solid fraction is below about 30%, the mechanical properties rapidly degrade. Shi *et al.* discovered that two dealloying steps allow for the creation of a silver-gold alloy with a solid fraction as low as 12%. Unexpectedly, this process does not degrade the mechanical properties while allowing for large samples to be synthesized. The strategy should be applicable to other alloy systems, providing a pathway for creating strong and lightweight materials. —BG

*Science*, this issue p. 1026

### EXOPLANETS

#### A transiting rocky planet 8 parsecs away

Most exoplanets have been detected using either the radial velocity (RV) method or the transit method, which provide only limited information on the planet's physical properties. In the rare cases in which both methods detect the same planet, the combination determines the planet's mass, radius, and density. Trifonov *et al.* identified a planet, Gliese 486 b, using both RV and transit data. The host star is a red dwarf only 8 parsecs away, making this one of the closest exoplanet systems known. A rocky super-Earth, Gliese 486 b has an equilibrium surface temperature of 700 kelvin. The authors

say that it is observationally favorable for searches for an atmosphere. —KTS

*Science*, this issue p. 1038

### SPECTROSCOPY

#### Electron dynamics in time and space

Following molecular excitation and electron transfer processes in time and space within a single experiment is a long-standing goal of spectroscopy in the field of chemistry. Wallauer *et al.* combined tomographic photoemission imaging with a femtosecond pump-probe scheme to trace the excited state molecular orbitals of surface-adsorbed molecules with both spatial and temporal resolution. The present

demonstration opens a new window for investigating the ultrafast electron transfer dynamics in such processes as chemical reactions on surfaces and intermolecular charge transfers. —YS

*Science*, this issue p. 1056

### MICROBIOLOGY

#### Phenazines liberate phosphate

Bacteria secrete a wide range of small molecules with chemical reactivity that offers multiple functions in different contexts. Phenazines are commonly considered to be antibiotics, but they can also participate in environmental redox reactions, especially with iron. McRose and Newman found that phenazines,



when added exogenously or made by bacteria in situ, can liberate phosphorous (P) in the form of phosphate from mineral surfaces, and that the production of these molecules is regulated by signaling pathways that respond to P limitation. Strains unable to produce these molecules grew more slowly under P limitation but could be rescued by the addition of exogenous phenazines. The authors hypothesize that reductive dissolution of iron oxides has the benefit of liberating P, and that this could be one mechanism of microbial P acquisition in some environments. —MAF

*Science*, this issue p. 1033

## INFLUENZA

### Toward a universal influenza vaccine

The development of a universal influenza vaccine is of paramount importance because seasonal vaccines vary in terms of protection. Darricarrère *et al.* have now moved a universal influenza vaccine one step closer to the clinic. The authors vaccinated nonhuman primates with headless hemagglutinin-stabilized stem antigens presented on ferritin nanoparticles. The vaccines elicited antibodies that neutralized a diverse array of influenza strains, suggesting that they would provide broad protection against influenza infection in vivo. These vaccines, which are now in clinical trials, are promising candidates as broadly protective influenza vaccines. —CSM

*Sci. Transl. Med.* **13**, eabe5449 (2021).

## PHYSIOLOGY

### The source of the leak in sepsis

A challenge in treating the systemic inflammation that occurs in sepsis is the increase in endothelial permeability that leads to widespread tissue edema and immune cell infiltration. Maier-Begandt *et al.* uncovered a pathway activated specifically in

veins by tumor necrosis factor- $\alpha$  (TNF $\alpha$ ), a proinflammatory cytokine whose circulating levels increase greatly during sepsis. TNF $\alpha$  treatment resulted in the activation of Pannexin 1 channels, which ultimately led to disrupted tight junctions in veins but not in arteries. Sepsis induced less lung edema and was less fatal to Pannexin 1-deficient mice compared with control mice. —WW

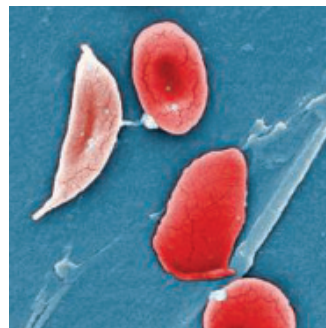
*Sci. Signal.* **14**, eaba2940 (2021).

## HEMATOLOGY

### A red-letter day for RBC research

The study of primary human red blood cell (huRBC) disorders such as sickle cell disease (SCD) and infectious diseases such as malaria has been hampered by a lack of in vivo models of human erythropoiesis. Song *et al.* transferred human fetal liver cells into MISTRG mice, which are immunodeficient and are genetically engineered with several human genes involved in hematopoiesis. This approach was unsuccessful because mature huRBCs are rapidly destroyed in the mouse liver. They then used CRISPR-Cas9 to mutate these mice into a fumarylacetoacetate hydrolase-deficient strain, allowing them to replace the mouse liver with engrafted human hepatocytes. These mice exhibited enhanced human erythropoiesis and circulating huRBC survival and could recapitulate SCD pathology when reconstituted with SCD-derived HSCs. —STS

*Science*, this issue p. 1019

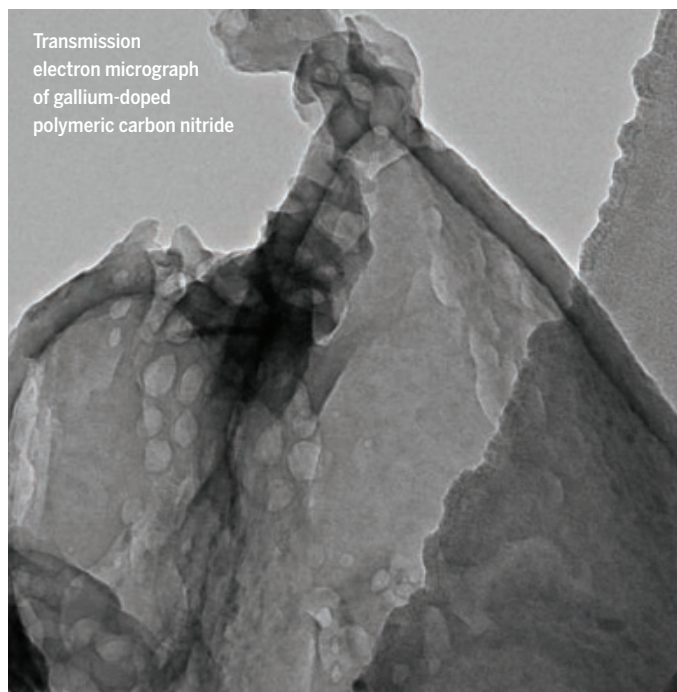


Colored scanning electron microscopy image of sickle cell red blood cells

## IN OTHER JOURNALS

Edited by **Caroline Ash**  
and **Jesse Smith**

Transmission electron micrograph of gallium-doped polymeric carbon nitride



## PHOTOCATALYSIS

### All-in-one photocatalyst

**P**hotocatalysis is a complex process that involves multiple steps such as light absorption, electron-hole separation, and surface reactions. Introduction of cocatalysts is the most traditional approach to promoting or suppressing certain steps. However, this may come at the cost of lower overall stability caused by heterojunctions formed between the catalyst and cocatalyst(s). Jiang *et al.* designed a gallium-doped polymeric carbon nitride as a single photocatalyst that promotes the key steps of photocatalytic hydrogen production. The proposed photocatalyst displays excellent catalytic performance without the assistance of any cocatalyst, and indicates a promising direction toward the development of cocatalyst-free approaches for photocatalytic hydrogen production and other related processes. —YS

*Angew. Chem. Int. Ed.* **10.1002/anie.202015779** (2021).

## NEURODEVELOPMENT

### First in place may not be the winner

The human brain matures more slowly than the brains of nonhuman primates. A key question is to what extent the timing of neuronal development is determined by the neurons themselves rather than by their setting within the developing brain. Schörnig *et al.* overexpressed the neurogenic

transcription factor neurogenin 2 (NGN2) to convert chimpanzee, bonobo, and human pluripotent stem cells (PSCs) into neurons. Functional and transcriptional analyses tracked the development of these cells into excitatory neurons. The authors found that as expression of stem cell markers declined, neurites developed and the cells became synaptically networked. Subsequently, cortical and sensory neurons differentiated. The

## NEUROSCIENCE

## Left- and right-brain projections

**M**ultiple pathways transmit movement commands from the brain down the spinal cord. In mammals, especially in primates, the corticospinal tract is the dominant system. The powerful corticospinal connections enable fine dexterous abilities. An important parallel system involved in posture and gross motor function is called the reticulospinal tract. This tract also contributes to upper limb movement and even to fine hand control. Fisher *et al.* used electrophysiological recordings in macaques to characterize inputs from the main neocortical motor areas to reticulospinal cells of the medulla. They found extensive convergence from the primary motor cortex, as well as the supplementary motor area in both hemispheres, onto neurons in the reticular formation. This knowledge may become helpful for the development of therapies after stroke. —PRS

*J. Neurosci.* **41**, 1005 (2021).

Electrophysiological studies on upper limb movement and fine hand control in macaques are important in developing therapies for stroke.



ape neurons got off to a quicker start than human neurons in terms of both morphology and spontaneous activity. Delays in morphological and functional activity may support the development of greater complexity in the human brain. —PJH

*eLife* **10**, e59323 (2021).

## TRANSCRIPTION

## Shorter is not enough

RNA polymerase II (Pol II) is responsible for the synthesis of all messenger RNA and most small nuclear RNA and microRNA in eukaryotic cells. It is subject to complex regulation, some of which impinges on the C-terminal domain (CTD) of the largest subunit of the polymerase complex. This contains 52 heptapeptide (seven amino acid) repeats in humans. This domain is essential for Pol II activity. Sawicka *et al.* addressed the paradox of variation in the frequency and number of repeats among species by looking at transcriptional output in human cells with only 25 repeats. The authors found

that cells with half the number of repeats were fine in a static state but responded poorly to growth stimulation. This indicates that full-length CTD is required to mediate interactions between proximal and distant elements in gene loci. —DJ

*EMBO J.* **8**, e107015 (2021).

## CANCER

## An ATLAS to find tumor neoantigens

Tumor neoantigens are cancer-specific antigens that are not found in healthy cells and play a major role in anticancer immune responses. Immunotherapies such as cancer vaccines can be based on known neoantigens, but it is often difficult to identify suitable targets. By using a bioassay called ATLAS, Lam *et al.* identified potential neoantigens in patients with lung cancer, and then characterized the immune responses to these antigens in a murine tumor model. A similar approach was applied to patients with multiple cancer types who

were participating in a cancer vaccine trial. ATLAS-identified neoantigens include promising immunogenic candidates for vaccination that offer safe targets and potential for good clinical responses. —YN

*Cancer Discov.* **10**, 1158/2159-8290.CD-20-0377 (2021).

## SEAFLOOR BATHYMETRY

## Sky-high to the sea floor

The ICESat-2 satellite, launched in 2018, was developed primarily to measure the surface elevation of polar ice sheets, but it can do much more than that. One of its other capabilities is determining water depths to as much as 40 meters. Thomas *et al.* used this ability, combined with remote optical imagery, to map the shallow seafloor in coastal areas of Florida, Crete, and Bermuda. This work demonstrates the viability of using ICESat-2 to help make global, space-borne estimates of nearshore bathymetry in shallow, clear water environments. —HJS

*Geophys. Res. Lett.* **10**, 1029/2020GL092170 (2021).

## EDUCATION EQUALITY

## Closing the enrollment income gap

Informing high-achieving, low-income students about the financial aid they would qualify for if accepted to a selective college before they applied to the school increased their application and enrollment rates relative to those of similar students who only learned that they were eligible for the same aid after they had applied for and been accepted to the school. Dynarski *et al.* show, in a randomized controlled trial at the University of Michigan, that reframing when and how this financial aid information is presented, without changing the actual aid itself, boosted the likelihood of applying from 26 to 68% and the likelihood of enrolling at a highly selective college from 13 to 28%. —BW

*Amer. Econ. Rev.* <https://www.aeaweb.org/articles?id=10.1257/aer.20200451> (2021).



## REVIEW SUMMARY

## INFECTIOUS DISEASE

## Infectious diseases and social distancing in nature

Sebastian Stockmaier\*, Nathalie Stroeymeyt, Eric C. Shattuck, Dana M. Hawley, Lauren Ancel Meyers, Daniel I. Bolnick

**BACKGROUND:** Contagious pathogens can trigger diverse changes in host social behaviors, rewiring their social networks and profoundly influencing the extent and pace of pathogen spread. Although “social distancing” is now an all too familiar strategy to manage COVID-19, nonhuman animals also exhibit a suite of pathogen-induced changes in social interactions, either as precautionary measures by healthy hosts or as physiological consequences of infection in sick individuals. These diverse changes in the social behaviors of both healthy and infected hosts in response to pathogens are widespread across taxa, but we still have much to learn about their underlying mechanisms and epidemiological and evolutionary consequences. Studies of social distancing behaviors in nonhuman animals have the

potential to provide important and unique insights into ecological and evolutionary processes relevant to human public health, including pathogen transmission dynamics and virulence evolution.

**ADVANCES:** We synthesize the literature on pathogen-induced changes in sociality in nonhuman animals and in humans. These include active and passive changes in pathogen-exposed and -unexposed group members occurring both before and after individuals develop an active infection. Behavioral changes that reduce social interactions—and thus pathogen spread—include changes driven by infectious hosts, such as sickness behaviors and active self-isolation, as well as changes driven by healthy hosts, including active avoidance or

exclusion of infectious individuals and proactive social distancing in the face of pathogenic threats. Although species have evolved behavioral social distancing because it reduces infection risk, these behaviors also incur costs by limiting access to the many benefits of group living, such as protection against predators and cooperative food finding. Thus, many species appear to have evolved the ability to alter the expression of these behaviors in ways that maximize benefits and minimize costs. The most susceptible individuals of some species show the strongest avoidance of sick conspecifics, and social distancing behaviors are sometimes foregone in interactions with close relatives. Pathogen-induced changes in sociality also apply important selection pressures on pathogens. Because social distancing reduces transmission and thus fitness, pathogens may evolve lower levels of virulence, presymptomatic transmission, or the ability to disguise cues that enable hosts to recognize their presence. Finally, pathogen infection can also increase social interactions when healthy individuals lend aid to pathogen-contaminated or sick conspecifics. Helping sick individuals is a major part of human and eusocial insect societies but is less commonly observed in other, nonhuman animals. Whether pathogens can evolve to elicit helping behavior in hosts, thus augmenting their own transmission, remains unknown.

**OUTLOOK:** The structure and dynamics of social contact networks fundamentally determine the fate of disease outbreaks, that is, how fast and far they spread and who will be infected. In the race to combat the COVID-19 pandemic, numerous studies have begun to address the public health utility of unprecedented social distancing efforts. Nonhuman animal systems, particularly those with social structures similar to those of humans, present unique opportunities to inform relevant public health questions such as the effectiveness, variability, and required duration of social distancing measures. Further, the experimental tractability of nonhuman animal systems allows study of the coevolutionary dynamics generated by social distancing behaviors, which themselves have public health implications. Selection for or against social distancing behaviors has the potential to create a conflict of interest and could incentivize selfish behaviors that are not in the best interest of everyone. ■

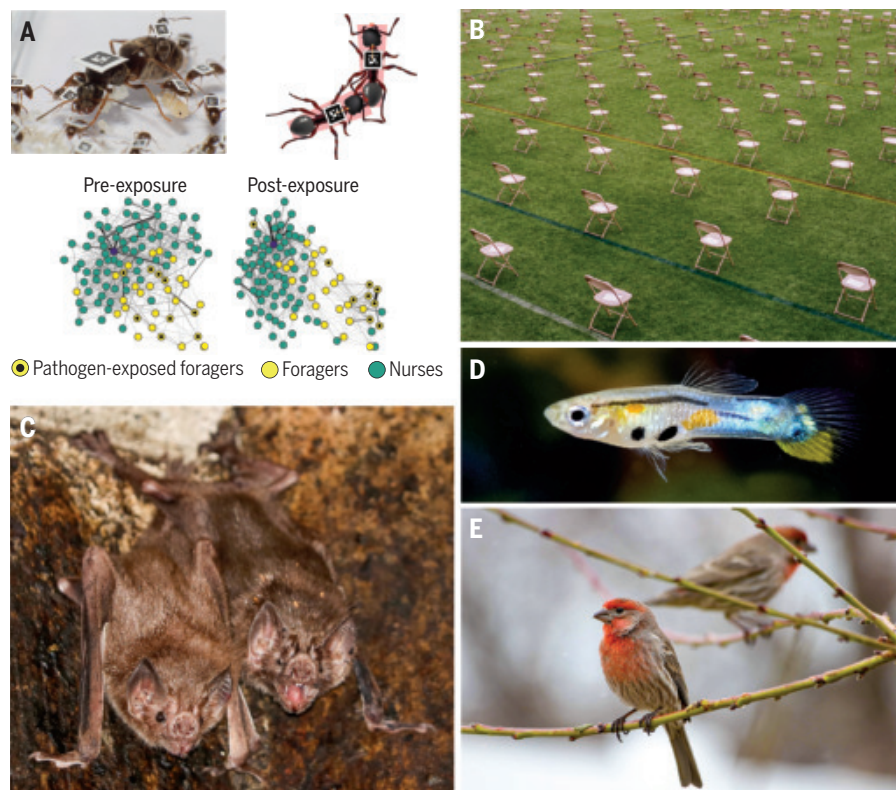
The list of author affiliations is available in the full article online.

\*Corresponding author. Email:

sebastian.stockmaier@utexas.edu

Cite this article as S. Stockmaier *et al.*, *Science* 371, eabc8881 (2021). DOI: 10.1126/science.abc8881

**S READ THE FULL ARTICLE AT**  
<https://doi.org/10.1126/science.abc8881>



**Social distancing in humans and nonhuman animals.** (A) Pathogen-exposed forager ants self-isolate and their nestmates increase social distance to each other (image: Timothée Brüttsch). (B) People social distance during COVID-19 (image: Forest Simon). (C) Sick vampire bats reduce grooming non-close kin (image: Gerald Carter). (D and E) Under certain conditions, Trinidadian guppies avoid parasitized individuals (D), (image: Sean Earnshaw, University of St. Andrews) and house finches avoid sick conspecifics (E) (image: Jeremy Stanley).

## RESEARCH ARTICLE SUMMARY

## SPERM GENOMICS

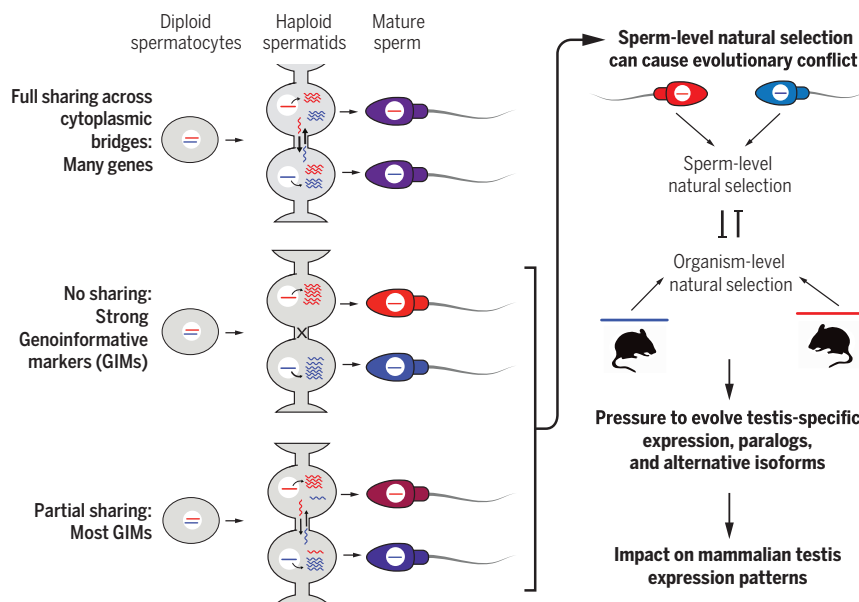
# Widespread haploid-biased gene expression enables sperm-level natural selection

Kunal Bhutani\*, Katherine Stansifer\*, Simina Ticau\*, Lazar Bojic, Alexandra-Chloé Villani, Joanna Sliasz, Claudia M. Cremers, Christian Roy, Jerry Donovan, Brian Fiske, Robin C. Friedman†

**INTRODUCTION:** Mendel's first law dictates that alleles are distributed equally among progeny, which requires sperm to be functionally independent of their genetic payload. Although mammalian spermatogenesis includes a long haploid stage with extensive gene expression, gene products are shared through spermatid cytoplasmic bridges, which decreases phenotypic differences between individual haploid sperm. However, there are known exceptions to the rule of complete sharing of transcripts between spermatids, including a gene product encoded by the *t* haplotype in mice that has restricted localization and therefore does not cross cytoplasmic bridges. This results in functional differences between sperm depending on their genotype and leads to preferential transmission of the *t* haplotype, causing it to act as a selfish genetic element.

**RATIONALE:** Given that many mammalian transcripts have specific subcellular localization, we reasoned that many spermatid gene products would not be completely shared across cytoplasmic bridges and would therefore exhibit allele-specific bias reflecting the haploid genotype of the cell. Here, we performed single-cell RNA sequencing in four mammalian species to quantify allele-specific biases in spermatids and develop a new computational technique to jointly infer genotype and allelic expression biases (both technical and biological) in single haploid cells.

**RESULTS:** We show that a large class of mammalian genes exhibit allelic bias linked to the haploid genotype of the cell, which we call "genoinformative markers" (GIMs). Confident GIMs comprise 31 to 52% of spermatid-



**Incomplete transcript sharing leads to sperm-level functional differences.** Left: Models for sharing of gene products between adjacent haploid spermatids across cytoplasmic bridges. Genes with complete sharing (top) have no differences in allelic expression; genes with no sharing (middle) lead to allele-specific gene expression and potentially phenotypic differences in mature sperm; genes with partial sharing (bottom) lead to quantitative allelic biases and potential quantitative phenotypic differences in mature sperm. Most GIMs fall into the partial sharing category. Right: Phenotypic differences between mature sperm that are linked to the genotype (top) can lead to sperm-level natural selection, which may conflict with organism-level natural selection. This creates an evolutionary pressure that may be resolved by testis-specific expression, paralogs, and alternative isoforms. This suggests a possible explanation for the high prevalence of testis-specific gene expression patterns in mammals.

expressed genes in mice, bulls, cynomolgus macaques, and humans, and at least 62% of GIMs had at least a twofold mean allelic bias. Most GIMs identified were autosomal genes, but we did find evidence for genoinformativity in sex chromosome genes as well. Genoinformativity tends to be conserved between individuals and between homologs of different species, suggesting that it is governed by slow-evolving features. GIMs are enriched for specific subcellular localization patterns and 3' untranslated region motifs and are depleted from chromatoid bodies (subcellular structures that transit across cytoplasmic bridges), consistent with the model of genoinformativity by evasion of cytoplasmic bridges. For GIMs with proteins that are also not shared across cytoplasmic bridges, sperm function may be affected by allelic differences, leading to sperm competition and sperm-level natural selection. Genes expressed in spermatogenesis are known to experience heightened selective forces on average, but a subset of GIMs experience further increases, as evidenced by statistically significant enrichment for signatures of selective sweeps, loss-of-function intolerance, and transmission ratio distortion in humans, mice, and bulls. These forces are consistent with a subset of GIMs acting as selfish genetic elements that spread alleles unevenly. For GIMs with functions both in sperm and in somatic tissues, this could cause an evolutionary conflict for genes because optimal function in highly specialized sperm cells may be detrimental in somatic cells. We identified evolutionary pressure to avoid this conflict, because GIMs are significantly enriched for testis-specific gene expression, paralogs, and isoforms.

**CONCLUSION:** Our work demonstrates that at least one-third of spermatid transcripts are GIMs across a variety of mammalian species. Many of the corresponding proteins may not have genoinformative expression, but we provide evolutionary evidence that a subset of GIMs show signatures of sperm-level natural selection, implying an effect of protein-level genoinformativity during mammalian evolution. This phenomenon may help to explain why testis gene expression patterns are an outlier relative to all other tissues, with a large fraction of testis-specific gene expression, paralogs, and isoforms. ■

The list of author affiliations is available in the full article online.

\*These authors contributed equally to this work.

†Corresponding author. Email:

robin.friedman@ohanabio.com

Cite this article as: K. Bhutani et al., *Science* 371, eabb1723 (2021). DOI: 10.1126/science.abb1723

**S READ THE FULL ARTICLE AT**  
<https://doi.org/10.1126/science.abb1723>



## RESEARCH ARTICLE SUMMARY

## CANCER

Targeting a neoantigen derived from a common *TP53* mutation

Emily Han-Chung Hsiue\*, Katharine M. Wright\*, Jacqueline Douglass\*, Michael S. Hwang, Brian J. Mog, Alexander H. Pearlman, Suman Paul, Sarah R. DiNapoli, Maximilian F. Konig, Qing Wang, Annika Schaefer, Michelle S. Miller, Andrew D. Skora, P. Aitana Azurmendi, Michael B. Murphy, Qiang Liu, Evangeline Watson, Yana Li, Drew M. Pardoll, Chetan Bettgowda, Nickolas Papadopoulos, Kenneth W. Kinzler, Bert Vogelstein†, Sandra B. Gabelli†, Shibin Zhou†

**INTRODUCTION:** *TP53* (tumor protein P53), a tumor suppressor gene, is the most commonly mutated cancer-driver gene. Nevertheless, drugs that target mutant p53, the protein product, remain unavailable today, decades after the discovery of its critical role in cancer. Although drugs that inactivate proteins encoded by mutant oncogenes, such as epidermal growth factor receptor (*EGFR*) or *BRAF*, are available, proteins encoded by tumor suppressor genes are already inactivated through mutation. Reactivating such proteins by use of pharmacologic agents is very challenging. Thus, new approaches to target such inactivated proteins, including those encoded by *TP53*, are actively being sought.

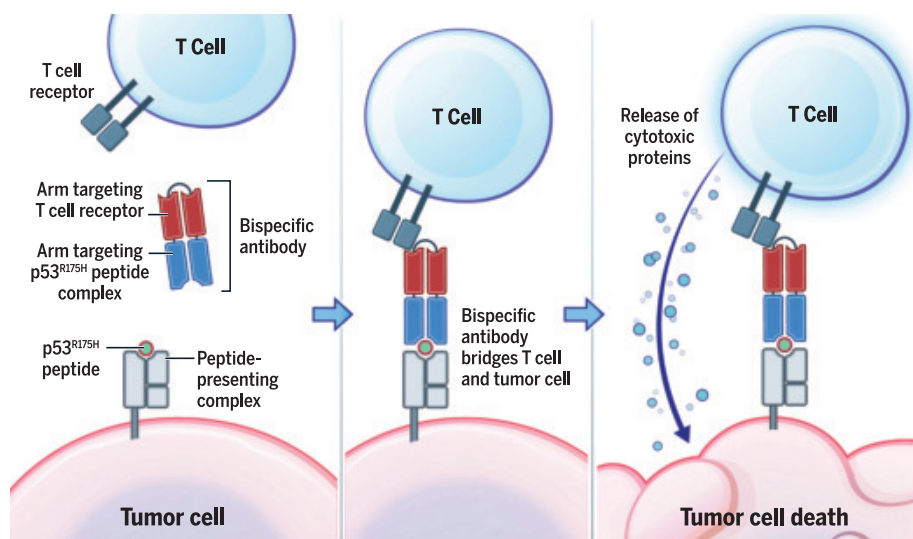
**RATIONALE:** We attempted to develop an immunotherapeutic approach to target proteins encoded by a mutant *TP53* gene. p53 is an intracellular protein, primarily located within the nucleus, thus out of reach for conventional

antibody-based therapies. However, proteins are degraded into peptides by the proteasome, and a fraction of these peptides can be presented by the human leukocyte antigen (HLA) on the cell surface. This in principle makes it possible for suitably designed proteins to recognize peptide fragments of intracellular proteins when bound to HLA on the cell surface. The arginine-to-histidine substitution at codon 175 (R175H) is the most common *TP53* mutation and is the most frequent mutation in any tumor suppressor gene. The peptide HMTEVVRHC (mutant amino acid underlined), derived from the p53<sup>R175H</sup> mutation, can bind to a particular HLA allele (HLA-A\*02:01) and form a peptide-HLA complex on the cell surface. HLA-A\*02:01 is the most frequent HLA-A type in the U.S. population. Thus, the p53<sup>R175H</sup>/HLA-A\*02:01 complex is a particularly attractive therapeutic target, shared among many cancer patients. However, such neoantigen peptide-HLA complexes typically exist at low density on cell

surfaces, and a potent therapeutic format will be required to achieve meaningful therapeutic effects. T cells can be activated in the presence of a very low number of antigens. We therefore attempted to generate a T cell-based therapy that links T cells to cancer cells through a newly developed antibody that specifically binds to the p53<sup>R175H</sup> peptide-HLA complex.

**RESULTS:** Using a large phage library that displays diverse antibody variable fragments, we identified H2, an antibody fragment that binds with high affinity to the p53<sup>R175H</sup> peptide-HLA complex but not to its wild-type counterpart. We converted H2 into a T cell-based immunotherapeutic agent—a bispecific single-chain diabody—by fusing it with an antibody fragment that binds to the T cell receptor-CD3 complex on T cells. This bispecific antibody binds to the p53<sup>R175H</sup> peptide-HLA complex with an affinity [dissociation constant ( $K_d$ ) = 86 nM] higher than that typical for T cell receptors and redirects T cells to recognize cancer cells that express the complex. Despite a very low density of the peptide-HLA complex on the cell surface, as quantified with mass spectrometry, the bispecific antibody effectively activated T cells to secrete cytokines and kill target cancer cells. This killing was dependent on the expression of both the cognate HLA and particular *TP53* mutation. The bispecific antibody also resulted in regression of human xenograft tumors in mice, both when treatment was initiated soon after tumor engraftment and when the tumors were already well established. Structure of the H2 antibody fragment with the p53<sup>R175H</sup> peptide-HLA complex showed that H2 formed a cage-like structure around the mutant amino acid (His<sup>175</sup>) and one adjacent amino acid (Arg<sup>174</sup>). The stability imparted by this cage provided the structural basis for the highly specific recognition of the mutant peptide-HLA complex by H2.

**CONCLUSION:** We developed an antibody-based therapeutic approach that targets a neoantigen derived from a common *TP53* mutation in a highly specific fashion. It effectively activated T cells and lysed tumor cells both in vitro and in vivo despite the low antigen density on their surface. This approach could in theory be used to treat cancers containing other mutations that are difficult to target by conventional means. ■



**Mechanism of action of bispecific antibody H2-scDb.** A mutant peptide containing the common *TP53* mutation R175H can form a complex with HLA-A\*02:01 on the tumor cell surface. H2-scDb, a bispecific antibody, binds to the p53<sup>R175H</sup> peptide-HLA complex with one arm and the T cell receptor complex with the other arm, activating T cells to kill tumor cells.

The list of author affiliations is available in the full article online. \*These authors contributed equally to this work.

†Corresponding author. Email: vogelbe@jhmi.edu (B.V.); gabelli@jhmi.edu (S.B.G.); sbzhou@jhmi.edu (S.Z.)  
Cite this article as E. H. Hsiue et al., *Science* 371, eabc8697 (2021). DOI: 10.1126/science.abc8697

**READ THE FULL ARTICLE AT**  
<https://doi.org/10.1126/science.abc8697>

## RESEARCH ARTICLE SUMMARY

## ENZYME EVOLUTION

## Parallel molecular mechanisms for enzyme temperature adaptation

Margaux M. Pinney\*, Daniel A. Mokhtari, Eyal Akiva, Filip Yabukarski, David M. Sanchez, Ruibin Liang, Tzanko Doukov, Todd J. Martinez, Patricia C. Babbitt, Daniel Herschlag\*

**INTRODUCTION:** Over billions of years, organisms and their enzymes have been evolving and adapting in response to selection pressures from their environments. In particular, livable temperature varies from about  $-15^{\circ}$  to  $121^{\circ}\text{C}$  and exerts an evolutionary force that manifests in the adaptation of enzyme stabilities and activities: At increased temperatures, enzymes evolve greater stability to combat thermal denaturation and maintain a folded structure, whereas at decreased temperatures, nearly all chemical reactions necessary for life slow, placing evolutionary pressure on cold-adapted enzymes to be more active. An understanding of the molecular and evolutionary mechanisms that underlie enzyme tempera-

ture adaptation are integral to our understanding of how living systems have evolved and can reveal hidden aspects of how enzyme activity and stability is achieved, helping to define rules that can be used for enzyme design.

**RATIONALE:** We have dissected the molecular and evolutionary mechanisms underlying enzyme temperature adaptation both deeply and broadly. We first turned to the bacterial enzyme ketosteroid isomerase (KSI), combining mechanistic and structural studies with sequence and phylogenetic analyses to reveal the mechanisms underlying its activity and stability adaptation at the atomic and residue levels. Building on these results, we performed

sequence and phylogenetic analyses, examining enzyme temperature adaptation in 2194 bacterial enzyme families to identify residue changes associated with growth temperature differences (referred to as “temperature-associated residues”) and analyzing their physical properties and interactions.

**RESULTS:** We show that temperature adaptation in KSI arises primarily from a single active-site residue change with minimal epistasis. In cold-adapted KSI orthologs, a stronger active-site hydrogen-bond donor, protonated Asp<sup>103</sup> (D103), improves activity. Conversely, warm-adapted KSI orthologs are stabilized by Ser<sup>103</sup> (S103), which decreases activity but increases stability by removing the protonation-coupled folding of D103. Phylogenetic analyses showed that this active-site amino acid change (D103/S103) has occurred in diverse KSI sequence backgrounds from diverse bacteria, further supporting limited epistasis and suggesting parallel adaptation.

Our broad sequence and phylogenetic analyses revealed 158,184 statistically significant temperature-associated residues from 1005 enzyme families. Most of these residues are found in sequences from phylogenetically diverse bacteria, suggesting widespread temperature adaptation and parallel evolution. By mapping temperature-associated residues to structure, we found that these residues typically change with temperature on their own or with one other residue in physical contact, suggesting limited epistasis at these sites. Analyses of these temperature-associated residues reveal molecular and physical trends that test, hone, and revise nearly all prior mechanisms for enzyme temperature adaptation and identify networks of residues that appear to coadapt to temperature, perhaps cooperatively influencing catalysis stability, and/or allostery.

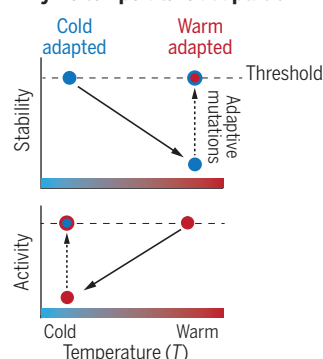
**CONCLUSION:** Our results broadly and deeply addressed enzyme temperature adaptation, revealing molecular mechanisms underlying the adaptation of KSI and identifying 158,184 temperature-associated residues; these data reveal physical trends and provide extensive data that can be further mined to understand molecular evolution and applied to enzyme design. These data further suggest that enzyme adaptation has repeatedly followed evolutionary paths of low epistasis, advancing our understanding of the evolutionary mechanisms that underly adaptation of nature's repertoire of enzymes. ■

The list of author affiliations is available in the full article online.

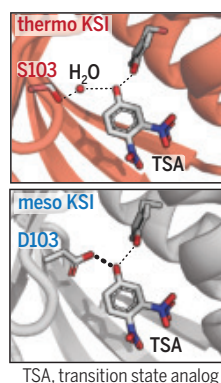
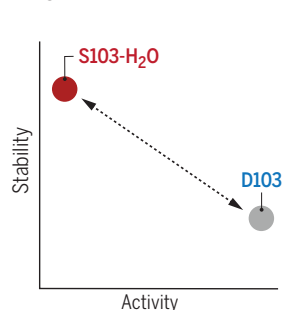
\*Corresponding author. Email: margauxp@stanford.edu (M.M.P.); herschla@stanford.edu (D.H.)  
Cite this article as M. M. Pinney *et al.*, *Science* 371, eaay2784 (2021). DOI: 10.1126/science.aay2784

**READ THE FULL ARTICLE AT**  
<https://doi.org/10.1126/science.aay2784>

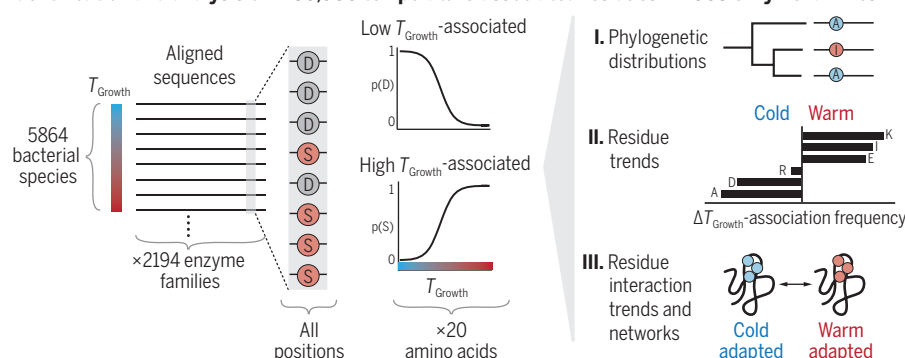
## Enzyme temperature adaptation



## Activity and stability adaptation from a single active-site residue in KSI



## Identification and analysis of &gt;150,000 temperature-associated residues in 1005 enzyme families



**Analyses of enzyme temperature adaptation.** Enzymes adapt to low or high temperatures by modifying their activities or stabilities, respectively (top left). Temperature adaptation in KSI arises primarily from one active-site change (top right). Sequence analyses identify residues whose identity is associated with bacterial growth temperature ( $T_{\text{Growth}}$ ) (bottom left). The phylogenetic distribution of these residues, their physical trends, and structural interactions were then analyzed (bottom right).



## RESEARCH ARTICLE SUMMARY

## HEART DEVELOPMENT

# Characterization of a common progenitor pool of the epicardium and myocardium

Richard C. V. Tyser\*, Ximena Ibarra-Soria\*, Katie McDole, Satish Arcot Jayaram, Jonathan Godwin, Teun A. H. van den Brand, Antonio M. A. Miranda, Antonio Scialdone, Philipp J. Keller, John C. Marioni†, Shankar Srinivas†

**INTRODUCTION:** The vertebrate heart is composed of diverse cell types, all essential for normal cardiac function. In the mouse, the earliest mesodermal progenitors of cardiomyocytes, formed during gastrulation, migrate rostrally from the primitive streak to form the cardiac crescent and initiate contractile activity. The cardiac crescent subsequently undergoes remodeling to form the linear heart tube. There are at least two distinct groups of mesodermal cardiac progenitors, the first and second heart fields (FHF and SHF, respectively), defined broadly on the basis of marker genes expressed in different but overlapping regions of the early embryo. Cells from outside these heart fields can also contribute to the heart. One such structure, the proepicardium, gives rise to the epicardium, the outermost layer of cells of the vertebrate heart. The epicardium provides important paracrine signals and can also generate several cardiac cell types, including cardiomyocytes, vascular smooth muscle, and fibroblasts.

**RATIONALE:** Our current understanding of when and how different cardiac cell types arise during early development is limited. Single-cell transcriptomics offers a powerful approach to

characterize the various cell types of the embryonic heart and generate hypotheses about their origin and fate. We therefore combined single-cell RNA sequencing with high-resolution volume imaging and time-lapse microscopy to precisely characterize the cells of the mouse embryonic heart at single-cell resolution. This powerful combinatorial approach provides a unified transcriptional and anatomical definition of cardiac progenitor types and their differentiation trajectories toward cardiomyocytes.

**RESULTS:** We used manual microdissection to isolate the cardiac region of mouse embryos, from early cardiac crescent to linear heart tube stages, and performed single-cell RNA sequencing. This enabled us to transcriptionally define the cardiac progenitor populations in this region, including FHF and SHF. As a user-friendly community resource, we created a web interface to investigate these data, accessible at <https://marionilab.cruk.cam.ac.uk/heartAtlas/>. To identify the anatomical locations of these cell populations at single-cell resolution, we used whole-mount immunohistochemistry, multiplexed fluorescence in situ hybridization, and high-resolution volume imaging of com-

binations of markers. This comprehensive imaging analysis revealed the discrete locations of these transcriptional clusters and highlighted the spatially ordered maturation of cardiomyocytes. It also identified a population of progenitor cells located rostral to the cardiac crescent, at the confluence of the embryonic and extraembryonic mesoderm, which we call the juxta-cardiac field (JCF). Using single-cell resolution time-lapse imaging and genetic lineage labeling, we established that the JCF can contribute to both cardiomyocytes and the proepicardium. The JCF therefore represents the earliest known progenitors of the epicardium, the outermost layer of the vertebrate heart.

**CONCLUSION:** This study provides a detailed characterization of the transcriptional states and anatomical locations of cardiac progenitors, as well as their transition states during differentiation toward cardiomyocytes, thereby representing a valuable community resource. Furthermore, it provides fresh insights into the formation of the heart. By identifying the juxta-cardiac field, our work widens the cardiac progenitor region and identifies the earliest progenitors of the proepicardium. This study will contribute to a better understanding of the origin of congenital cardiac defects and provide basic insights for informing the development of regenerative approaches to treat heart disease. ■

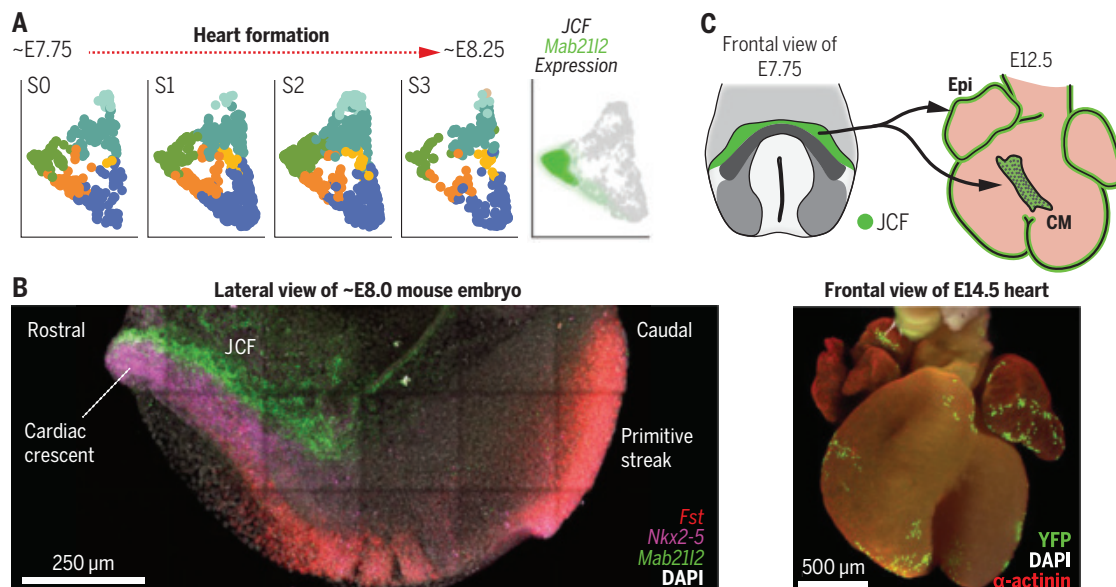
The list of author affiliations is available in the full article online.  
\*These authors contributed equally to this work.

†Corresponding author. Email: [john.marioni@cruk.cam.ac.uk](mailto:john.marioni@cruk.cam.ac.uk) (J.C.M.); [shankar.srinivas@dpag.ox.ac.uk](mailto:shankar.srinivas@dpag.ox.ac.uk) (S.S.)  
Cite this article as R. C. V. Tyser *et al.*, *Science* 371, eabb2986 (2021). DOI: 10.1126/science.abb2986

**READ THE FULL ARTICLE AT**  
<https://doi.org/10.1126/science.abb2986>

## Identification of a progenitor pool for cardiomyocytes and epicardium.

(A) Single-cell RNA sequencing of the developing heart identified a cell population characterized by *Mab21l2* expression. E, embryonic day. (B) These cells lie rostral to the cardiac crescent and represent a juxta-cardiac field (JCF). DAPI, 4',6-diamidino-2-phenylindole. (C) This progenitor pool gives rise to both cardiomyocytes (CM) and epicardium (Epi). Yellow fluorescent protein (YFP) cells (bottom panel) are JCF-derived epicardial cells and cardiomyocytes.



## RESEARCH ARTICLE SUMMARY

## STRUCTURAL BIOLOGY

## A structure of human Scap bound to Insig-2 suggests how their interaction is regulated by sterols

Renhong Yan\*, Pingping Cao\*, Wenqi Song\*, Hongwu Qian, Ximing Du, Hudson W. Coates, Xin Zhao, Yaning Li, Shuai Gao, Xin Gong, Ximing Liu, Jianhua Sui, Jianlin Lei, Hongyuan Yang, Andrew J. Brown, Qiang Zhou, Chuangye Yan†, Nieng Yan‡

**INTRODUCTION:** Cholesterol homeostasis is controlled by the sterol regulatory element-binding protein (SREBP) pathway. SREBPs (SREBP-1a, -1c, and -2) are transcription factors with an N-terminal transcription factor domain and a C-terminal regulatory domain (CTD) connected by a transmembrane (TM) hairpin. Among the key players in this pathway, two membrane proteins—Scap and Insig (Insig-1 or -2)—together monitor the sterol level in the endoplasmic reticulum (ER) membrane.

SREBP-CTD constitutively interacts with the C-terminal WD40 domain of Scap. The N terminus of Scap comprises eight TM segments, among which S2 to S6 constitute the sterol-sensing domain (SSD). The SSD is also found in several membrane proteins that are involved in cholesterol metabolism or transport. When the cellular cholesterol level surpasses a certain threshold, the SREBP-2–Scap complex is anchored to the ER membrane through a sterol-dependent interaction between the Scap-SSD and Insig. The interaction is more sensitive to some

cholesterol derivatives, like 25-hydroxycholesterol (25HC), than to cholesterol. When cholesterol levels drop, Scap dissociates from Insig. The SREBP-2–Scap complex is subsequently translocated by the COPII vesicles to the Golgi, where the transcription factor domain of SREBP-2 is liberated after two sequential proteolytic cleavages and is transported into the nucleus to activate gene expression for cholesterol synthesis and uptake. Despite rigorous characterizations, the molecular basis for sterol-regulated interaction between Scap and Insig remains elusive.

**RATIONALE:** The structure of the Scap-Insig-25HC ternary complex will not only reveal the basis for sterol sensing by Scap and Insig but also facilitate the development of potential therapeutics against viral infections and for cancer treatment. Modern methods of single-particle cryo-electron microscopy (cryo-EM) provide a powerful tool to elucidate the structure of this relatively small and highly dynamic membrane protein complex.

**RESULTS:** WD40-deleted human Scap (residues 1 to 752) and full-length human Insig-2 were transiently coexpressed in HEK293F cells. Supplementation of 25HC during protein expression and isolation was necessary to maintain an intact complex. For cryo-EM analysis, a guided multi-reference three-dimensional classification method was combined with Relion and CryoSPARC. The TM region was determined at resolutions of 3.3 to 3.9 Å, whereas the luminal domains were of lower resolutions, insufficient for model building. Seven TMs—including the entire SSD—in Scap and all six TMs in Insig-2 were resolved.

TMs 1, 2, 3, and 6 of Insig-2 enclose a hydrophobic pocket in which there is no density corresponding to a sterol. A stretch of density that can perfectly fit 25HC is sandwiched by the two proteins in the luminal leaflet of the membrane. Whereas the binding site is mainly constituted by hydrophobic residues on TMs 3 and 4 of Insig-2 and S4, S5, and S6 of Scap, the 25-OH group at the end of the iso-octanol tail of 25HC is exposed to the cytosolic milieu through a hydrophilic cavity enclosed by Scap and Insig-2, which affords a potential explanation for the preference of 25HC over cholesterol in promoting the interaction between Scap and Insig.

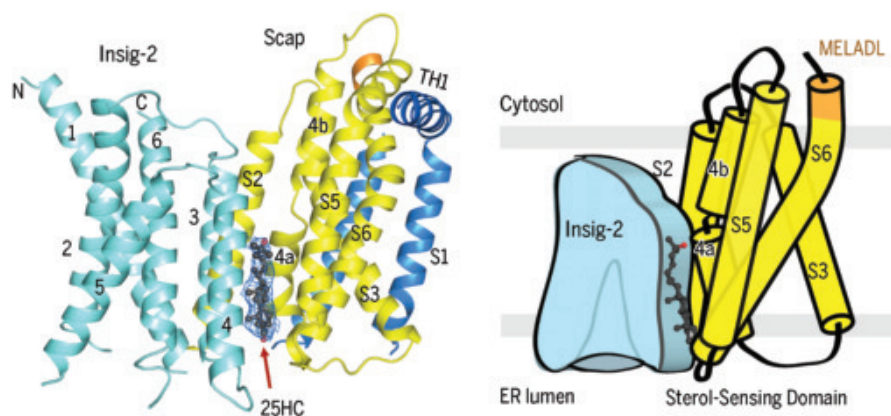
S4 in Scap is broken in the middle, resulting in two half helices, S4a and S4b. Compared with the structures of SSD-containing proteins NPC1 and patched 1, in which S4 is straight, the tilting of S4a toward the interior of the SSD creates the space for 25HC accommodation and for the displacement of S2, which constitutes a major interface with Insig. The sandwiched 25HC functions as more than a molecular glue. Its presence stabilizes the unwound conformation of Scap-S4 that is crucial for Insig association. Scap mutations, such as D428A (Asp<sup>428</sup> → Ala) and Q432A (Gln<sup>432</sup> → Ala), that may lower the energy penalty for S4 unwinding, allow for complex formation with Insig in the absence of sterols. Therefore, the interdependence of S4 unwinding, 25HC accommodation, and Insig binding establishes the molecular basis for sterol sensing.

**CONCLUSION:** The cryo-EM structure of the human Scap and Insig-2 complex bound to 25HC, together with biochemical analyses, shed light on the mechanistic understanding of sterol sensing in the SREBP pathway. Unwinding of Scap-S4 serves as the switch for 25HC binding and Insig association. Our studies also provide structural interpretations for two well-characterized Scap mutations, the gain-of-function D428A and loss-of-function Y298C (Tyr<sup>298</sup> → Cys). ■

The list of author affiliations is available in the full article online.  
\*These authors contributed equally to this work.

†Corresponding author. Email: nyan@princeton.edu (N.Y.); yancy2019@tsinghua.edu.cn (C.Y.)  
Cite this article as R. Yan et al., *Science* 371, eabb2224 (2021). DOI: 10.1126/science.abb2224

**READ THE FULL ARTICLE AT**  
<https://doi.org/10.1126/science.abb2224>



**Cryo-EM structure of the complex of human Scap and Insig-2 in the presence of 25HC.** (Left) The TM region of the complex was resolved at resolutions of 3.3 to 3.9 Å, with the highest resolution at the interface between the two proteins. Insig-2 is colored cyan, the SSD of Scap is colored yellow, and the last four resolved residues 447–MELADL of Scap are colored orange. A 25HC molecule is sandwiched between Scap and Insig-2 in the luminal leaflet of the membrane. Formation of the 25HC binding pocket in the complex requires the unwinding of the S4 segment of Scap in the middle of the membrane. The density for 25HC, shown as the blue mesh, is contoured at 5  $\sigma$ . TH1, transverse helix 1. (Right) A cartoon of the complex structure highlights the 25HC binding site, the broken Scap-S4, and a hydrophobic central pocket in Insig-2. MELADL, the Scap motif that can be recognized by COPII.



## RESEARCH ARTICLE SUMMARY

## IMMUNOLOGY

## Primordial GATA6 macrophages function as extravascular platelets in sterile injury

J. Zindel, M. Peiseler, M. Hossain, C. Deppermann, W. Y. Lee, B. Haenni, B. Zuber, J. F. Deniset, B. G. J. Surewaard, D. Candinas, P. Kubes\*

**INTRODUCTION:** Most multicellular organisms have a major body cavity that harbors immune cells. In primordial species such as the purple sea urchin, these cells—called coelomocytes—fulfill dual functions. Sea urchin coelomocytes clear pathogens from the peritoneal compartment, but they have also been shown to form multicellular aggregates that adhere to injured tissue and are crucial for repair. In mammals, the peritoneal, pleural, and pericardial cavities are filled with vast numbers of resident GATA6<sup>+</sup> cavity macrophages. The role of peritoneal cavity macrophages as phagocytes in clearing pathogens has been established for decades. Recent evidence suggests that these cells migrate to injuries within the peritoneal cavity, where they have been shown to promote tissue repair.

**RATIONALE:** It remains unclear how cavity macrophages, which are suspended in the fluid phase (peritoneal fluid), can identify injuries, which can be several thousand micrometers away, and how they can exhibit chemotaxis over that distance through a fluid-filled compartment that is under constant convective flow. In this study, we developed an intravital

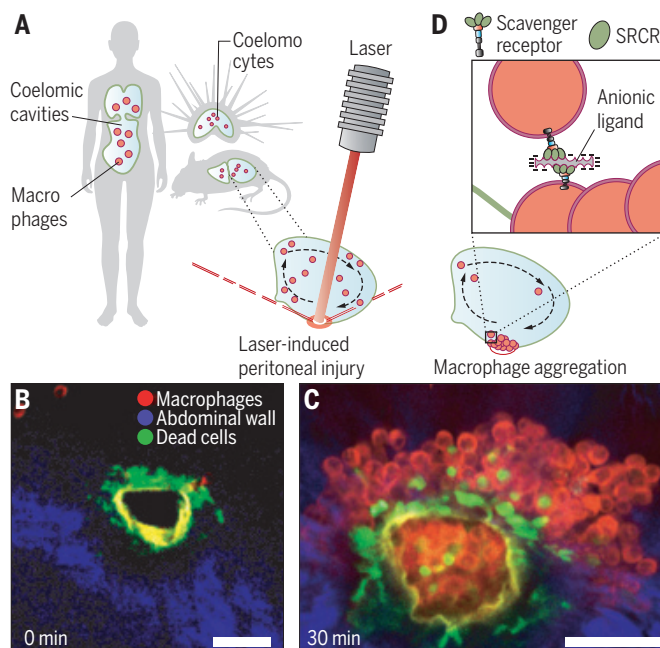
microscopy (IVM) model to study the dynamics and molecular mechanisms of resident GATA6<sup>+</sup> macrophage recruitment in the peritoneal cavity after injury.

**RESULTS:** By using inverted multiphoton IVM with extremely sensitive non-descanned hybrid detectors, we were able to image the peritoneal cavity through the intact abdominal wall in living animals. The tracks of the rapidly moving peritoneal macrophages showed that they passively traversed the peritoneal cavity in a respiration-dependent and seemingly random pattern. Next, we used a focused high-power infrared laser beam to induce focal injuries to the peritoneum, and we imaged the subsequent immune response. We found that peritoneal macrophages were rapidly recruited through a two-step process: (i) an initial tether of macrophages to the injury site, followed by (ii) secondary tethers that formed an aggregate reminiscent of a thrombus-like structure in response to injury. Macrophage aggregation mirrored and rivaled the speed of platelet aggregation (thrombus formation) in the adjacent vasculature. By probing the transcriptome

of peritoneal macrophages and a targeted series of knockout and inhibition IVM experiments, we found that peritoneal macrophage aggregation was independent of canonical mammalian adhesion molecules such as integrins, selectins, and immunoglobulin-like adhesion molecules. Instead, peritoneal macrophage aggregation was dependent on primordial scavenger receptor cysteine-rich (SRCR) domains. SRCR domains are highly conserved among species, with many homologs expressed by sea urchin coelomocytes and sea sponges, and some of these proteins have been identified as cell-cell adhesion molecules in these primordial organisms. Aggregates of cavity macrophages physically sealed injuries and promoted rapid repair of focal peritoneal lesions. However, in abdominal surgery models that reflect iatrogenic surgical situations in which the peritoneal cavity is opened and foreign suture material is introduced, these cavity macrophages formed extensive aggregates that promoted the growth of intra-abdominal scar tissue called peritoneal adhesions. These peritoneal adhesions cause substantial morbidity for patients and considerable costs for health care systems. We showed that the number and tenacity of peritoneal adhesions was significantly reduced by either depleting peritoneal macrophages or therapeutically inhibiting their scavenger receptor-dependent recruitment and aggregation.

**CONCLUSION:** Our results unveil a platelet-like extravascular fluid-phase response by macrophages. This rapid response seals the peritoneal leaks within minutes and serves an important function in repairing small injuries such as focal thermal or laser-induced peritoneal injuries. We hypothesize that such focal injuries reflect a type of injury for which the immune system has evolved a beneficial response. By contrast, iatrogenic procedures, such as abdominal surgery involving implantation of foreign material, reflect a type of injury that has no evolutionary precedent. In this scenario, peritoneal macrophages may cause detrimental scarring, instead of restitution ad integrum, in an attempt to repair the wound. Thus, macrophage aggregation and its inhibition by scavenger receptor antagonists are of clinical importance and may provide a therapeutic target to prevent scar formation after surgery in the peritoneal cavity. Furthermore, these findings may extend to other cavities, including pleural and pericardial spaces. ■

**Aggregation of GATA6<sup>+</sup> peritoneal cavity macrophages in response to laser-induced peritoneal injury.** (A) Human, mouse, and sea urchin coelomic cavities (mouse example enlarged) with circulating coelomocytes and macrophages. Injuries were induced by a multiphoton laser. (B) IVM image immediately after injury. Scale bar, 50  $\mu$ m. (C) IVM image 30 min after injury. Scale bar, 50  $\mu$ m. (D) Aggregation was dependent on scavenger receptors and a (yet unknown) polyanionic ligand.



The list of author affiliations is available in the full article online  
\*Corresponding author. Email: pkubes@ucalgary.ca  
Cite this article as J. Zindel et al., *Science* 371, eabe0595 (2021). DOI: 10.1126/science.abe0595

**READ THE FULL ARTICLE AT**  
<https://doi.org/10.1126/science.abe0595>

## RESEARCH ARTICLES

## CLIMATE VARIABILITY

# Multidecadal climate oscillations during the past millennium driven by volcanic forcing

Michael E. Mann<sup>1\*</sup>, Byron A. Steinman<sup>2</sup>, Daniel J. Brouillette<sup>1</sup>, Sonya K. Miller<sup>1</sup>

Past research argues for an internal multidecadal (40- to 60-year) oscillation distinct from climate noise. Recent studies have claimed that this so-termed Atlantic Multidecadal Oscillation is instead a manifestation of competing time-varying effects of anthropogenic greenhouse gases and sulfate aerosols. That conclusion is bolstered by the absence of robust multidecadal climate oscillations in control simulations of current-generation models. Paleoclimate data, however, do demonstrate multidecadal oscillatory behavior during the preindustrial era. By comparing control and forced “Last Millennium” simulations, we show that these apparent multidecadal oscillations are an artifact of pulses of volcanic activity during the preindustrial era that project markedly onto the multidecadal (50- to 70-year) frequency band. We conclude that there is no compelling evidence for internal multidecadal oscillations in the climate system.

**A**n analysis of state-of-the-art climate model simulations spanning the past millennium provides no evidence for an internally generated, multidecadal oscillatory Atlantic Multidecadal Oscillation (AMO) signal in the climate system and instead suggests the presence of a 50- to 70-year “AMO-like” signal driven by episodes of high-amplitude explosive volcanism with multidecadal pacing.

Modes of internal climate system variability, such as the El Niño–Southern Oscillation (ENSO), lead to interannual oscillatory behavior, i.e., coherent large-scale variability with a well-defined time scale, distinct from simple “red noise.” Researchers, however, continue to debate the existence of longer-term oscillatory internal modes of climate variability. Past research analyzing observations, paleoclimate proxies, and model simulations has argued for distinct interdecadal (1–11) and multidecadal (8, 9, 12–15) climate oscillations, but more recent work (16–27) has challenged these findings.

Evidence for a 50- to 70-year North Atlantic-centered oscillation originated in observational studies by Folland and colleagues during the 1980s (12, 13). In the 1990s, Mann and Park (8, 9) and Turrett *et al.* (14) applied a multivariate signal detection approach (the multitaper method singular value decomposition or “MTM-SVD” method) to global surface temperature data, to separate distinct long-term surface temperature signals, whereas Schlesinger and Ramankutty (15) provided evidence for a residual multidecadal signal

using a model to estimate and remove the forced trend from observations. These analyses collectively argued for a multidecadal (50- to 70-year) time-scale signal centered in the North Atlantic, but with hemispheric-scale impacts, which was subsequently termed the Atlantic Multidecadal Oscillation (AMO) (28).

The confident identification of a signal has been hampered by the short instrumental climate record and confounding influences of forced long-term climate trends. Though numerous studies have attributed the AMO to internal oscillatory behavior tied to the Atlantic Meridional Overturning Circulation (AMOC) (29–35), others have dismissed the AMO as the response of North Atlantic surface temperatures to stochastic atmospheric forcing (17–19) or external radiative forcing (20–24). Yet others maintain that an internal AMO signal may exist but has been misidentified in studies that do not properly distinguish forced from internal variability (16, 25–27).

Spectral analyses of paleoclimate proxy data (36, 37) do show evidence for multidecadal AMO-like oscillations in past centuries. Using the MTM-SVD approach, Mann *et al.* (36) found evidence for a statistically significant 50- to 70-year spectral peak in a set of 27 proxy records dating back to 1400 CE. Other recent studies, however, have analyzed proxy-based reconstructions of climate indices (38–42), yielding conflicting results.

Cook *et al.* (39) used tree rings from regions bordering the North Atlantic to reconstruct a winter North Atlantic Oscillation (NAO) index back to 1400 CE and argued that multidecadal oscillations were limited to the modern period, with no evidence prior to 1900 CE. By contrast, D’Arrigo *et al.* (38) produced a warm-season Arctic Oscillation (AO) index with North American and Eurasian tree rings and found a multi-

decadal spectral peak prior to the 20th century. Gray *et al.* (42) and Wang *et al.* (43) reconstructed a North Atlantic sea-surface temperature (SST)-based AMO index from tree rings back to 1567 CE and 800 CE, respectively. Each found evidence for persistent 50- to 70-year oscillations prior to the 20th century.

Although these AMO reconstructions appear similar during the modern period, they diverge in past centuries (44). An important caveat applies to such reconstructions: They require calibration of proxy data against a single index during the modern period, but the governing mechanisms may be different during the modern period and the past. Such problems can be partly avoided using climate-field reconstruction methods that employ multiple independent patterns of variability (45).

This caveat holds in the present case. Anthropogenic greenhouse gas and sulfate aerosols affecting North Atlantic temperatures compete during the 20th century (16, 25–27) but are weak or absent before this time. The impact of this nonstationarity on calibration procedures may explain the observed divergence in these various AMO-related indices.

Mann *et al.* (45) used a global multiproxy dataset to reconstruct surface temperatures over the past millennium. They derived an AMO index averaging over the North Atlantic; however, use of a decreasing number of patterns back in time limits insights into multidecadal variability at regional scales. Fischer and Mieding (41) inferred long-term North Atlantic climate variability from Greenland ice cores, but it is difficult to extrapolate North Atlantic-wide climate trends from a single region like Greenland. Singh *et al.* (40) used a data-assimilation approach, combining model physics and paleoclimate data by assimilating proxies into two Fifth Coupled Model Intercomparison Project (CMIP5) “Last Millennium” model simulations. Their AMO indices, estimated from reconstructed North Atlantic surface-temperature fields, show no multidecadal spectral peaks. A caveat with data-assimilation approaches is that model states (e.g., atmospheric teleconnection patterns) are typically biased relative to the real world, leading to loss of variance and fidelity in the resulting reconstruction (46, 47).

In summary, there is no well-defined, agreed-upon preinstrumental AMO time series. Consequently, there is no consensus on the relative role of internal variability and external forcing in multidecadal AMO-like variability in past centuries (46, 47). We can nonetheless obtain key insights within the synthetic world of model simulations, where such complications do not apply.

Control coupled ocean-atmosphere model simulations provide an important laboratory for understanding the origins of multidecadal variability because forcing remains constant and oscillatory signals can be attributed to

<sup>1</sup>Department of Meteorology and Atmospheric Science, The Pennsylvania State University, 514 Walker Building, University Park, PA 16802-5013, USA. <sup>2</sup>Department of Earth and Environmental Sciences and Large Lakes Observatory, University of Minnesota Duluth, 2205 East 5th Street, Duluth, MN 55812, USA.

\*Corresponding author. Email: mann@psu.edu



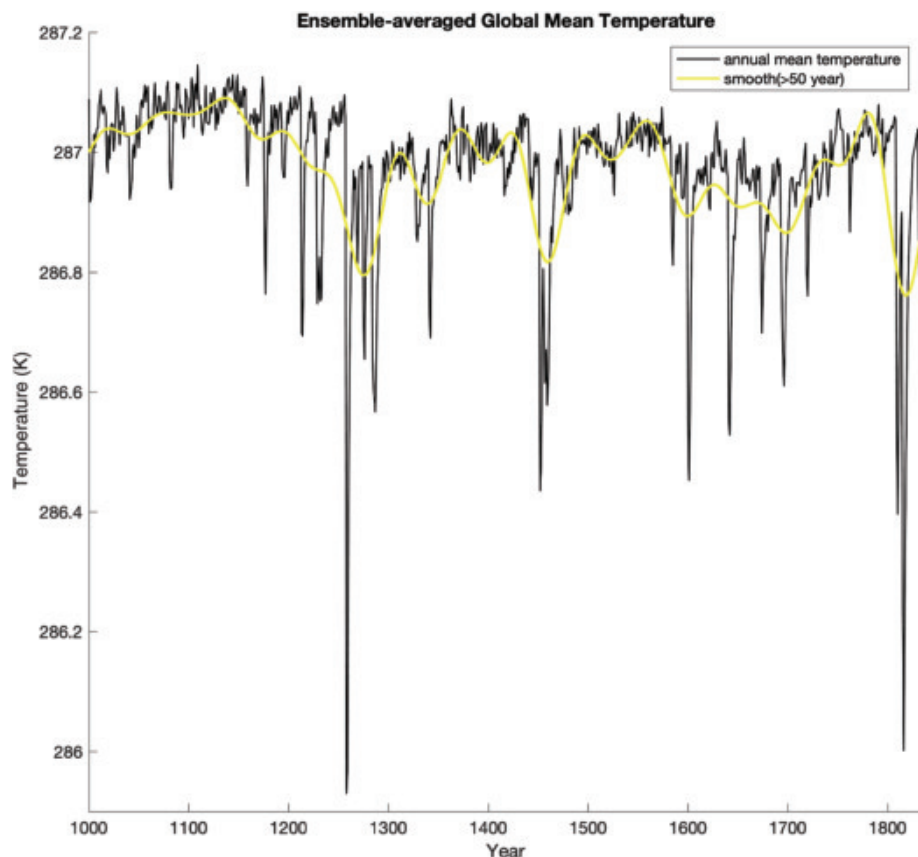


**Fig. 1. Ensemble-averaged global mean temperature for CMIP5 Last Millennium experiments (representing the average over  $M = 16$  simulations during the 1000–1835 CE overlap of all simulations).**

Shown are both the raw annual averages (black) and a smoothed [50-year lowpass using the method of Mann (60)] version (yellow) of the series, emphasizing the multidecadal and longer-term variability.

internal variability alone. If such signals exist, they should be associated with coherent large-scale patterns of variability with a well-defined time scale that is statistically significant relative to a simple red noise null hypothesis. However, because a prospective signal may largely redistribute heat over Earth's surface (rather than change the global surface heat budget), the signal projection onto hemispheric or global mean temperature may be weak or nonexistent. Any signal detection approach should thus be applied to the full surface temperature field rather than regionally or globally averaged temperature.

The MTM-SVD method of Mann and Park (8–10), which identifies narrowband spatiotemporal oscillatory signals in multivariate datasets, is well suited to this task. Using the MTM-SVD approach, Delworth and Mann (48) provided evidence for a distinct narrowband (40- to 60-year) multidecadal oscillation in a long (1000-year) control simulation of the Geophysical Fluid Dynamics Laboratory (GFDL) coupled model, whereas Knight *et al.* (49) found an AMO signal in a 1400-year control simulation of the Hadley Centre (HadCM3) coupled model. In both cases, the signal displayed peak variations of  $\sim 0.5^\circ\text{C}$  in the high-latitude North

Atlantic but more modest amplitude  $\sim 0.1^\circ\text{C}$  variations in tropical Atlantic and hemispheric mean temperature.

Mann *et al.* (50) recently used MTM-SVD to analyze global temperature fields from the suite of CMIP5 control simulations for low-frequency oscillatory climate signals. They found no consistent evidence across the ensemble for narrowband signals in the decadal and interdecadal range (contrasting with clear evidence for interannual ENSO signals). Using the CMIP5 historical simulations, they furthermore demonstrated that an AMO-like signal in the modern era is an artifact of competing, time-varying influences from steadily increasing greenhouse gases and the post-1970 ramp-down in sulfate aerosols.

Collectively, these observations are enigmatic. They fail to explain why multidecadal AMO-like oscillations are observed in paleoclimate proxy data prior to the industrial era. One possible reconciliation is that AMO-like oscillations in past centuries might too be forced but by natural changes in solar irradiance and explosive volcanic activity.

Here, we analyze the CMIP5 multimodel “Last Millennium” simulation ensemble, in which

models were driven by estimated natural forcing (51), for evidence of narrowband AMO-like oscillatory signals using the MTM-SVD method. Using the ensemble mean, wherein internal variability components from individual ensemble members cancel (26, 27, 52), we also estimate the forced-only temperature response in the model ensemble. We compare against a previous MTM-SVD analysis of CMIP5 control simulations by Mann *et al.* (50), where there is no forced variability. Collectively these analyses allow us to assess evidence—in the context of current-generation models—for persistent multidecadal AMO-like oscillations over the past millennium and to determine whether they are externally forced or internally generated.

## Results

The CMIP5 Last Millennium multimodel experiments provide a pseudo-ensemble of  $N = 16$  simulations (see supplementary materials) driven with estimated natural forcing (volcanic and solar, with minor additional contributions from astronomical, greenhouse gases, and land-use change) over the preindustrial period (the interval 1000 to 1835 CE is common to all simulations). We estimate the forced-only component of temperature variation by averaging over the ensemble, based on the principle that independent noise realizations cancel in an ensemble mean (16, 25–27). The multidecadal variation in ensemble-averaged global mean temperature (Fig. 1) (highlighted;  $\sim 0.3^\circ\text{C}$  typical peak-to-peak amplitude), notably, is dominated by the cooling response to major volcanic forcing episodes.

We used MTM-SVD to assess evidence for narrowband multidecadal oscillatory signals in the individual CMIP5 surface temperature fields. MTM-SVD performs a spatiotemporal decomposition of data locally in the frequency domain, determining whether any large-scale pattern within a narrow frequency band describes a larger fraction of variance than would be expected for colored noise (including the standard “red noise” null hypothesis invoked in climate studies). The fractional variance, as a function of frequency [the “local fractional variance” (LFV) spectrum], yields a detection variable, with significance levels estimated by Monte Carlo simulations (see materials and methods).

Comparing the LFV spectra for the CMIP5 control ensemble from Mann *et al.* (50) (Fig. 2A) with those for the Last Millennium ensemble (Fig. 2B) reveals pronounced differences. In the former case, as noted earlier, there is no ensemble-wide evidence for a multidecadal spectral peak, with no structure evident in the ensemble mean LFV spectrum over the decadal and multidecadal frequency range. In the latter case, however, we see substantial structure, with peaks common to numerous members of

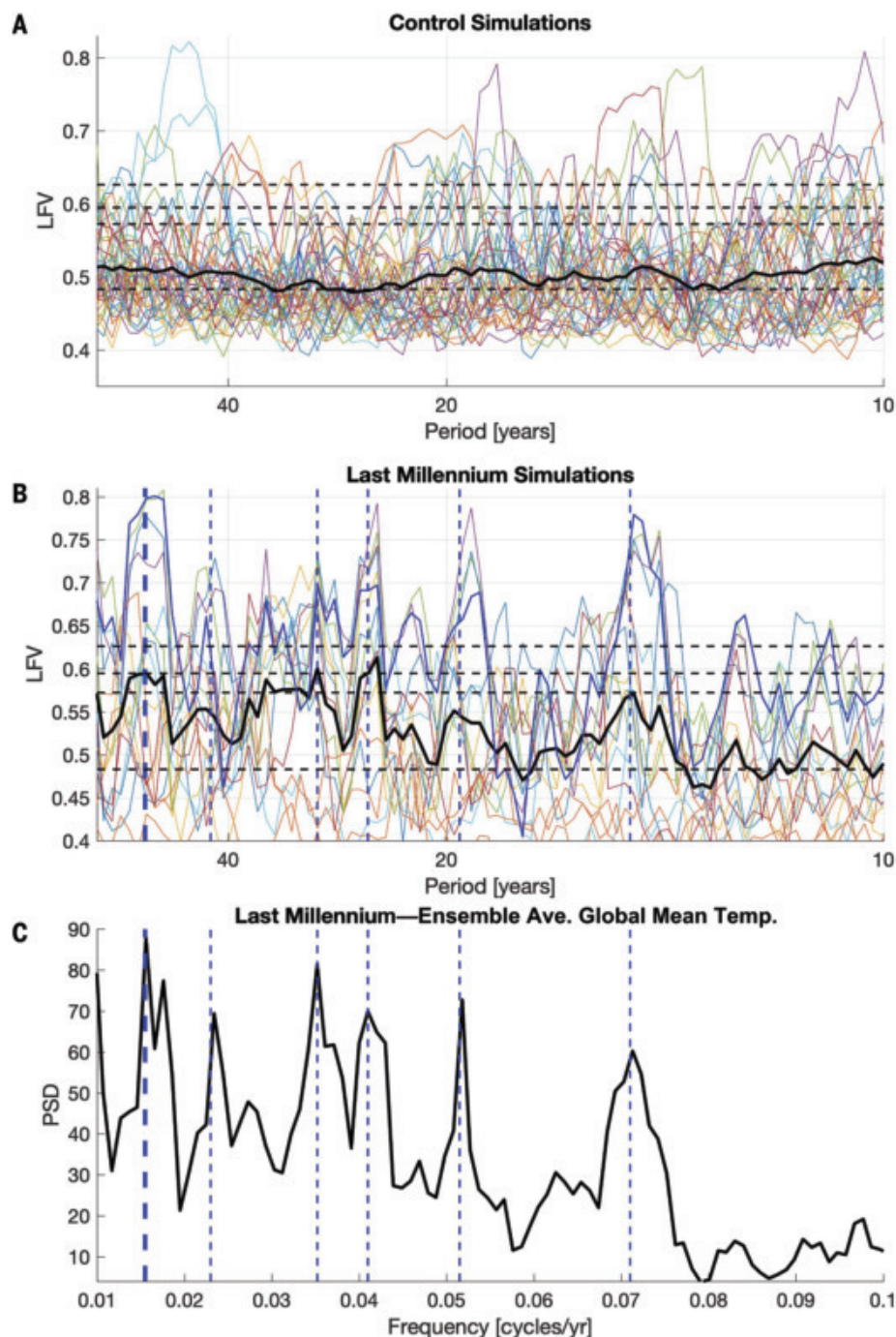


**Fig. 2. Spectra for CMIP5 surface temperature data.** (A) MTM-SVD local fraction variance (LFV) spectrum for CMIP5 control simulations. Individual colored curves depict results for all  $N = 44$  simulations, whereas the ensemble mean is shown by the thick black curve. Lower ( $f = 0.01$  cycle per year) and upper ( $f = 0.1$  cycle per year) bounds on frequencies shown correspond to the edge of the secular band and decadal band, respectively. Horizontal dashed lines correspond to median ( $p = 0.5$ ) and  $p = 0.1$ ,  $0.05$ , and  $0.01$  significance levels relative to colored noise null hypothesis. (B) Same as (A) but for the  $N = 16$  CMIP5 Last Millennium simulations (the more prominent blue curve denotes the GISS-E2-R simulation examined in Fig. 3). (C) MTM power spectral density of the ensemble-averaged global mean temperature series shown in Fig. 1 over the same frequency range as above, as calculated using the multitaper spectral analysis routine described in Mann and Lees (52). The vertical blue dashed lines show the peaks that are common between (B) and (C) (thick dashed line denotes the multidecadal 50- to 70-year period signal of interest).

the ensemble and statistically significant at the  $p < 0.05$  level in the ensemble mean in the ~20- to 30-year interdecadal range (centered at frequency  $f = 0.04$  cycle per year) and ~50- to 70-year multidecadal range (centered at  $f = 0.016$  cycle per year). The latter breaches the  $p = 0.1$  significance level for 12 of 16 ensemble members (11 at the  $p = 0.01$  level) and for 6 of 8 of the distinct models (see supplementary materials for further details).

The power spectrum (Fig. 2C) of the CMIP5 ensemble-averaged global temperature series of Fig. 1 exhibits spectral peaks at the same frequencies (e.g.,  $f \sim 0.04$  and  $f \sim 0.016$ ) as the LFV spectra for the full temperature fields (Fig. 2B). Because the structure in the ensemble-averaged global mean series reflects forced variability alone, the origin of the spectral peaks in the LFV spectra can be presumed to be the same—i.e., driven by long-term changes in radiative forcing, primarily the volcanic forcing, which happens to contain a pronounced multidecadal periodicity (53). Although solar-only and volcanic-only simulations are not part of the CMIP5 Last Millennium experiment protocol, simulations with an energy-balance model (EBM) driven by the CMIP5 forcing series (supplementary materials) show that the multidecadal spectral peak arises from volcanic forcing alone. Indeed, of the four simulations lacking a multidecadal LFV peak, volcanic forcing turns out to be absent in two models.

To examine the detailed characteristics of the signal, we focus on the simulation (one of the nine GISS-E2-R simulations) that displays the largest LFV spectral peak, but similar results apply to other simulations (see supplementary materials). The signal is characterized by its spatial pattern of explained variance (Fig. 3A), its time-domain projection using a reference gridbox in the tropical Atlantic (Fig. 3B), and the characteristic spatio-temporal evolution over a typical (~60-year) “oscillation” (Fig. 4).

The spatial pattern of variance (Fig. 3A) shows the highest amplitude in the tropics, consistent with the established pattern of response to tropical volcanic forcing. There is also an indication of coupling to extratropical atmospheric and oceanic dynamics. Especially notable is the prominent signature in the North Atlantic, where an enhanced signal is seen in the vicinity of the Gulf Stream and North Atlantic drift, and well into the extratropical and subpolar North Atlantic.

In examining the temporal projection of the signal (Fig. 3B), the apparent multidecadal oscillation, as originally hinted at in Fig. 1, is seen to be associated with a response to well-spaced pulses of tropical volcanic activity, with major troughs almost exclusively corresponding to prominent volcanic forcing episodes.



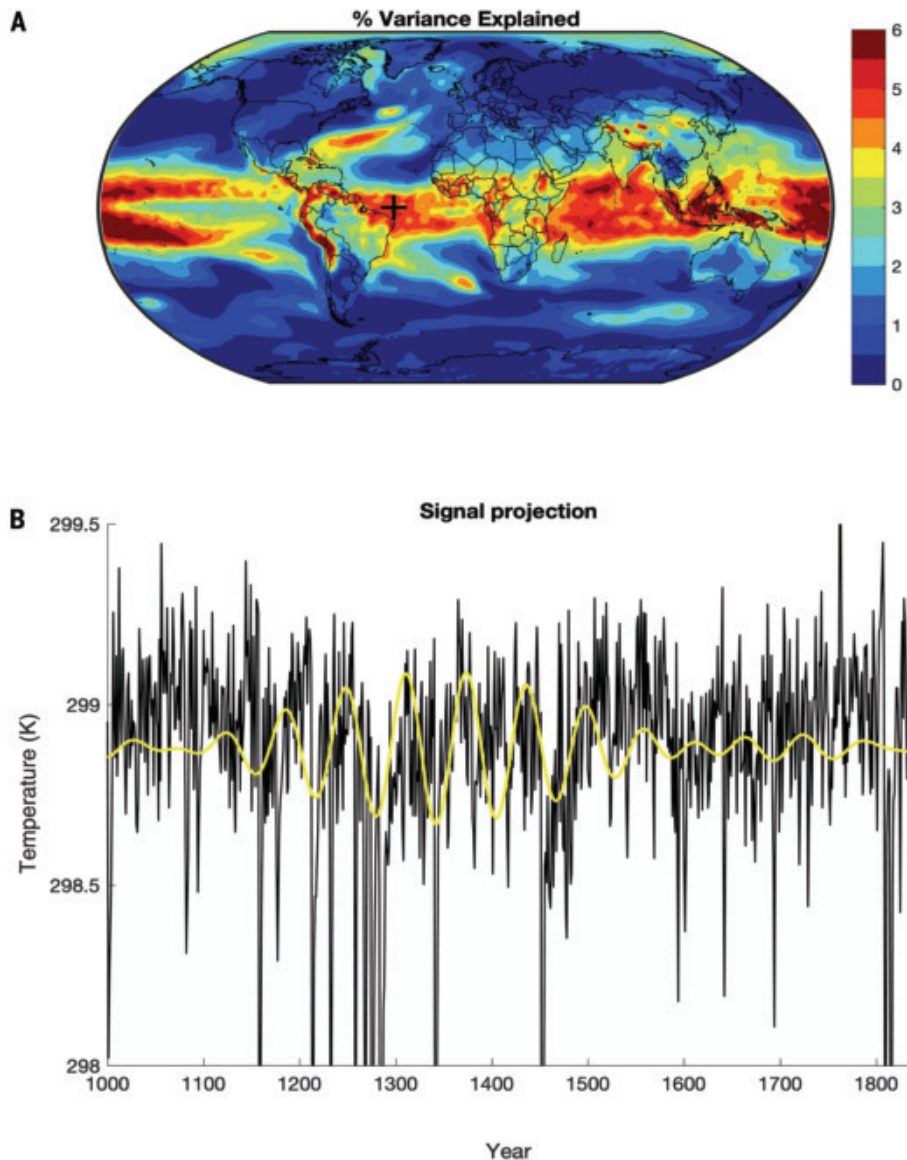


**Fig. 3. Spatial and temporal characteristics of multidecadal “signal” (centered at  $f = 0.016$  cycle per year, ~63-year period) for CMIP5 GISS E2-R Last Millennium simulation. (A) Spatial pattern of percentage resolved variance associated with signal and (B) reconstructed time-domain signal for representative equatorial eastern Atlantic grid box (grid box centered on longitude 35°W and latitude 0°; location denoted by the large black “+” in (A)).**

The connection with volcanic forcing is also observed in the spatiotemporal evolution of the signal (Fig. 4). We adopt the convention that the  $t = 0$  (zero phase) pattern corresponds to the peak tropical (and global mean) cooling, i.e., the main expected direct response to volcanic forcing. The pattern also shows evidence of extratropical linkages, including a dynamical AO or NAO-like response in the Northern Hemisphere (54) and a warming off Antarctica, consistent with a dynamical coupling with the Southern Annular Mode (55–57).

The signal evolution over the subsequent quarter cycle (from  $t = 0$  to  $t = 16$ -year lag, i.e.,

90° phase) suggests a possible additional role for delayed ocean-dynamical responses. Of particular interest is the horseshoe pattern of warming and cooling that develops in extratropical North Atlantic SSTs, reminiscent of the pattern of AMO-like internal variability noted in some simulations (48, 49).

### Discussion

Our analysis reveals a robust multidecadal, narrowband (50- to 70-year) oscillatory “AMO-like” signal in simulations of the past millennium; the oscillation is driven by episodes of high-amplitude explosive volcanism that happen, in

past centuries, to display a multidecadal pacing. We find no evidence for an internally generated 50- to 70-year multidecadal oscillatory signal despite continued claims that proxy data reveal such a signal (58).

We reconcile some apparent contradictions in past work. Our analysis, for example, supports previous studies arguing for a multidecadal (50- to 70-year) spectral peak in AMO-related proxy records and index reconstructions (36–38, 42, 43) and supports past studies that attribute this signal at least partly to natural radiative forcing (43, 44). Where our findings differ from these latter studies, however, is in the degree, and nature, of the radiative forcing.

Our analysis indicates that apparent AMO-like oscillatory variability during the past millennium is driven exclusively by volcanic radiative forcing because (i) spectral peaks are evident in the CMIP5 forced Last Millennium simulations but not in the control simulations; (ii) there is a common 50- to 70-year spectral peak in the LFV spectra of the individual ensemble members and the power spectrum of the ensemble average global average temperature series and EBM simulations (which reflect radiatively forced changes alone); and (iii) the associated signal exhibits a spatiotemporal pattern consistent with the response to tropical volcanic forcing, with peak tropical cooling synchronized with major volcanic-forcing episodes.

Other past studies have argued for a weaker and more limited role for radiative forcing (43, 44). Knudsen *et al.* (44) assert that radiative forcing plays a dominant role only after 1800 CE and an “ambiguous” role before (1400 to 1800 CE). Wang *et al.* (43) claim a more consistent but still minor role, attributing only 30% of the AMO variance to the combined impact of solar and volcanic forcing and arguing for a multidecadal internal oscillation after the estimated forced component is removed. Both these studies, however, use a lagged correlation and regression analysis in an attempt to estimate and remove the forced signal, interpreting the residual series as an internal AMO oscillation. Attempts to remove estimates of forced variability from a time series containing both forced and unforced components, however, require a direct estimate of the forced component of response rather than simply the time series of the forcings alone, because a simple regression approach using raw forcing series cannot account for the temporal structure in the response to forcing (e.g., the decadal-time scale exponential recovery following impulsive volcanic forcing). That can be obtained using an EBM driven by estimated radiative forcings (16) or by averaging across an ensemble of forced coupled model simulations (16, 25–27). We infer that these previous studies did not

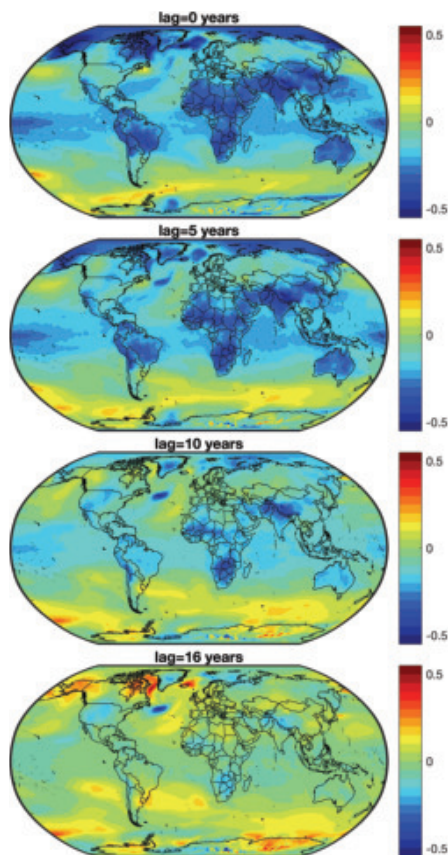


**Fig. 4. Spatiotemporal evolution of multidecadal “signal” (centered at  $f = 0.016$  cycle per year, ~63-year period) for CMIP5 GISS E2-R Last Millennium simulation.** Shown is the progression of the signal during the first quarter cycle of evolution, depicting phase = 0 (lag = 0 years), 30° (lag = 5 years), 60° (lag = 10 years), and 90° (lag = 16 years), where the zero reference phase corresponds to peak tropical cooling. Color scale indicates temperature anomaly (°C).

fully account for, or remove, the forced signal before estimating the internal variability component.

The discrepancy with the Singh *et al.* (40) data-assimilation experiments is more perplexing. Although they find no evidence of narrow-band multidecadal oscillatory behavior, our analysis of the same [Max Planck Institute (MPI)] simulation that they use in one of their two experiments shows a highly significant ( $p < 0.01$ ) spectral peak (Fig. 2B and supplementary materials). There are at least two potential explanations for the discrepancy. First, as remarked earlier, their null result could simply be a consequence of a bias between the atmospheric states sampled by the real-world proxy data and the atmospheric states generated by the two models used, which would limit the fidelity of the resulting reconstruction in both the temporal and frequency domain. With data-assimilation experiments, it

is difficult to determine if the source of a discrepancy can be attributed to the models used, the proxy data assimilated, or some combination of the two.

Second, Singh *et al.* (40) perform a spectral analysis of an AMO index defined as the average sea-surface temperature over the entire North Atlantic. Our multivariate (MTM-SVD) approach, by contrast, is based on an analysis of the entire field and the estimated spatial pattern of the signal. Substantial variation is displayed (Fig. 4) not just in the amplitude but also in the sign of associated temperature anomalies across the North Atlantic, implying some signal cancellation when averaging over the full North Atlantic domain. An index based on a simple average over the North Atlantic, consequently, tends to average away the signal and lower the effective signal-to-noise ratio, potentially rendering a true signal undetectable.

An additional feature of interest in the signal pattern (Fig. 4) is the apparent role of ocean dynamics in the delayed North Atlantic response to forcing, as noted earlier, which hints at features recognized in the limited modeling studies that have identified an internal AMO-oscillatory signal (48, 49). For example, though focusing on solar rather than volcanic forcing, Waple *et al.* (59) speculate about the possibility that natural radiative forcing might resonate with internal modes of Atlantic multidecadal ocean-atmosphere variability.

The collective available evidence from instrumental and proxy observations and control and forced historical and Last Millennium climate model simulations points toward the existence of externally forced multidecadal oscillations that are a consequence of competing anthropogenic forcings during the historical era and the coincidental multidecadal pacing of explosive tropical volcanic activity in past centuries. There is no compelling evidence for a purely internal multidecadal AMO-like cycle.

A comprehensive analysis of the expanded paleoclimate proxy data now available should allow for further testing and refinement of these hypotheses, as should a detailed analysis of next-generation (CMIP6) control and forced last millennium multimodel ensembles, which may better capture ocean-atmosphere dynamics relevant to multidecadal climate variability.

## REFERENCES AND NOTES

- S. Power, T. Casey, C. Folland, A. Colman, V. Mehta, *Clim. Dyn.* **15**, 319–324 (1999).
- B. Kirtman *et al.*, in *Climate Change 2013: The Physical Science Basis. Contribution of Working Group I to the Fifth Assessment Report of the Intergovernmental Panel on Climate Change*, T. F. Stocker *et al.*, Eds. (Cambridge Univ. Press, 2013).
- G. A. Meehl, H. Teng, J. M. Arblaster, *Nat. Clim. Change* **4**, 898–902 (2014).
- G. A. Meehl *et al.*, *Bull. Am. Meteorol. Soc.* **95**, 243–267 (2014).
- N. J. Mantua, S. R. Hare, Y. Zhang, J. M. Wallace, R. C. Francis, *Bull. Am. Meteorol. Soc.* **78**, 1069–1079 (1997).
- B. Henley, *Global Planet. Change* **155**, 42–55 (2017).
- M. Newman *et al.*, *J. Clim.* **29**, 4399–4427 (2016).
- M. E. Mann, J. Park, *J. Geophys. Res.* **99**, 25819 (1994).
- M. E. Mann, J. Park, *J. Clim.* **9**, 2137–2162 (1996).
- M. E. Mann, J. Park, *Adv. Geophys.* **41**, 1–131 (1999).
- M. Latif, T. P. Barnett, *Science* **266**, 634–637 (1994).
- C. K. Folland, D. E. Parker, F. E. Kates, *Nature* **310**, 670–673 (1984).
- C. K. Folland, T. N. Palmer, D. E. Parker, *Nature* **320**, 602–607 (1986).
- Y. M. Tourre, B. Rajagopalan, Y. Kushnir, *J. Clim.* **12**, 2285–2299 (1999).
- M. E. Schlesinger, N. Ramankutty, *Nature* **367**, 723–726 (1994).
- M. E. Mann, B. A. Steinman, S. K. Miller, *Geophys. Res. Lett.* **41**, 3211–3219 (2014).
- A. Clement *et al.*, *Science* **350**, 320–324 (2015).
- A. Clement *et al.*, *Science* **352**, 1527–1527 (2016).
- M. A. Cane, A. C. Clement, L. N. Murphy, K. Bellomo, *J. Clim.* **30**, 7529–7553 (2017).
- B. Booth, N. J. Dunstone, P. R. Halloran, T. Andrews, N. Bellouin, *Nature* **484**, 228–232 (2012).
- A. Bellucci, A. Mariotti, S. Gualdi, *J. Clim.* **30**, 7317–7337 (2017).
- L. N. Murphy, K. Bellomo, M. Cane, A. Clement, *Geophys. Res. Lett.* **44**, 2472–2480 (2017).
- K. Bellomo, L. N. Murphy, M. A. Cane, A. C. Clement, L. M. Polvani, *Clim. Dyn.* **50**, 3687–3698 (2018).
- K. Haustein *et al.*, *J. Clim.* **32**, 4893–4917 (2019).
- M. E. Mann, K. A. Emanuel, *Eos* **87**, 233–241 (2006).
- L. M. Frankcombe, M. H. England, M. E. Mann, B. A. Steinman, *J. Clim.* **28**, 8184–8202 (2015).
- L. M. Frankcombe, M. H. England, J. Kajtar, M. E. Mann, B. A. Steinman, *J. Clim.* **31**, 5681–5693 (2018).
- R. A. Kerr, *Science* **288**, 1984–1985 (2000).
- K. E. Trenberth, D. J. Shea, *Geophys. Res. Lett.* **33**, L12704 (2006).
- M. Ting, Y. Kushnir, R. Seager, C. Li, *J. Clim.* **22**, 1469–1481 (2009).
- J. R. Knight, *J. Clim.* **22**, 1610–1625 (2009).
- S. Wu, Z. Liu, R. Zhang, T. L. Delworth, *J. Oceanogr.* **67**, 27–35 (2011).
- T. DelSole, M. K. Tippett, J. Shukla, *J. Clim.* **24**, 909–926 (2011).
- D. Zanchettin, O. Bothe, W. Müller, J. Bader, J. H. Jungclauss, *Clim. Dyn.* **42**, 381–399 (2014).
- R. Zhang, *Geophys. Res. Lett.* **44**, 7865–7875 (2017).
- M. E. Mann, J. Park, R. S. Bradley, *Nature* **378**, 266–270 (1995).
- T. F. Stocker, L. A. Mysak, *Clim. Change* **20**, 227–250 (1992).
- R. D. D’Arrigo, E. R. Cook, M. E. Mann, G. C. Jacoby, *Geophys. Res. Lett.* **30**, 1549 (2003).
- E. R. Cook, R. D. D’Arrigo, M. E. Mann, *J. Clim.* **15**, 1754–1765 (2002).
- H. K. A. Singh, G. J. Hakim, R. Tardif, J. Emile-Geay, D. C. Noone, *Clim. Past* **14**, 157–174 (2018).
- H. Fischer, B. A. Mieling, *Clim. Dyn.* **25**, 65–74 (2005).
- S. T. Gray, L. J. Graumlich, J. L. Betancourt, G. T. Pederson, *Geophys. Res. Lett.* **31**, L2205 (2004).
- J. Wang *et al.*, *Nat. Geosci.* **10**, 512–517 (2017).
- M. F. Knudsen, B. H. Jacobsen, M.-S. Seidenkrantz, J. Olsen, *Nat. Commun.* **5**, 3323 (2014).
- M. E. Mann *et al.*, *Science* **326**, 1256–1260 (2009).
- H. G. Goussé *et al.*, *J. Geophys. Res.* **115**, D09108 (2010).
- H. Goussé *et al.*, *Clim. Dyn.* **39**, 2847–2866 (2012).
- T. L. Delworth, M. E. Mann, *Clim. Dyn.* **16**, 661–676 (2000).
- J. R. Knight, R. J. Allan, C. K. Folland, M. Vellinga, M. E. Mann, *Geophys. Res. Lett.* **32**, L20708 (2005).
- M. E. Mann, B. A. Steinman, S. K. Miller, *Nat. Commun.* **11**, 49 (2020).
- Intergovernmental Panel on Climate Change, in *Climate Change 2013: The Physical Science Basis*, T. F. Stocker *et al.*, Eds. (Cambridge Univ. Press, 2013).
- M. E. Mann, J. Lees, *Clim. Change* **33**, 409–445 (1996).
- C. M. Ammann, P. Naveau, *Geophys. Res. Lett.* **30**, 1210 (2003).
- B. A. Steinman, M. E. Mann, S. K. Miller, *Science* **347**, 988–991 (2015).
- D. T. Shindell, G. A. Schmidt, M. E. Mann, G. Faluvegi, *J. Geophys. Res.* **109**, D05104 (2004).
- Specifically, as in (55), we observe the highest-amplitude cooling responses over the tropical and subtropical continents. In addition, however, there is warming over mid-latitude regions of North America and Eurasia and cooling in polar and subpolar regions of North America and Siberia. Using model simulations with GISS ModelE, the authors show that these latter features are dynamically induced, associated with a positive AO-NAO-like cold-season atmospheric circulation response to tropical volcanic radiative forcing (see supplementary materials for a direct comparison).



57. J. Yang, C. Xiao, *Int. J. Climatol.* **38**, 1706–1717 (2018).  
 58. G. Müller-Plath, *Front. Earth Sci.* **8**, 559337 (2020).  
 59. A. Waple, M. E. Mann, R. S. Bradley, *Clim. Dyn.* **18**, 563–578 (2002).  
 60. M. E. Mann, *Geophys. Res. Lett.* **35**, L16708 (2004).

## ACKNOWLEDGMENTS

We acknowledge the World Climate Research Programme's Working Group on Coupled Modelling, which is responsible for CMIP, and we thank the climate modeling groups for producing

and making available their model output. **Funding:** M.E.M., B.A.S., D.J.B., and S.K.M. were supported by grants 1748097 and 1748115 from the NSF Paleoclimate Program. **Author contributions:** M.E.M. conceived, designed, and performed the research and wrote the paper. B.A.S., D.J.B., and S.K.M. performed some aspects of the research and co-wrote the paper. **Competing interests:** The authors declare no competing financial interests. **Data and materials availability:** All raw data and results from our analysis, as well as all Matlab code, are available at [http://www.meteo.psu.edu/~mann/supplements/Mann\\_MTMSVD\\_2020](http://www.meteo.psu.edu/~mann/supplements/Mann_MTMSVD_2020).

## SUPPLEMENTARY MATERIALS

[science.sciencemag.org/content/371/6533/1014/suppl/DC1](https://science.sciencemag.org/content/371/6533/1014/suppl/DC1)  
 Materials and Methods  
 Supplementary Text  
 Figs. S1 to S10  
 Tables S1 to S3  
 References (61–97)

1 May 2020; accepted 25 January 2021  
 10.1126/science.abc5810

## HEMATOLOGY

# Combined liver–cytokine humanization comes to the rescue of circulating human red blood cells

Yuanbin Song<sup>1,2,3\*</sup>, Liang Shan<sup>4,5\*†</sup>, Rana Gbyli<sup>1,2\*</sup>, Wei Liu<sup>1,2</sup>, Till Strowig<sup>4,6</sup>, Amisha Patel<sup>1,2</sup>, Xiaoying Fu<sup>1,2,7</sup>, Xiaman Wang<sup>1,2,8</sup>, Mina L. Xu<sup>9</sup>, Yimeng Gao<sup>1,2</sup>, Ashley Qin<sup>1,2</sup>, Emanuela M. Bruscia<sup>10</sup>, Toma Tebaldi<sup>1,2,11</sup>, Giulia Bianconi<sup>1,2</sup>, Padmavathi Mamillapalli<sup>1,2</sup>, David Urbonas<sup>4</sup>, Elizabeth Eynon<sup>4</sup>, David G. Gonzalez<sup>12</sup>, Jie Chen<sup>4</sup>, Diane S. Krause<sup>2,9,13</sup>, Jonathan Alderman<sup>4</sup>, Stephanie Halene<sup>1,2,†</sup>, Richard A. Flavell<sup>4,14,†‡</sup>

In vivo models that recapitulate human erythropoiesis with persistence of circulating red blood cells (RBCs) have remained elusive. We report an immunodeficient murine model in which combined human liver and cytokine humanization confer enhanced human erythropoiesis and RBC survival in the circulation. We deleted the fumarylacetoacetate hydrolase (*Fah*) gene in MISTRG mice expressing several human cytokines in place of their murine counterparts. Liver humanization by intrasplenic injection of human hepatocytes (huHep) eliminated murine complement C3 and reduced murine Kupffer cell density. Engraftment of human sickle cell disease (SCD)–derived hematopoietic stem cells in huHepMISTRGFah<sup>−/−</sup> mice resulted in vaso-occlusion that replicated acute SCD pathology. Combined liver–cytokine–humanized mice will facilitate the study of diseases afflicting RBCs, including bone marrow failure, hemoglobinopathies, and malaria, and also preclinical testing of therapies.

**H**uman red blood cells (huRBCs), one of the most common cell types in the body, have been under intense genetic selection throughout human evolution, the deleterious consequences of which place a heavy burden on many human populations and health care systems (1). Species-specific differences in the erythropoietic program (2) demand in vivo models of human erythropoiesis (3), yet no humanized immunodeficient mouse models exist with persistent mature huRBCs in peripheral blood (PB), the effective readout of functional human erythropoiesis and RBC integrity (4–6). Comprehensive analysis of hematopoietic and RBC disorders, such as sickle cell disease (SCD), require mature RBCs in the circulation both for disease manifestations and to test therapies.

## Liver humanization rescues human RBCs in circulation

MISTRG mice carry knock-ins for the human cytokines granulocyte-monocyte and macrophage colony-stimulating factor (M-CSF), interleukin-3 (I), thrombopoietin (T), and for signal regulatory protein alpha (S), the receptor for the “don’t eat me” signal regulatory protein CD47, in the *Rag2*<sup>−/−</sup>*Il2rg*<sup>−/−</sup> (RG) background

(7, 8). Engraftment of MISTRG mice with fetal liver (FL) CD34<sup>+</sup> cells resulted in robust leukocyte (huCD45<sup>+</sup>) engraftment in PB (~30%) and bone marrow (BM) (~50%) 8 to 12 weeks after intrahepatic injection into newborn livers. Erythroid (huCD235a<sup>+</sup>) engraftment in BM was modest (~5%), and huRBCs were absent in PB (fig. S1, A to C), suggesting destruction of huRBCs in the circulation, as previously described (4–6). To determine the kinetics and sites of huRBC destruction, we injected fluorescently labeled human and murine (mu) RBCs into MISTRG mice (fig. S1D) and confirmed rapid preferential clearance of huRBCs from circulation (Fig. 1A and fig. S1E). Infused labeled huRBCs but not muRBCs accumulated in liver and spleen, reaching a peak at 60 min after infusion (Fig. 1B and fig. S1F), suggesting sequestration and destruction by murine phagocytes. Previous studies have shown that huRBCs in the murine host are coated with murine complement 3 (muC3), which likely targets huRBCs to murine macrophages and other phagocytes (9). The huRBCs but not muRBCs infused into MISTRG mice were rapidly coated with muC3 (Fig. 1C). huRBCs isolated from the liver contained with the murine macrophage marker F4/80<sup>+</sup> (Fig. 1D), suggest-

ing sequestration of huRBCs by murine liver phagocytes. We performed intravital imaging of the liver immediately after injection of fluorescently labeled human or murine RBCs together with dextran to define blood vessels (fig. S1G). We observed that huRBCs (movie S1), but not muRBCs (movie S2), became rapidly and persistently trapped within the liver vasculature. Thus, the mouse liver represents one of the major sites of huRBC sequestration and destruction.

The liver produces numerous proteins essential for the innate immune defense, including complement, and contains a large number of tissue macrophages (10, 11). We deleted the fumarylacetoacetate hydrolase (*Fah*) gene by using CRISPR-Cas9 in MISTRG to generate MISTRGFah<sup>−/−</sup> (MISTRGFah) mice and confirmed deletion of *Fah* by protein immunoblotting (fig. S2A). We successfully humanized the liver in MISTRGFah mice with adult huHep as previously described (12, 13) by intrasplenic injection of adult human hepatocytes and gradual withdrawal of 2-(2-nitro-4-trifluoromethylbenzoyl)-1,3-cyclohexanedione (NTBC) in the drinking water, resulting in the death of *Fah*<sup>−/−</sup> murine hepatocytes and regeneration with human hepatocytes. Murine

<sup>1</sup>Section of Hematology, Department of Internal Medicine, Yale Cancer Center, and Yale Center for RNA Science and Medicine, Yale University School of Medicine, New Haven, CT, USA. <sup>2</sup>Yale Stem Cell Center, Yale University School of Medicine, New Haven, CT, USA. <sup>3</sup>Department of Hematologic Oncology, Sun Yat-sen University Cancer Center, State Key Laboratory of Oncology in South China, Collaborative Innovation Center for Cancer Medicine, Guangzhou, China. <sup>4</sup>Department of Immunobiology, Yale University School of Medicine, New Haven, CT, USA. <sup>5</sup>Department of Medicine, Pathology and Immunology, Center for Human Immunology and Immunotherapy Programs, Washington University School of Medicine, St. Louis, MO, USA. <sup>6</sup>Helmholtz Centre for Infection Research, Braunschweig, Germany. <sup>7</sup>Department of Laboratory Medicine, Shenzhen Children's Hospital, Shenzhen, People's Republic of China. <sup>8</sup>Department of Hematology, the Second Affiliated Hospital of Xi'an Jiaotong University, Xi'an, People's Republic of China. <sup>9</sup>Department of Pathology, Yale University School of Medicine, New Haven, CT, USA. <sup>10</sup>Department of Pediatrics, Yale University School of Medicine, New Haven, CT, USA. <sup>11</sup>Department of Cellular, Computational and Integrative Biology (CIBIO), University of Trento, Trento, Italy. <sup>12</sup>Department of Genetics, Yale University School of Medicine, New Haven, CT, USA. <sup>13</sup>Department of Laboratory Medicine, Yale University School of Medicine, New Haven, CT, USA. <sup>14</sup>Howard Hughes Medical Institute, Yale University, New Haven, CT, USA.

\*These authors contributed equally to this work.

†Corresponding author. Email: [liang.shan@yale.edu](mailto:liang.shan@yale.edu) (L.S.); [stephanie.halene@yale.edu](mailto:stephanie.halene@yale.edu) (S.H.); [richard.flavell@yale.edu](mailto:richard.flavell@yale.edu) (R.A.F.)

‡These authors contributed equally to this work.

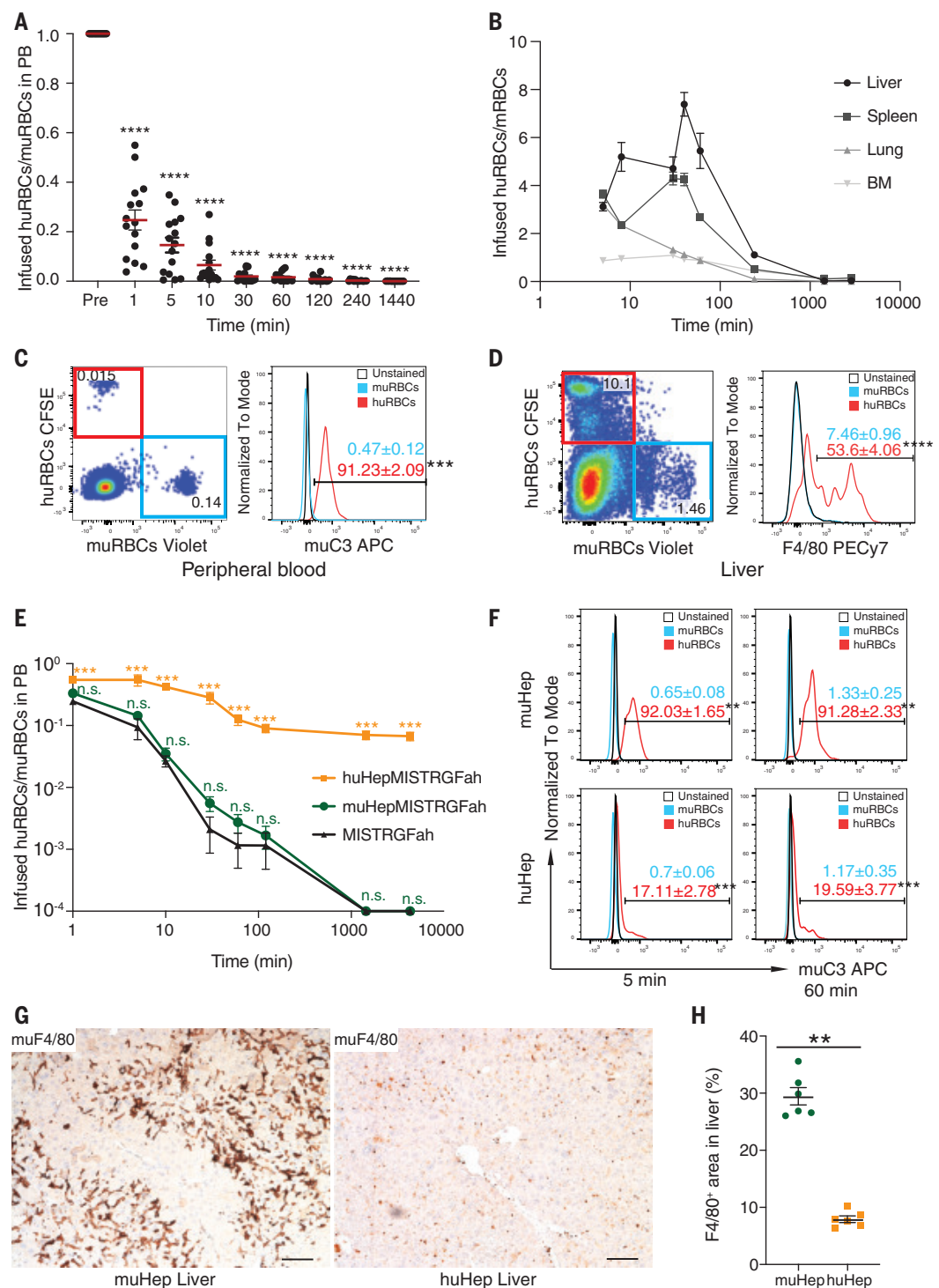
hepatocyte (muHep)-engrafted MISTRGFah mice (muHepMISTRGFah) served as controls. Human plasma albumin (huALB) concentrations reached a plateau around 8 weeks after huHep engraftment (fig. S2B). Human albumin concentrations were validated as surrogate measurements for human hepatocyte regeneration, with levels above 4 mg/ml indicating that 80 to 95% of hepatocytes were human as

determined by FAH histology (fig. S2D). To determine the effects of liver humanization on huRBC survival, we repeated infusion of fluorescently labeled RBCs and compared huHepMISTRGFah and muHepMISTRGFah with MISTRGFah mice (fig. S1D). Survival of huRBCs was significantly prolonged in the PB of huHepMISTRGFah mice compared with those in MISTRGFah and muHepMISTRGFah

mice, with persistence of huRBCs for >72 hours (Fig. 1E). Only a small percentage of huRBCs in PB of huHepMISTRGFah mice were coated with muC3, compared with the high muC3 positivity of huRBCs in muHepMISTRGFah mice (Fig. 1F). Infused huRBCs isolated from the livers of huHepMISTRGFah mice no longer costained with murine F4/80<sup>+</sup>, suggesting reduced targeting of huRBCs to murine

### Fig. 1. Liver humanization prolongs the survival of infused huRBCs in circulation through elimination of muC3 and reduction of murine macrophages.

Equal numbers of fluorescently labeled huRBCs (labeled with carboxyfluorescein diacetate succinimidyl ester) and muRBCs (violet) were premixed and injected retro-orbitally into mice. (A and B) Ratios of infused huRBCs to muRBCs in PB ( $n = 15$ ) (A) and in liver, spleen, lung, and BM (B) at designated time points ( $n = 8$ ). (C) muC3 staining of infused huRBCs (red) and muRBCs (blue) 5 min after infusion into MISTRG mice ( $n = 11$ ). APC, cells were stained with allophycocyanin. (D) Representative flow cytometry plots and histograms of murine F4/80 staining of infused huRBCs (red) and muRBCs (blue) collected from MISTRG livers at 60 min after infusion ( $n = 8$ ). (E) Comparison of huRBC survival in PB of MISTRGFah ( $n = 6$ ), muHepMISTRGFah ( $n = 8$ ), and huHepMISTRGFah ( $n = 8$ ) mice. (F) Representative flow plots and histograms of muC3 staining of infused huRBCs and muRBCs in PB at 5 min and 60 min after infusion. (G and H) Representative histologic images showing F4/80<sup>+</sup> murine macrophages (G) and quantification of F4/80<sup>+</sup> area (H) in the livers of muHepMISTRGFah ( $n = 6$ ) and huHepMISTRGFah ( $n = 6$ ) mice at 12 weeks after hepatocyte engraftment. Scale bars, 100  $\mu$ m; original magnification, 10 $\times$ . Histological images were quantified with ImageJ, and individual mice are represented by symbols. Data (means  $\pm$  SEM) are representative of three independent experiments with three different donors.  $P$  values were determined by Mann-Whitney  $U$  test: \*\* $P < 0.01$ , \*\*\* $P < 0.001$ , \*\*\*\* $P < 0.0001$ .





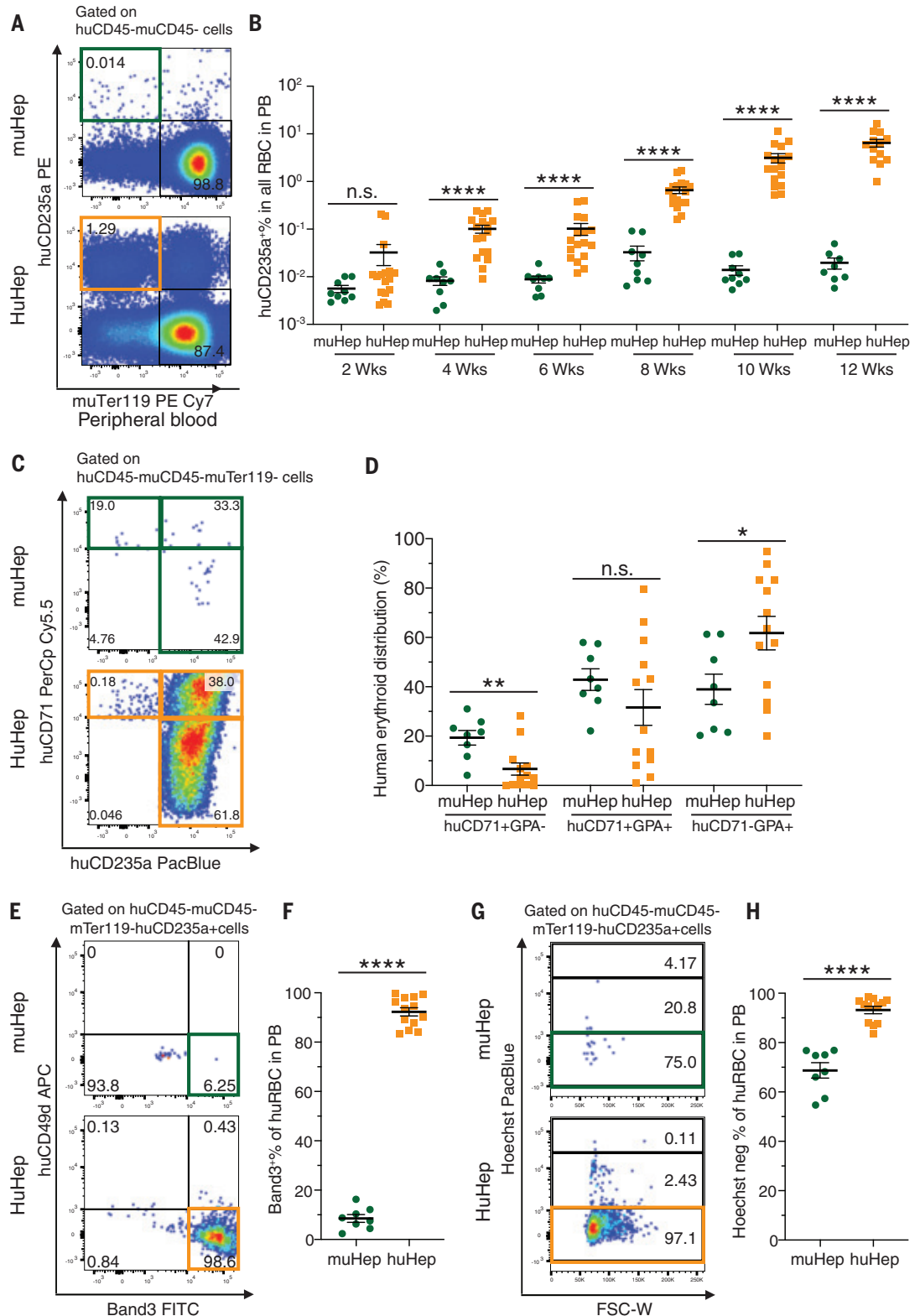
phagocytes in the liver (fig. S2, E and F). In addition, the overall numbers of F4/80<sup>+</sup> macrophages in huHepMISTRGFah livers were significantly decreased in comparison with those in muHepMISTRGFah livers (Fig. 1, G

and H). Thus, liver humanization prolongs the survival of infused huRBCs and decreases muC3 concentrations, murine phagocyte numbers in the liver, the coating of huRBCs with muC3, and their subsequent destruction.

### huRBCs circulate in engrafted huHepMISTRGFah mice

To determine whether liver humanization would spare huRBCs produced within the murine host, we measured huRBCs in circulation

**Fig. 2. Enucleated, mature huRBCs circulate in huHepMISTRGFah mice.** (A and B) Representative flow cytometry plots (A) and quantitation (B) of human (huCD235a<sup>+</sup>) and murine (muTer119<sup>+</sup>) erythroid cells in PB of muHepMISTRGFah (*n* = 8) versus huHepMISTRGFah (*n* = 13) mice. PE-Cy7, phycoerythrin-Cy7 fluorophore. (C to F) Representative flow cytometry analysis and quantitation of human erythropoietic differentiation on the basis of huCD71 and huCD235a expression (C and D) and huCD49d and Band3 expression (E and F) in PB of muHepMISTRGFah (*n* = 8) versus huHepMISTRGFah (*n* = 13) mice. PacBlue, Pacific blue label; PerCP Cy5.5, peridinin chlorophyll protein Cy5.5. (G and H) Representative flow cytometry plots (G) and quantitation (H) of enucleated human RBCs, determined by Hoechst staining of the PB of muHepMISTRGFah (*n* = 8) versus huHepMISTRGFah (*n* = 13) mice. FSC-W, forward scatter width. Individual mice are represented by symbols; data are presented as means ± SEM. *P* values were determined by Mann-Whitney *U* test: n.s., not significant; \**P* < 0.05; \*\**P* < 0.01; \*\*\*\**P* < 0.0001. Data are representative of three independent experiments with three different donors of hepatocytes and FL cells.



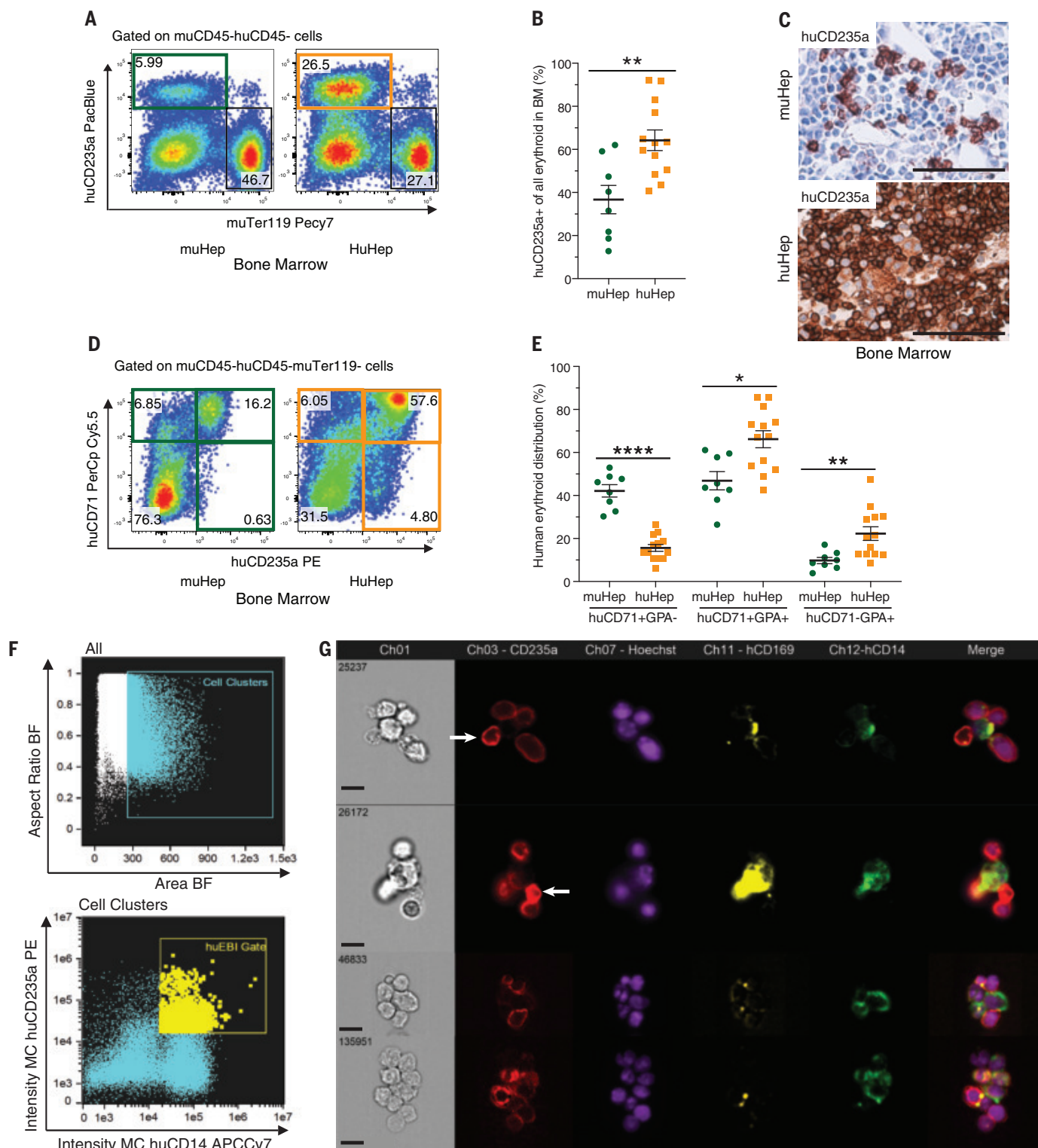


**Fig. 3. Liver humanization enhances human erythropoiesis. (A and B)** Representative flow cytometry plots (A) and quantitation (B) of human erythroid progenitors in BM of muHepMISTRGFah ( $n = 8$ ) and huHepMISTRGFah ( $n = 13$ ) mice. **(C)** Representative BM histology images of huCD235 staining from muHepMISTRGFah ( $n = 8$ ) and huHepMISTRGFah ( $n = 13$ ) mice. Scale bars, 100  $\mu\text{m}$ ; original magnification, 10 $\times$ . **(D and E)** Representative flow cytometry plots (D) and quantitation (E) of erythroid lineage differentiation determined on the basis of huCD71 and huCD235 expression in BM of muHepMISTRGFah ( $n = 8$ ) versus

huHepMISTRGFah ( $n = 13$ ) mice. GPA, glycophorin A. **(F)** Gating strategy in multispectral imaging flow cytometry of human EBIs in the huHepMISTRGFah mouse. BF, bright field. **(G)** Representative images of human EBIs. Enucleated reticulocytes in contact with the central macrophage are marked by white arrows. Scale bars, 10  $\mu\text{m}$ ; original magnification, 40 $\times$ . Individual mice are represented by symbols, and data are means  $\pm$  SEM.  $P$  values were determined by Mann-Whitney  $U$  test: \* $P < 0.05$ ; \*\* $P < 0.01$ ; \*\*\*\* $P < 0.0001$ . Data are representative of three independent experiments with three different donors of hepatocytes and FL cells.



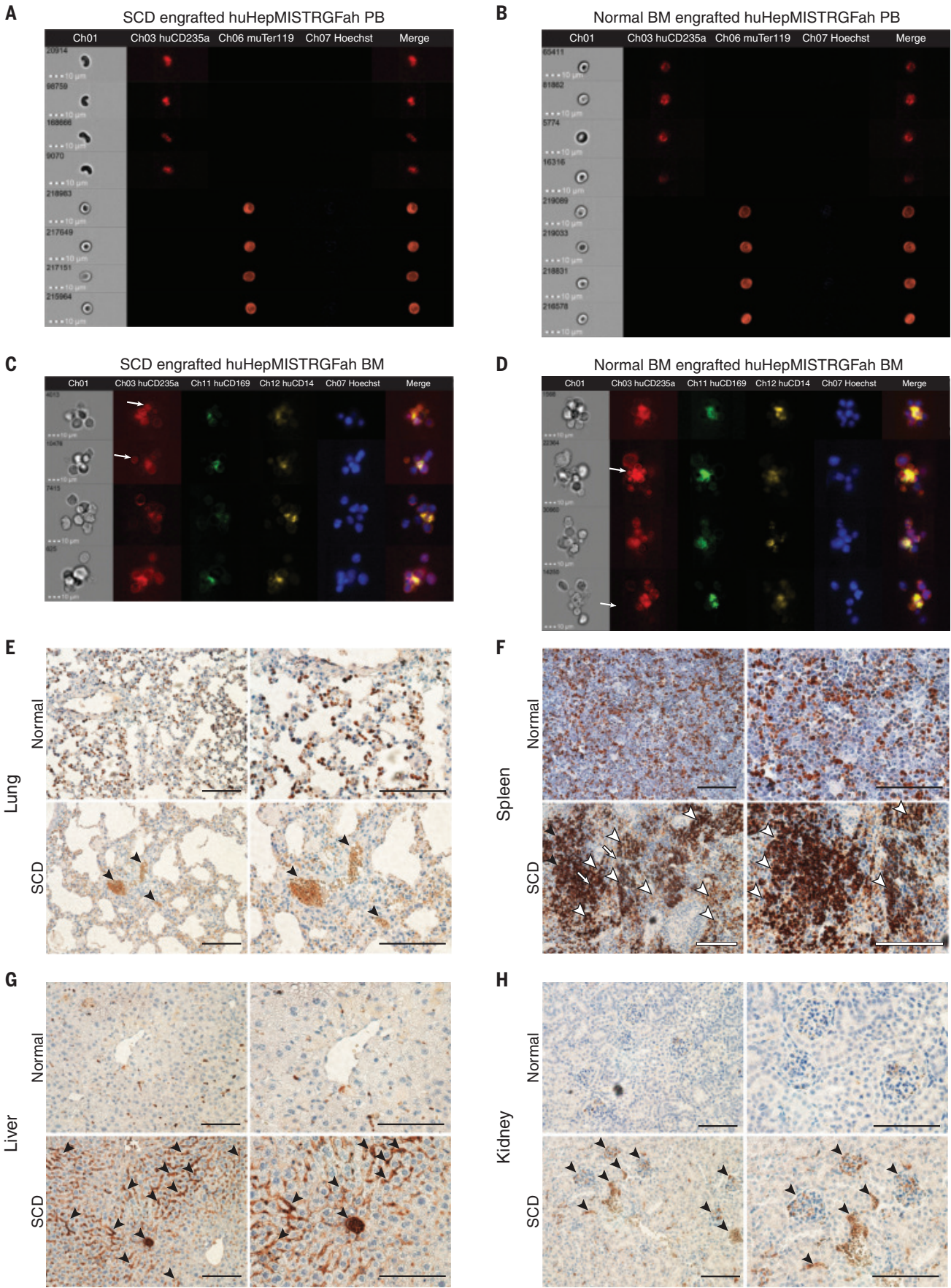


**Fig. 4. Modeling sickle cell disease in huHepMISTRGFah mice. (A and B)**

Representative multispectral imaging flow cytometry images of mature enucleated huRBCs (huCD235a<sup>+</sup>, Hoechst<sup>-</sup>) and muRBCs (muTer119<sup>+</sup>, Hoechst<sup>-</sup>) in the PB of SCD (A) and normal (B) BM CD34<sup>+</sup> cell-engrafted huHepMISTRGFah mice (*n* = 3). (C and D) Representative images of human EBIs in the BM of SCD (C) and normal (D) BM CD34<sup>+</sup> cell-engrafted huHepMISTRGFah mice (*n* = 6 for each BM). (E to H) Representative histologic images of tissues stained with human-specific anti-hemoglobin alpha (HBA) antibody from SCD (*n* = 6) and normal (*n* = 6) BM CD34<sup>+</sup>

cell-engrafted huHepMISTRGFah mice. Scale bars, 100  $\mu$ m; original magnification, 20 $\times$ . Arrowheads in (E) mark lung alveolar hemorrhages and thrombosis, in (F) they mark erythroid precursor expansion, sickled erythrocytes in sinusoids, vascular occlusion, and thrombosis in the spleen, in (G) they mark sickled RBCs in sinusoids and microvascular thrombosis in liver, and in (H) they mark congestion of capillary loops and peritubular capillaries and engorged glomeruli in kidneys of SCD-engrafted huHepMISTRGFah mice. Data are representative of two independent experiments with two different donors of normal and SCD CD34<sup>+</sup> cells.

in human FL hematopoietic stem and progenitor cell (HSPC)-engrafted, liver-reconstituted huHepMISTRGFah and muHepMISTRGFah mice (fig. S3A). The huHepMISTRGFah mice showed higher human leukocyte (huCD45<sup>+</sup>) contributions to PB cells at 6, 8, and 10 weeks (fig. S3B). Additionally, huHepMISTRGFah mice displayed persistent circulating huRBCs (huCD235a<sup>+</sup>) that represented up to 12% of the total RBCs in PB as early as 4 weeks and until at least 12 weeks after engraftment. The huRBCs remained absent in muHepMISTRGFah mice (<0.1% of total RBCs) (Fig. 2, A and B). Qualitative analysis of huRBCs, which was somewhat limited in muHepMISTRGFah mice because of the very low numbers of circulating huRBCs, showed improved maturity with a shift toward a huCD71<sup>+</sup>huCD235<sup>+</sup> (Fig. 2, C and D) and huCD49d<sup>+</sup>Band3<sup>+</sup> (Fig. 2, E and F) phenotype and near-complete enucleation of circulating huRBCs (Fig. 2, G and H) in huHepMISTRGFah mice. Neither huHepMISTRGFah mice nor muHepMISTRGFah mice harbored circulating huRBCs positive for surface muC3, consistent with rapid clearance of C3-coated RBCs by the innate immune system (fig. S3C). Lack of muC3 coating and survival of huRBCs in huHepMISTRGFah mice suggested that liver humanization abrogated muC3 expression. Indeed, muC3 protein concentrations in plasma were significantly reduced in huHepMISTRGFah mice (fig. S3D). Absent muC3 expression (fig. S3E) with acquired huC3 expression (fig. S3F) confirmed the proposed mechanism by liver humanization in huHepMISTRGFah mice. Liver macrophages are composed of liver-resident Kupffer cells and BM-derived recruited macrophages (14). We assessed whether liver humanization would alter liver macrophage composition by preferentially recruiting human HSPC-derived macrophages. Indeed, liver regeneration by human hepatocytes in huHepMISTRGFah mice resulted in replacement of murine F4/80<sup>+</sup> macrophages by human CD68<sup>+</sup> macrophages, whereas muHepMISTRGFah mice still contained a significant number of murine macrophages in addition to human macrophages (fig. S3, G to I). Thus, huRBCs are spared from destruction in huHepMISTRGFah mice, at least in part by elimination of complement-mediated opsonization and their recognition by the murine innate immune system.

### Liver humanization enhances human erythropoiesis

Liver humanization prolonged circulating huRBC survival. To determine whether liver humanization also affected generation of huRBCs, we analyzed human erythropoiesis within the BM. Overall, huCD45<sup>+</sup> engraftment was higher in huHepMISTRGFah than in muHepMISTRGFah mouse BM (fig. S4, A to C) without significant differences in the distribution of myeloid (huCD33<sup>+</sup>), B lymphoid (huCD19<sup>+</sup>), and T lymphoid (huCD3<sup>+</sup>) lineages (fig. S4D). Enhanced engraftment levels translated across all progenitor subpopulations (fig. S4, E to K). Human erythroid engraftment (huCD235a<sup>+</sup>) was significantly higher in huHepMISTRGFah BM (Fig. 3, A to C) and also in the spleen (fig. S5, A to C) with progressive down-regulation of huCD71, acquisition of huCD235a expression (Fig. 3, D and E), down-regulation of huCD49d, and acquisition of Band3 (15) (fig. S5, D and E) in the BM. Thus, liver humanization in huHepMISTRGFah improved human erythroid engraftment and maturation. We hypothesized that reduction in muC3 expression in huHepMISTRGFah mice would also spare human erythroid progenitors and RBCs in the BM. Indeed, muC3 staining was very low in huHepMISTRGFah mice, whereas nearly 100% of human erythroid progenitors within the BM of muHepMISTRGFah were coated with muC3 (fig. S5, F and G).

Before the exit of mature RBCs from the bone marrow, their condensed nuclei are removed by macrophages within so-called erythroblastic islands (EBIs), composed of a central macrophage surrounded by erythroid precursors at varying stages of maturation (16, 17). Expression of human M-CSF in MISTRG mice is required for full maturation of monocytes to tissue macrophages (7, 18). We assessed formation of EBIs by multispectral imaging flow cytometry (19) in BM of huHepMISTRGFah mice. EBIs contained numerous fully human EBIs characterized by huCD169<sup>+</sup>huCD14<sup>+</sup> double-positive central macrophages surrounded by huCD235a<sup>+</sup> erythroid progenitors of varying sizes, including enucleated huRBCs (Fig. 3F). Quantitation of enucleation by Hoechst staining indicated equal percentages of enucleated human red cells in the BM of both muHepMISTRGFah and huHepMISTRGFah mice (fig. S5, H and I).

Thus, liver humanization increases overall erythroid engraftment and maturation but does not affect terminal enucleation. However, enucleated huRBCs that exit the BM are protected from destruction by the lack of muC3 expression and reduction in murine liver phagocytes in huHepMISTRGFah mice.

### Modeling SCD in huHepMISTRGFah mice

Single-nucleotide point mutations in the globin  $\beta$  chain in SCD cause polymerization of hemoglobin under low oxygen tension that results in progressive damage to the RBC membrane. Vaso-occlusion and tissue hypoxia ensue, because of the adhesion of sickle RBCs in postcapillary venules and selective trapping of dense sickled RBCs enhanced by additional factors, such as endothelial activation and leukocyte adherence (20, 21). To determine whether enhanced erythropoiesis and, most notably, circulating huRBCs would be sufficient to replicate SCD in huHepMISTRGFah mice, we engrafted HSPCs from adult SCD patients and age-matched controls into huHepMISTRGFah mice (fig. S6, A and B). Overall, huCD45<sup>+</sup> engraftment, lineage distribution, and erythroid engraftment in BM (fig. S6, C to E) and PB (fig. S6, F to G) were similar between mice engrafted with normal or SCD HSPCs. Both normal and SCD HSPC-engrafted mice developed mild anemia as previously described (7) (fig. S6, H to E). We observed sickling huRBCs (7 to 11 sickling huRBCs per 100 huRBCs) in the PB of SCD HSPC-engrafted mice (Fig. 4A) but not in normal HSPC-engrafted mice (Fig. 4B). Both SCD (Fig. 4C) and normal (Fig. 4D) HSPC-engrafted mice exhibited EBIs in their respective BM. To determine whether circulating sickle huRBCs would result in vaso-occlusion and associated findings, we compared histological sections of lung, liver, spleen, and kidney from normal and SCD HSPC-engrafted mice. Tissues from SCD HSPC-engrafted mice showed significant abnormalities consistent with SCD vaso-occlusion caused by huRBCs, identified by human-specific anti-hemoglobin A antibody staining (Fig. 4, E to H), which were absent in normal HSPC-engrafted mice. Lungs showed an increase in alveolar macrophages (fig. S7, A and B) associated with alveolar hemorrhage and thrombosis (Fig. 4E). Spleens showed erythroid precursor expansion, sickled erythrocytes in the sinusoids, and vascular occlusion



and thrombosis (Fig. 4F and fig. S7, C and D). Liver architecture was disrupted in SCD-engrafted mice, with RBCs in sinusoids and microvascular thromboses (Fig. 4G and fig. S7, E and F). Congestion of capillary loops and peritubular capillaries and glomeruli engorged with sickled RBCs were evident in kidneys (Fig. 4H and fig. S7, G and H) of SCD but not of normal HSPC-engrafted mice.

Thus, this model allows the successful engraftment of adult HSPCs and establishment of robust erythropoiesis from both normal and SCD patients. Moreover, circulating human RBCs from a sickle cell donor replicate the hallmark of SCD, vaso-occlusion in hematopoietic and nonhematopoietic organs in the murine host.

## Discussion

Immunodeficient mouse models have historically been poor hosts for human erythropoiesis. Despite recent improvements of the BM niche by human cytokine knock-in (6, 7) or mutation of the murine host's stem cell factor receptor (4, 5), huRBCs in PB are universally absent. Elimination of phagocytes by liposomal clodronate results in transient circulation of huRBCs, confirming the involvement of the innate immune system (4, 5, 22). Liposomal clodronate is toxic with significant mortality and provides only temporary benefit due to regeneration of phagocytes within 1 to 2 weeks. A recent study showed that muC3 mediates adherence of huRBCs to mouse phagocytes, yet in vivo depletion of muC3 only improves huRBC survival when phagocytes are concurrently abrogated by clodronate treatment (9). In our studies, we identified the mouse liver as the major site of huRBC sequestration. Liver humanization significantly reduced muC3 synthesis and resulted in reduced density of murine macrophages in the regenerated liver in human HSPC-engrafted huHepMISTRGFah mice. Therefore, liver humanization, likely by elimination of muC3 and reduction of liver Kupffer cells, results in persistent enucleated, mature huRBCs in circulation.

Human HSPC-engrafted huHepMISTRGFah mice show enhanced human erythropoiesis. Unlike all other humanized immunodeficient mouse models, MISTRG mice express human M-CSF, which allows mature functional resident tissue macrophages to populate host tissues (6, 7). We determined that a subset of human macrophages in huHepMISTRGFah mice express the central macrophage marker CD169<sup>+</sup> (19, 23, 24) and are found within EBIs in close contact with human erythroid progenitors of several differentiation stages. Human erythroid precursors in BM of huHepMISTRGFah mice also lack coating with muC3. Hence, liver humanization combined with cytokine humanization enables study of the role played by the central macrophage in human erythropoiesis

in health and disease in an immunologically advantageous context.

SCD is an inherited blood disorder caused by a single point mutation in the  $\beta$ -globin gene, mutating the sixth amino acid glutamine to valine (25). The most common murine models of SCD (26) exclusively express human globins in muRBCs in the background of murine globin knockouts (27–29). Mouse models have notably contributed to the elucidation of many of the mechanisms of SCD pathology. However, they exclusively contain muRBCs and fail to capture the genetic heterogeneity encountered in patients, making a flexible model of human SCD highly desirable. We successfully engrafted SCD HSPCs in huHepMISTRGFah mice and detected circulating, sickling huRBCs in the mouse PB. In addition, we observed pathological changes in the lung, spleen, liver, and kidney that were comparable to changes in patients (30–33) and established SCD mouse models (27, 29).

We herein present our huHepMISTRGFah mouse model with enhanced reconstitution of human erythropoiesis and, more notably, mature circulating huRBCs. Our findings highlight the potential of this model for use in studies of the numerous life-threatening RBC diseases, which involve  $\approx$ 5% of the population worldwide (34), including alpha and beta thalassemia (35) and SCD (25). Moreover, this model may be important in studies of hematopoietic stem cell diseases, such as myelodysplasia; in erythroleukemia; and in pathologies that intricately link RBCs and the liver, such as malaria. This mouse model may therefore open additional avenues for the study of disease pathophysiological mechanisms and the preclinical screening of therapeutics.

## REFERENCES AND NOTES

1. R. Carter, K. N. Mendis, *Clin. Microbiol. Rev.* **15**, 564–594 (2002).
2. E. Dzierzak, S. Philipsen, *Cold Spring Harb. Perspect. Med.* **3**, a011601 (2013).
3. N. C. Walsh et al., *Annu. Rev. Pathol.* **12**, 187–215 (2017).
4. A. Yurino et al., *Stem Cell Reports* **7**, 425–438 (2016).
5. S. Rahmig et al., *Stem Cell Reports* **7**, 591–601 (2016).
6. Y. Song et al., *Nat. Commun.* **10**, 366 (2019).
7. A. Rongvaux et al., *Nat. Biotechnol.* **32**, 364–372 (2014).
8. K. Deng et al., *Nature* **517**, 381–385 (2015).
9. B. Chen et al., *Stem Cell Reports* **9**, 1034–1042 (2017).
10. M. W. Robinson, C. Harmon, C. O'Farrelly, *Cell. Mol. Immunol.* **13**, 267–276 (2016).
11. M. Bilzer, F. Roggel, A. L. Gerbes, *Liver Int.* **26**, 1175–1186 (2006).
12. K. D. Bissig, T. T. Le, N. B. Woods, I. M. Verma, *Proc. Natl. Acad. Sci. U.S.A.* **104**, 20507–20511 (2007).
13. H. Azuma et al., *Nat. Biotechnol.* **25**, 903–910 (2007).
14. A. Guillot, F. Tacke, *Hepatol. Commun.* **3**, 730–743 (2019).
15. J. Hu et al., *Blood* **121**, 3246–3253 (2013).
16. J. A. Chasis, N. Mohandas, *Blood* **112**, 470–478 (2008).
17. Y. Sadahira, T. Yoshino, Y. Monobe, *J. Exp. Med.* **181**, 411–415 (1995).
18. C. Rathinam et al., *Blood* **118**, 3119–3128 (2011).
19. K. G. Seu et al., *Front. Immunol.* **8**, 1140 (2017).

20. P. S. Frenette, *Curr. Opin. Hematol.* **9**, 101–106 (2002).
21. D. K. Kaul, M. E. Fabry, *Microcirculation* **11**, 153–165 (2004).
22. Z. Hu, N. Van Rooijen, Y. G. Yang, *Blood* **118**, 5938–5946 (2011).
23. A. Chow et al., *Nat. Med.* **19**, 429–436 (2013).
24. T. Ulyanova, S. R. Phelps, T. Papayannopoulou, *Blood* **128**, 1756–1765 (2016).
25. F. B. Piel, M. H. Steinberg, D. C. Rees, *N. Engl. J. Med.* **376**, 1561–1573 (2017).
26. R. L. Nagel, M. E. Fabry, *Br. J. Haematol.* **112**, 19–25 (2001).
27. C. Pászty et al., *Science* **278**, 876–878 (1997).
28. J. C. Chang et al., *Proc. Natl. Acad. Sci. U.S.A.* **95**, 14886–14890 (1998).
29. T. M. Ryan, D. J. Ciavatta, T. M. Townes, *Science* **278**, 873–876 (1997).
30. Y. Liu et al., *Blood* **134**, 579–590 (2019).
31. R. P. Naik, V. K. Derebail, *Expert Rev. Hematol.* **10**, 1087–1094 (2017).
32. J. I. Malowany, J. Butany, *Semin. Diagn. Pathol.* **29**, 49–55 (2012).
33. J. R. Thogmartin, C. I. Wilson, N. A. Palma, S. S. Ignacio, W. A. Pellam, *Am. J. Forensic Med. Pathol.* **30**, 36–39 (2009).
34. H. L. Muncie Jr., J. Campbell, *Am. Fam. Physician* **80**, 339–344 (2009).
35. D. Rund, E. Rachmilewitz, *N. Engl. J. Med.* **353**, 1135–1146 (2005).

## ACKNOWLEDGMENTS

We thank H. Yan at the New York Blood Center for providing human anti-Band3 antibody. We thank A. Ploss at Princeton University for critical suggestions. We thank our patients for donating BM to research. We thank our colleagues G. Yancopoulos, D. Valenzuela, A. Murphy, and W. Auerbach at Regeneron Pharmaceuticals who generated, in collaboration with our groups, the individual knock-in alleles to generate the MISTRG mouse. We thank the Yale Pathology Tissue Services, the Yale Animal Resource Center, and the Yale Flow Cytometry Core for all their support. **Funding:** This study was supported by the Animal Modeling Core of the YCCEH (NIDDK U54DK106857), a YCCEH Pilot grant (to Y.S.), in part by the Bill and Melinda Gates Foundation (to R.A.F.), in part by NIH/NIDDK R01DK102792 (to S.H.), The Frederick A. Deluca Foundation (to S.H.), and the Howard Hughes Medical Institute (to R.A.F.). Y.S. and X.F. were supported by the National Science Foundation for Young Scientists of China (Grant Nos. 81800122, 81801588). L.S. was supported by NIH/NIAD K99AI125065. Y.G. was supported by a James Hudson Brown–Alexander Brown Cox Postdoctoral Fellowship.

**Author contributions:** Conceptualization: S.H., R.A.F., Y.S., and L.S.; methodology: S.H., R.A.F., Y.S., and L.S.; investigation: Y.S., L.S., R.G., A.P., X.F., X.W., A.Q., W.L., Y.G., E.M.B., M.L.X., T.S., D.G.G., J.C., T.T., G.B., P.M., and D.U.; data analysis: Y.S., L.S., R.G., D.S.K., and S.H.; validation: Y.S., L.S., R.G., and S.H.; writing original draft: S.H., Y.S., L.S., and R.G.; writing review and editing: S.H., R.A.F., Y.S., and L.S.; funding acquisition: S.H. and R.A.F.; resources: R.G., A.P., and J.A.; project administration: S.H., R.A.F., E.E., and J.A.; supervision: S.H. and R.A.F. **Competing interests:** R.A.F., S.H., L.S., and Y.S. are inventors on a patent related to this study (PCT/US20/42475). R.A.F. provides consultancy to Zai labs and Glaxo-Smith-Kline. **Data and materials availability:** All data are available in the main text or the supplementary materials. The MISTRG mice are available from the corresponding authors under a material agreement with Yale University, HHMI, and Regeneron Pharmaceuticals. These mice are also in the process of being deposited at the Jackson laboratory and will soon be available through that repository.

## SUPPLEMENTARY MATERIALS

science.sciencemag.org/content/371/6533/1019/suppl/DC1  
Materials and Methods  
Figs. S1 to S7  
Tables S1 to S3  
References (36–39)  
MDAR Reproducibility Checklist  
Movies S1 and S2

9 August 2020; accepted 1 February 2021  
10.1126/science.abe2485

## METALLURGY

## Scaling behavior of stiffness and strength of hierarchical network nanomaterials

Shan Shi<sup>1,2\*</sup>, Yong Li<sup>1,2</sup>, Bao-Nam Ngo-Dinh<sup>1,3</sup>, Jürgen Markmann<sup>1,2</sup>, Jörg Weissmüller<sup>1,2\*</sup>

Structural hierarchy can enhance the mechanical behavior of materials and systems. This is exemplified by the fracture toughness of nacre or enamel in nature and by human-made architected microscale network structures. Nanoscale structuring promises further strengthening, yet macroscopic bodies built this way contain an immense number of struts, calling for scalable preparation schemes. In this work, we demonstrated macroscopic hierarchical network nanomaterials made by the self-organization processes of dealloying. Their hierarchical architecture affords enhanced strength and stiffness at a given solid fraction, and it enables reduced solid fractions by dealloying. Scaling laws for the mechanics and atomistic simulation support the observations. Because they expose the systematic benefits of hierarchical structuring in nanoscale network structures, our materials may serve as prototypes for future lightweight structural materials.

**H**ierarchical structures, featuring several relevant length scales, are common in nature, engineering, and society. Often, the hierarchy is motivated by optimizing function—for instance, the transport of fluids (1–3) or vehicles (4). Another prominent use of hierarchy is in optimizing mechanical behavior while satisfying boundary conditions on material class, mass density, or manufacturing costs. Nature is well known to exploit hierarchy for optimizing fracture toughness in nacre, bone, and enamel (5–9). Strong and lightweight hierarchical truss structures at the macroscale have been used for more than a century (10). By exploiting modern three-dimensional (3D) manufacturing techniques, this approach has been transferred to the microscale. Architected truss structures have been demonstrated with extremely low density, high specific strength, and high resilience [(11–15); for a comprehensive review, see (16)].

Driving the size of architected truss structures into the regime of nanometers has been recognized as beneficial (13, 16, 17) because this exploits the high strength of metal nanostructures (18). Using struts of 10 nm in dimension would imply on the order of  $10^{14}$  struts in a cubic millimeter. Rather than 3D manufacturing, producing that many microstructural elements requires the self-organized processes that are characteristic of microstructure evolution in materials science. In other words, making truly nanoscale open-network structures by materials preparation routes that are scalable and so yield macroscopic bodies is an area of high interest. Micrometer-scale microstructures made by

spinodal decomposition or colloidal crystallization may act as templates for thin shells to provide macroscopic bodies in which one dimension—the shell thickness—is in the nanoscale (19–21). Yet, although such approaches exemplify the versatility of nature's self-organization processes, they have yet to achieve structural hierarchy. Various routes can lead to hierarchy in nanoporous metals (22, 23), yet homogeneous macroscopic bodies are the exception, and interesting mechanical properties remain to be demonstrated for this class of materials.

Network nanomaterials with a single characteristic size have been demonstrated on the basis of dealloying (24). In this process, corrosion removes one constituent from a solid solution, and the remaining constituent reorganizes to form an open-network material. Dealloying can produce homogeneous monolithic bodies that are millimeters or centimeters in size (25–27), whereas strut sizes reach down to a few nanometers (28). These bodies are deformable to large plastic strain without failure, and their effective macroscopic strength is consistent with the extremely high local strength of the nanoscale struts (29–33). Dealloying is best understood as a process for nanoporous gold (NPG), but protocols for lighter and stronger metals, such as Ti, Al, and high-entropy alloys, are becoming available (34–37).

Dealloying is also a pathway to hierarchical network materials and specifically to structures with a particularly stringent architecture in the form of two geometrically similar networks that are nested on two well-defined, distinctly different length scales (38–40). However, macrodefects have impaired investigations of the mechanical behavior of these materials.

Dealloying can provide solid volume fractions,  $\phi$ , down to  $\sim 0.25$  in single-length-scale networks. Reducing  $\phi$  requires increasing the aspect ratio of the struts, yet long and thin

struts tend to be Plateau-Rayleigh instable (33, 41, 42). This problem is generally relevant for nanomaterials, and it applies specifically for metallic nanostructures that emerge from diffusion-driven self-organization, which is the active process during dealloying. Consequently, the connectivity of dealloying-made network materials deteriorates when  $\phi$  falls below  $\sim 0.3$ , and so do stiffness and strength (43). This observation provides an incentive for hierarchical nanoscale network materials. To reach low  $\phi$  in a stable structure, short and thick struts on any given hierarchy level can be built as a network made of a set of much smaller struts, which are also short and thick (and thus stable) on a lower structural hierarchy level. In this way, self-organized (and thus scalable) processes may be expected to build low-density (and thus lightweight) nanoscale (and thus strong) networks with good connectivity and high strength and stiffness.

We report a dealloying route toward the scalable and controllable preparation of macroscopic monolithic bodies of nested-network nanoporous gold (N<sup>3</sup>PG) that are free of macrodefects. The characteristic size at the lower hierarchy level is as small as 15 nm, and  $\phi$  can be as low as 0.12. This value has been very challenging to attain in nanoscale network materials made by dealloying. Macroscale compression tests show that the stiffness and strength increase when going from the single scale to the hierarchical material. Our findings are explained by scaling laws that emerge from recursive homogenization approaches on the individual hierarchy levels, and we corroborated them using molecular dynamics (MD) simulation of the mechanical behavior.

## Preparing nested-network nanomaterials

Our monolithic N<sup>3</sup>PG samples were made by a refined variant of the “dealloying-coarsening-dealloying” protocol (Fig. 1A) (39, 44). Our preparation goes through three stages, an as-dealloyed nanoporous Ag-Au (stage i), a coarsened nanoporous Ag-Au (stage ii), and N<sup>3</sup>PG (stage iii). Stage i is generated when the Ag<sub>93</sub>Au<sub>7</sub> master alloy is electrochemically dealloyed in 0.01 M H<sub>2</sub>SO<sub>4</sub>. During this process, nanoporous Ag-Au forms by surface diffusion as the Ag is partially dissolved. Stage ii is obtained by coarsening the stage i material through a vacuum anneal. This establishes the structure of the upper hierarchy level. The final, stage iii hierarchical material is obtained when the residual Ag is removed during a second electrochemical dealloying process in 1.0 M HClO<sub>4</sub>. This process creates a much smaller porous structure inside the larger struts of the coarsened stage ii material. The smaller structure represents the lower hierarchy level.

Scanning electron microscopy (SEM) images of the stage i material (Fig. 1B) exhibit the

<sup>1</sup>Institute of Materials Research, Materials Mechanics, Helmholtz-Zentrum Geesthacht, 21502 Geesthacht, Germany.

<sup>2</sup>Institute of Materials Physics and Technology, Hamburg University of Technology, 21073 Hamburg, Germany.

<sup>3</sup>Institute for Materials, Technical University of Braunschweig, 38106 Braunschweig, Germany.

\*Corresponding author. Email: shan.shi@hzg.de (S.S.); weissmueller@tuhh.de (J.W.)



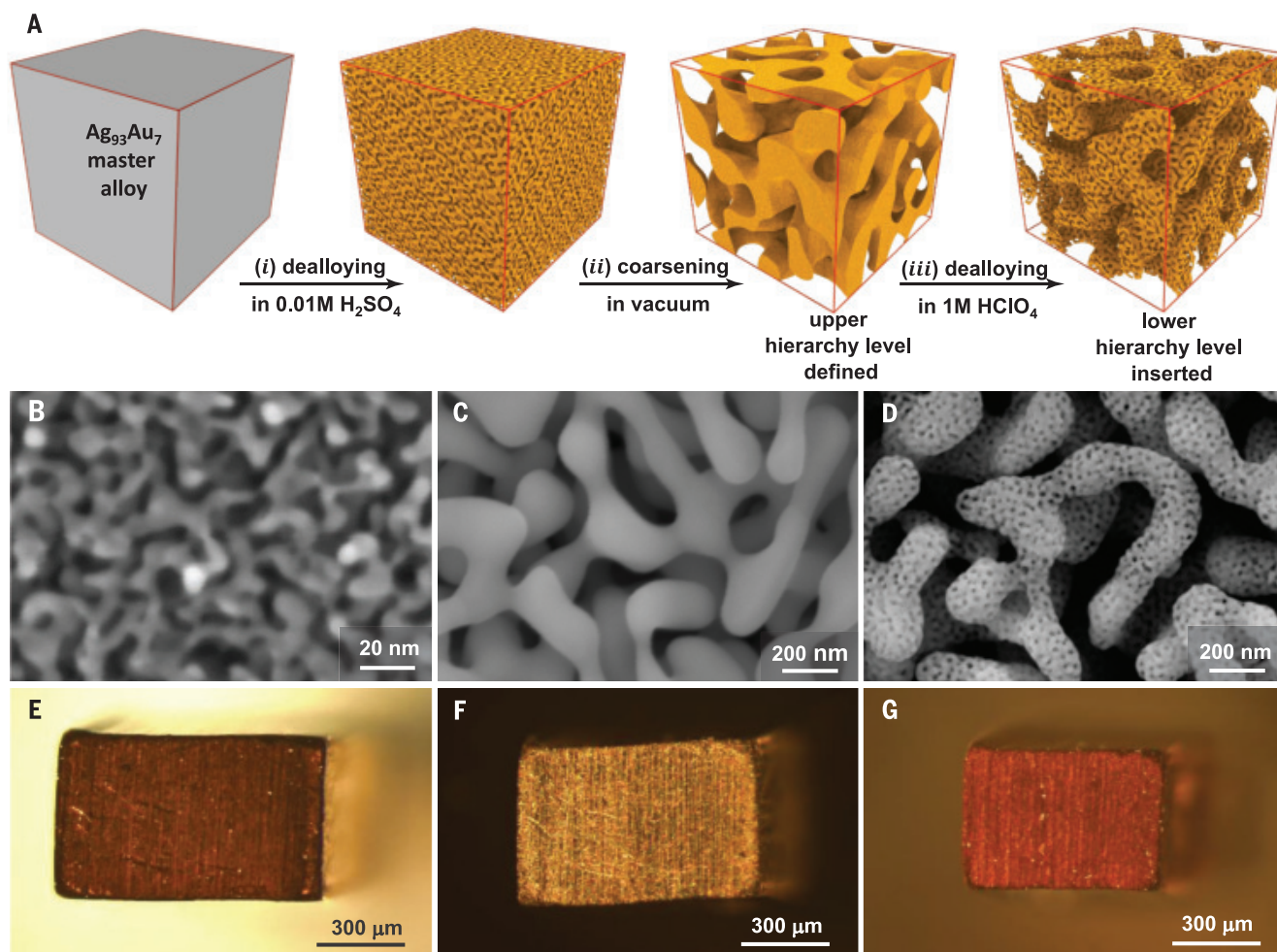


**Fig. 1. Fabrication and microstructure characterization of N<sup>3</sup>PG.**

(A) Schematic describing the synthesis route of monolithic, crack-free N<sup>3</sup>PG. Stage i: Electrochemical dealloying of Ag<sub>93</sub>Au<sub>7</sub> master alloy in 0.01 M H<sub>2</sub>SO<sub>4</sub> aqueous electrolyte creates a monomodal bicontinuous porous structure and remains a substantial amount of Ag. Stage ii: Annealing as-dealloyed nanoporous Ag-Au alloy in vacuum leads to coarser microstructure (see much larger solid strut and pore size). Stage iii: A second electrochemical dealloying process on

coarsened nanoporous Ag-Au alloy in 1.0 M HClO<sub>4</sub> substantially dissolves residual Ag and creates bicontinuous porous structure inside the solid strut. (B to D) SEM images showing fracture surface microstructure of (B) as-dealloyed nanoporous Ag<sub>76</sub>Au<sub>24</sub>, (C) coarsened nanoporous Ag<sub>76</sub>Au<sub>24</sub> (400°C for 30 min), and (D) as-prepared N<sup>3</sup>PG. (E to G) Optical microscope images showing crack-free overview of (E) as-dealloyed nanoporous Ag<sub>76</sub>Au<sub>24</sub>, (F) coarsened nanoporous Ag<sub>76</sub>Au<sub>24</sub> (400°C for 30 min), and (G) as-prepared N<sup>3</sup>PG.

characteristic network structure of dealloying. The strut size, defined as the mean strut diameter, is as low as  $L = 7$  nm. In stage ii (Fig. 1C), the Ag-Au alloy of stage i has coarsened to the larger strut size of  $L = 110$  nm, whereas the microstructure appears geometrically similar to that of stage i. We found, using energy-dispersive x-ray spectroscopy (EDX), a Ag atom fraction,  $x_{\text{Ag}}$ , of 76%. The hierarchical nested-network nanostructure of the stage iii material appears after the second dealloying (Fig. 1D). The struts of stage ii acquired an internal porosity after the second dealloying, and two well-defined strut sizes of  $L_1 = 15$  nm and  $L_2 = 110$  nm form the lower and upper hierarchy levels, respectively. The size of  $L_2$  is close to  $L$  at stage ii. Our EDX measurements suggest that  $x_{\text{Ag}} < 5$  atomic % (at %) in stage iii samples. Samples with these charac-

teristics could be reproducibly made and mechanically tested.

Optical images suggest that the samples are monolithic and free of macroscale cracks (Fig. 1, E to G). The smaller dimensions of the stage iii sample indicate shrinkage during the second dealloying. The net volumetric shrinkage during the entire preparation is 48%, substantially less than previously reported (39). By using SEM on fracture surfaces, we found that the nested-network nanostructure (Fig. 1D) is perfectly uniform throughout the bulk of millimeter-sized samples (Fig. 1G).

We recognized that the careful selection of electrolyte and dealloying potential at stage i is decisive for making homogeneous monolithic samples. As compared with the standard electrolyte, 1.0 M HClO<sub>4</sub>, we achieved superior retention of Ag with 0.01 M H<sub>2</sub>SO<sub>4</sub>. We spec-

ulate that this is related to the high surface diffusivity of Au in H<sub>2</sub>SO<sub>4</sub> (45), which promotes passivation and hence the burying of Ag within the stage i struts. Furthermore, working only slightly above the critical dealloying potential (0.359 V), as determined from the polarization plot (fig. S1), at stage i enabled dealloying throughout the bulk with little shrinkage. The residual Ag varies between 79 and 69 at % in the very small interval of dealloying potentials, 0.359 to 0.368 V (fig. S2). This range is above the parting limit, 55 at % Ag (46), which affords complete dealloying at stage iii.

By tuning the preparation conditions, the microstructure parameters of our nested-network materials can be varied. We focused on two series of samples. In the first series, we varied the initial (of the as-prepared stage iii

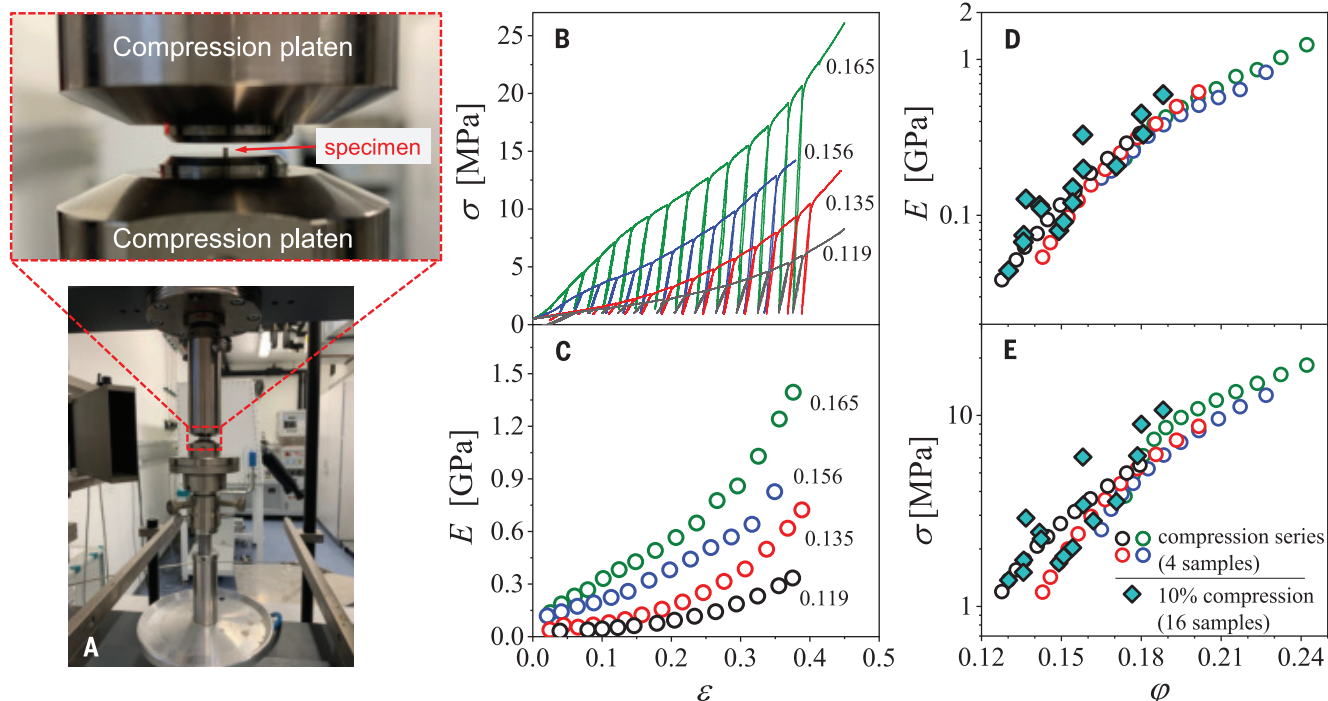


**Fig. 2. Uniaxial macrocompression on N<sup>3</sup>PG with various solid fractions.**

(A) Photograph of a conventional macroscale testing device for compression tests. Partial enlarged figure (top) shows a millimeter-sized specimen on the compression platen. (B) Engineering stress-strain ( $\sigma$ – $\epsilon$ ) curves, including unload-and-reload segments for N<sup>3</sup>PG with initial solid fraction ( $\phi$ ) ranging

from 0.119 to 0.165. (C) Effective Young's modulus ( $E$ ) versus  $\epsilon$  during compression. (D to E)  $E$  and  $\sigma$  versus  $\phi$ . Solid symbols, 16 individual samples at 10% strain. Open symbols, the four individual samples from (B), with  $\phi$  varying from 0 to 30% during the compression series. Labels in (B) and (C) specify initial  $\phi$ .

material before deformation) value of the overall  $\phi$  by adjusting the dealloying potential in the interval 0.359 to 0.368 V at stage i while the strut sizes remained constant. In the second series, we varied  $L_2$  by adjusting the stage ii annealing conditions.

### Impact of solid fraction on Young's modulus and strength

We explored the mechanical behavior of N<sup>3</sup>PG samples with similar strut sizes,  $L_1 = 15$  nm and  $L_2 = 110$  nm, but different initial  $\phi$ . We conducted our uniaxial compression tests on the millimeter-sized samples using a conventional mechanical testing device (Fig. 2A).

We measured engineering stress-strain curves with unload-and-reload segments for N<sup>3</sup>PG with initial  $\phi$  in the range of 0.119 to 0.165 (Fig. 2B). All samples can be deformed to large strain without failure. Pronounced and continuously increasing strain hardening is apparent, suggesting homogeneous plastic deformation. We determined the effective Young's modulus ( $E$ ) as the secant modulus of unload-and-reload segments during plastic deformation (Fig. 2C). Samples with higher initial  $\phi$  are stiffer, and  $E$  increases with increasing plastic strain.

We have followed the variation of  $E$  and the effective, macroscopic strength ( $\sigma$ ) as  $\phi$  is varied (i) by densification during deformation for one and the same sample or (ii) by preparation for separate samples predeformed

identically (to 10% plastic strain). All data agree well (Fig. 2, D and E), supporting the reproducibility of our preparation protocol as well as the homogeneity of the millimeter-sized monoliths. Furthermore, the consistency suggests that, within the restricted regime of solid fractions studied in this work,  $\phi$  is an appropriate descriptor of the material, irrespective of whether  $\phi$  was established by tuning the preparation conditions or by imposing plastic deformation.

We compare the  $E$  of hierarchical N<sup>3</sup>PG with experimental data from the literature for as-prepared NPG with a single length scale (Fig. 3). The known consistency of the experimental literature data is apparent (Fig. 3A). The figure includes finite-element simulation data (43) for  $E$  of spinodal and self-organized nanoscale network structures with a single hierarchy level. Those simulation data extend the range of solid fractions downward. The combination of experiment and simulation illustrates the established (33, 43) pronounced drop of the stiffness of network materials formed by dealloying for  $\phi$  substantially below 0.3. At such low  $\phi$ , our hierarchical samples appear substantially stiffer than the trends suggested from the nonhierarchical ones. Furthermore, the hierarchical samples extend the range of solid fractions accessible to dealloyed network materials to substantially lower values.

The Gibson-Ashby scaling law for  $E$  (eq. S2) approximates the scaling for some of the architected lattice structures (fig. S4C). The lesser  $E$  at low  $\phi$  in our data arises from the loss in connectivity when going from geometrically optimized architected structures with a restricted number of struts to scalable network materials made by nanoscale self-organization. The architected structures with  $\phi$  comparable to our material exhibit  $<10^4$  struts, orders of magnitude below the  $10^{12}$  struts (44) of our N<sup>3</sup>PG samples.

We determined the effective, macroscopic strength versus the solid fraction (Fig. 3B). We normalized the strength to the value at the strut level,  $\sigma_0$ , which is size dependent. We adopted the values in (47) for this dependency. All of our samples have a sensibly identical lower-level strut size,  $L_1 = 15$  nm. We estimated the value of  $\sigma_0$  at that size to be 2.3 GPa (47). As we found for the stiffness, the data for the strength of nonhierarchical NPG from different literature sources (44) are quite consistent, and the hierarchical material explores a range of solid fractions that are substantially below those of the nonhierarchical material.

### Scaling laws for Young's modulus and strength

Our discussion of scaling laws adopts the suggestion of a recursive homogenization scheme for modeling the mechanical behavior of



hierarchical structures or materials (6, 10). When applied to nested networks, the underlying assumption is that the effective (homogenized) value,  $P_{\text{eff}}$ , of the mechanical materials property  $P$  at any hierarchy level  $j$  of the network can be understood as the product of the local value,  $P_{\text{loc}}$ , of  $P$  in the struts at that level and of a function  $p$  that depends on the geometry of the microstructure, in the simplest case through the strut volume fraction,  $\varphi_j$ , at the respective level. Because  $P_{\text{loc}}$  embodies the effective material's behavior at the next lower hierarchy level, one obtains the recursive formula and the result for the net value,  $P_{\text{net}}$ , of  $P$  as

$$P_{\text{eff},j} = P_{\text{eff},j-1} p(\varphi_j) \quad (1)$$

$$P_{\text{net}} = P_0 \prod_{j=1}^n p(\varphi_j) \quad (2)$$

for a material with  $n$  hierarchy levels.  $P_0$  is the local value of  $P$  in the massive material that forms the elementary structural units (in this work, the struts) at the lowest hierarchy level.

Often, the  $P_{\text{eff}}$  depend on  $\varphi$  by a power law, so that  $P_{\text{eff}} = b P_{\text{loc}} \varphi^\beta$  with  $b$  and  $\beta$  constants. Consider, for simplicity, a “strong” self-similarity, characterized by a common value,  $\bar{\varphi}$ , of the solid fraction at each of the  $n$  hierarchy levels. The net values of the solid fraction and of  $P$  are then  $\varphi_{\text{net}} = \bar{\varphi}^n$  and (by Eq. 2)  $P_{\text{net}} = P_0 b^n \varphi_{\text{net}}^\beta$ , respectively. As has been pointed out (10), the impact of hierarchical structuring on the mechanics is here simply represented by the factor  $b^n$ . Hierarchy then has no impact on the mechanics if  $b = 1$ , as for Young's modulus of foams, and it will lead to a progressive deterioration of the behavior if  $b < 1$ , as for the strength of foams (10, 48).

Power-law scaling is well established for materials with a macroscale microstructure, such as conventional foams (48). Yet power laws may generally not be expected for materials in which a nanoscale bicontinuous microstructure forms by self-organization. Nanoscale struts with a high aspect ratio, required for low  $\varphi$ , tend to disconnect because of the Plateau-Rayleigh instability (33, 41, 42). The result is a progressive loss of connectivity in the network as  $\varphi$  decreases, abutting in a percolation threshold at a finite value,  $\varphi_{\text{per}}$ , of the solid fraction. A modified Roberts-Garboczi law has been proposed for the mechanical behavior of such materials. Limited to not-too-large  $\varphi$ , this law takes the form (43)

$$P_{\text{eff}} = P_{\text{loc}} C \left( \frac{\varphi - \varphi_{\text{per}}}{1 - \varphi_{\text{per}}} \right)^m \quad (3)$$

with  $C$  and  $m$  constants.

For the effective  $E$  of bicontinuous materials formed by spinodal decomposition or deal-

loying and for  $\varphi \leq 0.5$ , the constants in Eq. 3 take the values  $\varphi_{\text{per}} \approx 0.16$ ,  $C \approx 2$ , and  $m \approx 5/2$ . Because the predicted values of  $E$  agree well with experimental data for as-prepared dealloyed NPG (43), we explored the ramifications of Eq. 3 for N<sup>3</sup>PG. Combining the scaling law with the recursive homogenization scheme of Eq. 2 and assuming strong self-similarity, we obtained for the net effective Young's modulus

$$E_{\text{net}} = E_0 2^n \left( \frac{\varphi_{\text{net}}^{1/n} - \varphi_{\text{per}}}{1 - \varphi_{\text{per}}} \right)^{5n/2} \quad (4)$$

for  $\varphi_{\text{net}} \leq 2^{-n}$ .

Experiment provides strong evidence for a systematic correlation between the stiffness and strength of nanoscale metal network materials made by dealloying (47, 49). The underlying notions are that (i) disconnected regions of the network will contribute to the solid fraction but, because they bear no load, not to the effective mechanical behavior and that (ii) the Gibson-Ashby scaling relations for open-cell foams (Fig. 3) apply to the well-connected, load-bearing part of the material. These findings can be combined with the modified Roberts-Garboczi law for  $E$  to obtain a tentative scaling law for the strength of NPG, accounting for the percolation threshold (44).

For  $\varphi \leq 0.5$ , this law again takes the form of Eq. 3, but with the modified parameters  $C \approx 1/2$  and  $m \approx 15/8$  (eq. S6). The estimated value of  $m$  agrees well with the empirical value,  $m = 1.84$  (49), obtained by fitting experimental strength data for dealloyed nanoporous Fe-Cr with Eq. 3. Combining this scaling law with Eq. 2, we obtained the yield strength of the hierarchical material as

$$\sigma_{\text{net}} = \sigma_0 \frac{1}{2^n} \left( \frac{\varphi_{\text{net}}^{1/n} - \varphi_{\text{per}}}{1 - \varphi_{\text{per}}} \right)^{15n/8} \quad (5)$$

for  $\varphi_{\text{net}} \leq 2^{-n}$ . The scenario underlying Eqs. 4 and 5 of strong self-similarity (identical  $\varphi$  at each hierarchy level) provides the optimum stiffness and strength for a given  $\varphi_{\text{net}}$  (44).

We used Eqs. 4 and 5 to predict the variations of stiffness and strength with the  $\varphi$  in structures with different numbers of hierarchy levels, assuming a strong self-similarity with equal density at each level (Fig. 3). The hierarchical structuring enables load-bearing materials with  $\varphi$  below the percolation threshold of the conventional, nonhierarchical material. The hierarchical material is also substantially stiffer and stronger than the nonhierarchical one with the same net  $\varphi$ , and this applies particularly near the percolation threshold. This enhanced mechanical behavior at low  $\varphi$

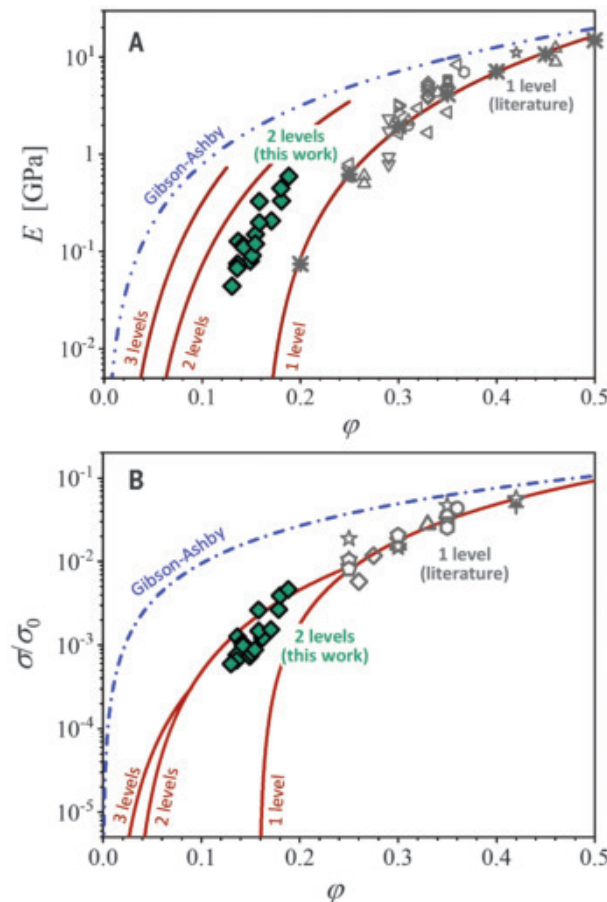


**Fig. 3. Scaling behavior of stiffness and strength with solid fraction for NPG with different numbers of hierarchy levels. (A)** Effective Young's modulus ( $E$ ) versus solid fraction ( $\varphi$ ). **(B)** Normalized yield strength ( $\sigma/\sigma_0$ ) versus  $\varphi$ .  $\sigma_0$  denotes local strut strength at the lowest hierarchical level (47). Solid symbols, experimental N<sup>3</sup>PG ( $n = 2$ ). Open symbols, literature data for experimental nonhierarchical NPG ( $n = 1$ ) taken from various sources [for details and a version with log-log axis scaling, see fig. S4 (44)]. Asterisks, simulated data of spinodal and self-organized nanoscale network structures with a single hierarchy level ( $n = 1$ ) (43). Lines, theory recursive homogenization, Eqs. 4 and 5; broken lines, Gibson-Ashby laws (44).

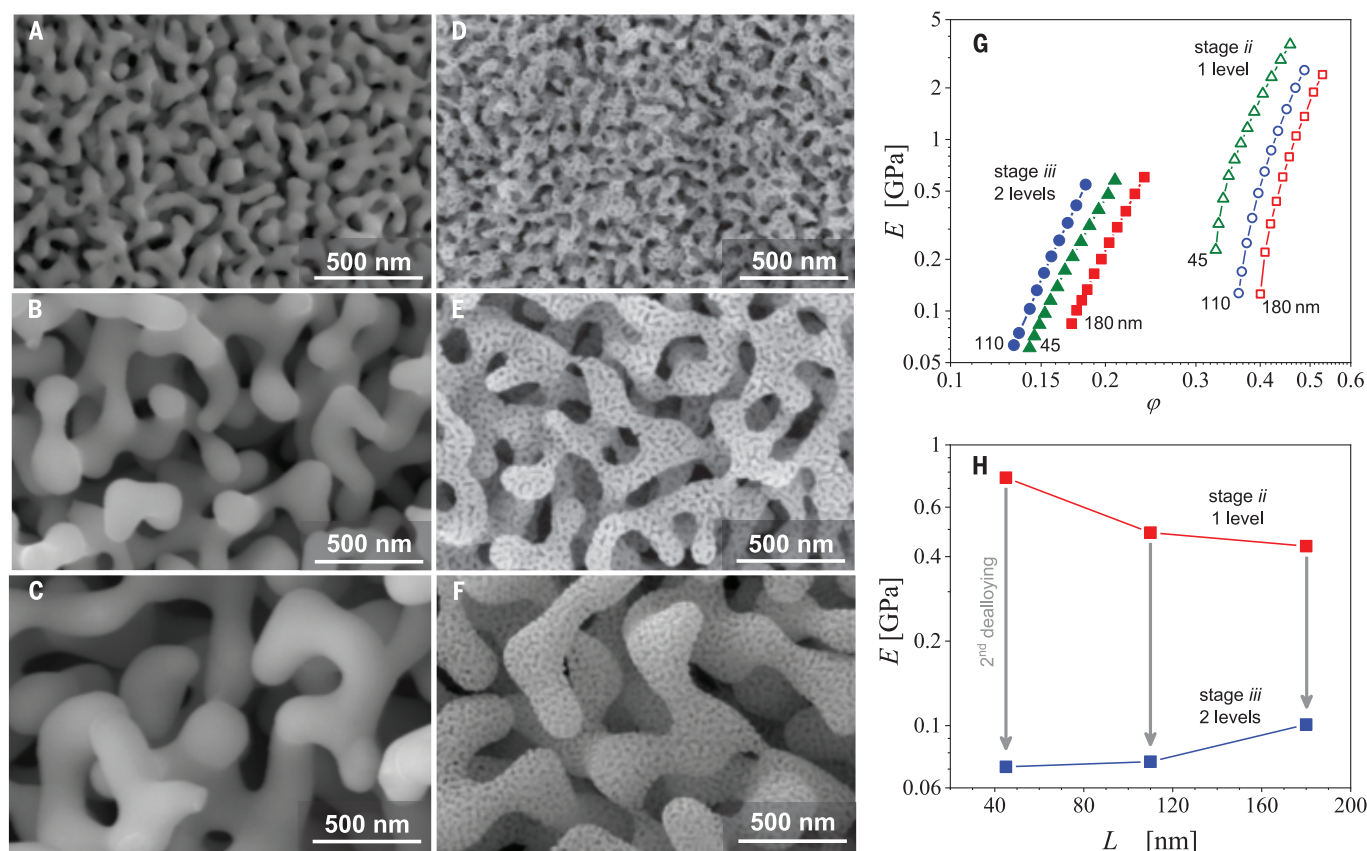


**Fig. 4. Size effects on the mechanical performance of N<sup>3</sup>PG.** (A to C) SEM images of stage ii (coarsened nanoporous Ag-Au) samples with different strut sizes: (A) 45 nm, (B) 110 nm, and (C) 180 nm. (D to F) SEM images of stage iii (N<sup>3</sup>PG) based on the samples in (A) to (C). Strut sizes are similar at the lower hierarchical level,  $L_1 = 15$  nm, but different strut sizes exist at the upper hierarchical level,  $L_2 = 45$  to 180 nm. (G) Log-log plot of effective Young's

modulus ( $E$ ) versus solid fraction ( $\phi$ ) for stage ii and stage iii samples as in (A) to (F). The value of  $L_2$  is indicated with labels. (H) Log-linear plot of  $E$  at 10% compressive strain versus  $L_2$  for samples from (G). The arrows denote the reduction in  $E$  between the two states. Relatively higher reduction occurs for smaller  $L_2$ , suggesting a size-dependent elasticity of the struts of the upper hierarchy level.

is one of the incentives for an interest in structural hierarchy as a pathway to load-bearing, low-density nanoscale network structures.

### Comparing the scaling laws with experiment

We compared the model predictions with the experiment, focusing first on the elasticity data (Fig. 3A). We reemphasize the agreement of the literature data for  $n = 1$  with the modified Roberts-Garboczi law, specifically including the trend toward a complete disintegration of the material at the percolation threshold (43). Our data show the hierarchical material as load bearing at densities far below that (single-level) percolation threshold (Fig. 3A). Thereby, its effective  $E$  is substantially above that of the nonhierarchical material. With  $n = 2$ , the scaling law of Eq. 4 overestimates the stiffness of the experimental hierarchical material. Yet the trend for the variation of stiffness with solid fraction is still well reproduced.

The agreement between the model and experiment is even better when it comes to the strength. For nonhierarchical NPG, the scaling law of Eq. 5 with  $n = 1$  is in excellent

agreement with the experiment. Furthermore, with  $n = 2$  the equation almost interpolates the experimental data for the N<sup>3</sup>PG. The strength of the hierarchical material is systematically and substantially above the scaling law for nonhierarchical NPG, and this observation is well reproduced by our Eq. 5.

Our model does overestimate the stiffness of the experimental hierarchical nanoscale network structures. One obvious conceivable reason is the model's assumption of identical  $\phi$  at each hierarchy level. The material of the experiment may have different  $\phi$  at its two hierarchy levels, so that its stiffness falls below the prediction. A second, more inherent aspect is that size effects may exist on the mechanical behavior at the upper hierarchy level.

### Size effect at upper hierarchical level

Size effects on the strength are well established for metal nanostructures in general (18) and in particular for the struts of NPG (25, 29–31, 47, 50), which are the elementary structural units at the lowest hierarchy level of our material. By contrast, in NPG the elastic

response at that level is essentially size independent (33). Systematic size effects in struts of the higher hierarchy levels of nested-network nanomaterials have not been considered in other experiments.

We started with stage i (as-dealloyed nanoporous Ag-Au) samples with  $76 \pm 2$  at % Ag and  $\phi = 0.31$  and prepared a series of stage ii samples with different  $L$  by annealing at temperatures between 300° and 500°C. We studied samples with  $L = 45$ , 110, and 180 nm (Fig. 4, A to C). Dealloying produced stage iii (N<sup>3</sup>PG) samples with  $L_1 \approx 15$  nm (Fig. 4, D to F). Consistent with our observation in Fig. 1, C and D,  $L_2$  retains the value of the underlying stage ii material.

We compression-tested two individual samples for each strut size using the same method as previously described. The results are highly consistent (figs. S5 to S7). We determined  $E$  versus  $\phi$  using the unload-and-reload segments (Fig. 2). For the stage ii samples, we found that  $E$  at any  $\phi$  systematically decreases with increasing  $L$  (Fig. 4G). As an intrinsic size dependence of the local effective elasticity of the



struts can be excluded, we can only explain this trend with a loss of connectivity during the coarsening process by which  $L$  is established. This phenomenon has been reported on the basis of experiment (32, 47) and confirmed by numerical simulation (42). Samples with large  $L$  made by coarsening are thus expected to have lesser strength and stiffness than as-prepared ones, and the scaling laws based on Eq. 3 will not automatically hold for such samples. Because the second dealloying, leading from stage ii to stage iii, is not expected to substantially change the connectivity at the upper hierarchy level, we expect that the individual stage iii hierarchical samples show different connectivity at their upper hierarchy level, depending on  $L_2$ . This provides for an implicit dependence of the mechanical behavior on the size at the upper hierarchy level.

A second aspect of size dependence emerges from inspection of the data for the stage iii samples (Fig. 4G). Those data do not reflect the size dependence of stage ii one-to-one. Instead, at a given value of  $\phi$ , the  $L_2 = 45$  nm sample is more compliant than the  $L_2 = 110$  nm one. Comparing the stiffness values that we computed from the unload-and-reload segments after  $\sim 10\%$  strain in the two stages (Fig. 4H) shows that the second dealloying leads to systematically more reduction in  $E$  at smaller  $L_2$ . Within the notion that the network connectivity at the upper hierarchy level remains invariant when the lower-level network is generated by the second dealloying, the size-dependent reduction of  $E$  implies a size-dependent local value of  $E$  of the upper-hierarchy-level struts. This observation is not unreasonable, because the “dangling” lower-level struts that end at the surface of upper-level struts can bear no load. This effectively reduces the connectivity of the network at the lower hierarchy level, thereby reducing the stiffness.

### Microstructure evolution during deformation

We performed MD simulations of the compression behavior of a computer-generated sample. The microstructural model at each of the two hierarchy levels is based on the leveled-wave model (43), which has been shown to reproduce  $E(\phi)$  of as-prepared NPG with high precision. We choose  $L_2 = 22.6$  nm,  $L_1 = 3.0$  nm, and initial  $\phi = 0.125$  (44). The ratio  $L_2/L_1 = 7.5$  of the model approximates that (7.3) of the samples underlying Fig. 2. Experimental stress-strain data of a sample with similar ratio and initial solid fraction ( $\phi = 0.119$ ) are included for comparison (Fig. 5). The simulation and experiment agree with regard to an early onset of plastic yielding, an extended elastic-plastic transition, and a subsequent pronounced strain hardening (Fig. 5, A and B). We plotted stiffness and strength derived from the two data sets against solid

fraction (Fig. 5, C and D). Our experiments and simulations are quite consistent and validate our hypothesis that the experimental observations are intrinsically related to the hierarchical structure of the material.

The comparison between cross sections of virtual samples in the plane containing the load axis at strain  $\varepsilon = 0$  and 0.29 (Fig. 5A, thick arrows) suggests that the compression is carried predominantly by densification at the upper hierarchy level, whereas the density at the lower hierarchy level varies little. New contacts are formed upon compression between the struts of the upper hierarchy level (Fig. 5A, thin arrows, and fig. S8). For comparison, we inspect the cross-sectional SEM image of an experimental sample deformed to 55% compressive strain (Fig. 5B). In agreement with the simulation, the SEM image shows that the upper-level struts have been squeezed closer together, whereas at the lower hierarchy level, their internal microstructure remains consistent with that of the undeformed samples.

As a signature of the deformation at the individual hierarchy levels, we investigated

the small-angle interference function,  $S$ , of the MD-generated model microstructure in various stages of deformation. For the non-deformed microstructure, the graphs of the orientation-averaged (over the full solid angle in reciprocal space)  $S(q)$  are dominated by two sharp maxima at the  $q$  values of the wave fields used in generating the initial microstructure (Fig. 6A) (here,  $q$  denotes the magnitude of the scattering vector). The peak positions measure a mean spacing,  $\bar{L}$ , between neighboring struts of the leveled-wave microstructure as  $\bar{L} = 1.23 \times 2\pi/q$  (43). As the deformation proceeds, the peak at  $q = 1.2 \text{ nm}^{-1}$ , representative of the lower hierarchy level, broadens but retains its position. This emphasizes that  $\bar{L}$  at that level is conserved, in keeping with the notion (suggested by the real-space structure of the deformed samples) that the lower hierarchy level does not substantially densify (Fig. 5B and fig. S8). The evolution of the peak at  $q = 0.20 \text{ nm}^{-1}$ , which represents the upper hierarchy level, can be more clearly followed by inspection of direction-resolved interference functions. We computed  $S$  separately in the direction of the load axis and in

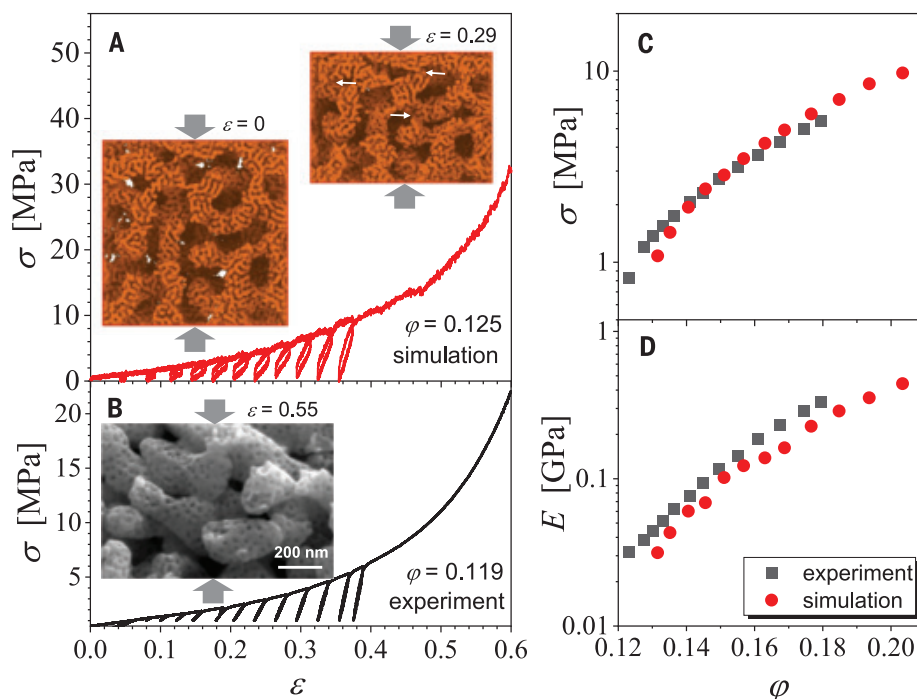


**Fig. 5. Comparing experiment and MD simulation of deformation.** (A) Compressive engineering stress-strain ( $\sigma$ – $\varepsilon$ ) curves by MD simulation. (Insets) Microstructure graphs of numerical sample, as relaxed (bottom) and after 29% compression (top). Thick arrows, compression axis; thin arrows, contacts formed during compression. Two well-defined strut sizes are retained. New contacts are formed exclusively at the upper hierarchy level. (B) Compressive stress-strain curves by experiment. (Inset) SEM image of cleavage surface (containing the load axis; arrows) of an experimental sample after 55% compressive strain. Despite high deformation, the two well-defined strut sizes and the high porosity at the lower hierarchy level are retained. (C and D) Evolution of flow stress ( $\sigma$ ) and effective Young's modulus ( $E$ ) versus solid fraction ( $\phi$ ). Data for simulation (red circles) and experiment (black squares) in (C) and (D) are derived from (A) and (B).

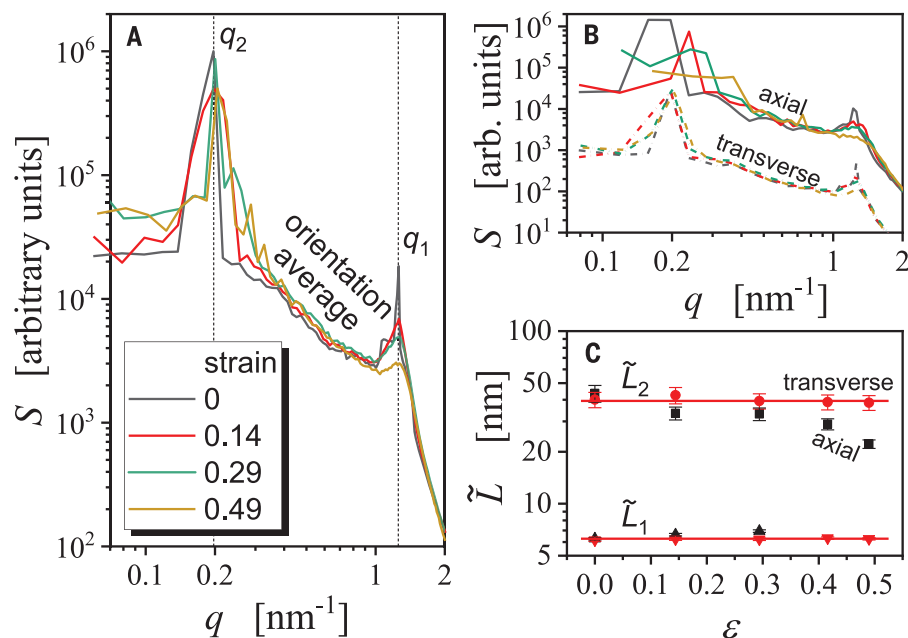


**Fig. 6. Variation of small-angle interference function during deformation.** (A) Log-log plot of orientation-averaged interference function,  $S$ , per atom versus wave vector magnitude,  $q$ , for the numerical model structure, unloaded after various engineering strains (legend). Dashed lines:  $q$  values of the wave fields generating the network structures of the two hierarchy levels. (B) Log-log plot of  $S(q)$ , here for  $\pm 15^\circ$  sector-averaged  $S$  in the direction of the load axis (axial) and in the plane normal to that axis (transverse). Graphs for transverse have been displaced vertically for clarity of presentation. (C) Log-linear plot of characteristic distance ( $\tilde{L}$ ) between neighboring struts as estimated from peak positions in (B). The distances are shown separately for the lower ( $\tilde{L}_1$ ) and upper ( $\tilde{L}_2$ ) hierarchy levels and for the axial and transverse directions. Error bars,  $q$ -resolution of the Fourier series underlying the computation of  $S$ . Strong compression occurs in the axial direction at the upper hierarchy level.

the plane transverse to that axis (Fig. 6B). As the strain increases, the transverse peak remains stationary, whereas the axial one shifts to higher values.

We evaluated  $\tilde{L}$  from the peak positions separately for each level and for each direction (Fig. 6C). All strut spacings are essentially conserved during the deformation, with the notable exception of the axial spacing at the upper hierarchy level. That latter spacing decreases from originally 40 to 22 nm at a compressive engineering strain of 0.49. In other words, the direction-resolved interference functions confirm that the densification is predominantly carried by densification at the upper hierarchy level.

The observation of densification predominantly at the upper hierarchy level reflects the level-dependent loading modes. At the uppermost level, the external load implies uniaxial compression, favoring densification at that level. By contrast, in random networks the struts that contain and form the lower hierarchy levels experience multiaxial loading states with a substantial bending component. Finite-element simulation for random networks similar to NPG supports plastic deformation predominantly in bending (51, 52). Contrary to

uniaxial compression, bending does not require densification. This observation is consistent with the low densification at the lower hierarchy level. Our considerations thus suggest that densification predominantly at the upper hierarchy level may be generic for hierarchical network structures loaded in compression. Observations on plastically deformed 2D hierarchical networks (53) appear consistent with that notion.

The upper-hierarchy-level struts of  $N^3PG$  appear to support ductile plastic bending, whereas NPG is typically brittle when loaded in bending (26). Observations of a tensile brittle-to-ductile transition in NPG as the ratio  $R$  of ligament size to sample size increases to  $R \gg 10^{-4}$  (54, 55) suggest an explanation. Because  $L_2/L_1$  is  $\sim 10$  in our samples, the  $R$  value of their upper-hierarchy-level struts is on the order of 0.1, large enough for ductile behavior.

### Summary

We explored the mechanical behavior of nanoscale network materials that are distinguished by a hierarchical structure with self-similar geometry on two distinct length scales. The macroscopic samples, made by dealloying,

contained on the order of  $10^{12}$  struts, orders of magnitude more than architected network structures. We suggest that structural hierarchy mitigates the loss in connectivity that can be inherent in nanoscale self-organization processes forming network nanomaterials. Indeed, for a given solid fraction, the stiffness and strength of our hierarchical materials were systematically enhanced as compared with materials with geometrically similar structure but only a single characteristic length scale. Our atomistic numerical simulations support the experiment. Furthermore, we derived scaling laws for the mechanical behavior that embody the impact of hierarchy and that reproduce the experimental trends.

Our findings suggest that, in spite of the self-similarity of the microstructure, the loading modes and the deformation behavior may generally differ between the individual hierarchy levels. The strength of our material is enhanced by its nanoscale struts at the lower hierarchy level, which exploit the established size-dependent strengthening of nanostructures. The data also indicate a size dependence of the mechanics of the upper-hierarchy-level struts.

Structural hierarchy can enhance the functional behavior of materials, specifically when it comes to transport phenomena. Our experiments advertise a class of model material for such behavior, and they show that the mechanical properties, which need to be understood irrespective of the material's role as a functional or structural material, are open to informed discussion. Although our experiments used dealloyed Au as the model material, current research generalizes dealloying to lighter, stronger, and less costly metals. This suggests that the approach established in our work offers opportunities for future lightweight nanomaterials with enhanced mechanical behavior at low solid fraction.

### REFERENCES AND NOTES

1. C. D. Murray, *Proc. Natl. Acad. Sci. U.S.A.* **12**, 207–214 (1926).
2. D. R. Emerson, K. Cieřlicki, X. Gu, R. W. Barber, *Lab Chip* **6**, 447–454 (2006).
3. P. Trogadas, V. Ramani, P. Strasser, T. F. Fuller, M. O. Coppens, *Angew. Chem. Int. Ed.* **55**, 122–148 (2016).
4. J. Y. Suen, S. Navlakha, *J. R. Soc. Interface* **16**, 20190041 (2019).
5. S. Weiner, H. D. Wagner, *Annu. Rev. Mater. Sci.* **28**, 271–298 (1998).
6. H. Gao, *Int. J. Fract.* **138**, 101–137 (2006).
7. P. Fratzl, R. Weinkamer, *Prog. Mater. Sci.* **52**, 1263–1334 (2007).
8. H. D. Espinosa, J. E. Rim, F. Barthelat, M. J. Buehler, *Prog. Mater. Sci.* **54**, 1059–1100 (2009).
9. E. D. Yilmaz, G. A. Schneider, M. V. Swain, *Philos. Trans. R. Soc. A* **373**, 20140130 (2015).
10. R. Lakes, *Nature* **361**, 511–515 (1993).
11. T. A. Schaedler et al., *Science* **334**, 962–965 (2011).
12. D. Jang, L. R. Meza, F. Greer, J. R. Greer, *Nat. Mater.* **12**, 893–898 (2013).
13. L. R. Meza et al., *Proc. Natl. Acad. Sci. U.S.A.* **112**, 11502–11507 (2015).
14. X. Zheng et al., *Nat. Mater.* **15**, 1100–1106 (2016).
15. J. T. Muth, P. G. Dixon, L. Woish, L. J. Gibson, J. A. Lewis, *Proc. Natl. Acad. Sci. U.S.A.* **114**, 1832–1837 (2017).
16. J. Bauer et al., *Adv. Mater.* **29**, 1701850 (2017).
17. J. R. Greer, V. S. Deshpande, *MRS Bull.* **44**, 750–757 (2019).



18. J. R. Greer, J. T. M. De Hosson, *Prog. Mater. Sci.* **56**, 654–724 (2011).
19. J. J. do Rosário et al., *Adv. Eng. Mater.* **17**, 1420–1424 (2015).
20. A. E. Garcia et al., *Nanoscale Adv.* **1**, 3870–3882 (2019).
21. C. M. Portela et al., *Proc. Natl. Acad. Sci. U.S.A.* **117**, 5686–5693 (2020).
22. X. Y. Yang et al., *Chem. Soc. Rev.* **46**, 481–558 (2017).
23. T. Juárez, J. Biener, J. Weissmüller, A. M. Hodge, *Adv. Eng. Mater.* **19**, 1700389 (2017).
24. J. Erlebacher, M. J. Aziz, A. Karma, N. Dimitrov, K. Sieradzki, *Nature* **410**, 450–453 (2001).
25. H. J. Jin et al., *Acta Mater.* **57**, 2665–2672 (2009).
26. K. Wang et al., *NPG Asia Mater.* **7**, e187 (2015).
27. S. Sun, X. Chen, N. Badwe, K. Sieradzki, *Nat. Mater.* **14**, 894–898 (2015).
28. H. J. Jin et al., *Nano Lett.* **10**, 187–194 (2010).
29. J. Biener et al., *Nano Lett.* **6**, 2379–2382 (2006).
30. C. Volkert, E. Lilleodden, D. Kramer, J. Weissmüller, *Appl. Phys. Lett.* **89**, 061920 (2006).
31. N. J. Briot, T. J. Balk, *Philos. Mag.* **95**, 2955–2973 (2015).
32. N. Mameka, K. Wang, J. Markmann, E. Lilleodden, J. Weissmüller, *Mater. Res. Lett.* **4**, 27–36 (2016).
33. H. J. Jin, J. Weissmüller, D. Farkas, *MRS Bull.* **43**, 35–42 (2018).
34. M. Tsuda, T. Wada, H. Kato, *J. Appl. Phys.* **114**, 113503 (2013).
35. I. V. Okulov et al., *Nano Res.* **11**, 6428–6435 (2018).
36. J. S. Corsi et al., *ACS Sustain. Chem. Eng.* **7**, 11194–11204 (2019).
37. S. H. Joo et al., *Adv. Mater.* **32**, e1906160 (2020).
38. Y. Ding, J. Erlebacher, *J. Am. Chem. Soc.* **125**, 7772–7773 (2003).
39. Z. Qi, J. Weissmüller, *ACS Nano* **7**, 5948–5954 (2013).
40. C. Wang, Q. Chen, *Chem. Mater.* **30**, 3894–3900 (2018).
41. J. Erlebacher, *Phys. Rev. Lett.* **106**, 225504 (2011).
42. Y. Li, B. N. D. Ngò, J. Markmann, J. Weissmüller, *Phys. Rev. Mater.* **3**, 076001 (2019).
43. C. Soyarslan, S. Bargmann, M. Pradas, J. Weissmüller, *Acta Mater.* **149**, 326–340 (2018).
44. Materials and methods are available as supplementary materials.
45. C. Alonso, R. C. Salvarezza, J. Vara, A. J. Arvia, *Electrochim. Acta* **35**, 1331–1336 (1990).
46. D. Artymowicz, J. Erlebacher, R. Newman, *Philos. Mag.* **89**, 1663–1693 (2009).
47. L. Z. Liu, X. L. Ye, H. J. Jin, *Acta Mater.* **118**, 77–87 (2016).
48. L. J. Gibson, M. F. Ashby, *Cellular Solids: Structure and Properties* (Cambridge Univ. Press, 1999).
49. Y. H. Xiang, L. Z. Liu, J. C. Shao, H. J. Jin, *Acta Mater.* **186**, 105–115 (2020).
50. A. Hodge et al., *Acta Mater.* **55**, 1343–1349 (2007).
51. N. Huber, R. N. Viswanath, N. Mameka, J. Markmann, J. Weissmüller, *Acta Mater.* **67**, 252–265 (2014).
52. M. T. Hsieh, B. Endo, Y. Zhang, J. Bauer, L. Valdevit, *J. Mech. Phys. Solids* **125**, 401–419 (2019).
53. D. Mousanezhad et al., *Sci. Rep.* **5**, 18306 (2015).
54. R. Li, K. Sieradzki, *Phys. Rev. Lett.* **68**, 1168–1171 (1992).
55. N. Badwe, X. Chen, K. Sieradzki, *Acta Mater.* **129**, 251–258 (2017).

## ACKNOWLEDGMENTS

**Funding:** This work was supported by Deutsche Forschungsgemeinschaft (Projektnummer 192346071 – SFB 986). The authors gratefully acknowledge U. Dette for her assistance with sample preparation. **Author contributions:** S.S. and J.W. designed the experiments and the theory. S.S. performed the experiments. Y.L. performed the simulation. All authors participated in analysis, discussion, and manuscript writing. **Competing interests:** The authors declare no competing interests. **Data and materials availability:** All data needed to evaluate the conclusions in the paper are presented in the main text or the supplementary materials.

## SUPPLEMENTARY MATERIALS

science.sciencemag.org/content/371/6533/1026/suppl/DC1  
Materials and Methods  
Supplementary Text  
Figs. S1 to S10  
Tables S1 to S3  
References (56–74)

21 July 2020; accepted 25 January 2021  
10.1126/science.abd9391

## REPORTS

### MICROBIOLOGY

# Redox-active antibiotics enhance phosphorus bioavailability

Darcy L. McRose<sup>1,2</sup> and Dianne K. Newman<sup>1,2\*</sup>

Microbial production of antibiotics is common, but our understanding of their roles in the environment is limited. In this study, we explore long-standing observations that microbes increase the production of redox-active antibiotics under phosphorus limitation. The availability of phosphorus, a nutrient required by all life on Earth and essential for agriculture, can be controlled by adsorption to and release from iron minerals by means of redox cycling. Using phenazine antibiotic production by pseudomonads as a case study, we show that phenazines are regulated by phosphorus, solubilize phosphorus through reductive dissolution of iron oxides in the lab and field, and increase phosphorus-limited microbial growth. Phenazines are just one of many examples of phosphorus-regulated antibiotics. Our work suggests a widespread but previously unappreciated role for redox-active antibiotics in phosphorus acquisition and cycling.

A vast number of secondary metabolites are produced by microbes in nature. Despite the growing recognition of their importance for microbial survival (*1–3*), most of their functions and regulatory logic are poorly understood. Although examples of their roles in signaling, energy conservation, and metal complexation have been reported (*1–3*), these molecules are conventionally assumed to be involved in microbial competition. That, alternatively, some might facilitate acquisition of a macronutrient such as phosphorus (P)—and that this is a regulated function—has not been considered.

Several bacterial species increase production of secondary metabolites (*4, 5*) in response to limitation for the essential nutrient P. Many of these metabolites are considered to be antibiotics, and their toxicity is conferred by a variety of mechanisms, including the ability to engage in redox reactions. P regulation of secondary metabolite production has been studied extensively in *Actinobacteria* but also occurs in *Proteobacteria* and *Firmicutes* (Fig. 1A). The reason for this regulation is not totally understood, but changes in cell metabolism under slow growth and nutrient stress, as well as a broad phosphate starvation-induced virulence response, have been suggested (*5, 6*). An alternative, unexplored explanation is that under P limitation, rather than having toxic roles, the redox activity of some of these antibiotics might directly facilitate P acquisition (Fig. 1B).

P availability affects global primary productivity in natural and agricultural systems (*7–10*). Many biological mechanisms for P solubilization by bacteria and plants [in particular the secretion of phosphatases, and organic acids (*11, 12*)] have been well studied. However, despite the important effects of microbial reduction of iron (Fe) oxides on P mobility (*7, 8, 13, 14*), the potential genetically regulated use of microbial redox-active secondary metabolites as a strategy for P solubilization remains mostly unexplored. Phosphate and organic P are often immobilized through adsorption to positively charged surface sites on Fe(III)-(oxy)hydroxide minerals and subsequently solubilized by microbial reduction of Fe(III) to Fe(II) under anoxic conditions (*7, 13–15*). Fe reduction by metabolites such as flavins (which are not known to be regulated by P) has been well studied (*16*). However, the primary purpose of these metabolites is thought to be respiration of Fe minerals, and any accompanying benefit from P solubilization has either been neglected or considered perfunctory.

On the basis of the precedent for P release through reductive dissolution of Fe oxides, we wondered whether some antibiotics with redox activity might have a previously unappreciated role in this process, thus reconciling their stimulation by P limitation (Fig. 1, A and B). We set out to quantify the stimulation of redox-active antibiotic production under P limitation and examine the resulting enhancement in P availability and microbial growth. Specifically, we sought to test the following hypotheses: (i) redox-active antibiotic biosynthesis is regulated by P availability in many organisms and occurs via a conserved molecular pathway, (ii) the reductive dissolution

<sup>1</sup>Division of Biology and Biological Engineering, California Institute of Technology, Pasadena, CA 91125, USA. <sup>2</sup>Division of Geological and Planetary Sciences, California Institute of Technology, Pasadena, CA 91125, USA.

\*Corresponding author. Email: dkn@caltech.edu

of Fe minerals by these metabolites results in the solubilization of adsorbed P, and (iii) the net result is increased P availability in lab cultures and natural microbial communities under P limitation.

We focused on phenazines (Figs. 1, A and B, and 2), a class of secondary metabolites with well-understood redox properties (17) that are made by several pseudomonads as well as many other types of bacteria and that confer

a variety of physiological benefits to the producing organism (3, 18). P limitation was linked to phenazine production in batch culture studies of *Pseudomonas aeruginosa* as early as 1947 (19), but whether this is widespread in pseudomonads has been unclear. Additionally, when studied in batch culture, secondary metabolites are typically produced at the end of growth because of a complex combination of nutrient exhaustion as well as the accumulation of quorum-sensing (QS) molecules, which regulate the biosynthesis of many secondary metabolites, including phenazines (20).

Chemostats provide a more controlled experimental setup than batch culture, allowing for precise tuning of both growth rate and cell density, thereby allowing specific variables to be tracked. We designed a growth medium that maintains low cell densities [optical density at 500 nm ( $OD_{500}$ ) ~0.1] based on limitation for either nitrogen or P and quantified phenazine production under these conditions in *P. aeruginosa*, *P. aureofaciens*, *P. chlororaphis*, and *P. fluorescens*. We found that in all four *Pseudomonas* species tested, chemostats limited for P had much higher phenazine concentrations than those limited for nitrogen, ranging between one and three orders of magnitude (Fig. 2A). In *P. aeruginosa*, slow growth rates also correlated with greater phenazine production (Fig. 2A and fig. S1), an observation that has been made by others (4, 21) and that could entail a secondary regulatory mechanism. These results are consistent with previous chemostat experiments in *P. aeruginosa* (21), as well as batch culture findings (4, 19, 20, 22), and show widespread enhancement of phenazine production under P limitation in pseudomonads.

In many bacteria, genes related to P acquisition are part of the phosphate (PHO) regulon, which is controlled by a two-component regulatory system comprising an inner-membrane histidine kinase (PhoR) and a cytoplasmic response regulator (PhoB) that controls transcription by binding to conserved regulatory “PHO boxes” [Fig. 2C and (6)]. To test whether PhoB regulation might explain the trends seen in our *Pseudomonas* chemostat experiments, we constructed unmarked deletions of the *phoB* gene in *P. fluorescens* and *P. chlororaphis*. In both cases, the deletion of *phoB* abolished phenazine production in P-limited chemostats, and complementation of *phoB* restored production (Fig. 2D). These results are supported by previous findings that a *P. aeruginosa phoB* mutant produces less of the phenazine pyocyanin under P limitation as well as in silico predictions of putative PHO boxes upstream of phenazine biosynthetic genes and QS genes (23). When considered with prior studies [Fig. 1A, table S1, and (24)], our findings suggest that PhoB

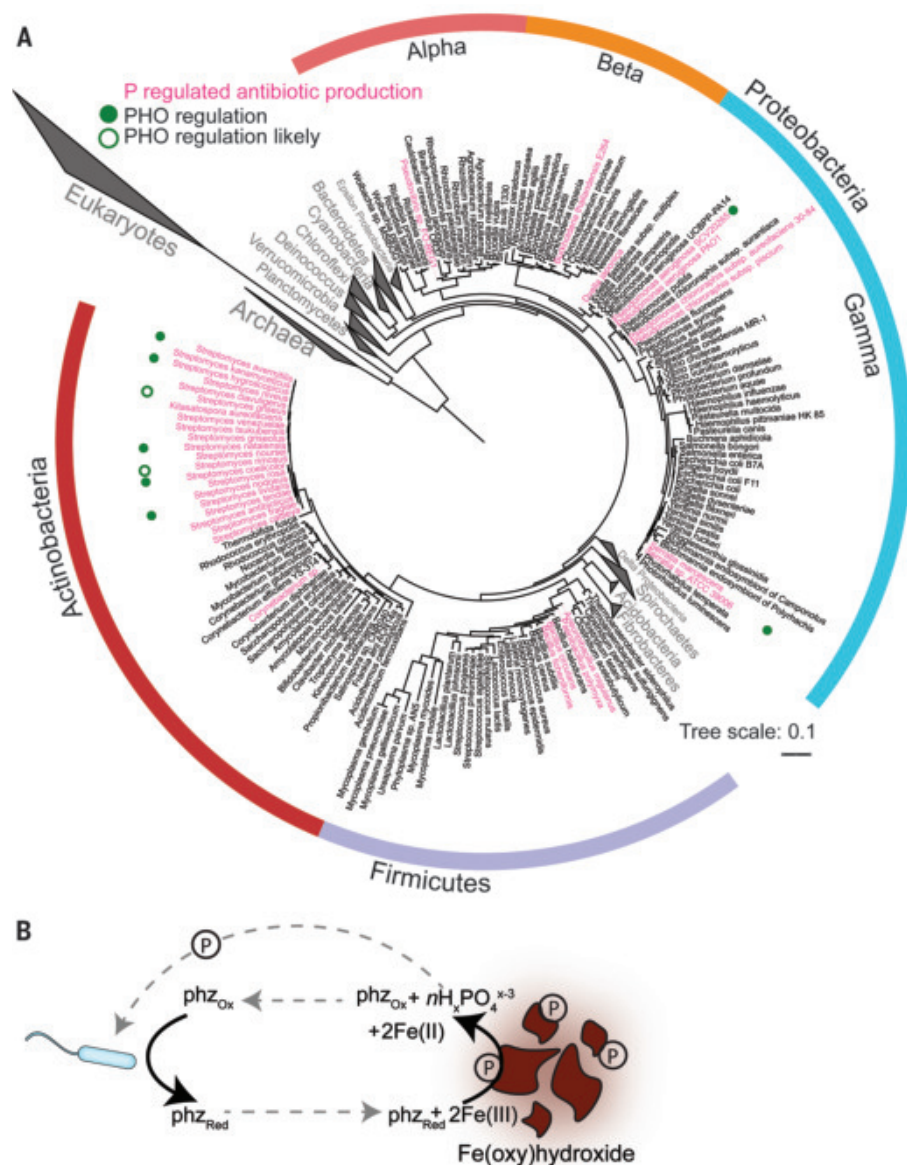


**Fig. 1. P regulates the production of antibiotics in diverse bacteria.** (A) Tree depicts species with experimental evidence for P-limited antibiotic production (pink text) and experimentally confirmed (solid green circle) or likely (open green circle) regulation by *phoB*/P and *phoR*. Data are largely from (5) and (6) (table S1). Metabolite production in *Burkholderia thailandensis* and *Serratia* ATCC39006 was tested by using chemostats (fig. S1). The tree was built from 242 small subunit ribosomal RNA sequences by using RaxML (33) and is rooted for display. Bacterial phyla containing organisms with evidence for P-limited antibiotic production are denoted in color on the outside ring; other groups are collapsed in gray triangles. (B) Model for how P-regulated redox-active antibiotic production could increase P bioavailability using phenazines as an example. Under P limitation, pseudomonads release phenazines that reduce Fe-oxides (at a distance; transport indicated by dashed line) and liberate P through reductive dissolution. Solubilized P is then taken up by the cell, alleviating P limitation. Oxidized phenazines can be re-reduced by cells, allowing for a single phenazine to be cycled multiple times. The reaction of phenazine with Fe(III) is a two-electron transfer that yields 2Fe(II) (17). Solubilized P (which is most commonly phosphate but could also be organic P) is variable (indicated by *n*) depending on the extent of P surface coordination as dictated by P concentration, mineral composition, and pH (29). *phz*<sub>Ox</sub>, oxidized phenazine; *phz*<sub>Red</sub>, reduced phenazine.



**Fig. 2. Phenazine production in different pseudomonads is regulated by phosphate through *phoB*.**

(A) Phenazine production in phosphorus- (P, blue) or nitrogen- (N, yellow) limited *Pseudomonas* chemostats. The phenazines produced are PCA (phenazine-1-carboxylic-acid), PCN (phenazine-1-carboxamide), and PYO (pyocyanin). ODs were maintained at ~0.1; the range of ODs across chemostats for each experiment  $\pm$  SD is listed. Data shown are for a single replicate, and duplicate experimental data are shown in fig. S1.

(B) Phenazine structures. (C) *PhoB* is thought to increase phenazine production by binding predicted PHO boxes upstream of phenazine biosynthetic (*phz* biosyn.) genes and QS genes (21, 23). (D) Phenazine production in *Pseudomonas* wild type (pink), *phoB* mutant (black), and complemented (comp; red) strains ( $\mu = 0.06$  for *P. chlororaphis* and 0.03 for *P. fluorescens*). Trends were maintained across growth rates, and the data displayed were chosen to best match the ODs across strains. The reported growth rate ( $\mu$ ) is the dilution rate; the two are equivalent at steady state.  $A_{364\text{ nm}}$ , absorbance at 364 nm; AU, arbitrary units; nd, not detected; OD, optical density at 500 nm; R, various phenazine modifications; WT, wild type.

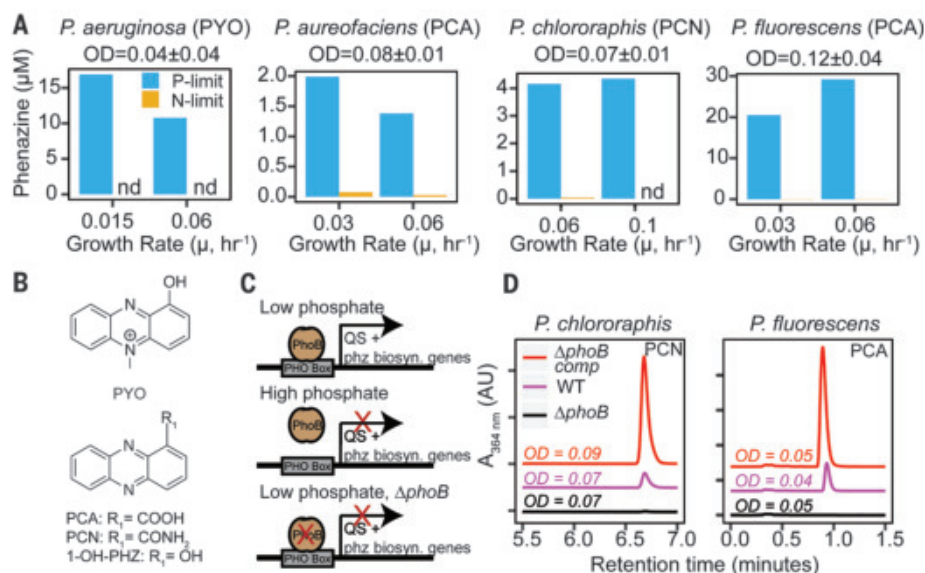
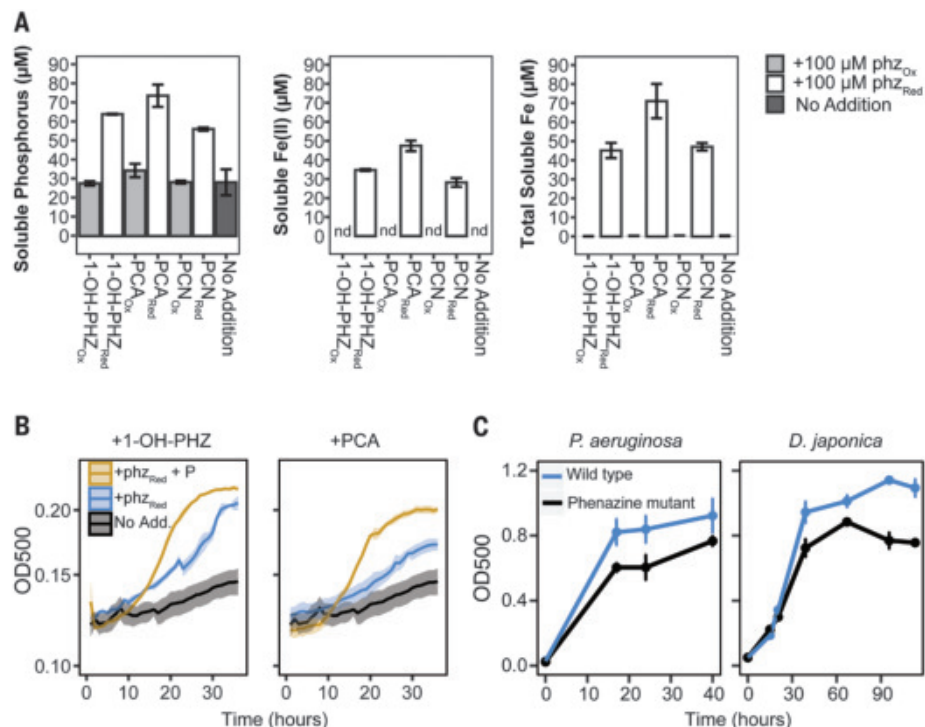


**Fig. 3. Phenazines solubilize P and promote microbial growth on HFO-P. (A)** Results of reactions between HFO-P and phenazines: total soluble P [inductively coupled plasma mass spectrometry (ICP-MS)], Fe(II) (ferrozine assay), and total soluble Fe (ICP-MS). Error bars represent the standard deviations for duplicates. See fig. S3 for details on P adsorption. Measurements were made after 5 hours of incubation and are not expected to reflect reaction stoichiometry because of secondary mineral formation from Fe(II) back-reactions with Fe(III)-oxides.

(B) Growth (as a denitrifier) of a *P. aeruginosa* mutant unable to make phenazines on HFO-P. Additions: 100  $\mu$ M (reduced phenazine) and 7 mM (phosphate). The shaded area represents the data range for biological duplicates. No-addition data are the same for both plots. No Add., no addition.

(C) Growth of wild-type and phenazine-null strains of *P. aeruginosa* and *D. japonica* on HFO-P. Cultures were grown aerobically and periodically allowed to sit statically, permitting oxygen drawdown by respiration (see materials and methods and fig. S2). Error bars represent standard deviations for triplicate (*P. aeruginosa*) or quadruplicate (*D. japonica*) cultures. For *D. japonica*, ODs at the initial time point represent the calculated inoculum rather than a measurement.



regulation of secondary metabolite production is conserved not only in pseudomonads but also across diverse species.

Phenazines are known to reduce Fe minerals (17), but the potential effects of this process on P solubilization have not been investigated. To test whether phenazines

could solubilize phosphate through reductive dissolution, phenazines were added to synthetic phosphated hydrous ferric oxides (here HFO-P), and the release of phosphate (as elemental P), Fe(II), and total Fe was tracked. Reduced 1-hydroxy-phenazine (1-OH-PHZ), phenazine-1-carboxamide (PCN), and phenazine-

1-carboxylic acid (PCA) increased the soluble P concentrations relative to controls, whereas the oxidized forms of these phenazines did not (Fig. 3A). In addition, Fe(II) was only produced in incubations with reduced phenazines (Fig. 3A), consistent with HFO-P reductive dissolution, a mechanism that has been well

**Fig. 4. Phenazines solubilize P in marine**

**sediments. (A)** Nitric acid–extractable iron and P from sampling sites. Error bars, SDs from triplicate digestions.

**(B to D)** P solubilization in Catalina Island sediments from site 1 collected in August (B) and site 2

collected in August (C) or October (D). y axes in (B) to (D) reflect the difference in total soluble P (ICP-MS) from the

initial time point, and horizontal lines depict no change. See also figs. S4 and S5. St., site; TO, initial time point. **(E)** PCA

reduction is suppressed in sediments treated with ethanol (EtOH). **(F)** PCA

reduction is stimulated by organic carbon (10 mM glucose + 10 mM lactate). Sediments in (F) were starved before

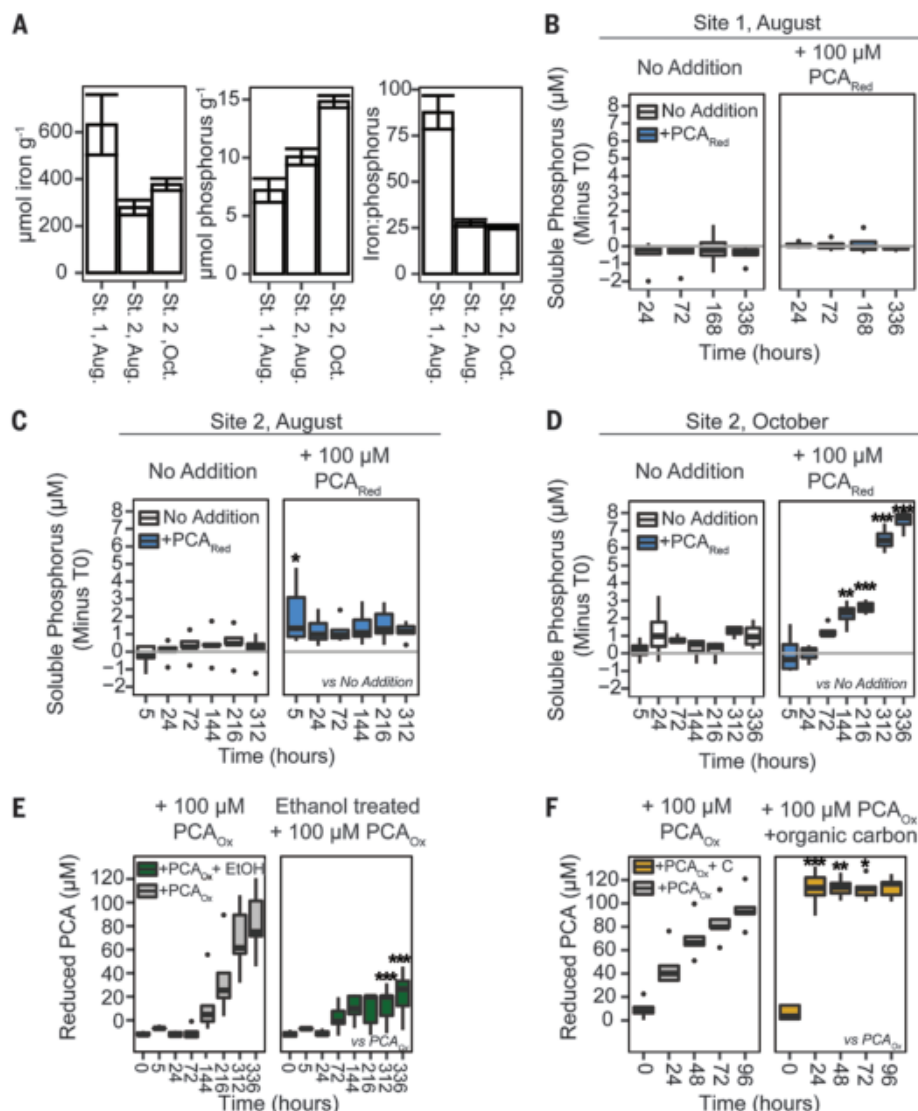
PCA additions and cannot be compared directly with (E). For (B) to (F), box and whisker plots reflect data from four or

five replicates, with data points that are >1.5 times interquartile range represented as single black dots; *P* values (as

determined by analysis of variance; see materials and methods) reflect comparison with the control treatment as

indicated on the figure [for (B), (C), and (D), no addition; for (E) and (F), oxidized PCA] at a specific time point.

\**P* < 0.05, \*\**P* < 0.005, \*\*\**P* < 0.0001.



established as an important control on environmental P availability (14).

To examine whether phenazines would stimulate microbial growth of P-limited cultures on HFO-P, we focused on 1-OH-PHZ and PCA because these phenazines are the most reactive with Fe oxides and are made by soil- and sediment-dwelling pseudomonads (17, 25, 26). A *P. aeruginosa* mutant that cannot make phenazines was cultured under Fe-replete conditions with HFO-P as the sole P source. To avoid the oxidation of phenazines by oxygen and to provide an alternative electron acceptor, cells were grown anaerobically with nitrate. The addition of either reduced PCA or reduced 1-OH-PHZ increased growth (Fig. 3B). A further increase in growth was observed upon the addition of P in the presence of phenazines (Fig. 3B), validating P limitation under these conditions. These results establish that reduced phenazines stimulate P-limited cultures in the presence of HFO-P,

demonstrating their ability to increase the bioavailability of P (and possibly Fe) from the particulate phase.

We next tested whether endogenous phenazine production could provide the same benefit by comparing the growth of wild-type phenazine producers to that of phenazine null mutants. To simulate transient anoxic events that may occur in sediments or periodically flooded soils, where P-regulated antibiotic production is most likely to be relevant, cells were grown aerobically and allowed to draw down oxygen by sitting statically for 1 hour at each time point. To broaden the taxonomic diversity of our study, we also conducted experiments with the xanthomonad *Dyella japonica*, a phenazine producer that is abundant in crop rhizospheres and makes phenazines in response to P limitation (27). When grown on HFO-P, both wild-type *P. aeruginosa* and *D. japonica* achieved higher yields than mutant strains (Fig. 3C). Notably,

*D. japonica* growth and phenazine production were highly sensitive to the starting conditions (see materials and methods and fig. S2). Growth on HFO-P with excess (1 mM) phosphate led to increased yields of the wild type and mutants in both *P. aeruginosa* and *D. japonica* (fig. S2), verifying P limitation. Fe(II) accumulated in the supernatants of *D. japonica* cultures (fig. S2), consistent with our hypothesis that P is being solubilized by a reductive dissolution mechanism. These results show that under P limitation, endogenous phenazine production can provide a growth benefit.

To determine whether phenazines could solubilize P in natural systems where the chemistry is more complex than the synthetic HFO-P used in the laboratory, we conducted anaerobic incubations of phenazines with soils (site 1, August 2019) and sediments (site 2, August and October 2019) collected from Catalina Harbor on Catalina Island, CA, a



location where pseudomonads have been previously isolated (28). Sediments represent an important test case for our experiments because reductive dissolution (as mediated by Fe-reducing bacteria, often by means of flavins) has been especially well studied in sediments and is a known control on P mobility in these systems (14). Our experiments showed a variety of P-solubilization responses to phenazine additions (Fig. 4), ranging from no change to significant increases. These differences were correlated with variations in the Fe/P ratios of soil or sediments, highlighting the importance of Fe in controlling P availability, even in locations with relatively high bulk P concentrations. The experiments from site 1, which had a very high Fe/P ratio of ~88 (Fig. 4A), showed little response to phenazine additions (Fig. 4B). Oxidation of a large fraction of added PCA by Fe at P-free mineral surface sites and readsorption of solubilized P could explain these muted effects. By contrast, at site 2, where the Fe/P ratio was substantially lower (~26) (Fig. 4A), reduced PCA significantly increased the total soluble P in two separate experiments but with very different temporal dynamics (Fig. 4, C and D, and figs. S4 and S5). In the first set of experiments conducted in August 2019, reduced PCA led to a significant increase in P concentration at the first time point. A more modest, but not significant, increase in soluble P was sustained throughout the experiment. In the experiments from October 2019, reduced PCA led to substantial but delayed increases in soluble P starting at 72 hours. The experiments with 1-OH-PHZ at site 2 in August showed little effect (figs. S4 and S5), possibly owing to the greater reactivity of 1-OH-PHZ with Fe minerals (17) and the subsequent formation of secondary mineral phases such as vivianite.

The measurements at the end of the experiments (see materials and methods) showed the presence of sulfide in incubations from October, but not August. The increased activity of sulfate-reducing bacteria (SRB) explains the sharp increase in P solubilization seen later in the year, as sulfide promotes the reductive dissolution of Fe(III) oxides and the release of sorbed P (29). Fe(III) reduction in the October incubations was directly observed as a peak in the dissolved Fe(II) at 72 hours (fig. S6), followed by a decrease as expected from the subsequent precipitation of Fe(II)-S phases with increasing S(-II) concentration. Sulfide was found only in reduced PCA treatments, suggesting that reduced PCA indirectly increases P solubilization by stimulating sulfate reduction, possibly by assuaging SRB limitation for Fe and/or P (30). Overall, our Catalina Island experiments show that phenazines can solubilize P from natural sediments through both direct and indirect processes.

Redox-active metabolites can be re-reduced and cycled by microbes (18), which, in principle, could catalyze P solubilization. There is some evidence for this occurrence in our experiments at Catalina Island; when oxidized phenazines were added (figs. S4 and S5), the treatments showed modest increases in soluble P over time, consistent with P solubilization through phenazine that was reduced *in situ*. To test this possibility, we tracked the reduction of PCA in samples of sediments (using a fluorescence assay; see materials and methods) from site 2 and either suppressed biological activity with ethanol or stimulated it with organic carbon. Ethanol markedly suppressed PCA reduction (Fig. 4E), whereas organic carbon stimulated it (Fig. 4F), as expected for a biologically driven process. Further investigation will be needed to identify the native phenazine producers in marine sediments and the P, Fe, and redox conditions under which this process is most beneficial. However, the capacity of native microbes to reduce phenazines is notable because it suggests that a small concentration of such metabolites could have a large effect on P solubilization, potentially benefitting the entire microbial community and not just the producer.

In conclusion, we demonstrate an eco-physiological role for redox-active antibiotics in P solubilization and acquisition. This phenomenon may be widespread because, like phenazines, phosphate-regulated metabolites including tetracyclines [which can reduce ferrihydrite (31)] and those with putatively redox-active moieties (quinone and phenoxazine) (table S1) may also solubilize P by means of reductive dissolution. Given that phenazine producers are found in crop soils (25), including the xanthomonad *D. japonica* (27), which appears to utilize reductive dissolution to solubilize P (Fig. 3C and fig. S2A), our findings may have relevance for the P cycle in agricultural contexts (32). Overall, this work expands our knowledge of beneficial physiological roles for redox-active antibiotics, indicating that they also contribute to the acquisition of macronutrients.

## REFERENCES AND NOTES

1. J. Davies, K. S. Ryan, *ACS Chem. Biol.* **7**, 252–259 (2012).
2. A. L. Demain, A. Fang, in *History of Modern Biotechnology*, A. Fletcher, Ed. (Springer, 2000), pp. 1–39.
3. A. Price-Whelan, L. E. P. Dietrich, D. K. Newman, *Nat. Chem. Biol.* **2**, 71–78 (2006).
4. M. A. Whooley, A. J. McLoughlin, *Eur. J. Appl. Microbiol. Biotechnol.* **15**, 161–166 (1982).
5. J. F. Martin, in *Advances in Biochemical Engineering* (Springer, 1977), vol. 6, pp. 105–127.
6. F. Santos-Beneit, *Front. Microbiol.* **6**, 402 (2015).
7. P. N. Froelich, M. L. Bender, N. A. Luedtke, G. R. Heath, T. DeVries, *Am. J. Sci.* **282**, 474–511 (1982).
8. P. Van Cappellen, E. D. Ingall, *Science* **271**, 493–496 (1996).
9. M. Obersteiner, J. Peñuelas, P. Ciais, M. van der Velde, I. A. Janssens, *Nat. Geosci.* **6**, 897–898 (2013).

10. E. Du et al., *Nat. Geosci.* **13**, 221–226 (2020).
11. H. Rodríguez, R. Fraga, *Biotechnol. Adv.* **17**, 319–339 (1999).
12. A. Canarini, C. Kaiser, A. Merchant, A. Richter, W. Wanek, *Front. Plant Sci.* **10**, 157 (2019).
13. S. A. Crosby, G. E. Millward, E. I. Butler, D. R. Turner, M. Whitfield, *Estuar. Coast. Shelf Sci.* **19**, 257–270 (1984).
14. T. Borch, S. Fendorf, in *Adsorption of Metals by Geomedia II*, vol. 7 of *Developments in Earth and Environmental Science*, M. O. Barnett, D. B. Kent, Eds. (Elsevier, 2008), chap. 12, pp. 321–348.
15. T. Peretyazhko, G. Sposito, *Geochim. Cosmochim. Acta* **69**, 3643–3652 (2005).
16. E. D. Brutinel, J. A. Gralnick, *Appl. Microbiol. Biotechnol.* **93**, 41–48 (2012).
17. Y. Wang, D. K. Newman, *Environ. Sci. Technol.* **42**, 2380–2386 (2008).
18. N. R. Glasser, S. H. Saunders, D. K. Newman, *Annu. Rev. Microbiol.* **71**, 731–751 (2017).
19. M. O. Burton, J. J. Campbell, B. A. Eagles, *Can. J. Res.* **26**, 15–22 (1948).
20. H. Sakhtah, A. Price-Whelan, L. E. P. Dietrich, in *Microbial Phenazines: Biosynthesis, Agriculture and Health*, S. Chincholkar, L. S. Thomashow, Eds. (Springer, 2013), pp. 19–42.
21. B. Mellbye, M. Schuster, *J. Bacteriol.* **196**, 1155–1164 (2014).
22. X.-J. Jin et al., *Sci. Rep.* **6**, 27393 (2016).
23. V. Jensen et al., *J. Bacteriol.* **188**, 8601–8606 (2006).
24. A. Sola-Landa, R. S. Moura, J. F. Martin, *Proc. Natl. Acad. Sci. U.S.A.* **100**, 6133–6138 (2003).
25. D. V. Mavrodi et al., *Appl. Environ. Microbiol.* **78**, 804–812 (2012).
26. L. Zhang et al., *Front. Microbiol.* **8**, 289 (2017).
27. D. Dar, L. S. Thomashow, D. M. Weller, D. K. Newman, *eLife* **9**, e59726 (2020).
28. A. R. Rowe, P. Chellamuthu, B. Lam, A. Okamoto, K. H. Nealson, *Front. Microbiol.* **5**, 784 (2015).
29. W. Stumm, B. Sulzberger, *Geochim. Cosmochim. Acta* **56**, 3233–3257 (1992).
30. P. V. Sundareshwar, J. T. Morris, E. K. Koepfler, B. Fornwalt, *Science* **299**, 563–565 (2003).
31. T. Wu et al., *Chem. Eng. J.* **366**, 577–586 (2019).
32. K. M. Dahlstrom, D. L. McRose, D. K. Newman, *Curr. Biol.* **30**, R1131–R1137 (2020).
33. A. Stamatakis, *Bioinformatics* **22**, 2688–2690 (2006).

## ACKNOWLEDGMENTS

We thank N. Dalleska (Caltech) for help with ICP-MS and liquid chromatograph-mass spectrometry analysis, K. Nealson (USC) as well as L. Sadler and K. Spafford (USC Wrigley Marine Science Center) for assistance with Catalina Island sampling, and S. Lim (Caltech) for help with sulfide measurements. We are grateful to Newman laboratory members M. Bergkessel and M. Spero for guidance on mutant construction, S. Wilbert for field assistance, and L. Tsybin for help with translation of papers. We also thank F. M. Morel for support and advice. We thank the Resnick Sustainability Institute for creating a supportive environment in which to do this work. **Funding:** This work was supported by grants from the ARO (W911NF-17-1-0024) and NIH (1R01AI127850-01A1) to D.K.N.; D.L.M. was supported by a division postdoctoral fellowship from Biology and Biological Engineering at Caltech, as well as the Simons Foundation postdoctoral fellowship in Marine Microbial Ecology. **Author contributions:** D.K.N. conceived the idea; D.K.N. and D.L.M. developed the project, designed and performed the experiments, analyzed and interpreted the data, and wrote the paper. **Competing interests:** The authors declare no competing interests. **Data and materials availability:** All data are available in the main text or the supplementary materials.

## SUPPLEMENTARY MATERIALS

science.sciencemag.org/content/371/6533/1033/suppl/DC1  
Materials and Methods  
Figs. S1 to S6  
Tables S1 to S3  
References (34–97)  
MDAR Reproducibility Checklist

15 June 2020; accepted 13 January 2021  
10.1126/science.abd1515

## EXOPLANETS

# A nearby transiting rocky exoplanet that is suitable for atmospheric investigation

T. Trifonov<sup>1\*</sup>, J. A. Caballero<sup>2</sup>, J. C. Morales<sup>3,4</sup>, A. Seifahrt<sup>5</sup>, I. Ribas<sup>3,4</sup>, A. Reiners<sup>6</sup>, J. L. Bean<sup>5</sup>, R. Luque<sup>7,8</sup>, H. Parviainen<sup>7,8</sup>, E. Pallé<sup>7,8</sup>, S. Stock<sup>9</sup>, M. Zechmeister<sup>6</sup>, P. J. Amado<sup>10</sup>, G. Anglada-Escudé<sup>3,4</sup>, M. Azzaro<sup>11</sup>, T. Barclay<sup>12,13</sup>, V. J. S. Béjar<sup>7,8</sup>, P. Bluhm<sup>9</sup>, N. Casasayas-Barris<sup>7,8</sup>, C. Cifuentes<sup>2</sup>, K. A. Collins<sup>14</sup>, K. I. Collins<sup>15</sup>, M. Cortés-Contreras<sup>2</sup>, J. de León<sup>16</sup>, S. Dreizler<sup>6</sup>, C. D. Dressing<sup>17</sup>, E. Esparza-Borges<sup>7,8</sup>, N. Espinoza<sup>18</sup>, M. Fausnaugh<sup>19</sup>, A. Fukui<sup>20,7</sup>, A. P. Hatzes<sup>21</sup>, C. Hellier<sup>22</sup>, Th. Henning<sup>1</sup>, C. E. Henze<sup>23</sup>, E. Herrero<sup>3,4</sup>, S. V. Jeffers<sup>6,24</sup>, J. M. Jenkins<sup>23</sup>, E. L. N. Jensen<sup>25</sup>, A. Kaminski<sup>9</sup>, D. Kasper<sup>5</sup>, D. Kossakowski<sup>1</sup>, M. Kürster<sup>1</sup>, M. Lafarga<sup>3,4</sup>, D. W. Latham<sup>14</sup>, A. W. Mann<sup>26</sup>, K. Molaverdikhani<sup>9</sup>, D. Montes<sup>27</sup>, B. T. Montet<sup>28</sup>, F. Murgas<sup>7,8</sup>, N. Narita<sup>29,30,31,7</sup>, M. Oshagh<sup>7,8</sup>, V. M. Passegger<sup>32,33</sup>, D. Pollacco<sup>34</sup>, S. N. Quinn<sup>14</sup>, A. Quirrenbach<sup>9</sup>, G. R. Ricker<sup>19</sup>, C. Rodríguez López<sup>10</sup>, J. Sanz-Forcada<sup>2</sup>, R. P. Schwarz<sup>35</sup>, A. Schweitzer<sup>32</sup>, S. Seager<sup>19,36,37</sup>, A. Shporer<sup>19</sup>, M. Stangret<sup>7,8</sup>, J. Stürmer<sup>9</sup>, T. G. Tan<sup>38</sup>, P. Tenenbaum<sup>19</sup>, J. D. Twicken<sup>39,23</sup>, R. Vanderspek<sup>19</sup>, J. N. Winn<sup>40</sup>

Spectroscopy of transiting exoplanets can be used to investigate their atmospheric properties and habitability. Combining radial velocity (RV) and transit data provides additional information on exoplanet physical properties. We detect a transiting rocky planet with an orbital period of 1.467 days around the nearby red dwarf star Gliese 486. The planet Gliese 486 b is 2.81 Earth masses and 1.31 Earth radii, with uncertainties of 5%, as determined from RV data and photometric light curves. The host star is at a distance of  $\sim 8.1$  parsecs, has a *J*-band magnitude of  $\sim 7.2$ , and is observable from both hemispheres of Earth. On the basis of these properties and the planet's short orbital period and high equilibrium temperature, we show that this terrestrial planet is suitable for emission and transit spectroscopy.

**T**he combination of transit photometry and Doppler radial velocity (RV) measurements can determine precise values of the masses, radii, bulk densities, and surface gravities of exoplanets. Determination of an exoplanet's atmospheric properties is possible using transmission and emission spectroscopy, but doing so for rocky exoplanets

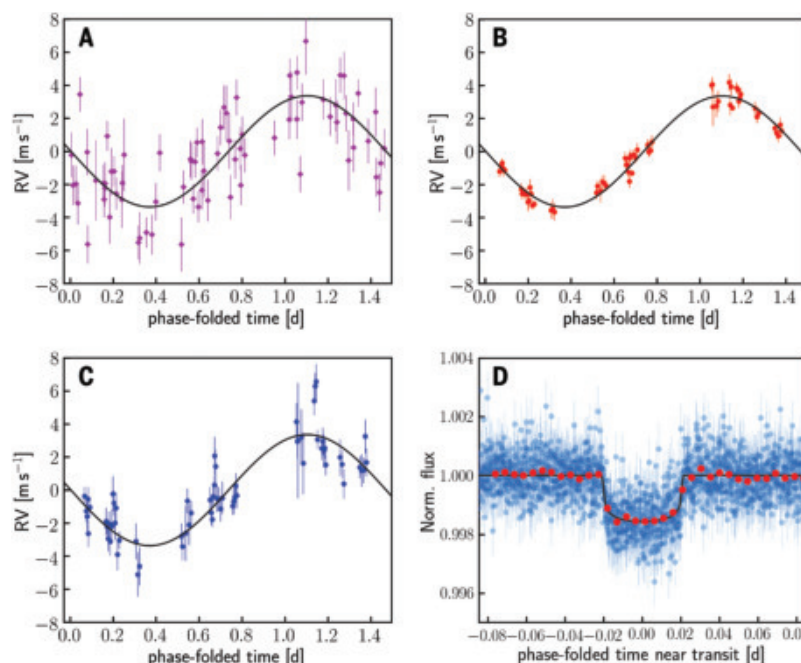
is challenging because of their small size. The CARMENES (Calar Alto high-Resolution search for M dwarfs with Exo-earths with Near-infrared and optical Echelle spectrographs) survey (1) and the Transiting Exoplanet Survey Satellite (TESS) mission (2) together have the sensitivity required to detect and, potentially, jointly investigate and characterize nearby exoplanet

systems. Small exoplanets are easier to detect around red dwarfs (main-sequence stars of spectral type M), as those stars are themselves small and of low mass. Particularly important are small, Earth-sized terrestrial planets in the habitable zone (3, 4), the region where liquid water could exist on the surface. The orbital periods expected for terrestrial planets in the habitable zone around M dwarfs are a few tens of days, and the predicted RV signals are large enough to be detectable.

M dwarfs are abundant in the Solar neighborhood; of the 357 cataloged main-sequence stars within 10 pc of the Sun, 283 (79%) are of type M (5, 6). Nearby exoplanets are favored for follow-up characterization, mainly because of their brighter host stars (producing a higher signal-to-noise ratio). Within 10 pc,  $\sim 80$  planets in 40 stellar systems are known, of which  $\sim 50$  planets orbit around 35 M dwarf hosts. These include the closest exoplanet systems, such as Proxima Centauri (7, 8) and Barnard's star (9).

We observed the nearby star Gliese 486 [Wolf 437, TESS Object of Interest (TOI) 1827], a red dwarf of spectral type M3.5 V, as one of the  $\sim 350$  targets in the CARMENES survey (10). RV monitoring of the star between 2016 and early 2020 showed a periodicity of 1.467 days with a false-alarm probability of  $< 0.1\%$  (11). No counterpart was found in stellar activity indices, suggesting that the signal was due to an orbiting planet rather than stellar variability, which is common in M dwarfs. We used photometric data from TESS to confirm the presence of the planet, identifying 13 transit events with a periodicity of 1.467 days (11). At a distance of 8.1 pc, Gliese 486 is the third-closest transiting exoplanet system known, and Gliese

**Fig. 1. Radial velocity and light curves of Gliese 486.** Phase-folded RV data from (A) CARMENES VIS, (B) MAROON-X red, and (C) MAROON-X blue, and (D) TESS photometric data. Blue circles in (D) represent the phase-folded 2-min cadence TESS transit photometry, whereas red circles are 1-hour bins of the phase-folded data. Error bars indicate  $1\sigma$  uncertainties of individual measurements. Black solid curves in all panels are the maximum likelihood orbital model from a joint fitting of all these data simultaneously. Norm. flux, normalized flux; d, days.





486 b is the closest transiting planet around a red dwarf with a measured mass.

We list the physical properties of the star Gliese 486 and planet Gliese 486 b in Table 1 (17).

From the CARMENES spectroscopic observations and a photometric data compilation (12), we computed a stellar radius of  $0.328 \pm 0.011$  solar radii ( $R_{\odot}$ ) and a mass of  $0.323 \pm$

$0.015$  solar masses ( $M_{\odot}$ ) following (13). Because of its closeness, Gliese 486 has been a target of direct-imaging exoplanet searches (14, 15), which placed upper limits on low-mass stellar and substellar companions at sky-projected physical separations between 1.2 and 161 astronomical units (au), larger than the orbit we find for Gliese 486 b.

We supplemented the TESS photometry with ground-based photometric monitoring and archival time series data to further characterize the transit events and determine the stellar rotation period. Using photometry of Gliese 486 collected by the Wide Angle Search for Planets (WASP) (16) between 2008 and 2014 and by the All-Sky Automated Survey for Supernovae (ASAS-SN) (17) between 2012 and 2020, we measured a stellar rotation period  $P_{\text{rot}} = 130.1^{+1.6}_{-1.2}$  days, which is consistent with our expectations for an old and weakly active M-dwarf star and much longer than the planet orbital period (fig. S4). We observed two additional transit events using the Multicolor Simultaneous Camera for studying Atmospheres of Transiting exoplanets 2 (MuSCAT2) (18) at the 1.5-m Telescopio Carlos Sánchez at Observatorio del Teide on 9 May 2020 and 12 May 2020 and three more transits with the 1.0-m Las Cumbres Observatory Global Telescope (LCOGT) (19) at Siding Spring Observatory on 15 May 2020, 24 May 2020, and 5 June 2020.

We complemented our CARMENES RV observations of Gliese 486 with data from the M-dwarf Advanced Radial velocity Observer Of Neighboring exoplanets (MAROON-X) spectrograph (20) at the 8.1-m Gemini North telescope. In total, we obtained 80 CARMENES spectra between 2016 and 2020 and 65 with MAROON-X between May and June 2020. These data provide complete phase coverage of the Gliese 486 b RV signal (Fig. 1), with a total weighted root mean square residual of  $1.05 \text{ m s}^{-1}$ .

We performed an orbital analysis using the EXO-STRIKER software (21). Global parameter

**Table 1. Measured properties of Gliese 486 and its planet.** We used gravitational constant  $G = 6.67430 \times 10^{-11} \text{ m}^3 \text{ kg}^{-1} \text{ s}^{-2}$ ,  $M_{\odot} = 1.98847 \times 10^{30} \text{ kg}$ ,  $R_{\odot} = 6.957 \times 10^8 \text{ m}$ ,  $M_{\oplus} = 5.9722 \times 10^{24} \text{ kg}$ , and  $R_{\oplus} = 6.3781 \times 10^6 \text{ m}$ . The tabulated rotation period is a proxy obtained from a quasi-periodic representation of the photometric variability. The eccentricity upper limit of  $<0.05$  is constrained at the 68.3% confidence level. The tabulated equilibrium temperature would be 60 K cooler if the Bond albedo were 0.30.

Parameters	Value
<i>Stellar</i>	
Right ascension (J2000 equinox)	12:47:56.62
Declination (J2000 equinox)	+09:45:05.0
Spectral type	M3.5 $\pm$ 0.5 V
J-band magnitude (mag)	7.195 $\pm$ 0.026
Mass ( $M_{\odot}$ )	0.323 $\pm$ 0.015
Radius ( $R_{\odot}$ )	0.328 $\pm$ 0.011
Luminosity ( $L_{\odot}$ )	0.01210 $\pm$ 0.00023
Effective temperature (K)	3340 $\pm$ 54
Distance (pc)	8.0761 $\pm$ 0.0041
Rotation period (days)	130.1 $^{+1.6}_{-1.2}$
Metallicity [Fe/H] (dex)	+0.07 $\pm$ 0.16
<i>Planetary</i>	
Orbital period (days)	1.467119 $^{+0.000031}_{-0.000030}$
Radial velocity semi-amplitude ( $\text{m s}^{-1}$ )	3.370 $^{+0.078}_{-0.080}$
Eccentricity	<0.05
Argument of periastron (degrees)	unconstrained
Time of inferior transit (barycentric Julian date)	2,458,931.15935 $^{+0.00042}_{-0.00042}$
Orbital semimajor axis (au)	0.01734 $^{+0.00026}_{-0.00027}$
Mass ( $M_{\oplus}$ )	2.82 $^{+0.11}_{-0.12}$
Radius ( $R_{\oplus}$ )	1.305 $^{+0.063}_{-0.067}$
Inclination (degrees)	88.4 $^{+1.1}_{-1.4}$
Insolation ( $S_{\oplus}$ )	40.3 $^{+1.5}_{-1.4}$
Mean density ( $10^{-3} \text{ kg m}^{-3}$ )	7.0 $^{+1.2}_{-1.0}$
Surface gravitational acceleration ( $\text{m s}^{-2}$ )	16.4 $^{+0.6}_{-0.5}$
Equilibrium temperature (K)	701 $^{+13}_{-13}$

<sup>1</sup>Max-Planck-Institut für Astronomie, D-69117 Heidelberg, Germany. <sup>2</sup>Centro de Astrobiología (Consejo Superior de Investigaciones Científicas – Instituto Nacional de Técnica Aeroespacial), E-28692 Villanueva de la Cañada, Madrid, Spain. <sup>3</sup>Institut de Ciències de l'Espai (Consejo Superior de Investigaciones Científicas), E-08193 Bellaterra, Barcelona, Spain. <sup>4</sup>Institut d'Estudis Espacials de Catalunya, E-08034 Barcelona, Spain. <sup>5</sup>Department of Astronomy and Astrophysics, University of Chicago, Chicago, IL 60637, USA. <sup>6</sup>Institut für Astrophysik, Georg-August-Universität, D-37077 Göttingen, Germany. <sup>7</sup>Instituto de Astrofísica de Canarias, E-38205 La Laguna, Tenerife, Spain. <sup>8</sup>Departamento de Astrofísica, Universidad de La Laguna, E-38206 La Laguna, Tenerife, Spain. <sup>9</sup>Landessternwarte, Zentrum für Astronomie der Universität Heidelberg, D-69117 Heidelberg, Germany. <sup>10</sup>Instituto de Astrofísica de Andalucía (Consejo Superior de Investigaciones Científicas), E-18008 Granada, Spain. <sup>11</sup>Centro Astronómico Hispano-Alemán, Observatorio de Calar Alto, E-04550 Gérgal, Almería, Spain. <sup>12</sup>NASA Goddard Space Flight Center, Greenbelt, MD 20771, USA. <sup>13</sup>University of Maryland, Baltimore County, Baltimore, MD 21250, USA. <sup>14</sup>Center for Astrophysics, Harvard & Smithsonian, Cambridge, MA 02138, USA. <sup>15</sup>Department of Physics and Astronomy, George Mason University, Fairfax, VA 22030, USA. <sup>16</sup>Department of Astronomy, Graduate School of Science, University of Tokyo, Tokyo 113-0033, Japan. <sup>17</sup>Astronomy Department, University of California at Berkeley, Berkeley, CA 94720, USA. <sup>18</sup>Space Telescope Science Institute, Baltimore, MD 21218, USA. <sup>19</sup>Department of Physics and Kavli Institute for Astrophysics and Space Research, Massachusetts Institute of Technology, Cambridge, MA 02139, USA. <sup>20</sup>Department of Earth and Planetary Science, Graduate School of Science, University of Tokyo, Tokyo 113-0033, Japan. <sup>21</sup>Thüringer Landessternwarte Tautenburg, D-07778 Tautenburg, Germany. <sup>22</sup>Astrophysics Group, Keele University, Staffordshire ST5 5BG, UK. <sup>23</sup>NASA Ames Research Center, Moffett Field, CA 94035, USA. <sup>24</sup>Max-Planck-Institut für Sonnensystemforschung, D-37077, Göttingen, Germany. <sup>25</sup>Department of Physics and Astronomy, Swarthmore College, Swarthmore, PA 19081, USA. <sup>26</sup>Department of Physics and Astronomy, University of North Carolina at Chapel Hill, Chapel Hill, NC 27599, USA. <sup>27</sup>Departamento de Física de la Tierra y Astrofísica and Instituto de Física de Partículas y del Cosmos, Facultad de Ciencias Físicas, Universidad Complutense de Madrid, E-28040 Madrid, Spain. <sup>28</sup>School of Physics, University of New South Wales, Sydney NSW 2052, Australia. <sup>29</sup>Komaba Institute for Science, University of Tokyo, Tokyo 153-8902, Japan. <sup>30</sup>Japan Science and Technology Agency, Precursory Research for Embryonic Science and Technology, Tokyo 153-8902, Japan. <sup>31</sup>Astrobiology Center, Tokyo 181-8588, Japan. <sup>32</sup>Hamburger Sternwarte, Universität Hamburg, D-21029 Hamburg, Germany. <sup>33</sup>Homer L. Dodge Department of Physics and Astronomy, University of Oklahoma, Norman, OK 73019, USA. <sup>34</sup>Department of Physics, University of Warwick, Coventry CV4 7AL, UK. <sup>35</sup>Patashnick Voorheesville Observatory, Voorheesville, NY 12186, USA. <sup>36</sup>Department of Earth, Atmospheric and Planetary Sciences, Massachusetts Institute of Technology, Cambridge, MA 02139, USA. <sup>37</sup>Department of Aeronautics and Astronautics, Massachusetts Institute of Technology, Cambridge, MA 02139, USA. <sup>38</sup>Perth Exoplanet Survey Telescope, Perth WA 6010, Australia. <sup>39</sup>Search for Extraterrestrial Intelligence Institute, Mountain View, CA 94043, USA. <sup>40</sup>Department of Astrophysical Sciences, Princeton University, Princeton, NJ 08544, USA.

\*Corresponding author. Email: trifonov@mpia.de

**Fig. 2. Mass-radius diagram for known transiting planets with measured masses between 0.5 and 5.5  $M_E$  and radii between 0.5 and 2.0  $R_E$ .** We show all cases with precision better than 30% (see supplementary text). Gliese 486 b is shown in red, planets orbiting around late-type stars with  $T_{\text{eff}} < 4000$  K are shown in orange, and hotter stars are shown in dark gray. Earth (blue circle with cross) and Venus (light gray circle with ♀ symbol) are shown for comparison. Curves show theoretical planet mass-radius relationships for compositions indicated in the legend: pure water ( $\text{H}_2\text{O}$ ), pure enstatite ( $\text{MgSiO}_3$ ) rock, an Earth-like mixture of 50% enstatite and 50% iron, and pure iron (Fe) (23).

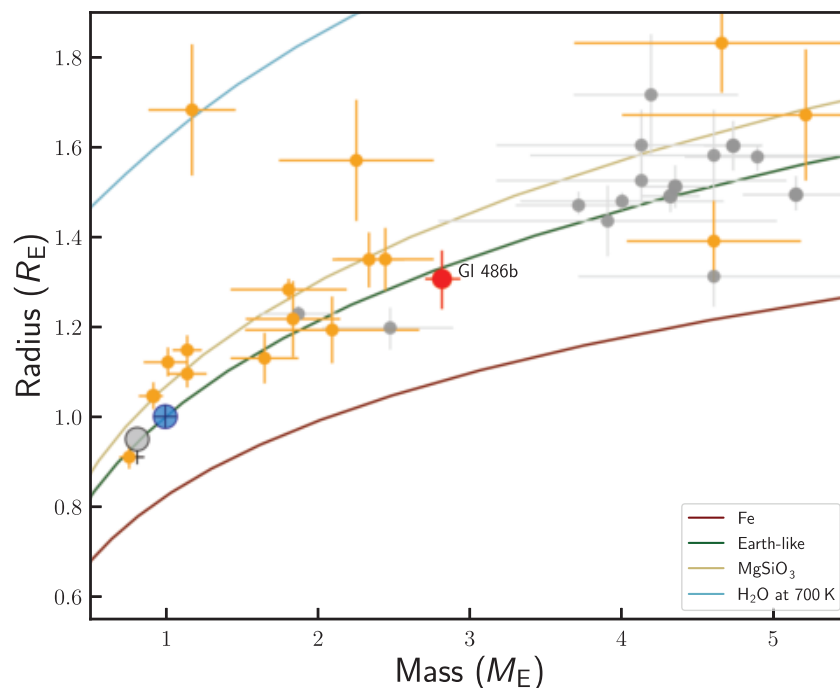
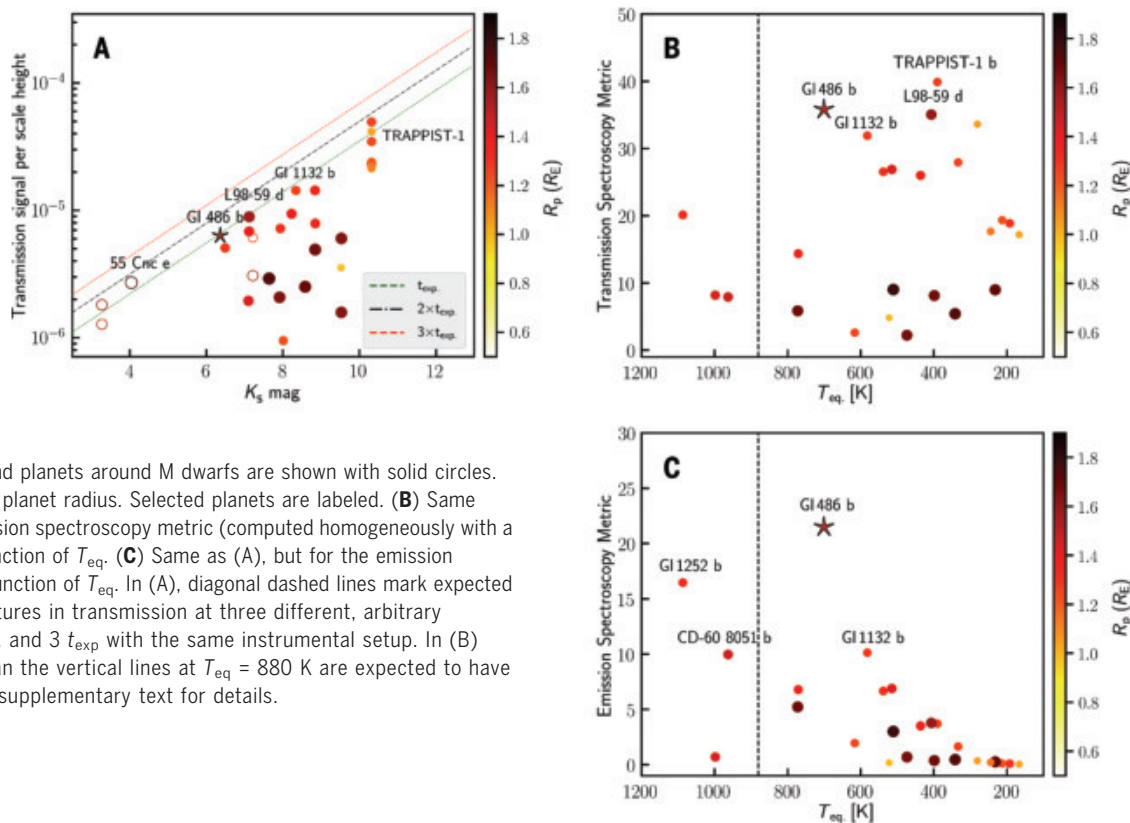


**Fig. 3. Metrics for transmission and emission spectroscopy for rocky planets with measured masses orbiting nearby M dwarfs.**

(A) Expected primary transit transmission signal per scale height as a function of  $K_s$ -band magnitude. Gliese 486 b is shown with a star, planets around bright G and K dwarfs at a distance of  $<30$  pc are shown with open circles, and planets around M dwarfs are shown with solid circles. The color bar indicates the planet radius. Selected planets are labeled. (B) Same as (A), but for the transmission spectroscopy metric (computed homogeneously with a scale factor 0.190) as a function of  $T_{\text{eq}}$ . (C) Same as (A), but for the emission spectroscopy metric as a function of  $T_{\text{eq}}$ . In (A), diagonal dashed lines mark expected amplitudes of spectral features in transmission at three different, arbitrary exposure times  $t_{\text{exp}}$ ,  $2 t_{\text{exp}}$ , and  $3 t_{\text{exp}}$  with the same instrumental setup. In (B) and (C), planets hotter than the vertical lines at  $T_{\text{eq}} = 880$  K are expected to have molten lava surfaces. See supplementary text for details.



optimization was performed by simultaneously fitting Keplerian orbit models to the CARMENES visual channel (VIS), MAROON-X red and blue

channels, and the TESS photometry. An alternative model that also includes transit data from MuSCAT2 and LCOGT provides consistent

results (11). For Gliese 486 b, we obtained a planet orbital period  $P_b = 1.467119^{+0.000031}_{-0.000030}$  days and an orbital inclination  $i_b = 88.4^{+1.1}_{-1.4}$



degrees. Using the RV semiamplitude  $K_b = 3.37^{+0.08}_{-0.08}$  m s<sup>-1</sup>, the stellar parameters of Gliese 486, and the orbital parameters, we derived a dynamical planet mass  $M_b = 2.82^{+0.11}_{-0.12}$  Earth masses ( $M_E$ ), a semimajor axis  $a_b = 0.01732^{+0.00027}_{-0.00027}$  au, and a planet radius  $R_b = 1.306^{+0.063}_{-0.067}$  Earth radii ( $R_E$ ). We concluded that Gliese 486 b has a circular orbit with an upper limit on the eccentricity  $e_b < 0.05$  at a 68.3% confidence level. This low eccentricity is consistent with the short orbital period, as star-planet tidal forces would act to circularize the orbit. We performed star-planet tidal simulations of the Gliese 486 system with the *EqTide* integrator (22) and found that the orbit of Gliese 486 b becomes fully circularized within ~1 million years.

From the planet mass and radius, we derived a planet bulk density  $\rho_b = 7.0^{+1.2}_{-1.0}$  10<sup>-3</sup> kg m<sup>-3</sup> (~1.3 times that of Earth) and a surface gravity  $g_b = 16.2^{+1.9}_{-1.6}$  m s<sup>-2</sup> (~1.7 times that of Earth), respectively. From the location of Gliese 486 b in a radius-mass diagram (Fig. 2), its density indicates an iron-to-silicate ratio similar to Earth's (23). The inferred mass and radius of ~2.82  $M_E$  and ~1.31  $R_E$  put Gliese 486 b at the boundary between Earth and super-Earth planets (24), but the bulk density indicates a massive terrestrial planet rather than an ocean planet (25). The escape velocity at 1  $R_b$  is  $v_e = 16.4^{+0.6}_{-0.5}$  km s<sup>-1</sup>. For an energy-limited atmospheric escape model (26) and the previously measured host star x-ray flux upper limit (27), we derive a low photo-evaporation rate of  $\dot{M}_{\text{phot}} < 10^7$  g s<sup>-1</sup>. From the stellar bolometric luminosity and the planet semimajor axis, we inferred a planet irradiance  $S_b$  of 40.3<sup>+1.5</sup><sub>-1.4</sub> times that of Earth. Assuming complete absorbance (a Bond albedo  $A_B = 0$ ), this equates to an equilibrium temperature  $T_{\text{eq}} = 701^{+13}_{-13}$  K, which is slightly cooler than that of Venus.

Figure 3 shows how Gliese 486 b compares with other possibly rocky planets around nearby M dwarfs (those with measured masses and radii  $R_p < 2.0 R_E$ ) using standard metrics for transmission and emission spectroscopy. Figure 3A shows the expected primary transit transmission signal  $\delta$  per atmospheric scale height  $H$  ( $\delta \approx 2HR_p/R_\star^2$ , where  $R_p$  is the radius of the planet, and  $R_\star$  is the radius of the star) as a function of apparent magnitude in the  $K_s$  band. Figure 3B shows the transmission spectroscopy metric as a function of  $T_{\text{eq}}$ , whereas panel Fig. 3C shows the emission spectroscopy metric, which is the signal-to-noise ratio expected for a single secondary eclipse observation by the James Webb Space Telescope (28). Figure 3, B and C, show planets around M dwarfs with measured masses. With a radius of 1.31  $R_E$ , Gliese 486 b is located well below the radius range of 1.4 to 1.8  $R_E$ , under which planets are expected to have lost their primordial hydrogen-helium atmospheres owing to photoevapo-

ration processes (29). It remains unknown how stellar irradiation and planet surface gravity affect the formation and retention of secondary atmospheres. Planets with  $T_{\text{eq}} > 880$  K, such as 55 Cancri e (30), are expected to have molten (lava) surfaces and no atmospheres, except for vaporized rock (31). Gliese 486 b is not hot enough to be a lava world, but its temperature of ~700 K makes it suitable for emission spectroscopy and phase curve studies in search of an atmosphere (28). Our orbital model constrains the secondary eclipse time to within 13 min (at 1 $\sigma$  uncertainty), which is necessary for efficient scheduling of observations. Compared with other known nearby rocky planets around M dwarfs, Gliese 486 b has a shorter orbital period and correspondingly higher equilibrium temperature of ~700 K and orbits a brighter, cooler, and less active stellar host.

## REFERENCES AND NOTES

- A. Quirrenbach et al., *Proc. SPIE Int. Soc. Opt. Eng.* **9908**, 990812 (2016).
- G. R. Ricker et al., *J. Astron. Telesc. Instrum. Syst.* **1**, 014003 (2015).
- J. F. Kasting, D. P. Whitmire, R. T. Reynolds, *Icarus* **101**, 108–128 (1993).
- J. C. Tarter et al., *Astrobiology* **7**, 30–65 (2007).
- I. N. Reid, J. E. Gizis, S. L. Hawley, *Astron. J.* **124**, 2721–2738 (2002).
- T. J. Henry et al., *Astron. J.* **132**, 2360–2371 (2006).
- G. Anglada-Escudé et al., *Nature* **536**, 437–440 (2016).
- M. Damasso et al., *Sci. Adv.* **6**, eaax7467 (2020).
- I. Ribas et al., *Nature* **563**, 365–368 (2018).
- A. Reiners et al., *Astron. Astrophys.* **612**, A49 (2018).
- Materials and methods are available as supplementary materials.
- C. Cifuentes et al., *Astron. Astrophys.* **642**, A115 (2020).
- A. Schweitzer et al., *Astron. Astrophys.* **625**, A68 (2019).
- S. B. Dieterich, T. J. Henry, D. A. Golimowski, J. E. Krist, A. M. Tanner, *Astron. J.* **144**, 64 (2012).
- K. Ward-Duong et al., *Mon. Not. R. Astron. Soc.* **449**, 2618–2637 (2015).
- D. L. Pollacco et al., *Publ. Astron. Soc. Pac.* **118**, 1407–1418 (2006).
- B. J. Shappee et al., *Astrophys. J.* **788**, 48 (2014).
- N. Narita et al., *J. Astron. Telesc. Instrum. Syst.* **5**, 015001 (2018).
- T. M. Brown et al., *Publ. Astron. Soc. Pac.* **125**, 1031–1055 (2013).
- A. Seifahrt, J. Stürmer, J. L. Bean, C. Schwab, *Proc. SPIE Int. Soc. Opt. Eng.* **10702**, 107026D (2018).
- T. Trifonov, The EXO-STRIKER: Transit and radial velocity interactive fitting tool for orbital analysis and N-body simulations, Astrophysics Source Code Library, record ascl:1906.004 (2019).
- R. Barnes, *Celestial Mech. Dyn. Astron.* **129**, 509–536 (2017).
- L. Zeng et al., *Proc. Natl. Acad. Sci. U.S.A.* **116**, 9723–9728 (2019).
- H. J. van Heck, P. J. Tackley, *Earth Planet. Sci. Lett.* **310**, 252–261 (2011).
- D. Valencia, D. D. Sasselov, R. J. O'Connell, *Astrophys. J.* **665**, 1413–1420 (2007).
- J. Sanz-Forcada et al., *Astron. Astrophys.* **532**, A6 (2011).
- B. Stelzer, A. Marino, G. Micela, J. López-Santiago, C. Liefke, *Mon. Not. R. Astron. Soc.* **431**, 2063–2079 (2013).
- E. M. R. Kempton et al., *Publ. Astron. Soc. Pac.* **130**, 114401 (2018).
- B. J. Fulton et al., *Astron. J.* **154**, 109 (2017).
- B. E. McArthur et al., *Astrophys. J.* **614**, L81–L84 (2004).
- M. Mansfield et al., *Astrophys. J.* **886**, 141 (2019).

## ACKNOWLEDGMENTS

This work was based on observations made with the CARMENES spectrograph at the 3.5-m telescope of the Centro Astronómico Hispano-Alemán de Calar Alto (CAHA, Almería, Spain), funded by the German Max-Planck-Gesellschaft (MPG), the Spanish Consejo Superior de Investigaciones Científicas (CSIC), the European Regional Development Fund, and the CARMENES consortium members and stored at the CARMENES data archive at CAB (INTA-CSIC); the MAROON-X spectrograph, which was funded by the David and Lucile Packard Foundation, the Heising-Simons Foundation, the Gemini Observatory, and the University of Chicago (the MAROON-X team thanks the staff of the Gemini Observatory for their assistance with the commissioning and operation of the instrument); the LCOGT network; the MuSCAT2 instrument, developed by the Astrobiology Center, at Telescopio Carlos Sánchez operated on the island of Tenerife by the Instituto de Astrofísica de Canarias in the Spanish Observatorio del Teide; and data collected by the TESS mission. **Funding:** Funding was provided by Deutsche Forschungsgemeinschaft through research unit FOR2544 “Blue Planets around Red Stars” and priority program SPP1992 “Exploring the Diversity of Extrasolar Planets”; Agencia Estatal de Investigación of the Ministerio de Ciencia e Innovación and the European Regional Development Fund through projects PID2019-109522GB-C51/2/3/4, PGC2018-098153-B-C33, SEV-2017-0709, MDM-2017-0737, AYA2016-79425-C3-1/2/3-P, ESP2016-80435-C2-1-R, and SEV-2015-0548; Klaus Tschira Stiftung; European Union's Horizon 2020 through Marie Skłodowska Curie grant 713673; “la Caixa” through INPhINT grant LCF/BQ/IN17/1162033; NASA through grants NNX17AG24G, 80NSSC19K0533, 80NSSC19K1721, and 80NSSC18K158 and the NASA Science Mission Directorate; Japan Society for the Promotion of Science KAKENHI through grants JP17H04574, JP18H01265, and JP18H05439; and Japan Science and Technology Agency PRESTO through grant JPMJPR1775. **Author contributions:** T.T. analyzed and interpreted the data and wrote the manuscript. J.A.C. is the CARMENES instrument astronomer and helped write the manuscript. J.C.M. scheduled the CARMENES observations and performed preliminary CARMENES RV analysis and transit predictions. I.R. and A.R. are the CARMENES project scientists and identified the periodic radial velocity signal. J.L.B., R.L., E.P., S.St., and K.M. contributed to writing the manuscript. A.Se. and M.Z. reduced the CARMENES and MAROON-X spectra. G.A.-E., P.B., N.E., and A.P.H. analyzed the RV and photometric time series. C.C., M.C.-C., V.M.P., J.S.-F., and A.Sc. determined stellar parameters. The following authors contributed to instrument operations, science coordination, and data analysis: P.J.A., M.A., V.J.S.B., S.D., T.H., S.V.J., A.K., D.Ko., M.K., M.L., D.M., A.Q., and C.R.L. for CARMENES; D.Ka., B.T.M., and J.S. for MAROON-X; N.C.-B., J.d.L., E.E.-B., A.F., F.M., N.N., and H.P., and M.S. for MuSCAT2; K.A.C., K.I.C., E.L.N.J., A.Sh., and R.P.S. for LCOGT; C.H., E.H., D.P., and T.G.T. for PEST, TJO, and SuperWASP; T.B., C.D.D., M.F., C.E.H., J.M.J., D.W.L., A.W.M., S.N.Q., G.R.R., S.Se., P.T., J.D.T., R.V., and J.N.W. for TESS. **Competing interests:** The authors declare no competing interests. **Data and materials availability:** All time series data used (RV, activity indices, and light curves from CARMENES, MAROON-X, HARPS, HRES, MuSCAT2, LCOGT, SuperWASP, ASAS-SN, TJO, and TESS) are available at the Centro de Astrobiología CARMENES data archive <http://carmenes.cab.inta-csic.es/> as machine-readable tables. The derived RVs and light curves are provided in tables S1 to S4 and data S1. The EXO-STRIKER code is available at <https://github.com/3fon3fonov/exostriker>, the JULIET code at <https://github.com/nespinoza/juliet>, and the EqTide code at <https://github.com/RoryBarnes/eqtide>.

## SUPPLEMENTARY MATERIALS

science.sciencemag.org/content/371/6533/1038/suppl/DC1  
Materials and Methods  
Supplementary Text  
Figs. S1 to S10  
Tables S1 to S6  
References (32–102)  
Data S1

10 July 2020; accepted 2 February 2021  
10.1126/science.abd7645

## INSECT DECLINES

# Fewer butterflies seen by community scientists across the warming and drying landscapes of the American West

M. L. Forister<sup>1\*</sup>, C. A. Halsch<sup>1</sup>, C. C. Nice<sup>2</sup>, J. A. Fordyce<sup>3</sup>, T. E. Dilts<sup>4</sup>, J. C. Oliver<sup>5</sup>, K. L. Prudic<sup>6</sup>, A. M. Shapiro<sup>7</sup>, J. K. Wilson<sup>6</sup>, J. Glassberg<sup>8,9</sup>

Uncertainty remains regarding the role of anthropogenic climate change in declining insect populations, partly because our understanding of biotic response to climate is often complicated by habitat loss and degradation among other compounding stressors. We addressed this challenge by integrating expert and community scientist datasets that include decades of monitoring across more than 70 locations spanning the western United States. We found a 1.6% annual reduction in the number of individual butterflies observed over the past four decades, associated in particular with warming during fall months. The pervasive declines that we report advance our understanding of climate change impacts and suggest that a new approach is needed for butterfly conservation in the region, focused on suites of species with shared habitat or host associations.

Shifts in the structure and function of ecosystems in the Anthropocene pose numerous and poorly understood threats to wild plants and animals and to human society (1). Of the changes being tracked by ecologists, few are as potentially consequential as reductions in insect abundance and diversity (2), with the status of pollinators being of particular concern (3, 4). Although debate continues on the magnitude and taxonomic scope of insect declines (5–7), there can be little doubt that insects (like most other major groups) are responding to stressors that include habitat loss, climate change, overuse of pesticides, and invasive species (8). However, most historical records of insect populations come from parts of the world—in particular, densely populated areas of Western Europe (9–11)—where habitat loss and degradation have been pervasive, thus limiting the ability of researchers to separate the signal of climate change from the effects of other stressors. In this work, we addressed this knowledge gap using community scientist and expert-collected data, focusing on a region, the western United States,

that is particularly useful for understanding the effects of climate change on insects because of warming and drying trends (12) observed across land-use gradients (from major cities to protected national parks) as well as elevational and latitudinal gra-

dients that contain great habitat and climatic diversity.

The three datasets that we studied are the Shapiro transect from northern California (13), the North American Butterfly Association (NABA) network of community scientist count data (14), and the iNaturalist web platform (15) of contributed observations (Fig. 1). These three sources encompass more than 450 species of butterflies and are complementary in that they represent gradients of geographic coverage, temporal extent, and expertise; the three sources also differ in coverage of urban and agricultural areas. The Shapiro dataset is expert run, the NABA counts are generated by teams of volunteer or community scientists, and the iNaturalist records are contributed by thousands of nature enthusiasts whose identifications are vetted by means of a machine learning algorithm and by at least two human experts. Previous work with the Shapiro data has uncovered pervasive reductions in the density of butterfly populations across a relatively narrow geographic area that includes large urban and agricultural areas (16). Whether similar population trajectories would be observed across wildlands and natural areas has been an open question (17). Estimating species-specific trends over time,

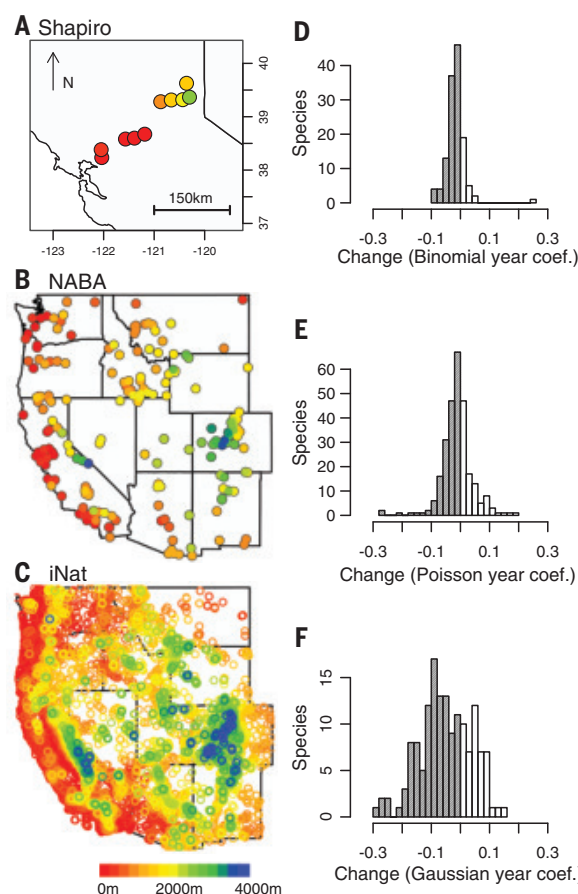


**Fig. 1. Three focal datasets and overview of species trends through time.** (A) Shapiro northern California data: 10 study sites from the Bay Area to the Sierra Nevada Mountains, with sites color coded by elevation (as in subsequent panels). (B) Western NABA locations: all are shown, and a subset (72 sites with 10 or more years of data) was used in many analyses. (C) Locations of iNaturalist butterfly records. iNat, iNaturalist. (D) to (F) Histograms summarizing species-specific year coefficients (with negative values in gray) for the three datasets: (D) Shapiro, 48 years; (E) NABA, 42 years; and (F) iNaturalist, 15 years. coef., coefficient. The interpretation of year coefficients is not identical across datasets, but in general, negative and positive values indicate decreases or increases in population density or the frequency with which individual species have been observed over time. The means of the three distributions are significantly different from zero (single sample *t* tests): (D)  $t_{130} = -5.6$ ,  $P < 0.001$ ; (E)  $t_{271} = -3.3$ ,  $P < 0.001$ ; and (F)  $t_{160} = -11.8$ ,  $P < 0.001$ .

<sup>1</sup>Department of Biology, Program in Ecology, Evolution, and Conservation Biology, University of Nevada, Reno, NV 89557, USA. <sup>2</sup>Department of Biology, Texas State University, San Marcos, TX 78666, USA. <sup>3</sup>Department of Ecology and Evolutionary Biology, University of Tennessee, Knoxville, TN 37996, USA. <sup>4</sup>Department of Natural Resources and Environmental Science, University of Nevada, Reno, NV 89557, USA. <sup>5</sup>Office of Digital Innovation and Stewardship, University Libraries, University of Arizona, Tucson, AZ 85721, USA. <sup>6</sup>School of Natural Resources and the Environment, University of Arizona, Tucson, AZ 85721, USA. <sup>7</sup>Center for Population Biology, University of California–Davis, Davis, CA 95616, USA. <sup>8</sup>North American Butterfly Association, Morristown, NJ 07960, USA. <sup>9</sup>Department of BioSciences, Rice University, Houston, TX 77251, USA.

\*Corresponding author. Email: forister@gmail.com



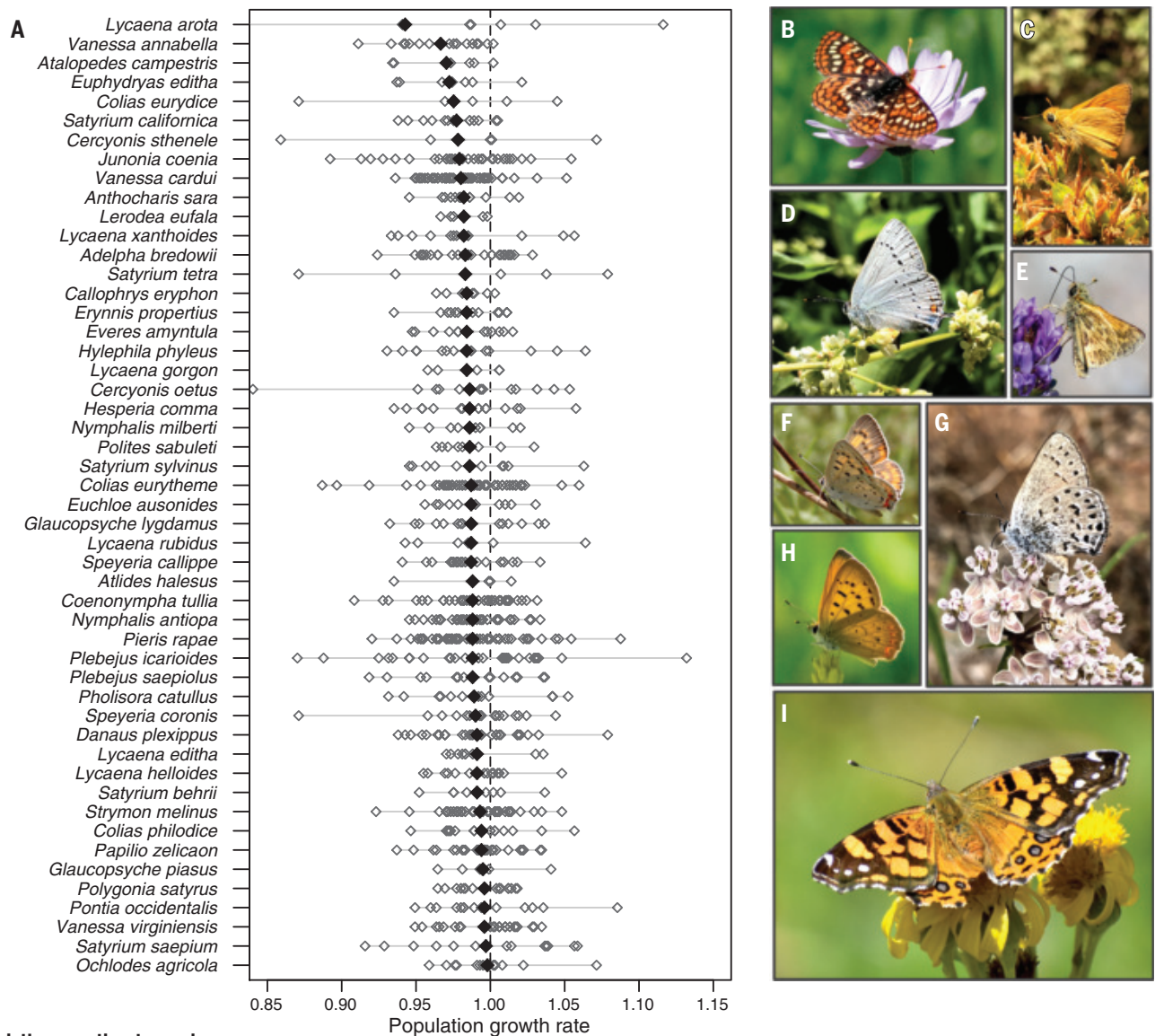


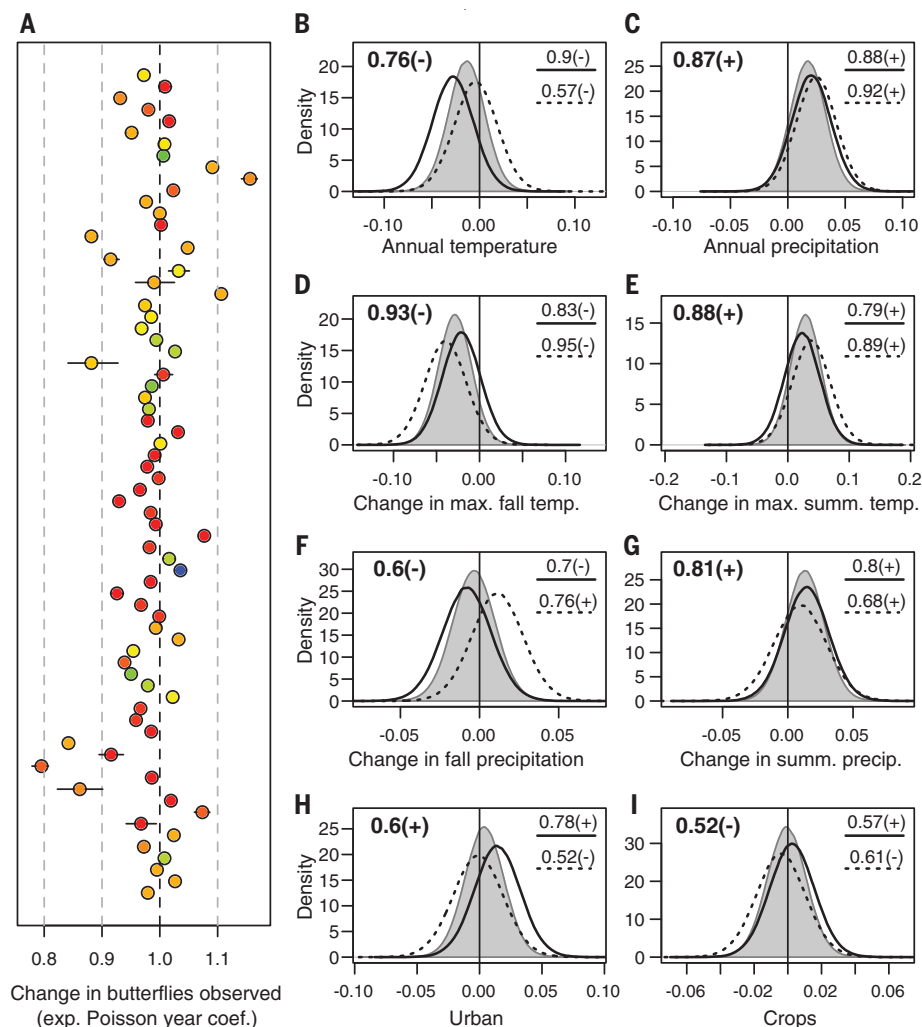
**Fig. 2. Population growth rates and example annual trajectories.** (A) Estimates of population growth rates from NABA counts at the level of species (dark diamonds) and individual locations (open diamonds) for a subset of species; these are 50 species that are estimated to have downward annual trends in at least two datasets (among NABA, Shapiro, and iNaturalist records), but growth rate estimates (shown here) are based only on NABA data, which are well suited for this purpose (see materials and methods).

(B to I) Photos of 8 of the 50 species: (B) *Euphydryas editha*; (C) *Ochlodes agricola*; (D) *Satyrus sylvinus*; (E) *Polites sabuleti*; (F) *Lycaena xanthoides* (J.C.O.); (G) *Satyrus behrii*; (H) *Lycaena helloides*; and (I) *Vanessa annabella*. (J to M) Time series plots are shown for four exemplar species (see table S2 for other species-specific results), with NABA in orange, Shapiro in blue, and iNaturalist in green; these values are effort corrected and averaged across locations (within each species) and shown as standardized deviations from long-term averages in counts (for NABA) and frequencies of observation (for Shapiro and iNaturalist). pop., population.

[Photo credits: (B) C.A.H.; (C) M.L.F.; (D) M.L.F.; (E) C.A.H.; (F) J.C.O.; (G) M.L.F.; (H) C.A.H.; (I) C.A.H.]

**Fig. 3. Location-specific changes in butterfly density and associations with climate and global change variables.** (A) Year coefficients from a hierarchical Bayesian Poisson model predicting total numbers of butterflies at NABA sites (intervals are 95% highest density intervals, which are small and not visible for most locations). Poisson coefficients have been exponentiated and can be interpreted as fractional change per year. The populations are ordered by latitude (more northern at the top) and color coded by elevation (as in Fig. 1).

Across all 72 sites (average of 21 years per site), we estimate a coefficient of 0.984, which corresponds to a reduction of 1.6%, with a 95% highest density interval from 0.966 (reduction of 3.4%) to 1.002 (increase of 0.2%); additional details are in supplementary box 2. exp., exponentiated. (B to I) Posterior probability distributions for the effects of particular variables on the total number of butterflies observed (gray-shaded curves) as well as on the 50 most common species (dark lines) and all other species (dotted lines). max., maximum; summ., summer; temp., temperature. The variables include static descriptions of climate [(B) and (C)], rates of climate change [(D) to (G)], and the fraction of land around sites converted to urban and agricultural spaces [(H) and (I)]. The variance explained (as the square of the observed versus predicted correlation) for the model is 0.39 (see table S4 for detailed results including covariates for spatial autocorrelation). The numbers shown in the upper left of each plot indicate the probability of a positive or negative effect on butterfly abundance; for example, there is an 87% probability that locations with more annual precipitation (precip.) are associated with increases in butterfly counts (C). The values in the upper right of each plot are the same probabilities but from models run separately for common species (solid lines) and all others (dotted lines); for example [also from (C)], there is an 88% probability of a positive effect of precipitation for common species and a 92% probability for all others.



we found that a majority of species in each of the three datasets have downward population trajectories, ranging from slightly downward trending to more severe reductions in abundance (Fig. 1, D to F). Declining taxa include, but are not limited to, wide-ranging species (for example, the west coast lady, *Vanessa annabella*) (Fig. 2J) and butterflies that thrive in disturbed and degraded habitats, such as the introduced cabbage white, *Pieris rapae*, for which decline has been reported from the midwestern United States (18). Overall, single-brooded species tend to be in slightly more severe decline, but in general, we found that life history traits (including geographic range size, body size, and host specialization) have little explanatory power (table S3).

Looking beyond individual species, we used the NABA data to investigate the change in the total number of individual butterflies and found

a 96% probability that the total abundance of butterflies is decreasing, with an estimated rate of 1.6% fewer individuals per year. That value was estimated across 72 locations (and 262 species) with 10 or more years of data (Fig. 3A and fig. S1), in total spanning 42 years, from 1977 to 2018 (the average length of time series from individual sites was 21 years) (see table S1). Using the same records to investigate geographic variation in changing abundance, we considered indices of land use and static descriptions of annual climate, as well as season-specific rates of climate change, and found the most influential predictors to be indices of climate change (table S4). Specifically, locations that have been warming in the fall months have seen fewer butterflies over time (Fig. 3D), whereas warming in the summer months is associated with the opposite effect (Fig. 3E). We hypothesize that warm-

ing in the summer influences adult activity times directly and hence increases the probability of detection, whereas fall warming likely induces physiological stress on active and diapausing stages, reduces host plant vigor, or extends activity periods for natural enemies (19, 20). The rate of warming is not homogeneous across seasons, and warming is greatest in the fall (fig. S2). The difference between fall and summer warming is itself a predictor of changing butterfly densities (Fig. 4). We also saw a positive effect of increasing summer precipitation on butterfly observations (Fig. 3G), which is likely associated with positive effects on nectar plants and larval hosts; the western United States, however, has been drying in recent decades (fig. S2). We have considered the possibility that the results are affected by the abundance of the most common species, but after excluding the 50 most



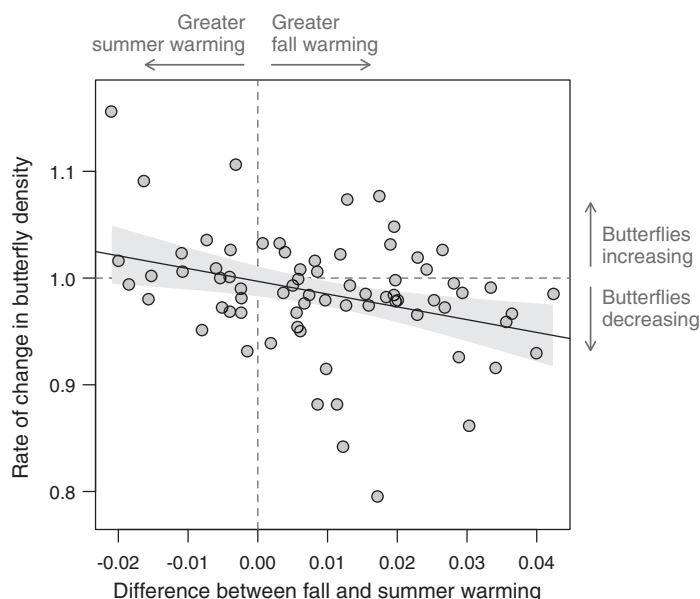


**Fig. 4. Differential seasonal warming associated with changes in butterfly density.** Rates of change in butterfly density for all sites (as in Fig. 3A) regressed against the difference between fall and summer warming. The fitted line and 95% confidence intervals are from a simple linear regression with slope =  $-1.2$  (standard error 0.41),  $F_{1,70} = 8.6$ ,  $P = 0.0046$ , and  $R^2 = 0.11$ .

abundant taxa, we still estimated a decline of 1.8% with 93% confidence (the effects of climate change and other predictors on more and less common butterflies are available in Fig. 3, and a power analysis of overall decline is available in fig. S3).

We did not detect an effect of proximity to either urban development or agriculture (Fig. 3, H and I), despite prior work illustrating that habitat loss and degradation have severe negative effects on insects (21, 22). Pesticide applications in California's Central Valley, in particular, have been implicated in recent declines (16). The NABA sites were not chosen with the goal of providing an unbiased sample of the landscape (and the same can be said of the other datasets), and the median fraction of urban and agricultural land around sites is less than 5% (fig. S4). The NABA sites do, however, include variation in proximity to development, but these factors appear to be less important in comparison with the influence of climate for the sites studied in this work.

In summary, we found that fewer individual butterflies are being observed across the western United States each year, with agreement from expert and volunteer datasets on that conclusion. In contrast to studies—for example, from Western Europe—that have found more straightforward signals of ecological specialization (among other traits) that predict the severity of decline, we have much yet to learn about the species-specific traits associated with population increase and decline in our fauna (23). The taxonomic and

geographic ubiquity of the declines that we report suggest that conservation efforts could profitably target suites of species, potentially defined by commonalities of geography, host plant, or habitat use, instead of conventional conservation and management practices focused on single species. These findings also contrast with a recent report across a number of arthropod taxa in North America that found no overall signal of decline (6). Although the analytical methods in that report are being discussed (24), it might also be the case that either temporally intensive sampling (as with the Shapiro dataset) or highly dispersed geographic sampling (as with the NABA data) have greater statistical power for the detection of directional change through time in highly variable insect populations.

The results reported here have implications for policy and for how society thinks about insect declines (25). The management of developed areas (such as reduction of pesticide use in agricultural margins and urban areas) can have immediate benefits for insect populations (26), but the impacts of climate change cannot be ignored. Society should not assume that the legal protection of open spaces is sufficient without the action to limit the advance of anthropogenic climate change (22). Although our analyses point to warming fall temperatures as an important factor in insect declines, we acknowledge the multifaceted nature of the problem and how much remains to be understood about climate

change interacting with habitat loss and degradation (8, 27).

## REFERENCES AND NOTES

1. R. Chaplin-Kramer *et al.*, *Science* **366**, 255–258 (2019).
2. P. Cardoso *et al.*, *Biol. Conserv.* **242**, 108426 (2020).
3. C. J. Rhodes, *Sci. Prog.* **101**, 121–160 (2018).
4. E. E. Zattara, M. A. Aizen, *One Earth* **4**, 114–123 (2021).
5. C. D. Thomas, T. H. Jones, S. E. Hartley, *Glob. Chang. Biol.* **25**, 1891–1892 (2019).
6. M. S. Crossley *et al.*, *Nat. Ecol. Evol.* **4**, 1368–1376 (2020).
7. B. I. Simmons *et al.*, *Ecol. Evol.* **9**, 3678–3680 (2019).
8. D. L. Wagner, *Annu. Rev. Entomol.* **65**, 457–480 (2020).
9. R. van Klink *et al.*, *Science* **368**, 417–420 (2020).
10. C. A. Hallmann *et al.*, *PLOS ONE* **12**, e0185809 (2017).
11. K. F. Conrad, M. S. Warren, R. Fox, M. S. Parsons, I. P. Woold, *Biol. Conserv.* **132**, 279–291 (2006).
12. P. Gonzalez, F. Wang, M. Notaro, D. J. Vimont, J. W. Williams, *Environ. Res. Lett.* **13**, 104001 (2018).
13. A. M. Shapiro, Art Shapiro's Butterfly Site (2020); <http://butterfly.ucdavis.edu/>
14. NABA, North American Butterfly Association Counts (2020); [naba.org/butter\\_counts.html](http://naba.org/butter_counts.html)
15. iNaturalist, iNaturalist Observations (2020); [inaturalist.org/observations](http://inaturalist.org/observations)
16. M. L. Forister *et al.*, *Biol. Lett.* **12**, 20160475 (2016).
17. G. A. Montgomery *et al.*, *Biol. Conserv.* **241**, 108327 (2020).
18. T. Wepprich, J. R. Adron, L. Ries, J. Wiedmann, N. M. Haddad, *PLOS ONE* **14**, e0216270 (2019).
19. A. S. Gallinat, R. B. Primack, D. L. Wagner, *Trends Ecol. Evol.* **30**, 169–176 (2015).
20. C. Parmesan, M. E. Hanley, *Ann. Bot.* **116**, 849–864 (2015).
21. D. Goulson, *J. Appl. Ecol.* **50**, 977–987 (2013).
22. E. Piano *et al.*, *Glob. Change Biol.* **26**, 1196–1211 (2020).
23. A. Eskildsen *et al.*, *Divers. Distrib.* **21**, 792–802 (2015).
24. E. A. R. Welti *et al.*, *EcoEvoRxiv* v3sr2 [Preprint]. 20 August 2020. <https://ecoevorxiv.org/v3sr2/>
25. D. M. Hall, R. Steiner, *Environ. Sci. Policy* **93**, 118–128 (2019).
26. M. R. Hunter, M. D. Hunter, *Insect Conserv. Divers.* **1**, 189–196 (2008).
27. D. E. Bowler *et al.*, *Nat. Ecol. Evol.* **1**, 67 (2017).
28. J. Oliver, [github.com/jcoliver/citsci-western-butterflies](https://github.com/jcoliver/citsci-western-butterflies): Post review release 3, Version v0.93, Zenodo, 10.5281/zenodo.4460647 (2021);

## ACKNOWLEDGMENTS

We thank all the volunteers in community science programs, past and present, who have made the NABA and iNaturalist data possible, including Adventure Scientists and their volunteers who observe butterflies in the backcountry. We thank J. Springer for help with NABA records, and NABA also thanks Redshift Technologies for software and website development. We thank S. Black, S. Jepsen, and E. Pelton, as well as two anonymous reviewers, for thoughtful comments on the manuscript.

**Funding:** M.L.F. was supported by a Trevor James McMinn professorship. K.L.P. and J.K.W. were supported by the College of Agriculture and Life Science, Research Innovation and Impact, and the University of Arizona Libraries. **Author contributions:** Overall concept and analyses: M.L.F., C.C.N., J.A.F., C.A.H., J.K.W., J.C.O., and K.L.P.; data management and curation: J.G., J.K.W., and C.A.H.; and data collection: A.M.S. and J.G.; all authors read and edited the manuscript. **Competing interests:** The authors declare no competing interests. **Data availability:** The data analyzed in this study and code are available on Zenodo (28).

## SUPPLEMENTARY MATERIALS

[science.sciencemag.org/content/371/6533/1042/suppl/DC1](https://science.sciencemag.org/content/371/6533/1042/suppl/DC1)  
Materials and Methods  
Figs. S1 to S4  
Tables S1 to S4  
References (29–49)

29 August 2020; resubmitted 10 November 2020  
Accepted 29 January 2021  
10.1126/science.abe5585

## BLACK HOLES

# Cygnus X-1 contains a 21-solar mass black hole—Implications for massive star winds

James C. A. Miller-Jones<sup>1\*</sup>, Arash Bahramian<sup>1</sup>, Jerome A. Orosz<sup>2</sup>, Ilya Mandel<sup>3,4,5</sup>, Lijun Gou<sup>6,7</sup>, Thomas J. Maccarone<sup>8</sup>, Coenraad J. Neijssel<sup>3,4,5</sup>, Xueshan Zhao<sup>6,7</sup>, Janusz Ziolkowski<sup>9</sup>, Mark J. Reid<sup>10</sup>, Phil Uttley<sup>11</sup>, Xueying Zheng<sup>6,7,†</sup>, Do-Young Byun<sup>12,13</sup>, Richard Dodson<sup>14</sup>, Victoria Grinberg<sup>15</sup>, Taehyun Jung<sup>12,13</sup>, Jeong-Sook Kim<sup>12</sup>, Benito Marcote<sup>16</sup>, Sera Markoff<sup>11,17</sup>, Maria J. Rioja<sup>14,18,19</sup>, Anthony P. Rushton<sup>20,21</sup>, David M. Russell<sup>22</sup>, Gregory R. Sivakoff<sup>23</sup>, Alexandra J. Tetarenko<sup>24</sup>, Valeriu Tudose<sup>25</sup>, Joern Wilms<sup>26</sup>

The evolution of massive stars is influenced by the mass lost to stellar winds over their lifetimes. These winds limit the masses of the stellar remnants (such as black holes) that the stars ultimately produce. We used radio astrometry to refine the distance to the black hole x-ray binary Cygnus X-1, which we found to be  $2.22^{+0.18}_{-0.17}$  kiloparsecs. When combined with archival optical data, this implies a black hole mass of  $21.2 \pm 2.2$  solar masses, which is higher than previous measurements. The formation of such a high-mass black hole in a high-metallicity system (within the Milky Way) constrains wind mass loss from massive stars.

Gravitational wave detections of black hole merger events have revealed a population of black holes with masses ranging from 7 to 50 solar masses ( $M_{\odot}$ ) (1). Black holes that interact with a companion star are visible to electromagnetic observations as an x-ray binary. Radial velocity measurements of these companion stars have shown that black holes in x-ray binaries all have masses below  $20 M_{\odot}$  (2). The highest measured black hole mass in an x-ray binary is  $15.65 \pm 1.45 M_{\odot}$  for the extragalactic system M33 X-7 (3).

The mass of a black hole is initially set by the properties of its progenitor star then can increase through accretion or mergers over its lifetime. The relevant properties of the progenitor include its initial mass and abundance of elements heavier than helium (its metallicity), the mass lost in stellar winds over its lifetime, and the evolutionary pathway that it followed, which can be strongly influenced by a binary companion. Mass measurements for massive stellar-mass black holes constrain stellar and binary evolution models (4) and predictions of the expected black hole merger rates.

The x-ray binary Cygnus X-1 (V1357 Cyg) (coordinates are provided in table S1) contains a black hole in a 5.6-day orbit with a more

massive supergiant donor star, of spectral type O. Previous estimates of its component masses were based on a parallax measurement, in which the apparent annual angular shift in the source position relative to more distant objects was measured by using radio very-long-baseline interferometry. With trigonometry, this gave a distance of  $1.86^{+0.12}_{-0.11}$  kpc (5). When combined with optical radial velocity measurements of the system, these data yielded a black hole mass of  $14.8 \pm 1.0 M_{\odot}$  (6). However, the derived system parameters are then inconsistent with the expected mass-luminosity relation for the donor, if it is a hydrogen-burning main sequence star (7). The optical parallax measurement of  $0.42 \pm 0.03$  milli-arc sec measured with the *Gaia* space telescope (8), after correction for a known zero-point offset of  $\approx 0.05$  milli-arc sec [with estimates ranging from 0.03 to 0.08 milli-arc sec (9)], becomes  $0.47 \pm 0.04$  milli-arc sec. This is inconsistent with the radio value of  $0.54 \pm 0.03$  milli-arc sec (5) and is unlikely to be due to orbital displacement of the donor star because the *Gaia* value is the average over 119 orbital periods.

Between 29 May 2016 and 3 June 2016, we performed six observations (one per day) of Cygnus X-1 with the Very Long Baseline Array (VLBA) at 8.4 GHz, sampling one full orbital

period. To reduce systematic uncertainties in our position measurements, we phase referenced the data to a nearby calibrator source  $0.4^{\circ}$  from Cygnus X-1 (10). These data resolve the orbital motion of the black hole as projected onto the downstream surface from which the jet emission can escape, which is called the photosphere. We found that the orbit is clockwise on the plane of the sky (Fig. 1), which is in agreement with previous observations (5).

Combining the orbital phase coverage of our VLBA data with archival observations (5), we simultaneously fitted the entire data set (covering a 7.4-year baseline) with a full astrometric solution that incorporated linear motion across the sky (proper motion), parallax, and orbital motion. Fitting both the right ascension and declination coordinates showed an orbital phase dependence in the direction of the residuals. We attribute this to the effect of free-free absorption in the stellar wind, which is known to modulate the radio emission of Cygnus X-1 on the orbital period (11). Electrons in the ionized wind of the O star can absorb radio photons in the presence of atomic nuclei, preventing the radio emission from the inner parts of the jet from reaching us. This free-free absorption is reduced as the stellar wind density decreases, as it moves away from the O star, allowing radiation to escape from further downstream. As the black hole (from which the jet is launched) moves around its orbit, the varying path length through the stellar wind imprints an orbital periodicity on the apparent radio position along the jet axis. When the black hole is on the far side of the donor star, the path length and hence absorption are maximized, pushing the radio photosphere downstream along the jet axis (10).

To negate the effect of the stellar wind absorption, we therefore repeated our astrometric model fitting in one dimension only, perpendicular to the known jet axis. This removed the orbital phase dependence of the fit residuals perpendicular to the jet axis (Fig. 2). Our measured semimajor axis of the black hole orbit is  $58 \pm 20$  micro-arc sec, and our revised parallax measurement is  $0.46 \pm 0.04$  milli-arc sec, which is consistent with the optical value from *Gaia* after correction for the zero point. After converting our measured

<sup>1</sup>International Centre for Radio Astronomy Research—Curtin University, Perth, WA 6845, Australia. <sup>2</sup>Astronomy Department, San Diego State University, San Diego, CA 92182-1221, USA. <sup>3</sup>School of Physics and Astronomy, Monash University, Clayton, VIC 3800, Australia. <sup>4</sup>OzGrav: The Australian Research Council Centre of Excellence for Gravitational Wave Discovery, Hawthorn, VIC 3122, Australia. <sup>5</sup>School of Physics and Astronomy, University of Birmingham, Edgbaston, Birmingham B15 2TT, UK. <sup>6</sup>Key Laboratory for Computational Astrophysics, National Astronomical Observatories, Chinese Academy of Sciences, Beijing 100012, China. <sup>7</sup>University of Chinese Academy of Sciences, Beijing 100012, China. <sup>8</sup>Department of Physics and Astronomy, Texas Tech University, Lubbock, TX 79409-1051, USA. <sup>9</sup>Nicolaus Copernicus Astronomical Center, PL-00-716 Warsaw, Poland. <sup>10</sup>Center for Astrophysics, Harvard and Smithsonian, Cambridge, MA 02138, USA. <sup>11</sup>Anton Pannekoek Institute for Astronomy, University of Amsterdam, 1098 XH Amsterdam, Netherlands. <sup>12</sup>Korea Astronomy and Space Science Institute, Daejeon 34055, Republic of Korea. <sup>13</sup>University of Science and Technology, Daejeon 34113, Republic of Korea. <sup>14</sup>International Centre for Radio Astronomy Research—University of Western Australia, Crawley, WA 6009, Australia. <sup>15</sup>Institut für Astronomie und Astrophysik, Universität Tübingen, 72076 Tübingen, Germany. <sup>16</sup>Joint Institute for Very Long Baseline Interferometry European Research Infrastructure Consortium, 7991 PD Dwingeloo, Netherlands. <sup>17</sup>Gravitation and Astroparticle Physics Amsterdam Institute, University of Amsterdam, NL-1098 XH Amsterdam, Netherlands. <sup>18</sup>Commonwealth Scientific and Industrial Research Organisation, Astronomy and Space Science, Perth, WA 6102, Australia. <sup>19</sup>Observatorio Astronómico Nacional, Instituto Geográfico Nacional, 28014 Madrid, Spain. <sup>20</sup>Department of Physics, Astrophysics, University of Oxford, Oxford OX1 3RH, UK. <sup>21</sup>School of Physics and Astronomy, University of Southampton, Southampton SO17 1BJ, UK. <sup>22</sup>Center for Astro, Particle, and Planetary Physics, New York University Abu Dhabi, Abu Dhabi, United Arab Emirates. <sup>23</sup>Department of Physics, Centennial Centre for Interdisciplinary Science, University of Alberta, Edmonton, AB T6G 2E1, Canada. <sup>24</sup>East Asian Observatory, Hilo, HI 96720, USA. <sup>25</sup>Institute for Space Sciences, 077125 Bucharest-Magurele, Romania. <sup>26</sup>Dr. Karl Remeis-Sternwarte and Erlangen Centre for Astroparticle Physics, Friedrich-Alexander-Universität Erlangen-Nürnberg, 96049 Bamberg, Germany.

\*Corresponding author. Email: james.miller-jones@curtin.edu.au. †Present address: Max-Planck-Institut für Extraterrestrische Physik, D-85748 Garching, Germany.



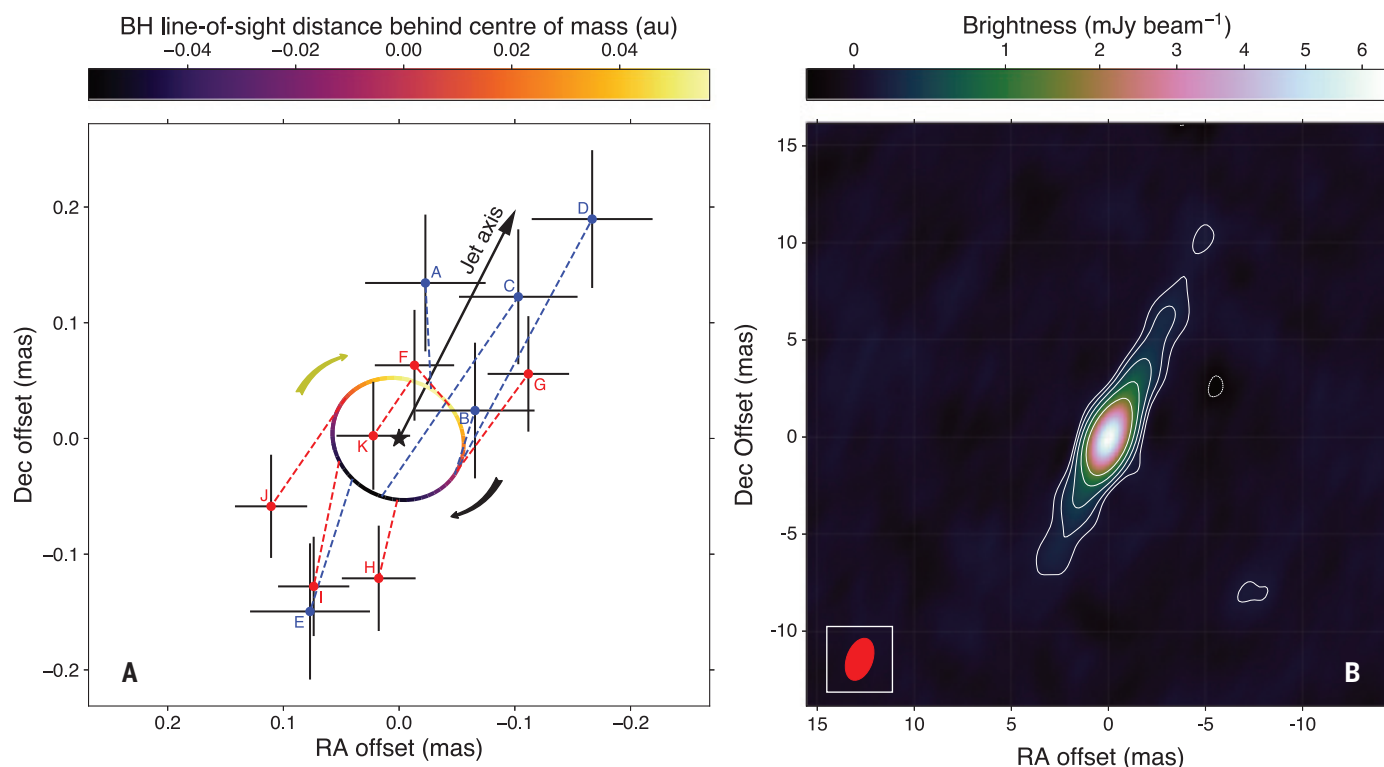


**Fig. 1. Cygnus X-1 and its best fitting model orbit on the plane of the sky.**

(A) Astrometric measurements from the new (red points) and archival (blue points) VLBA data (5). Error bars show the 68% confidence level. The letter labels indicate the chronological ordering of the observations, as detailed in table S1. Dashed lines link the measured positions to the location on the fitted orbit, shown as the colored ellipse. The color bar indicates the location of the black hole along the line of sight, relative to the center of mass of the system (shown as the black star), with positive values being behind the

center of mass. Arrows indicate the direction of orbital motion and the jet axis. (B) Stacked radio image of the jet in color, with white contours every  $\pm(\sqrt{2})$  times the root mean square noise level of 23 microjanskys ( $\mu$ Jy) per beam. The red ellipse indicates the size and shape of the synthesized beam. Although the measured positions scatter along the jet axis, the motion perpendicular to the jet axis is reproduced by the astrometric model (Fig. 2). Coordinates are given in right ascension (RA) and declination (Dec), J2000 equinox, mas, milli-arc seconds.

parallax to a distance by using an exponentially decreasing space density prior (12), we found a distance of  $2.22^{+0.18}_{-0.17}$  kpc.

This revised distance affects the system parameters derived from optical modeling (6). We reanalyzed the optical light curve (13) and radial velocity curves (14), adopting our revised distance and additional constraints on the effective temperature, surface gravity, and helium abundance of the donor star (15). We found substantially higher masses for both the black hole ( $21.2 \pm 2.2 M_{\odot}$ ) (fig. S8) and the donor star ( $40.6^{+7.7}_{-7.1} M_{\odot}$ ). The black hole orbital semimajor axis derived from this reanalysis of the optical data are  $0.160 \pm 0.013$  astronomical units (au) (Table 1), which equates to  $73 \pm 8$  micro-arc sec at our best-fitting distance of  $2.22^{+0.18}_{-0.17}$  kpc. This is consistent with the value derived directly from our VLBA astrometry (Fig. 2 and table S3).

The higher donor mass and greater luminosity inferred from the larger distance (Table 1) bring the system into closer agreement with the mass-luminosity relationship for main-sequence hydrogen-burning stars of solar composition (7, 10). However, the measured

surface composition shows that the helium-to-hydrogen ratio is enhanced by a factor of 2.6 relative to the solar composition (15). This would imply a slightly different mass-luminosity relationship if the surface abundance is indicative of the overall composition of the donor star but remains broadly consistent with our revised values (Fig. 3).

The higher mass and distance could also affect the black hole spin determined from spectral fitting of the x-ray continuum (16). We therefore reanalyzed archival x-ray data using a continuum-fitting method, assuming the black hole spin axis is aligned with the orbital plane. We found the black hole dimensionless spin parameter  $a_* > 0.9985$ , which is close to the maximum possible value of 1, although this could be affected by systematic uncertainties (10). Even if the true value is less extreme, it would still be very high, which is consistent with previous results derived from both the continuum and iron line-fitting methods (16, 17). Although the spin derived from our analysis would be reduced if the black hole spin axis were not aligned with the orbital plane, even a  $15^\circ$  misalignment would still require a high spin,  $a_* = 0.9696$ .

As an x-ray binary system with a high-mass donor star, the black hole in Cygnus X-1 cannot have been spun up by accretion from its companion at the maximum theoretical rate (known as the Eddington limit;  $\sim 2 \times 10^{-7} M_{\odot} \text{ year}^{-1}$  for Cygnus X-1) because that cannot occur for longer than the lifetime of the donor [ $\sim 4$  million years for our inferred mass (18)]. The accretion time may be close to the age of the jet-inflated nebula surrounding the source [a few tens of thousands of years (19)]. The current spin must therefore reflect the angular momentum of the core of the progenitor star. An evolutionary pathway that could explain this is main sequence mass transfer from the black hole progenitor to the secondary star [case A mass transfer (20)] with the core of the progenitor tidally locked and hence rapidly rotating, which can produce high black hole spins (21). This evolutionary pathway for Cygnus X-1 would imply a spin axis of the black hole progenitor that is aligned with the orbital angular momentum. Given the very low velocity kick of  $9 \pm 2 \text{ km s}^{-1}$  imparted to the system upon black hole formation [as determined with VLBA astrometry (22)], the

**Table 1. Fitted and derived physical parameters for Cygnus X-1.** The inclination  $i$ , eccentricity  $e$ , and argument of periastron  $\omega$  of the orbit; the mass  $M_1$ , Roche-lobe filling factor  $f_1$ , effective temperature  $T_{\text{eff}}$ , and semi-amplitude of the radial velocity curve  $K_1$  for the O-star; a phase shift parameter  $\phi$  to account for ephemeris errors; and the ratio  $\Omega_{\text{rot}}$  of the rotational frequency of the O-star to the orbital frequency (the top nine parameters) were directly fitted in the model. The black hole mass  $M_{\text{BH}}$ ; the radius  $R_1$  in solar radii  $R_\odot$ , luminosity  $L$  in solar luminosities  $L_\odot$ , and surface gravity  $g_1$  of the O-star; and the semimajor axes of the full orbit  $a$ , stellar orbit  $a_1$ , and black hole orbit  $a_{\text{BH}}$  (the bottom seven parameters) were derived from the fitted parameters, by using the known orbital period (13). Lower and upper bounds encompass the 68% confidence interval.

Parameter	Median	Mode	Lower bound	Upper bound
$i$ (deg)	27.51	27.33	26.94	28.28
$e$	0.0189	0.0186	0.0163	0.0217
$\omega$ (deg)	306.6	306.3	300.3	313.1
$M_1$ ( $M_\odot$ )	40.6	39.8	33.5	48.3
$f_1$	0.960	0.999	0.930	0.988
$T_{\text{eff}}$ (K)	31,138	31,158	30,398	31,840
$K_1$ (km s $^{-1}$ )	75.21	75.18	74.80	75.63
$\phi$	0.0024	0.0023	0.0013	0.0034
$\Omega_{\text{rot}}$	1.05	1.04	0.95	1.16
$M_{\text{BH}}$ ( $M_\odot$ )	21.2	21.4	18.9	23.4
$R_1$ ( $R_\odot$ )	22.3	22.2	20.6	24.1
$\log(L/L_\odot)$	5.625	5.606	5.547	5.698
$\log(g_1/\text{cm s}^{-2})$	3.348	3.351	3.335	3.360
$a$ (au)	0.244	0.243	0.231	0.256
$a_1$ (au)	0.0838	0.0840	0.0816	0.0856
$a_{\text{BH}}$ (au)	0.160	0.159	0.147	0.173

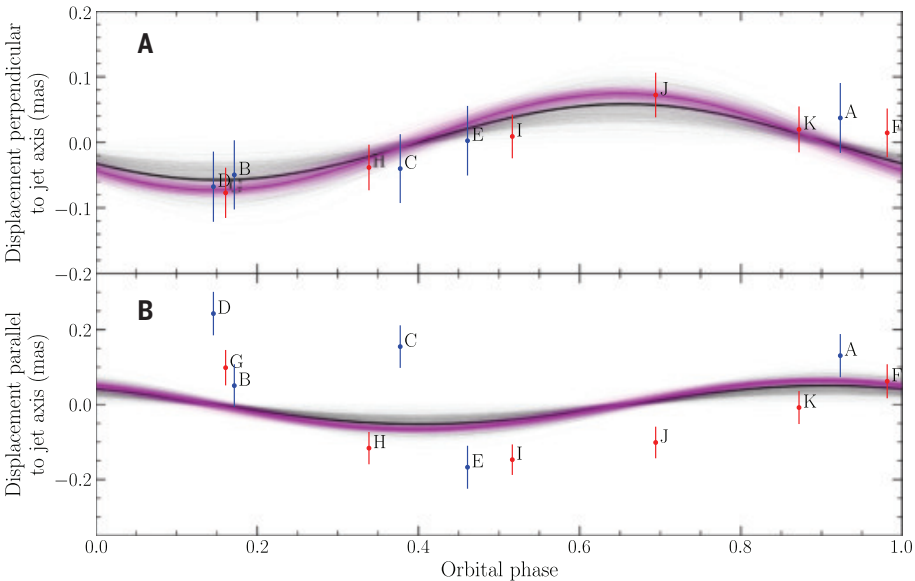


**Fig. 2. Orbital displacements relative to the best-fitting one-dimensional astrometric model.** Parallax and proper motion signatures have been subtracted. **(A)** The measured displacements perpendicular to the jet axis. Red points are our VLBA data, and blue points are the archival observations (5), with error bars showing the 68% confidence level. Labels reflect the chronological ordering of the observations, as listed in table S1. Black and magenta lines show 500 random draws from the posterior probability distribution of the orbital parameters for radio and optical models, respectively (with the posterior medians indicated with thicker lines), which are consistent within the uncertainties. The data were only fitted perpendicular to the jet axis. **(B)** The measured displacements parallel to the jet axis show that the measured core positions are primarily downstream of the model predictions when the black hole is close to superior conjunction (behind the donor star; phases close to 0.0) and upstream when the black hole is close to inferior conjunction (phases close to 0.5), as expected for wind absorption.

black hole spin should still be aligned with the orbital inclination, as we assumed above. This scenario is also consistent with the low orbital eccentricity (6) and the lack of strong quasi-periodic variability seen in the x-ray power density spectra of the source (23).

This evolutionary pathway is associated with enhanced nitrogen abundances, as observed in the donor spectrum (21). The transfer of enriched material from the black hole progenitor could also explain the high helium abundance in the spectrum of the donor star (15). In the absence of convection, which is expected to be limited to a very thin surface layer in the envelope of a 40  $M_\odot$  star of solar [or possibly supersolar (15)] metallicity, some fraction of this material would be retained on the surface for up to  $\sim 10^5$  years (supplementary text). As a surface contaminant, this would not be reflective of the overall composition of the donor. Our revised values for the mass and luminosity of the donor star are consistent with theoretical expectations (Fig. 3) (10).

The increase in the inferred black hole mass makes Cygnus X-1 more massive than previously observed black holes in x-ray binaries (24), surpassing M33 X-7. M33 X-7 has a substantially subsolar metallicity ( $\sim 0.1$  times the solar metallicity,  $Z_\odot$ ) (3). However, the metallicity of the mass donor in Cygnus X-1 is much higher. It has been estimated to be approximately twice solar (15), although the complexity of the system makes precise measurements challenging, and the true value may be closer to solar (10). The existence of a 21  $M_\odot$  black hole at solar (or supersolar) metallicity implies that mass loss rate prescriptions (4) overestimate the mass loss during the luminous blue variable or Wolf-Rayet stages of stellar evolution (25, 26). Assuming solar metallicity for the system, we found that either the mass loss rates in Wolf-Rayet winds from naked helium stars are reduced by a factor of three compared with those of current models (4), or those in luminous blue variable winds are reduced by at least a third, or both (supplementary text).

Reduced mass loss can lead to higher progenitor masses at the time of the supernova. It may also allow massive stars at moderate metallicities to retain hydrogen as they evolve [although probably not in the evolutionary history of Cygnus X-1, in which the black hole's progenitor likely had most of its hydrogen stripped off by the companion while the former was still on the main sequence (supplementary text)]. This would change the observational signatures of supernovae—for example, producing hydrogen-rich (pulsational) pair-instability supernovae (27). Enrichment of the interstellar medium by stellar winds could be reduced, and depending on which phases of the stellar evolution are most affected by reduced winds, the contribution of



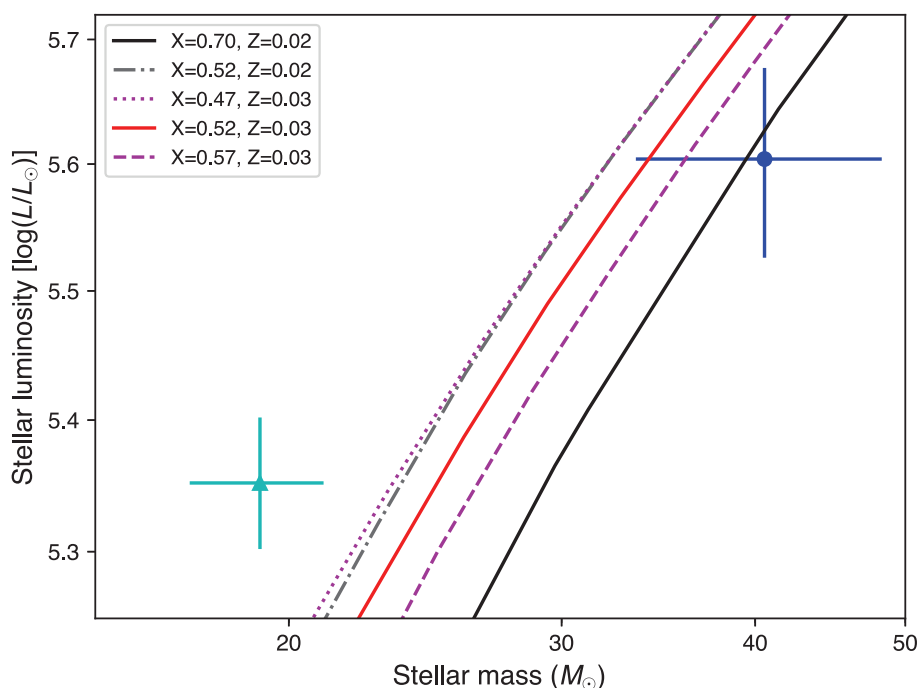


**Fig. 3. Predicted mass-luminosity relations for high-mass main sequence stars.** Masses are given in solar masses, and luminosities are relative to the solar luminosity  $L_{\odot}$ . The black solid line shows the predicted relation for a standard composition [hydrogen mass fraction  $X = 0.70$ ; mass fraction of heavy elements  $Z = 0.02$  (10)]. The gray dot-dashed line is for an enhanced helium abundance,  $X = 0.52$ ,  $Z = 0.02$  [as inferred for the surface abundance of the donor star (15)]. The red solid line shows the effect of an increased metallicity, with  $Z = 0.03$ ,  $X = 0.52$ . The magenta dotted line and dashed line show the effect of the uncertainty on the helium abundance (15). The mass and luminosity determined from previous observations (6) are shown as the cyan triangle. The values derived from our observations are shown as the blue circle, which lies closer to the theoretical relations, irrespective of composition or metallicity. Error bars show 68% confidence levels.

massive stars to the reionization of the Universe may be affected (supplementary text).

The black hole mass distribution inferred from gravitational wave events favors larger masses than predicted by stellar and binary evolution models. Variations in metallicity-specific star formation history that favor greater star formation at lower metallicities have been proposed as an explanation (28, 29). Reduced stellar winds would increase the mass of black holes that could be produced at all metallicities, so that massive gravitational wave sources could form at intermediate (not just very low) metallicities. This would imply that the progenitors of some gravitational wave events could have formed at a correspondingly lower redshift, with a shorter delay time between binary formation and merger.

The high spin of Cygnus X-1 [in common with most high-mass black hole x-ray binaries, which appear to be predominantly rapidly spinning (30)] implies that it followed an evolutionary pathway different to that of the majority of black holes detected in gravitational wave events, which have spins that are either low or misaligned (31). Given the current orbital separation, we do not expect Cygnus X-1 to undergo a binary black hole

merger in a time scale equal to the age of the Universe.

#### REFERENCES AND NOTES

1. B. P. Abbott *et al.*, *Astrophys. J.* **882**, L24 (2019).
2. J. Casares, P. G. Jonker, *Space Sci. Rev.* **183**, 223–252 (2014).
3. J. A. Orosz *et al.*, *Nature* **449**, 872–875 (2007).
4. K. Belczynski *et al.*, *Astrophys. J.* **714**, 1217–1226 (2010).
5. M. J. Reid *et al.*, *Astrophys. J.* **742**, 83 (2011).
6. J. A. Orosz *et al.*, *Astrophys. J.* **742**, 84 (2011).
7. J. Ziolkowski, *Mon. Not. R. Astron. Soc. Lett.* **440**, L61–L65 (2014).
8. Gaia Collaboration *et al.*, *Astron. Astrophys.* **616**, A1 (2018).
9. V. C. Chan, J. Bovy, *Mon. Not. R. Astron. Soc.* **493**, 4367–4381 (2020).
10. Materials and methods are available as supplementary materials.
11. C. Brocksopp, R. P. Fender, G. G. Pooley, *Mon. Not. R. Astron. Soc.* **336**, 699–704 (2002).
12. T. L. Astraatmadja, C. A. L. Bailer-Jones, *Astrophys. J.* **832**, 137 (2016).
13. C. Brocksopp, A. E. Tarasov, V. M. Lyuty, P. Roche, *Astron. Astrophys.* **343**, 861 (1999).
14. D. R. Gies *et al.*, *Astrophys. J.* **583**, 424–436 (2003).
15. V. V. Shimanskii *et al.*, *Astron. Rep.* **56**, 741–760 (2012).
16. L. Gou *et al.*, *Astrophys. J.* **742**, 85 (2011).
17. R. Duro *et al.*, *Astron. Astrophys.* **589**, A14 (2016).
18. A. Bressan *et al.*, *Mon. Not. R. Astron. Soc.* **427**, 127–145 (2012).
19. D. M. Russell, R. P. Fender, E. Gallo, C. R. Kaiser, *Mon. Not. R. Astron. Soc.* **376**, 1341–1349 (2007).
20. R. Kippenhahn, A. Weigert, *Z. Astrophys.* **65**, 251 (1967).
21. Y. Qin, P. Marchant, T. Fragos, G. Meynet, V. Kalogera, *Astrophys. J.* **870**, L18 (2019).
22. I. F. Mirabel, I. Rodriguez, *Science* **300**, 1119–1120 (2003).
23. V. Grinberg *et al.*, *Astron. Astrophys.* **565**, A1 (2014).
24. B. E. Tetarenko, G. R. Sivakoff, C. O. Heinke, J. C. Gladstone, *Astrophys. J.* **222**, 15 (2016).

25. J. R. Hurley, O. R. Pols, C. A. Tout, *Mon. Not. R. Astron. Soc.* **315**, 543–569 (2000).
26. J. S. Vink, A. de Koter, H. J. G. L. M. Lamers, *Astron. Astrophys.* **369**, 574–588 (2001).
27. I. Arcavi *et al.*, *Nature* **551**, 210–213 (2017).
28. C. J. Neijssel *et al.*, *Mon. Not. R. Astron. Soc.* **490**, 3740–3759 (2019).
29. M. Chruslinska, G. Nelemans, *Mon. Not. R. Astron. Soc.* **488**, 5300–5326 (2019).
30. M. C. Miller, J. M. Miller, *Phys. Rep.* **548**, 1–34 (2015).
31. W. M. Farr *et al.*, *Nature* **548**, 426–429 (2017).
32. J. C. A. Miller-Jones *et al.*, Cygnus X-1: Emerging view of a 21-solar mass black hole in the Milky Way. Zenodo (2021); doi:10.5281/zenodo.4548614.

#### ACKNOWLEDGMENTS

We acknowledge G. Pooley's contribution to the radio observing campaign. The VLBA is a facility of the National Science Foundation operated under cooperative agreement by Associated Universities Inc. This work made use of the Swinburne University of Technology software correlator, developed as part of the Australian Major National Research Facilities Programme and operated under license. This work has made use of data from the European Space Agency (ESA) mission *Gaia* ([www.cosmos.esa.int/gaia](http://www.cosmos.esa.int/gaia)), processed by the *Gaia* Data Processing and Analysis Consortium (DPAC; [www.cosmos.esa.int/web/gaia/dpac/consortium](http://www.cosmos.esa.int/web/gaia/dpac/consortium)). Funding for the DPAC has been provided by national institutions, in particular the institutions participating in the *Gaia* Multilateral Agreement. **Funding:** J.C.A.M.-J. and I.M. are recipients of Australian Research Council Future Fellowships (FT140101082 and FT190100574, respectively) funded by the Australian government. L.G. acknowledges support from the National Program on Key Research and Development Project through grant 2016YFA0400804, and from the National NSFC with grant U1838114, and by the Strategic Priority Research Program of the Chinese Academy of Sciences through grant XDB23040100. V.G. is supported through the Margaret von Wrangell fellowship by the ESF and the Ministry of Science, Research and the Arts Baden-Württemberg. B.M. acknowledges support from the Spanish Ministerio de Economía y Competitividad (MINECO) under grant AYA2016-76012-C3-1-P and from the Spanish Ministerio de Ciencia e Innovación under grants PID2019-105510GB-C31 and CEX2019-000918-M of ICCUB (Unidad de Excelencia "María de Maeztu" 2020–2023). S.M. was supported by the Netherlands Organization for Scientific Research (NWO) VICI grant (639.043.513). G.R.S. acknowledges support from an NSERC Discovery Grant (RGPIN-2016-06569). V.T. is supported by program Laplas VI of the Romanian National Authority for Scientific Research. J.W. acknowledges funding from the Bundesministerium für Wirtschaft und Technologie under Deutsches Zentrum für Luft- und Raumfahrt grant 50 OR 1606. J.Z. acknowledges the support from the Polish National Science Centre grant 2015/18/A/ST9/00746. **Author contributions:** J.C.A.M.-J. analyzed the VLBA data and led the manuscript preparation. A.B. conducted the astrometric fitting. J.A.O. conducted the optical light curve and radial velocity curve fitting. I.M. and C.J.N. performed the stellar wind modeling and led the discussion of the system's evolution, with input from T.J.M.; L.G., X.Zha., and X.Zhe. performed the analysis of the black hole spin. J.Z. calculated the mass-luminosity tracks. M.J.Re. provided the archival VLBA data and guidance on precision astrometry. P.U., V.G., J.C.A.M.-J. and J.W. coordinated the VLBA observing campaign, with theoretical input from S.M.; J.C.A.M.-J., P.U., T.J.M., V.T., A.P.R., J.W., and D.M.R. wrote the observing proposal, and D.-Y.B., R.D., T.J., J.-S.K., B.M., M.J.R.I., G.R.S., and A.J.T. contributed to the design and setup of the observations. All authors provided input and comments on the manuscript. **Competing interests:** The authors declare no conflicts of interest. **Data and materials availability:** The raw VLBA data are available from the NRAO archive at <https://archive.nrao.edu/archive/advquery.jsp> under project codes BRI41 and BM429. Our measured positions are listed in table S1. The COMPAS population synthesis code is available at <https://github.com/TeamCOMPAS/COMPAS>. Our software for performing the astrometric and optical model fitting, the spin fitting, and for calculating the mass-luminosity relationships, together with our COMPAS input and output files, are available at [https://github.com/bersavosh/CygX-1\\_JMJ2021](https://github.com/bersavosh/CygX-1_JMJ2021) and archived at <https://zenodo.org/record/4548614> (32).

#### SUPPLEMENTARY MATERIALS

science.sciencemag.org/content/371/6533/1046/suppl/DC1  
Materials and Methods  
Supplementary Text  
Figs. S1 to S11  
Tables S1 to S3  
References (33–118)

18 February 2020; accepted 23 December 2020  
Published online 18 February 2021  
10.1126/science.abb3363

## FERROELECTRICS

## Toroidal polar topology in strained ferroelectric polymer

Mengfan Guo<sup>1</sup>, Changqing Guo<sup>2</sup>, Jian Han<sup>1</sup>, Shulin Chen<sup>3</sup>, Shan He<sup>1</sup>, Tongxiang Tang<sup>1</sup>, Qian Li<sup>1,4</sup>, Joseph Strzalka<sup>4</sup>, Jing Ma<sup>1</sup>, Di Yi<sup>1</sup>, Ke Wang<sup>1</sup>, Ben Xu<sup>1</sup>, Peng Gao<sup>3</sup>, Houbing Huang<sup>5</sup>, Long-Qing Chen<sup>6</sup>, Shujun Zhang<sup>7</sup>, Yuan-Hua Lin<sup>1</sup>, Ce-Wen Nan<sup>1\*</sup>, Yang Shen<sup>1,8\*</sup>

Polar topological texture has become an emerging research field for exotic phenomena and potential applications in reconfigurable electronic devices. We report toroidal topological texture self-organized in a ferroelectric polymer, poly(vinylidene fluoride-*ran*-trifluoroethylene) [P(VDF-TrFE)], that exhibits concentric topology with anticoupled chiral domains. The interplay among the elastic, electric, and gradient energies results in continuous rotation and toroidal assembly of the polarization perpendicular to polymer chains, whereas relaxor behavior is induced along polymer chains. Such toroidal polar topology gives rise to periodic absorption of polarized far-infrared (FIR) waves, enabling the manipulation of the terahertz wave on a mesoscopic scale. Our observations should inform design principles for flexible ferroic materials toward complex topologies and provide opportunities for multistimuli conversions in flexible electronics.

**M**anipulation of spin, charge, orbit, and lattice degrees of freedom has led to numerous key discoveries in the past few decades, such as multiferroics (1–3), colossal magnetoresistance (4, 5), and high-temperature superconductors (6, 7). Assembly of real-space order parameters into toroidal topological patterns, such as magnetic skyrmions (spin) (8, 9), polar vortices (charge) (10), and polar skyrmions (charge) (11), has been the topic of extensive research. The response of the toroidal moment for these topologies to external stimuli is expected to give rise to pyrotoroidic effects, piezotoroidic effects, electric field control of chirality (12), and other emerging phenomena. Toroidal polar topologies have been observed in ferroelectric oxides, including strained PbTiO<sub>3</sub> films (13) and superlattices of alternating PbTiO<sub>3</sub>/SrTiO<sub>3</sub> layers (10–12). The closure of dipolar vector flux is caused by the competition among elastic, electric, and gradient energies, which involves the interplay of charge, orbital, and lattice degrees of freedom.

Organic ferroelectrics are interesting materials for applications because they can be solu-

tion processed, are lower in cost, and may have better flexibility than ceramic ferroelectrics (14–16). The most commonly studied organic ferroelectric system is poly(vinylidene fluoride) (PVDF) and its binary and ternary copolymers (17–20). The primary dipolar moments of PVDF are induced by alternating -CF<sub>2</sub> and -CH<sub>2</sub> groups along the polymer chains, whereas the permanent dipoles perpendicular to the polymer chain can be switched by electric field through crankshaft rotation about the chain axis (21). However, toroidal polar topology has never been observed in ferroelectric polymers. The origin of dipolar moments in PVDF is different from their oxide counterparts. The semicrystalline nature of PVDF leads to a large portion of amorphous phases with randomly distributed chains, hindering the formation of long-range polar order. This raises the question of whether toroidal polar topology can ever exist in ferroelectric polymers and the driving forces for the topology formation can be identified.

We demonstrate the emerging toroidal polar topology in a ferroelectric polymer, poly(vinylidene fluoride-*ran*-trifluoroethylene) [P(VDF-TrFE)]. The effective alignment of the P(VDF-TrFE) lamellar crystals with their interchain dipoles perpendicular to the polymer chains self-organizing into a concentric pattern generates a toroidal polar topology. In addition, intrachain ferroelectricity parallel to the polymer chains is observed in P(VDF-TrFE), giving rise to the observed ferroelectric relaxation behavior in the aligned lamellae. The two orthogonal polarizations are coupled to each other, inducing a toroidal distribution of intrachain piezoelectricity. The biaxial strain induced by the Curie transition of P(VDF-TrFE) is responsible for the toroidal order and relaxor behavior because the local strain and elastic energy are redistributed with the flattened energy land-

scape of polarization states. In addition, the P(VDF-TrFE) lamellae with toroidal polar topology exhibit spatially periodic absorption on terahertz wave, which can be used to realize high-resolution terahertz raster and spatial light modulator. Our observations provide insight and design principles for integrating complex topologies into flexible materials, and also show opportunities for multistimuli conversions in flexible electronics.

By incorporating trifluoroethylene (TrFE) groups into PVDF, P(VDF-TrFE) exhibits a dominant crystalline  $\beta$  phase with an all-trans conformational sequence, leading to the strongest ferroelectricity among the PVDF family. The copolymer tends to crystallize into pseudo-hexagonal (orthorhombic), large-aspect-ratio lamellae with polymer chains parallel to the lamellar normal (the *c* axis) (22). The interchain dipoles of P(VDF-TrFE), which we attributed to the electronegativity difference between the H and F atoms, are induced perpendicular to the polymer chains. As illustrated at the bottom layer of Fig. 1A, such a configuration leads to the spontaneous electrical polarizations (straight arrows with blue-to-red gradient color) lying in the in-plane directions (*ab* plane) of the lamellae. Therefore, these dipoles could rotate substantially in the lamellar plane (Fig. 1A, circular arrow), which is an additional degree of freedom that is not possible to obtain in either oxide or other molecular ferroelectric materials (23, 24). This degree of freedom might be a different approach to inducing toroidal order with high radial symmetry in a low symmetrical crystal lattice.

To understand the degree of freedom for in-plane dipolar rotation, we used a melt-recrystallization method (25, 26) on spin-coated thin film to produce face-on lamellae with polymer chains vertically aligned and permanent polarizations lying in the in-plane directions of the film (Fig. 1A). We confirmed the vertical alignment of polymer chains with Fourier-transform IR spectroscopy (fig. S1), where an apparent parallel band ( $\mu/c$  axis) occurs at 1400 cm<sup>-1</sup> (27, 28) under grazing-incident IR beam with electric field parallel to the film normal. Because of the rotational electrical polarizations distributed along the in-plane directions of the film, assembly of the dipoles can be characterized by in-plane piezo-response force microscopy (IP-PFM; Fig. 1). Exotic polar texture with hierarchical domain structure was observed in the face-on lamellae (Fig. 1, B to D), which consists of two parts, a central circle at the lamellar center and the surrounding ring-shaped bands (Fig. 1B). Angle-resolved IP-PFM images reveal that these two parts both consist of anticoupled stripe domains (fig. S2). In the central circle, the distribution of stripe domains reveals that the dominant orientations of polarizations are 58° to each other (Fig. 1C and fig. S2), which

<sup>1</sup>State Key Lab of New Ceramics and Fine Processing, School of Materials Science and Engineering, Tsinghua University, Beijing 100084, China. <sup>2</sup>School of Aerospace Engineering, Beijing Institute of Technology, Beijing 100081, China.

<sup>3</sup>Electron Microscopy Laboratory and International Center for Quantum Materials, School of Physics, Peking University, Beijing 100871, China. <sup>4</sup>X-ray Science Division, Argonne National Laboratory, Lemont, IL 60439, USA. <sup>5</sup>Advanced Research Institute of Multidisciplinary Science, Beijing Institute of Technology, Beijing 100081, China. <sup>6</sup>Department of Materials Science and Engineering, The Pennsylvania State University, University Park, State College, PA 16802, USA. <sup>7</sup>Institute for Superconducting and Electronic Materials, Australian Institute for Innovative Materials, University of Wollongong, Wollongong, New South Wales 2500, Australia. <sup>8</sup>Center for Flexible Electronics Technology, Tsinghua University, Beijing 100084, China.

\*Corresponding author. Email: cwnan@mail.tsinghua.edu.cn (C.-W.N.); shyang\_mse@mails.tsinghua.edu.cn (Y.S.)



indicates that the polarizations are mainly aligned along the  $[110]$  and  $[1\bar{1}0]$  directions in the pseudohexagonal lattice of P(VDF-TrFE). Conversely, in the surrounding ring-shaped bands, the polarizations continuously rotate about the center, forming chiral domains with uniformly distributed in-plane polarization (Fig. 1A). Furthermore, the chiral domains split into two types, with a  $45^\circ$  intersection angle between the net polarizations and band boundaries in clockwise or anticlockwise direction (Fig. 1, A and D), wherein we observed polarization discontinuity caused by the existence of head-to-head and tail-to-tail domain walls at the band boundaries (figs. S3 and S4). We transformed the circular pattern of the in-plane polarization with a two-dimensional fast Fourier transform (Fig. 1E), which also suggests the rotational symmetry of the in-plane polarizations. The bright green concentric circles in the low-frequency region correspond to the repetitively and alternately arranged bands, and the dark green shadow in the high-frequency region arises from the continuous rotation of real-space polarizations in the anti-coupled chiral domains.

To verify the existence of emergent order parameter in face-on P(VDF-TrFE) lamellae, we obtained detailed polarization distribution using phase-field simulation (29). On the basis of the polarization map (Fig. 1A), we then calculated the electric toroidal moment of the polar topology. Given the definition of electric toroidal moment (30–32) as  $\vec{G} = \frac{1}{2V} \int_V \vec{r} \times \vec{P} dV$ , the electric toroidal moment along the  $z$  axis [ $G_z$  along the out-of-plane direction of the P(VDF-TrFE) face-on lamellae] is supposed to be substantially larger than those along  $x$  and  $y$  axes if toroidal order is present in the  $xy$  plane [ $x$  and  $y$  being in-plane directions of the P(VDF-TrFE) face-on lamellae]. By integrating the electric toroidal moment throughout the entire map and along a circular ring in the polarization map (fig. S5), we observed that  $G_z$  was one to two orders of magnitudes higher than  $G_x$  and  $G_y$  for both cases (table S2), justifying the existence of toroidal order within the face-on lamellae. The surface morphology in the atomic force microscopy (AFM) image (Fig. 1F) shows that the recrystallized P(VDF-TrFE) film consists of face-on lamellae with large lateral size ( $\sim 50 \mu\text{m}$ ) when film thickness is controlled around 100 nm. We observed the toroidal polar topology in all of these face-on lamellae (Fig. 1G). We also observed very similar yet much weaker signals using out-of-plane (OOP) PFM in the as-grown film (fig. S6). The IP-PFM scanning on thin film with edge-on lamellae (lamellar face perpendicular to film plane with  $c$  axis parallel to film plane) that we fabricated (33) indicates that the toroidal polar topology is distributed throughout the thickness of the face-on lamellae (fig. S7).

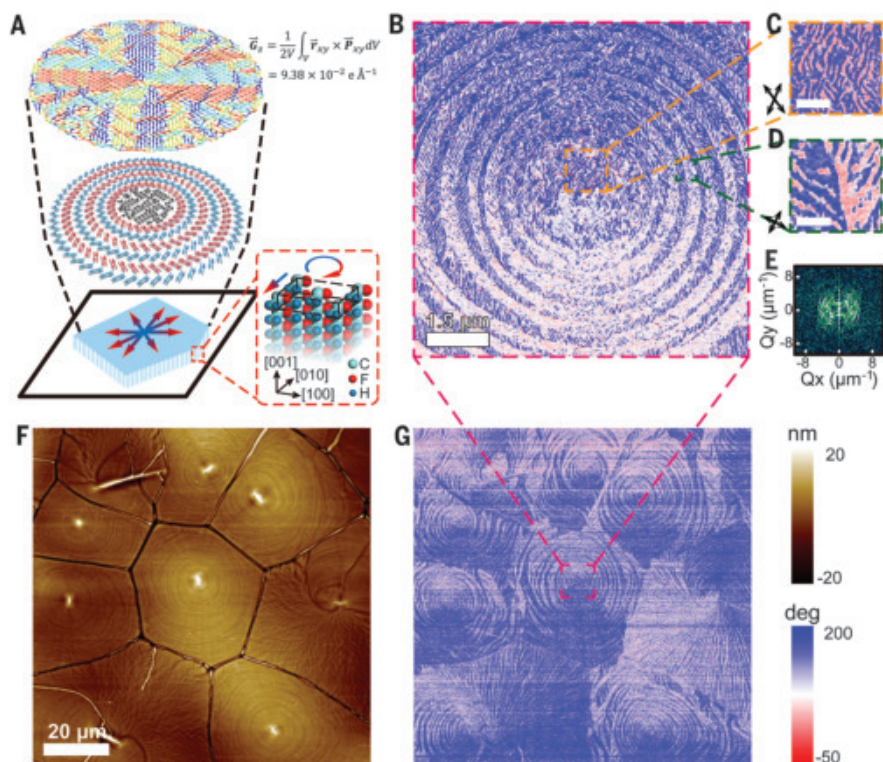


**Fig. 1. Observation of toroidal polar topology.** (A) Simulated polar topology (top) and schematic illustration of polarization (middle) and chain distribution (bottom) in a P(VDF-TrFE) lamella. Top layer is the simulated polarization map in a face-on lamella using the phase-field method. The electric toroidal moment of  $9.38 \times 10^{-2} \text{ e \AA}^{-1}$  along the  $z$  axis calculated accordingly suggests the existence of toroidal order in the polar topology. Middle layer is the schematic illustration of polarization distribution. In the central circle, the polarization states are mainly distributed along the  $\langle 110 \rangle$  and  $\langle 010 \rangle$  directions. In both types of bands, the polarization states show toroidal assembly uniformly oriented along in-plane directions. Bottom layer is the schematic illustration of a face-on lamella and its crystal orientation. The inset in the red dashed rectangle shows the oriented polymer chains and the lattice structure. In face-on lamellae, the polymer chains (denoted as the  $c$  axis) are aligned parallel to the lamellar normal. The straight arrows in blue-to-red gradient color denote the orientation of permanent dipoles. The circular arrow denotes the ability for these dipoles to rotate within the lamellar plane ( $ab$  plane) about the lamellar normal ( $c$  axis). (B) IP-PFM phase image showing hierarchical structures of the toroidal pattern [magnified from the area denoted by the red dashed square in (G)]. (C) IP-PFM phase image at the central circle [denoted by the orange dashed square in (B)], showing stripe domains in two dominant directions. Scale bar, 300 nm. (D) IP-PFM phase image at surrounding ring-shaped bands with band boundary [denoted by the green dashed square in (B)] showing the  $45^\circ$  intersection between stripes and band boundary in clockwise and anticlockwise direction. Scale bar, 150 nm. (E) Two-dimensional fast Fourier transform of (B) showing stronger concentric distribution in the low-frequency region and weaker shadow distribution in the high-frequency region. (F) Morphology of melt-recrystallized P(VDF-TrFE) consisting of face-on lamellae. (G) IP-PFM phase image of the same area in (F) exhibiting large-scale toroidal polar topologies in all lamellae.

The periodically banded structures (34–36) have often been observed in organic thin films during their melt-recrystallization processes, such as isotactic polystyrene (37), poly(L-lactide) (38), poly( $\epsilon$ -caprolactone) (39), and molecular semiconductors (40). The periodic surface topography is attributed to the competition between long-range mass transport from the surrounding melt and crystallization at the transformation front. We can use the same mechanism to explain the formation of the polar ring-shaped bands with chiral domains

in P(VDF-TrFE) during recrystallization from melt. In the case of the nonpolar molecules and macromolecules, however, the amplitude of periodic height undulation is on the order of film thickness, whereas for polar P(VDF-TrFE), the amplitude of surface undulation at the banded region is more than one order of magnitude smaller than the film thickness (Fig. 1F and fig. S8). Unlike those nonpolar organics, the strong polarity of PVDF-based polymers has a substantial impact on their crystallization behavior (41). Therefore, we

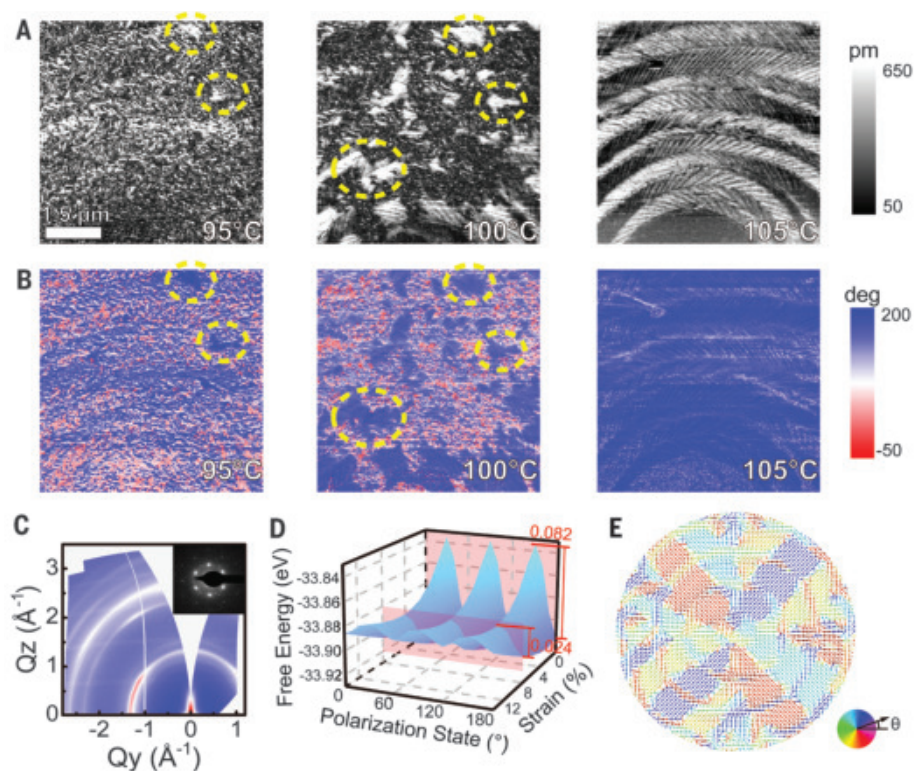


**Fig. 2. Characterization and calculations of P(VDF-TrFE) lamellae.** (A and B) Temperature-dependent IP-PFM (A) phase and (B) amplitude images of a face-on lamella. The yellow dashed circles denote several emerging paraelectric phase in the ferroelectric matrix. (C) GI-WAXS pattern of face-on lamellae. The main scattering arc appears at ( $Q_y = -1.31 \text{ \AA}^{-1}$ ,  $Q_z = 0 \text{ \AA}^{-1}$ ). Inset, SAED pattern of free-standing face-on lamellae. The pseudohexagonal pattern indicates that the face-on lamella is a single crystal with its  $c$  axis aligned parallel to the electron beam. (D) Energy levels of strained PVDF lattice at different polarization states. For simplification, instead of P(VDF-TrFE),  $\beta$ -phase PVDF chain is adopted, with  $[010]$  direction set as  $0^\circ$ . The lowest energy levels at  $60^\circ$ ,  $120^\circ$ , and  $180^\circ$  correspond to stable polarization states along  $[110]$ ,  $[\bar{1}\bar{1}0]$ , and  $[0\bar{1}0]$ , respectively. The free energy contrast of the strain free lattice is  $0.082 \text{ eV}$ , which reduces to  $0.024 \text{ eV}$  upon an 8% tensile strain, denoted by the red planes. (E) Polarization map of a face-on P(VDF-TrFE) lamella under tensile strain of 7.30% by phase-field simulations. Each arrow represents the direction of in-plane polarization as depicted in the colored disk. The diameter of simulated map is  $180 \text{ nm}$ .

believe that the permanent dipoles in banded structures is responsible for the partially alleviated surface undulation, resulting in the toroidal polar topology with less undulation amplitude in face-on P(VDF-TrFE) lamellae.

The formation of the toroidal polar topology is closely associated with the melt-recrystallization treatment, and thus we sought to understand the thermal evolution of the polar topology in P(VDF-TrFE) thin films. Two phase transitions exist in P(VDF-TrFE) when heating, the ferroelectric-paraelectric phase transition at  $\sim 100^\circ\text{C}$  and the paraelectric-disordered (molten) phase transition at  $\sim 135^\circ\text{C}$  (42). We used in situ, temperature-dependent PFM to observe the polar topology in the face-on lamellae as a function of temperature. To prevent the electrical interference of PFM tips on paraelectric face-on lamellae upon the transition to ferroelectric phase, we performed all of the observations upon heating.

Considering that P(VDF-TrFE) can be reversibly transformed among the ferroelectric, paraelectric, and disordered phases with thermal hysteresis (18), we believe that the evolution during heating could reversibly happen upon cooling. The ferro-to-paraelectric transition starts at  $95^\circ\text{C}$ , accompanied by the emerging paraelectric regions (Fig. 2, A and B, figs. S9 and S10). Increasing the temperature further induces the growth of the paraelectric phase. Notwithstanding the disappearance of anti-parallel stripe domains  $>105^\circ\text{C}$  (red color domains disappear in Fig. 2B at  $105^\circ\text{C}$ ), the toroidal topology still exists and can be clearly observed in paraelectric face-on lamellae (Fig. 2A at  $105^\circ\text{C}$ ). The paraelectric phase with disordered permanent dipoles is more responsive than the ferroelectric phase, which is contradictory to the concept that the paraelectric phase does not exhibit piezoelectricity. However, recent observations show the paraelectric and high-

temperature P(VDF-TrFE) adopting 3/1-helical chain conformation has a distortive degree of freedom (43). This structure is thought to account for the enhanced responsivity and more pronounced toroidal assembly observed at elevated temperatures. When we raise the temperature to  $>110^\circ\text{C}$ , the topology gradually weakens from the central circle of the face-on lamellae, and vanishes at  $140^\circ\text{C}$ , where the paraelectric phase completely changes to the disordered phase (fig. S11). We conclude from these observations that the toroidal order starts to form in the paraelectric phase at elevated temperature, whereas the ferroelectric order is assembled during the subsequent cooling to ferroelectric phase.

The continuous rotation of ferroelectric polarizations provides a solid foundation for the combination of ferroelectric and toroidal order. The measurements on crystalline structure and computation on corresponding free energy suggest that large biaxial tensile strain in the face-on lamellae stabilizes the polarization states along all the in-plane directions. We observed biaxial strain of 7.3% in P(VDF-TrFE) film with face-on lamellae by measuring the grazing-incident wide angle x-ray scattering (GI-WAXS) and selected area electron diffraction (SAED). In the GI-WAXS pattern of face-on lamellae (Fig. 2C), the main scattering arc appears with its center at ( $Q_y = -1.31 \text{ \AA}^{-1}$ ,  $Q_z = 0 \text{ \AA}^{-1}$ ), corresponding to the  $(110)/(200)$  duplicate units. For the SAED pattern (Fig. 2C), we observed only pseudohexagonal diffraction points corresponding to  $(110)/(200)$  planes, which verifies that the  $a$  and  $b$  axes are oriented along in-plane directions. We obtained the  $(110)/(200)$  spacing from these patterns, which are  $4.803$  and  $4.80 \text{ \AA}$  according to GI-WAXS and SAED patterns, respectively. These values are much larger than the  $(110)/(200)$  spacing of  $4.457 \text{ \AA}$  measured in a strain-free reference sample (fig. S12). Thus, the enhanced spacing in the face-on lamellae reveals a biaxial tensile strain of 7.3%, because all the  $(hk0)$  planes are vertically aligned in the face-on lamellae. By moving the sample in steps around a few microns with the diameter of selected area around  $190 \text{ nm}$ , we observed no change in lattice spacing and orientation within one lamella (fig. S13). Electron diffractions with multiple tilting angles and aperture diameter as large as  $3.8 \text{ \mu m}$  (figs. S14 and S15) also show distinct pseudohexagonal diffraction points, demonstrating that the strain is uniform in a single-crystalline lamella. Thermal expansion contrast between P(VDF-TrFE) and rigid substrate can only account for  $\sim 1\%$  of biaxial strain. Thus, other mechanisms should be responsible for such large strain.

The substantial changes in the lattice parameters during the Curie transition of P(VDF-TrFE) (44) could explain the large biaxial



strain in face-on lamellae. By measuring the temperature-dependent x-ray diffraction of the strain-free P(VDF-TrFE) (fig. S16) near its Curie point ( $\sim 100^\circ\text{C}$  in heating process), we can observe a large expansion along the  $a$  and  $b$  axes over the ferroelectric-to-paraelectric phase transition. Unlike Curie transition of ferroelectric oxides where polarization evolution is caused by the displacive movements of cations with minor lattice parameter change (45), the Curie transition of P(VDF-TrFE) involves substantial intramolecular changes in conformation sequence (46). For example, the disappearance of the all-trans sequence and the emergence of the gauche bond in paraelectric phase would lead to the rearrangement of the permanent dipoles. Consequently, the intermolecular interaction will be weakened and result in large expansion of interchain distance in the paraelectric phase of PVDF-based polymers while retaining the pseudo-hexagonal symmetry. During the Curie transition, the (110)/(200) lattice spacing increases from 4.48 Å in the ferroelectric phase to 4.93 Å in the paraelectric phase, accounting for a 9% biaxial shrinkage (close to the measured strain of 7.3%) during the paraelectric-to-ferroelectric transition. For a thin film with face-on lamellae where the  $a$  and  $b$  axes are oriented along the in-plane directions, a large biaxial tensile strain is introduced as the lamellae are clamped by the substrate (fig. S16). This clamping effect mainly relies on the inherent lattice change of the film, different from the lattice mismatch mechanism in epitaxially grown oxide films. The clamping effect is also revealed by the large-scale parallel stripes in face-on lamellae with large portion of gaps serving as strain-releasing sites when lamellar thickness is  $< 60$  nm (fig. S17).

To further explore the effect of strain on the in-plane ferroelectric polarization rotation, we performed first-principle calculations to examine the free energy of P(VDF-TrFE) film with different polarization orientations under different strain levels [figs. S18 to S21 (29)]. For the strain-free lattice (Fig. 2D), the chain rotation angles at  $0^\circ$ ,  $60^\circ$ , and  $120^\circ$  with corresponding polarization states along  $[010]$ ,  $[110]$ , and  $[\bar{1}\bar{1}0]$  exhibit the lowest free energy level. These results are consistent with the pseudo-hexagonal symmetry of  $\beta$ -phase PVDF-based polymers. Deviation from these low-energy states induces substantial increases in free energy, which therefore does not favor the continuous rotation of polarizations to form the toroidal polar topology. When large tensile strain is applied, the barrier between energy minimum and maximum in the energy landscape reduces substantially, leading to an almost degenerate state as polarization rotates in the  $ab$  plane. For instance, with biaxial tensile strain of 8% (close to the measured value of 7.3%; Fig. 2D, red plane), the energy

barrier between different polarization orientations reduces from 0.082 to 0.024 eV, almost one-fourth of the original value. The energy landscape should be further flattened when larger chain distance and lower interchain dipoles of P(VDF-TrFE) are considered. Thus, the strain-suppressed anisotropy within the  $ab$  plane could enable easier chain rotation for continuous rotation of polarizations. We note that this chain rotation degree of freedom is universal to all crystalline polymers.

For phenomenological understanding, we performed phase-field modeling to learn more about the effect of strain on the polarization distribution. The simulated polarization map of the wrinkled P(VDF-TrFE) nanodisk under a strain level of 7.30% (Figs. 1A and 2E) shows a toroidal polar topology with features similar to the IP-PFM phase image (Fig. 1B), where we observed the alternating bands with anticoupled domains. We chose a P(VDF-TrFE) nanodisk with a diameter of 180 nm to simulate the polarization evolution because the spatial scale in the phase-field simulations (hundreds of nanometers) is much smaller than the scale of lamellae in the experiments ( $> 10$   $\mu\text{m}$ ). Therefore, the phase-field simulations are applied to qualitatively analyze the polarization distribution. In fact, the large strain induced by the paraelectric-to-ferroelectric phase transition changes the interplay between

the electric and elastic energies (22). However, the toroidal assembly of polarizations is mainly attributed to the periodic undulation of the wrinkled surface, which redistributes the strain and consequent elastic energy in a concentric manner (fig. S22), affecting the local interplay among elastic, electric, and gradient energies. Thus, the film thickness plays an important role as it determines the application and redistribution of strain by controlling the film morphology (fig. S17). With the larger tensile strain applied, the polarizations rotate more continuously as the lateral size of anticoupled domains decreases with increasing strains (fig. S23), which is consistent with the degenerate free energies of all polarization states calculated by the first-principle calculations. Therefore, strain in the face-on lamellae is critical for the development of toroidal polar topology and enables continuous rotation of the in-plane polarizations in face-on P(VDF-TrFE) lamellae.

The flat energy landscape based on first-principle calculations suggests that tensile strain facilitates the chain rotation degree of freedom. Recent work on ferroelectric nylon also shows that the introduction of conformational defects can enable easier chain rotation and effectively induce relaxor-like behavior by suppressing the interchain hydrogen bond (47). Analogous to this, we believe that the

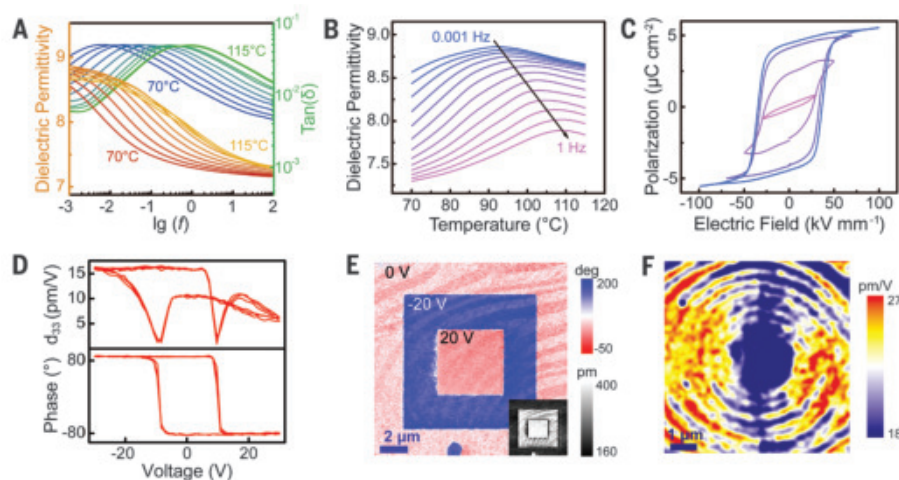


**Fig. 3. Properties of face-on P(VDF-TrFE) lamellae.** (A) Temperature-dependent broadband dielectric spectroscopy of face-on lamellae from 70 to  $115^\circ\text{C}$ . A relaxation peak related to ferroelectricity along the chain direction at ultra-low-frequency shifts to higher region with increasing temperature. (B) Temperature-dependent profiles of dielectric peaks along chain direction showing evident relaxor behavior. (C) P-E loops of multilayered face-on lamellae from Sawyer-Tower circuit. (D) PFM-switching spectrum of single-layered face-on lamellae measured by interferometric displacement sensor (IDS). (E) PFM phase image of face-on lamellae poled by conducting tip. The blue area was poled by  $-20$  V. The red area with square shape at the center was poled by  $20$  V. The outer red area was unpoled. Inset is the PFM amplitude image of the same area. The negatively poled area shows similar amplitude to the positively poled one. (F) PFM switching spectra mapping of face-on lamellae. Areas with stronger piezo responses are organized into a concentric pattern showing strong coupling between the toroidal topology and the ferroelectricity along the chain direction.

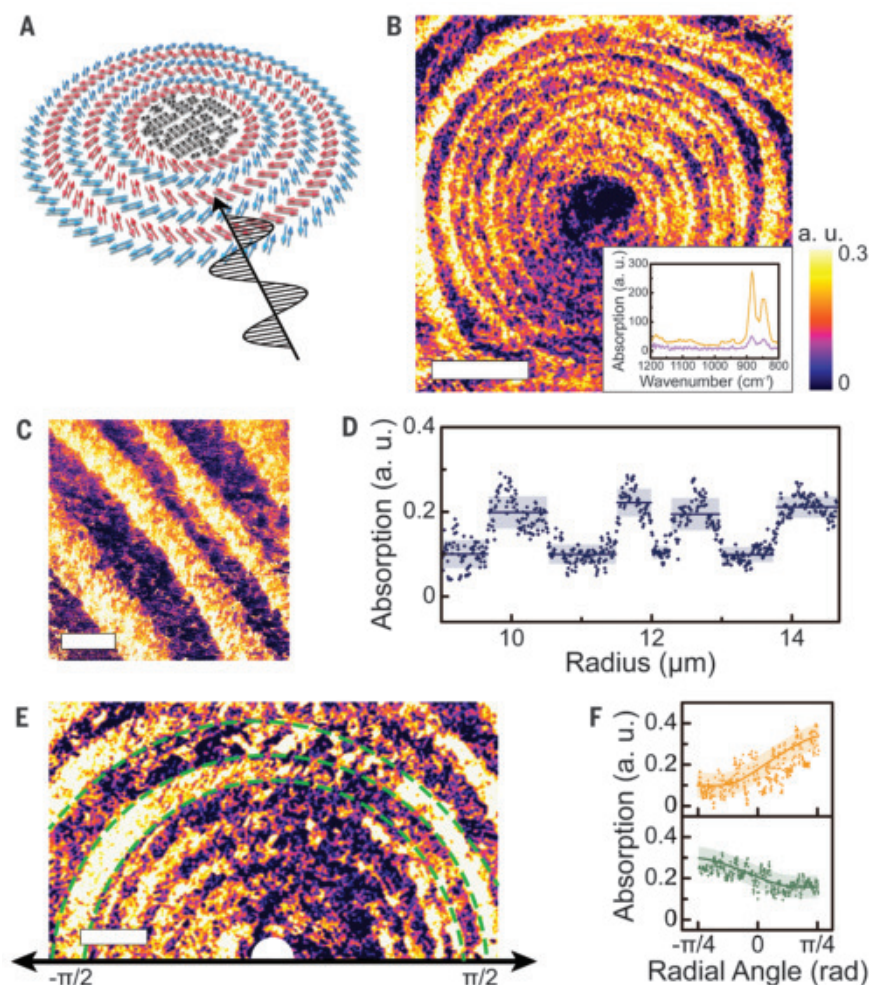


**Fig. 4. Spatially periodic absorption of FIR waves.** (A) Schematic illustration of the configuration of polarized IR beam and face-on lamellae in AFM-IR measurements. (B) Absorption mapping of face-on lamellae exhibiting toroidal topology on an FIR wave with wavenumber of  $880\text{ cm}^{-1}$ . Inset, AFM-IR spectra measured at neighboring bands, showing one-order-of-magnitude contrast. Scale bar,  $3\text{ }\mu\text{m}$ . (C and D) FIR absorption (C) mapping and (D) profile along radius direction in polar coordinate showing alternate low and high absorption level in neighboring bands. Scale bar,  $100\text{ nm}$ . (E and F) FIR absorption mapping (E) and profiles (F) along the radial angle direction in polar coordinate showing changes in absorption level within the same band; absorption distributions in the neighboring bands are inverse because of their orthogonal polarization states. Scale bar,  $100\text{ nm}$ .

relaxation behavior can also exist in face-on P(VDF-TrFE) lamellae. Using a customized holder for soft thin film [fig. S24 (29)], we obtained temperature-dependent dielectric spectra of the face-on lamellae (fig. S25). We measured the room temperature dielectric permittivity of the face-on P(VDF-TrFE) to be  $\sim 7$  and identified a relaxation peak at low frequency at elevated temperatures. Therefore, we conducted temperature-dependent broadband dielectric spectroscopy with frequency as low as  $10^{-3}\text{ Hz}$  (Fig. 3A), showing typical relaxation behavior in the temperature-dependent profiles (Fig. 3B). We note that this relaxation at low frequency should not be attributed to the space charge polarization be-

cause the slope of loss tangent versus frequency in logarithmic scale is  $-0.283$ , much smaller than  $-1$ , which is the main characteristic of ionic relaxation. We further fitted the experimental data to the Vogel-Fulcher law (20, 43, 48), confirming the relaxor nature in the strained face-on lamellae (fig. S26). The fitting yielded a freezing temperature of  $85.63^\circ\text{C}$ , which could rationalize the emergence of the distinct ferroelectric domains observed at room temperature (Fig. 1B). Conversely, the strain-free edge-on lamellae show no relaxation behavior over the entire frequency range (figs. S27 and S28). It is worth noting that the dielectric peak in fig. S27 around  $10^7\text{ Hz}$  is attributed to the relaxation of interchain dipoles perpendicular

to the polymer chains. For the face-on lamellae with vertically aligned polymer chains, the interchain dipoles are lying in the film plane and should be undetectable during the dielectric measurements. However, we can still measure a dielectric permittivity of  $\sim 7$ , which should be attributed to the dielectric response along the polymer chains. The special chain alignment in face-on lamellae exposes the polymer chains parallel to the electric field, and thus facilitates the dielectric response of the carbon backbone along the  $c$ -axial direction. Given the large size of the carbon backbone along polymer chains ( $100\text{ nm}$ ,  $\sim 1000$  atoms) compared with the rotational  $-\text{CH}_2-\text{CF}_2-$  groups about the  $c$  axis ( $\sim 0.3\text{ nm}$ ), this mechanism will also explain the relaxation process at low frequencies, as shown in Fig. 3A. The relaxor behavior is consistent with degenerate energy landscape with applied strain (Fig. 2D), which indicates that the relaxor property is associated with the tensile strain. Analogous to the bulky side groups (19) and electron irradiation (49) in PVDF-based polymers that break the long-range ferroelectric order, the biaxial strain induced by the Curie transition may also serve as a new route to transform normal ferroelectric P(VDF-TrFE) into relaxors.

Given the robust dielectric response along the  $c$  axis of the face-on P(VDF-TrFE) lamellae, we further explored the ferroelectricity along the  $c$  axis, the existence of which is still under debate. Park *et al.* reported the polarization extinction in P(VDF-TrFE) film with face-on lamellae (25), whereas Lee *et al.* still observed a P-E hysteresis loop in P(VDF-TrFE) film with the same orientation (26). The dielectric behavior that we observed (Fig. 3B) is distinctly different from that of interchain dipoles (figs. S27 and S28), suggesting that the  $c$ -axial ferroelectricity could rely on the intramolecular dipolar behaviors of the long chains. We then verified the ferroelectricity along polymer chains by measuring polarization hysteresis loops using a Sawyer-Tower circuit (Fig. 3C). We obtained typical hysteresis loops in the film with stacking, multilayered face-on lamellae, where we found the saturated polarization ( $P_s$ ) to be  $\sim 5\text{ }\mu\text{C cm}^{-2}$ . This value was  $\sim 50\%$  lower than the edge-on P(VDF-TrFE) lamellae (18) and similar to the value reported by Lee *et al.* (26). Furthermore, we used PFM equipped with an interferometric displacement sensor to measure the piezoelectric  $d_{33}$  of the face-on lamellae. We measured a butterfly-shaped curve with maximum  $d_{33}$  of  $\sim 15\text{ pm V}^{-1}$  (Fig. 3D), evidence of piezoelectricity along the  $c$  axis. By applying DC bias on the scanning tip, we can also switch the ferroelectric polarization along the  $c$  axis. As shown in the OOP-PFM scanning (Fig. 3E), both the negative and positive biases can activate the piezoelectric response (Fig. 3E, inset) with opposite phase.



Our observations confirmed that the dipoles along the chain direction ( $c$  axis in an orthogonal lattice) can be switched between bistable states. To eliminate the interference from charge injection, we characterized the polarization retention of the face-on P(VDF-TrFE) lamellae (fig. S29). The phase and amplitude of the switched areas remain unchanged after 150 min, confirming that the ferroelectric switching along the  $c$  axis of the face-on P(VDF-TrFE) lamellae was triggered upon the application of a tip voltage. Ultimately, ring-shaped reinforced regions with similar pattern to a toroidal topology were obtained by mapping the switching spectra of face-on lamella (Fig. 3F). Between the two types of chiral domains, one of them exhibits a 50% higher piezoelectric response. Our observations provide convincing evidence for ferroelectricity and piezoelectricity along the polymer chain direction (the  $c$  axis of the face-on lamellae) in the PVDF-family ferroelectric polymer materials. Furthermore, the in-plane ( $ab$  plane) toroidal polar topology is strongly coupled with the out-of-plane ferroelectricity along  $c$  axis according to the concentric distribution of  $c$ -axis piezoelectric coefficient.

The strong coupling between ferroelectric polarization and toroidal polar topology has great potential for multifunctional coupling in our films. Bulk P(VDF-TrFE) or its thick films were reported to exhibit macroscopic selective absorption on IR and terahertz waves (50–53). Considering that the scale of face-on lamellae (10–50  $\mu\text{m}$ ) and the toroidal bands (0.1 to 1  $\mu\text{m}$ ) are within the range of the terahertz wavelength (0.1 to 10 THz, 30 to 0.3  $\mu\text{m}$ ), we expect the toroidal polar topology to have the ability to microscopic manipulation on terahertz waves. This might enable terahertz raster and spatial light modulator (54, 55) with high spatial resolution. Therefore, we used an AFM equipped with tunable polarized IR beam (AFM-IR) to explore the potential application of the toroidal polar topology in terahertz optics. For face-on lamellae, the toroidal distribution of in-plane polarization could give rise to spatially resolved absorption modulation of IR waves. For the IR band of P(VDF-TrFE) in far-infrared (FIR) region at  $880\text{ cm}^{-1}$  (26.4 THz), the absorption is caused by the IR excitation of the symmetric stretching of  $\text{CF}_2$  groups, the transition dipoles of which are parallel to the in-plane ferroelectric polarizations [fig. S30 (27, 28)]. When a polarized FIR beam with electric field parallel to the film plane is projected to the face-on lamellae (Fig. 4A), the local absorptions of face-on lamellae continuously vary because of the alternated toroidal ferroelectric polarizations. We indeed observed the periodic absorption pattern of FIR beam on the toroidal topology (Fig. 4B). The IR absorption decreased by an order of magnitude (Fig. 4B,

inset) as the local polarization is vertical to the electric field of polarized FIR beam. By contrast, when the FIR beam was polarized with electric field perpendicular to the in-plane directions of the face-on lamellae, the absorption level in face-on lamellae is uniform (fig. S31). Despite the switching of ferroelectric polarization along the chain direction, we observed no coupling between the OOP polarizations and OOP absorptions.

The face-on lamellae with toroidal polar topologies exhibit strong selective FIR absorption with spatial periodicity. In polar coordinates, because the polarization states are orthogonal in neighboring bands, the absorption level varies periodically along the radius directions (Fig. 4, C and D). The spatial period depends on the width of the surrounding bands ( $\sim 200\text{ nm}$ ). In addition, the polarization states in the same band at different radial angles will change as the local polarization rotates. For the two neighboring bands (Fig. 4, E and F, green dashed lines), the absorption in the upper one changes from low level (purple) to high level (yellow) when radial angle increases, whereas absorption in the lower band with orthogonal polarization varies in an opposite manner (yellow to purple). Therefore, the IR absorption of the face-on lamellae shows spatial periodicity along the radius and radial angle in the polar coordinates. In addition, when the incident beam power is magnified, the local temperature will become high enough to enable preferential decomposition in face-on lamellae (fig. S32). For the P(VDF-TrFE) film that we studied with toroidal polar topology, the featured scale of spatially periodic absorption is smaller than the terahertz wavelength by one to two orders of magnitudes, and the scale of lamella itself is within the range of terahertz wavelength. Face-on lamellae with these characteristic sizes are also expected to enable the design of selective Rayleigh scattering (in which the size of the scattering body is smaller than the wavelength by more than one order of magnitude) and Mie scattering (in which the size of the scattering body is close to the wavelength) in the terahertz region. We believe that this behavior has great potential for near-field interconversion for terahertz applications, including sensing (52), imaging (56), and communications (57, 58).

The toroidal polar topology that we observed in P(VDF-TrFE) could be common to other organic ferroelectric systems because the strong lattice change during phase transition and the periodic surface topography after crystallization are common for molecular (macromolecular) crystals with low melting points. The manipulation of terahertz waves by toroidal and polar order through molecule orientation should also be applicable to other order-disorder ferroelectrics. In addition, be-

cause the ferroelectric properties of P(VDF-TrFE) change greatly near its morphotropic phase boundary (20), we would expect that the composition could be another dimension to manipulate the polar topology and the corresponding absorption behavior of electromagnetic waves. Thus, our observation of toroidal polar topology in a ferroelectric polymer may provide design opportunities for the interconversion of multistimuli in terahertz optics and enable the development of flexible device integrated with ferroic topology because the face-on lamellae can be fabricated directly on flexible substrates (see fig. S33).

## REFERENCES AND NOTES

- M. Dawber, K. M. Rabe, J. F. Scott, *Rev. Mod. Phys.* **77**, 1083–1130 (2005).
- R. Ramesh, N. A. Spaldin, *Nat. Mater.* **6**, 21–29 (2007).
- C. W. Nan, M. I. Bichurin, S. X. Dong, D. Viehland, G. Srinivasan, *J. Appl. Phys.* **103**, 031101 (2008).
- A. J. Millis, *Nature* **392**, 147–150 (1998).
- Y. Tokura, Y. Tomioka, *J. Magn. Magn. Mater.* **200**, 1–23 (1999).
- E. Dagotto, *Rev. Mod. Phys.* **66**, 763–840 (1994).
- Y. Tokura, N. Nagaosa, *Science* **288**, 462–468 (2000).
- S. Mühlbauer et al., *Science* **323**, 915–919 (2009).
- X. Z. Yu et al., *Nature* **465**, 901–904 (2010).
- A. K. Yadav et al., *Nature* **530**, 198–201 (2016).
- S. Das et al., *Nature* **568**, 368–372 (2019).
- A. R. Damodaran et al., *Nat. Mater.* **16**, 1003–1009 (2017).
- Y. L. Tang et al., *Science* **348**, 547–551 (2015).
- R. B. Meyer, L. Liebert, L. Strzelecki, P. Keller, *J. Phys. Lett.* **36**, 69–71 (1975).
- S. Horiuchi, Y. Tokura, *Nat. Mater.* **7**, 357–366 (2008).
- P. P. Shi et al., *Chem. Soc. Rev.* **45**, 3811–3827 (2016).
- A. J. Lovinger, *Science* **220**, 1115–1121 (1983).
- T. Furukawa, *Phase Transit.* **18**, 143–211 (1989).
- B. Neese et al., *Science* **321**, 821–823 (2008).
- Y. Liu et al., *Nature* **562**, 96–100 (2018).
- Y. Tajitsu, T. Masuda, T. Furukawa, *Jpn. J. Appl. Phys.* **26**, 1749–1753 (1987).
- E. Bellet-Amalric, J. F. Legrand, *Eur. Phys. J. B* **3**, 225–236 (1998).
- D. W. Fu et al., *Science* **339**, 425–428 (2013).
- H. Y. Ye et al., *Science* **361**, 151–155 (2018).
- Y. J. Park et al., *Appl. Phys. Lett.* **88**, 242908 (2006).
- J. S. Lee, A. A. Prabu, K. J. Kim, *Polymer (Guildf.)* **51**, 6319–6333 (2010).
- F. J. Boerio, J. L. Koenig, *Polymer Phys.* **9**, 1517–1523 (1971).
- M. Kobayashi, K. Tashiro, H. Tadokoro, *Macromolecules* **8**, 158–171 (1975).
- Materials and methods are available as supplementary materials.
- I. I. Naumov, L. Bellaiche, H. Fu, *Nature* **432**, 737–740 (2004).
- H. Schmid, *J. Phys. Condens. Matter* **20**, 434201 (2008).
- S. Prosandeev et al., *Phys. Rev. B* **87**, 195111 (2013).
- M. Guo et al., *Adv. Sci.* **6**, e1801931 (2019).
- A. G. Shtukenberg, Y. O. Punin, A. Gujral, B. Kahr, *Angew. Chem. Int. Ed.* **53**, 672–699 (2014).
- E. M. Woo, G. Lugito, *Eur. Polym. J.* **71**, 27–60 (2015).
- B. Crist, J. M. Schultz, *Prog. Polym. Sci.* **56**, 1–63 (2016).
- P. Poudel, S. Majumder, S. Chandran, H. Zhang, G. Reiter, *Macromolecules* **51**, 6119–6126 (2018).
- S. Nurkhamidah, E. M. Woo, *Macromol. Chem. Phys.* **214**, 673–680 (2013).
- Z. Wang et al., *Macromolecules* **40**, 4381–4385 (2007).
- J. S. Bangsund et al., *Nat. Mater.* **18**, 725–731 (2019).
- R. H. Gee, L. E. Fried, *J. Chem. Phys.* **118**, 3827–3834 (2003).
- T. Yagi, M. Tatemoto, J. Sako, *Polym. J.* **12**, 209–223 (1980).
- Y. Liu et al., *Nat. Mater.* **19**, 1169–1174 (2020).
- A. J. Lovinger, T. Furukawa, G. T. Davis, M. G. Broadhurst, *Polymer (Guildf.)* **24**, 1225–1232 (1983).
- A. R. Damodaran, E. Breckenfeld, Z. Chen, S. Lee, L. W. Martin, *Adv. Mater.* **26**, 6341–6347 (2014).
- K. Tashiro, K. Takano, M. Kobayashi, Y. Chatani, H. Tadokoro, *Ferroelectrics* **57**, 297–326 (1984).

47. Z. Zhang, M. H. Litt, L. Zhu, *Macromolecules* **50**, 9360–9372 (2017).
48. Y. Liu, Z. Han, W. Xu, A. Haibibu, Q. Wang, *Macromolecules* **52**, 6741–6747 (2019).
49. Q. M. Zhang, V. Bharti, X. Zhao, *Science* **280**, 2101–2104 (1998).
50. S. Bauer *et al.*, *Sens. Actuator A Phys.* **37–38**, 497–501 (1993).
51. T. D. Binnie, H. J. Weller, Z. He, D. Setiadi, *IEEE Trans. Ultrason. Ferroelectr. Freq. Control* **47**, 1413–1420 (2000).
52. A. Hassani, M. Skorobogatiy, *Opt. Express* **16**, 20206–20214 (2008).
53. J. Petzelt *et al.*, *Phys. Status Solidi. A Appl. Mater. Sci.* **210**, 2259–2271 (2013).
54. A. P. Mosk, A. Lagendijk, G. Lerosey, M. Fink, *Nat. Photonics* **6**, 283–292 (2012).
55. S.-Q. Li *et al.*, *Science* **364**, 1087–1090 (2019).
56. B. Ferguson, X.-C. Zhang, *Nat. Mater.* **1**, 26–33 (2002).
57. M. Lee *et al.*, *Science* **298**, 1401–1403 (2002).
58. S. Koenig *et al.*, *Nat. Photonics* **7**, 977–981 (2013).

## ACKNOWLEDGMENTS

We thank Z. Dan, Y. Liang, W. Wang, and S. Ren for helpful discussions and the Electron Microscopy Laboratory at Peking University for the use of electron microscopes. This research used resources at the Advanced Photon Source, a U.S. Department of Energy (DOE) Office of Science User Facility operated for the DOE Office of Science by Argonne National Laboratory under contract no. DE-AC02-06CH11357. **Funding:** This work was supported by the Basic Science Centre Program of NSFC (grant no. 51788104), the NSF of China (grant no. 51625202), and the National Key Research & Development Program (grant no. 2017YFB0701603). L.-Q.C. acknowledges support from the Hamer Foundation for the Hamer Professorship. **Author contributions:** M.G. and Y.S. conceived and performed the experiments. M.G., S.H., and T.T. fabricated the films. J.H. and B.X. performed the first-principle computations. C.G., H.H., and L.-Q.C. performed the phase-field simulations. S.C. and P.G. performed the TEM measurements. M.G., K.W., and J.M. performed the PFM measurements. Q.L. and J.S. performed the WAXS measurements. M.G. and S.H. conducted

the dielectric and ferroelectric measurements. M.G. and D.Y. performed the AFM-IR measurements. M.G. wrote the first draft of the manuscript. Y.S., S.Z., Y.-H.L., and C.-W.N. revised the manuscript. All authors discussed the results and edited the manuscript. **Competing interests:** The authors declare no competing interests. **Data and materials availability:** All relevant data are available in the main text or the supplementary materials.

## SUPPLEMENTARY MATERIALS

science.sciencemag.org/content/371/6533/1050/suppl/DC1  
Materials and Methods  
Supplementary Text  
Figs. S1 to S33  
Tables S1 and S2  
References (59–68)

26 April 2020; resubmitted 25 May 2020  
Accepted 14 January 2021  
10.1126/science.abc4727

## SPECTROSCOPY

## Tracing orbital images on ultrafast time scales

R. Wallauer<sup>1</sup>, M. Rath<sup>2,3,4</sup>, K. Stallberg<sup>1</sup>, L. Münster<sup>1</sup>, D. Brandstetter<sup>5</sup>, X. Yang<sup>2,3,4</sup>, J. Güdde<sup>1</sup>, P. Puschnig<sup>5</sup>, S. Soubatch<sup>2,3</sup>, C. Kumpf<sup>2,3,4</sup>, F. C. Bocquet<sup>2,3</sup>, F. S. Tautz<sup>2,3,4,\*</sup>, U. Höfer<sup>1,\*</sup>

Frontier orbitals determine fundamental molecular properties such as chemical reactivities. Although electron distributions of occupied orbitals can be imaged in momentum space by photoemission tomography, it has so far been impossible to follow the momentum-space dynamics of a molecular orbital in time, for example, through an excitation or a chemical reaction. Here, we combined time-resolved photoemission using high laser harmonics and a momentum microscope to establish a tomographic, femtosecond pump-probe experiment of unoccupied molecular orbitals. We measured the full momentum-space distribution of transiently excited electrons, connecting their excited-state dynamics to real-space excitation pathways. Because in molecules this distribution is closely linked to orbital shapes, our experiment may, in the future, offer the possibility of observing ultrafast electron motion in time and space.

The basis for a quantum-mechanical description of matter is the many-electron wave function. At various levels of approximation, up to the exact configuration interaction wave function, this can be written in terms of single-electron wave functions: the orbitals. The advantage is that orbitals provide a link between spectral properties and spatial electron distributions, which is of obvious benefit in chemistry (1, 2). Consequently, there has been a lot of interest in measuring orbitals (3–6), despite considerable subtleties (7, 8). With photoemission tomography, a powerful technique has recently been introduced by which the electron distribution in orbitals of molecules adsorbed at surfaces can be imaged in momentum space (9–12).

Addressing molecular orbitals of excited states in pump-probe experiments would bring photoemission tomography to its culmination, because it would empower it to provide access to molecular excitation and electron transfer processes at surfaces not only in time but also in space: Instead of just recording the photoemission intensity from the corresponding energy level, the evolution of the electron wave function after excitation could be traced by monitoring the orbitals in momentum space. Photoemission by conventional lasers with photon energies of a few electron volts can access only small electron momenta parallel to the surface. The prominent features in frontier orbital photoemission from organic molecules, as determined by the periodicity of the molecular C–C bond network, are therefore out of reach (9). Recently, however, probe photon energies that are high enough have become available through laser high-harmonic generation (HHG) and have enabled time-resolved photoemission experiments to record band structure movies of solids, i.e., to trace the temporal evolution of the electron system over the complete Brillouin zone (13–16). In their investigation of the laser-induced

phase transition of In nanowires on Si(111), Nicholson *et al.* (15) related this information to real-space chemical bond formation in a lattice. However, photoemission tomography of unoccupied states of molecules, the missing element to following molecular electron dynamics in time and space, has not yet been accomplished. In gas-phase photochemistry, it has long been recognized that femtosecond time-resolved photoelectron spectroscopy is a powerful method to investigate the coupled electron and nuclear dynamics (17–19). There, it is difficult to align molecules in all three dimensions to record momentum maps in the molecular frame (19–21). At metal surfaces, molecules are readily fixated in space (9–12). The spectroscopy of unoccupied states, however, requires sufficient electronic decoupling from the substrate at the same time.

The present experiments were performed on 3,4,9,10-perylene-tetracarboxylic-dianhydride (PTCDA) molecules that were decoupled from the Cu(001) substrate by an ultrathin oxide layer (22). The submonolayer oxygen coverage also provides a  $(\sqrt{2} \times \sqrt{2})R45^\circ - 2O$  surface corrugation that imposes two clearly defined azimuthal orientations of PTCDA, labeled  $0^\circ$  and  $90^\circ$  with respect to the laboratory frame of reference [Fig. 1A and (23)]. We used tunable visible pump pulses for resonant excitation of the molecules, combined it with a HHG light source (24) for photoemission, and detected the photoelectron distribution at high parallel momenta (up to  $\sim 2 \text{ \AA}^{-1}$ ) with a momentum microscope (23, 25).

Figure 1A displays the scheme of our experiment. We excited the molecules with 2.3-eV pump pulses and used 21.7-eV probe pulses at variable delay times  $t_p$  for photoemission. The parallel photoelectron momenta  $k_x$  and  $k_y$  were mapped onto the detector, and the energy  $E$  was retrieved simultaneously by a time-of-flight measurement. The recorded four-dimensional data cube  $I(E, k_x, k_y, t_p)$ , where  $I$  denotes the photoemission intensity, enables one to deduce the spatial electron distribution

<sup>1</sup>Fachbereich Physik und Zentrum für Materialwissenschaften, Philipps-Universität Marburg, Renthof 5, 35032 Marburg, Germany. <sup>2</sup>Peter Grünberg Institut (PGI-3), Forschungszentrum Jülich, 52425 Jülich, Germany. <sup>3</sup>Jülich Aachen Research Alliance (JARA), Fundamentals of Future Information Technology, 52425 Jülich, Germany.

<sup>4</sup>Experimentalphysik IV A, RWTH Aachen University, Otto-Blumenthal-Straße, 52074 Aachen, Germany. <sup>5</sup>Institute of Physics, University of Graz, NAWI Graz, 8010 Graz, Austria.

\*Corresponding author. Email: hoef@physik.uni-marburg.de (U.H.); s.tautz@fz-juelich.de (F.S.T.)



in terms of orbitals in momentum space, their energy position, and their time evolution.

Figure 1B shows a cut through a data cube, displaying  $I(E, k_x)$  at zero delay time. As expected for  $\pi$ -orbitals of flat lying PTCDA molecules, photoemission occurred at parallel momenta of  $\sim 1.4$  to  $1.6 \text{ \AA}^{-1}$ . The pronounced intensity at 1.3 to 2.3 eV below the Fermi energy  $E_F$  (defined as  $E = 0$ ) derived from standard one-photon photoemission from the highest occupied molecular orbital (HOMO) sitting on top of the Cu d-band onset and O 2p states of the oxide (23), whereas the weaker intensity at 0.25 eV above  $E_F$  originated from two-photon photoemission of the lowest unoccupied molecular orbital (LUMO), populated by the pump pulse before photoionization. These assignments are unambiguous, because constant energy intensity maps, evaluated at orbital energies  $E$  as a function of  $k_x$  and  $k_y$ , are fingerprints of individual orbitals. If the final state of the photoemission process is approximated as a plane wave, these so-called momentum maps are closely related to the Fourier transform of the orbitals (9, 23). Theoretical momentum maps that have been generated by Fourier transforming the calculated Kohn-Sham HOMO and LUMO of PTCDA are displayed in the excitation scheme (Fig. 1A).

In Fig. 2, A and B, we present measured momentum maps at the energies of the LUMO and HOMO for three different delay times. Each orbital shows a distinct momentum distribution that can be traced on the ultrafast time scale of the experiment. The detailed structure of the patterns can be explained from the two orthogonal molecular orientations that coexist on the surface. We expect to observe a superposition of the two corresponding momentum maps, as shown for the theoretical ones in Fig. 2, C and D. The agreement between the theoretical and measured momentum maps is indeed excellent, both for the LUMO around temporal overlap  $t_p = 0$  (Fig. 2, A and C) and for the HOMO (Fig. 2, B and D). The direction of the incident light broke the symmetry of the generic momentum maps. That the LUMO was not populated for negative delay time (Fig. 2A;  $-46$  fs) confirms that there is no static charge transfer from the Cu(001)-2O surface to the molecules (22). It is also important to note that the maximum LUMO intensity was about three orders of magnitude lower than the HOMO intensity. Saturation effects due to optical pumping as well as cross-talk between excited molecules can thus be neglected for the data analysis.

The measured Dyson orbital (23, 26) in Fig. 2A resembles the Kohn-Sham LUMO of PTCDA (Fig. 2C), a finding that is confirmed by a calculation of the Dyson orbital (23). This indicates that, to a good approximation, the excited  $N$  electron wave function

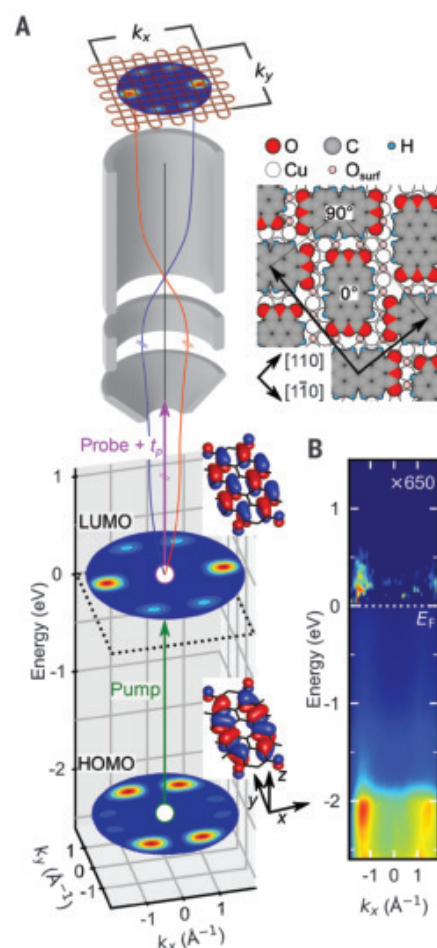


**Fig. 1. Femtosecond time-resolved photoemission tomography of molecular orbitals.**

(A) Scheme of the experiment. An electron from the HOMO is excited into the LUMO by the pump pulse (green) and then photoemitted by the probe pulse (purple) after a variable delay time  $t_p$  (left). The  $k_x$ ,  $k_y$  momentum maps indicate the distribution of photoelectrons, recorded with the momentum microscope simultaneously with the kinetic energy. The momentum maps and corresponding real-space orbitals have been calculated with density functional theory. Schematic view of a PTCDA layer on the Cu(001)-2O surface (right). Each unit mesh contains two molecules, labeled  $0^\circ$  and  $90^\circ$  (23). surf, surface. (B) Experimental  $I(E, k_x)$  map, extracted from  $I(E, k_x, k_y, t_p)$ , integrated in the interval  $k_y \in [-0.2; 0.2] \text{ \AA}^{-1}$ , and plotted around temporal overlap of pump and probe pulses. The energy  $E$  is plotted with respect to the Fermi energy  $E_F \equiv 0$ . For  $E > 0$ , the experimental Fermi-Dirac distribution has been subtracted by using the most negative delay time  $t_p = -46$  fs.

contains the LUMO as a single-electron orbital and that the subsequent photoemission removed the excited electron from the LUMO. We stress that this intuitive picture of the excitation process in terms of frontier orbitals in the independent electron approximation requires photoemission tomography, and, in

particular, the observation of a good agreement between measured Dyson orbitals and calculated Kohn-Sham orbitals, for its confirmation. In conventional femtosecond spectroscopy without momentum-space information, we would be following the evolution of a peak in the energy distribution curve but would not be able to identify the underlying state as an approximate single-particle orbital.

An obvious question addresses the lifetime of the excited state. The single-photon pattern for the HOMO in Fig. 2B shows no dependence on the delay time. Obviously, only a small fraction of the molecules were excited by the pump pulse. By contrast, integrated intensities revealed that after about 100 fs, the LUMO population suffered a single-exponential decay with a lifetime of  $T_1 \approx 250$  fs (23). Importantly, no changes in the excited orbital as such took place during this lifetime, as revealed by its constant pattern in momentum space (Fig. 2A). For an excited molecule at a metal surface, this longevity is quite notable (27, 28). It not only confirms the potency of the atomically thin oxide as a decoupling layer but also makes future time-resolved investigations of chemical bond breaking highly promising, because a lifetime of 250 fs exceeds the time scale of typical vibrational motion.

Next, we used the tomographic information to investigate real-space excitation pathways. To this end, we broke the symmetry between the two differently oriented PTCDA molecules, aligning the plane of light incidence with the long axis of the  $0^\circ$  molecule (Fig. 3), and followed, through their momentum-space patterns, both molecules separately. We found that s-polarized light only excited the  $90^\circ$  molecule [Fig. 3A; in agreement with a group theory analysis (23)], and p-polarized light was able to excite both molecules, albeit with surprisingly different excitation dynamics (Fig. 3B): The LUMO pattern of the  $0^\circ$  molecule lit up much earlier and much brighter than that of the  $90^\circ$  molecule. A plot of integrated intensities over the relevant regions of parallel momentum confirmed the markedly different behavior (Fig. 3C): Whereas for the  $90^\circ$  molecule the LUMO signal gradually built up over the duration of the pump pulse and subsequently decayed with the time constant of  $T_1 \approx 250$  fs, it rose quickly for the  $0^\circ$  molecule and reached a pronounced maximum after 15 fs, before exhibiting at later times ( $t_p > \sim 75$  fs) the same slow decay as for the  $90^\circ$  molecule. Upon excitation with s-polarized light, the  $90^\circ$  molecule behaved similar to the  $0^\circ$  molecule under p-polarized excitation (Fig. 3C).

A possible explanation for the occurrence of the pronounced maximum near  $t_p = 0$  would be the presence of a very fast decaying intermediate state that is excited under certain

excitation conditions. The analysis of the momentum maps, however, excludes this possibility. Not only are the momentum maps of Fig. 3 characteristic of that of the LUMO for all delay times, patterns at higher energies also do not indicate the excitation of another state in our experiment (23). Instead, we suggest that the differences in the excitation dynamics are due to two distinct real-space excitation pathways of the electron in the sample before it is photoemitted. Our model describes the experiment by a four-level sys-

tem consisting of the HOMO  $|\phi_1\rangle$  and an occupied substrate state  $|\phi_1'\rangle$  as initial states, the LUMO as intermediate state  $|\phi_2\rangle$ , and the photoemission final state  $|\phi_3\rangle$  (Fig. 3D). In a perturbative description of light-matter interaction, the pump pulse creates a coherent polarization  $|\Psi, t\rangle$  between the ground state  $|\phi_1\rangle$  or  $|\phi_1'\rangle$  and excited state  $|\phi_2\rangle$  in the first order of the electric field. The conversion of this polarization in the second order of the electric field into an excited-state population  $n_2$  is governed by phase-destroying elastic

scattering processes. In one limit, if this dephasing is fast and the inelastic decay of  $|\phi_2\rangle$  is slow, the build-up of  $n_2$  follows the time-integrated intensity of the pump pulse. This was the situation for the 90° molecule excited with p-polarized light (Fig. 3C). The field component  $\mathbf{E}_\perp$  drives a perpendicular electron motion between substrate and molecule, involving the initial state  $|\phi_1'\rangle$  that is coupled to a bath, which resulted in fast dephasing. In this limit, the emitted photoelectron could be traced back to the metal. Although this mechanism applies to both the 0° and 90° molecules (Fig. 3C), in the case of the 0° molecule, a competing process takes place (see below), such that the signature of the fast dephasing was only seen in the data for the 90° molecule.

In the opposite limit, if dephasing is slow, the oscillating polarization between ground and excited states decays slowly. In this coherent regime, the interaction of the electric field of the probe pulse with  $|\Psi, t\rangle$  can contribute to the two-photon photoemission process for short delay times. In addition, if the driving pump laser is slightly detuned from the transition energy, the excited state can be populated and depopulated by the pump pulse. Both effects give rise to a pronounced peak in the photoemission signal, as observed in Fig. 3C for the 90° molecule excited with s-polarized light as well as for the 0° molecule excited with p-polarized light.

For a quantitative evaluation of the data, we applied a density matrix approach and solved the optical Bloch equation for the four-level system (Fig. 3D). We found that the experimental data are described well with an extremely short dephasing time  $T_2^* \approx 3$  fs of the substrate state  $|\phi_1'\rangle$  and a surprisingly long

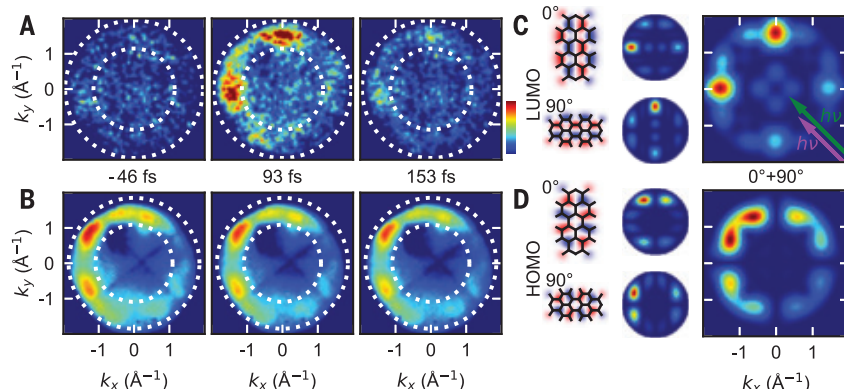
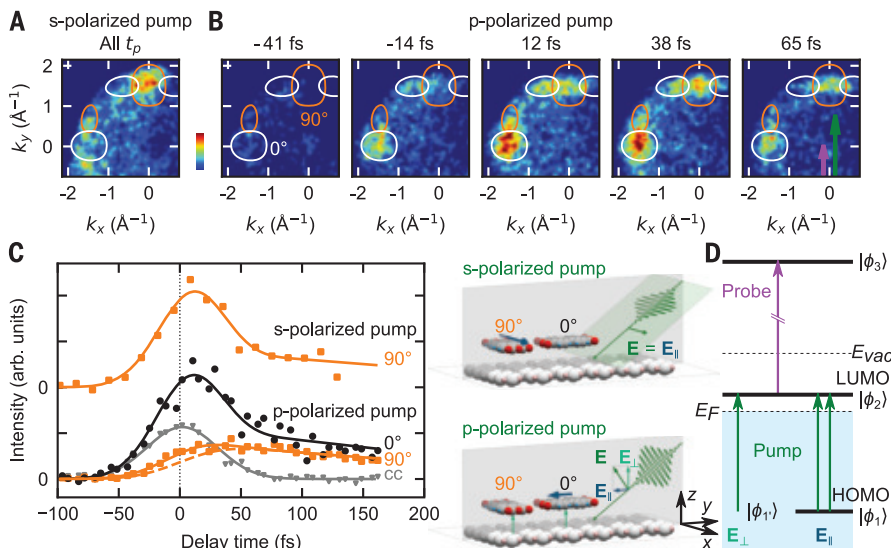


**Fig. 2. Momentum maps of the frontier orbitals.** (A) Experimental momentum maps obtained at selected delay times  $t_p$  and  $E = +0.45$  eV. Both pump and probe beams are p-polarized. The two dotted circles indicate the momentum integration range (23). (B) Same as for (A) but at  $E = -2.18$  eV (intensity reduced by a factor 1850). (C) Two-dimensional cuts through the Kohn-Sham LUMO of gas-phase PTCDA (left) and corresponding theoretical momentum maps with polarization factor  $P(\mathbf{k})$  plotted for two orientations 0° and 90° (middle) and their sum (right). (D) Same as for (C) but for the HOMO. Both orbitals have been calculated for neutral, closed-shell PTCDA. However, an open-shell calculation of the highest occupied orbital for the PTCDA anion yields almost indistinguishable results from the LUMO of neutral PTCDA (23). The colored arrows indicate projected light incidence (45°).  $h\nu$ , photon energy.

**Fig. 3. Momentum-resolved LUMO dynamics for different excitation pathways.** (A) Momentum map integrated over all delay times  $t_p$  for an s-polarized pump pulse. The momentum map is overlaid by theoretical constant-intensity contours as expected for the 0° (white) and 90° molecules (orange). (B) Momentum maps for a p-polarized pump pulse at selected delay times. (C) Temporal evolution of the photoelectron intensity of the two LUMOs (0°, black circles; 90°, orange squares) for s- and p-polarized pump pulses. Intensities are integrated within circular regions with a radius of  $0.2 \text{ \AA}^{-1}$  centered within the main lobes of each molecular orientation. The experimental geometries are illustrated schematically. Solid lines indicate the best fit solution to the optical Bloch equations for the four-level system discussed in the text. The dashed orange line illustrates a completely incoherent excitation. It is obtained within the same model by setting the decoherence time to zero. Gray triangles show the cross-correlation (cc) of the pump and probe pulses. (D) Schematic representation of the four-level model used to fit the data in (C).  $E_{vac}$ , vacuum level.





decoherence time  $T_2^{12}$  in excess of 150 fs for the polarization between  $|\phi_1\rangle$  and  $|\phi_2\rangle$  (23). The existence of such a long-lived coherence in an electronic excitation at a metal surface is unexpected (28, 29). It has previously only been observed for image-potential states with high quantum numbers where the electron is mainly located in the vacuum, tens of angstroms above the surface (28). In the present experiment, this long coherence time can be rationalized by the fact that the pump pulse induced an in-plane oscillatory electron motion that is confined to the molecule: For both combinations, s-polarization-90° molecule and p-polarization-0° molecule, there is an **E** field component along the long axis of the respective molecule (Fig. 3C), i.e., parallel to the HOMO-LUMO transition dipole, thus permitting an excitation directly from the HOMO  $|\phi_1\rangle$  into the LUMO  $|\phi_2\rangle$ . If the hybridization of the molecule with the metal beneath the oxide is negligible, which is also revealed by the long inelastic lifetime  $T_1$  measured for the LUMO, this spatial confinement of electron motion in  $|\Psi, t\rangle$  to the molecule explains the long coherence. Our modeling thus suggests that for this excitation pathway, the emitted photoelectron can be traced back to the HOMO (30).

We have shown that photoemission tomography, in combination with laser pump-probe techniques, makes it possible to image orbital momentum maps of excited electronic states. This allows the identification of excitation mechanisms by tracing electrons not only in time but also in space. We expect that future experiments of this type will enable studies of molecular electron transfer processes at surfaces and interfaces with unprecedented detail. With progress in laser alignment, one may envision that the field of gas-phase photochemistry will also benefit from time-resolved photoemission tomography (19–21). Moreover, an extension to attosecond time resolution seems feasible. The availability of momentum-space information relaxes pertinent requirements on energy resolution, allowing in turn for an increase in time resolution. In this way, the temporal and spatial evolution of electronically excited states should become resolvable by photoemission tomography even before the nuclei start to move.

## REFERENCES AND NOTES

- R. B. Woodward, R. Hoffmann, *J. Am. Chem. Soc.* **87**, 395–397 (1965).
- K. Fukui, *Science* **218**, 747–754 (1982).
- J. Itatani et al., *Nature* **432**, 867–871 (2004).
- J. Repp, G. Meyer, S. M. Stojković, A. Gourdon, C. Joachim, *Phys. Rev. Lett.* **94**, 026803 (2005).
- M. Meckel et al., *Science* **320**, 1478–1482 (2008).
- T. L. Cocker, D. Peller, P. Yu, J. Repp, R. Huber, *Nature* **539**, 263–267 (2016).
- D. G. Truhlar, P. C. Hiberty, S. Shaik, M. S. Gordon, D. Danovich, *Angew. Chem. Int. Ed.* **58**, 12332–12338 (2019).
- A. I. Krylov, *J. Chem. Phys.* **153**, 080901 (2020).
- P. Puschnig et al., *Science* **326**, 702–706 (2009).
- M. Wießner et al., *Nat. Commun.* **5**, 4156 (2014).
- D. Lüftner et al., *Proc. Natl. Acad. Sci. U.S.A.* **111**, 605–610 (2014).
- S. Weiß et al., *Nat. Commun.* **6**, 8287 (2015).
- T. Rohwer et al., *Nature* **471**, 490–493 (2011).
- S. Eich et al., *Sci. Adv.* **3**, e1602094 (2017).
- C. W. Nicholson et al., *Science* **362**, 821–825 (2018).
- M. X. Na et al., *Science* **366**, 1231–1236 (2019).
- A. Stolow, A. E. Bragg, D. M. Neumark, *Chem. Rev.* **104**, 1719–1758 (2004).
- A. von Conta et al., *Nat. Commun.* **9**, 3162 (2018).
- C. Z. Bisgaard et al., *Science* **323**, 1464–1468 (2009).
- L. Holmegaard et al., *Nat. Phys.* **6**, 428–432 (2010).
- A. Trabattini et al., *Nat. Commun.* **11**, 2546 (2020).
- X. Yang et al., *Chem. Commun.* **54**, 9039–9042 (2018).
- Material, methods, and supplementary text are available as supplementary materials.
- C. M. Heyl, J. Güdde, A. L'Huillier, U. Höfer, *J. Phys. B At. Mol. Opt. Phys.* **45**, 074020 (2012).
- C. Tuschke et al., *Appl. Phys. Lett.* **108**, 261602 (2016).
- J. V. Ortiz, *J. Chem. Phys.* **153**, 070902 (2020).
- X.-Y. Zhu, *Surf. Sci. Rep.* **56**, 1–83 (2004).
- P. M. Echenique et al., *Surf. Sci. Rep.* **52**, 219–317 (2004).
- X. Cui et al., *Nat. Phys.* **10**, 505–509 (2014).
- We note that for nonresonant excitation, the coherent interaction of pump and probe light can lead to the emission of photoelectrons from the HOMO in a true two-photon process without involving an intermediate state (28). The observed momentum map, which in our experiment was that of the molecular LUMO  $|\phi_2\rangle$  and not that of the HOMO  $|\phi_1\rangle$ , however, provided clear experimental evidence that this was not the case here.
- R. Wallauer et al., Data used in: Tracing orbital images on ultrafast time scales. Jülich Data (2020); <https://doi.org/10.26165/JUELICH-DATA/9UUIPE>.

## ACKNOWLEDGMENTS

We thank A. Haags for fruitful discussions. **Funding:** R.W., U.H., F.C.B., C.K., and F.S.T. acknowledge financial support from the Deutsche Forschungsgemeinschaft (DFG), project-ID 223848855-SFB 1083. D.B. and P.P. acknowledge financial support from the Austrian Science Fund (FWF), project I3731. S.S., F.C.B., and F.S.T. acknowledge financial support from the DFG, project-ID 396769409. **Author contributions:** C.K., F.S.T., and U.H. conceived the research. X.Y., S.S., C.K., and F.S.T. chose the sample. M.R. and F.C.B. prepared the samples, and C.K. analyzed its structure. R.W., M.R., K.S., L.M., and J.G. performed the experiment. R.W., K.S., C.K., F.C.B., F.S.T., and U.H. analyzed the data and developed the physical model. D.B., P.P., and S.S. simulated the momentum maps of the PTCD molecule in the gas phase. R.W., C.K., P.P., and F.C.B. prepared the figures. R.W., C.K., F.C.B., F.S.T., and U.H. wrote the paper. **Competing interests:** The authors have no competing interests. **Data and materials availability:** All data needed to evaluate the conclusions in the paper are present in the paper or the supplementary materials. Raw data used to produce the figures in the main text and supplementary materials are available at the Jülich DATA public repository (31).

## SUPPLEMENTARY MATERIALS

[science.sciencemag.org/content/371/6533/1056/suppl/DC1](https://science.sciencemag.org/content/371/6533/1056/suppl/DC1)  
Materials and Methods  
Supplementary Text  
Figs. S1 to S6  
Table S1  
References (32–49)

26 October 2020; accepted 1 February 2021  
Published online 18 February 2021  
10.1126/science.abf3286

## SENSORY PERCEPTION

# C. elegans discriminates colors to guide foraging

D. Dipon Ghosh<sup>1,2\*</sup>, Dongyeop Lee<sup>2</sup>, Xin Jin<sup>1†</sup>, H. Robert Horvitz<sup>2</sup>, Michael N. Nitabach<sup>1,3,4\*</sup>

Color detection is used by animals of diverse phyla to navigate colorful natural environments and is thought to require evolutionarily conserved opsin photoreceptor genes. We report that *Caenorhabditis elegans* roundworms can discriminate between colors despite the fact that they lack eyes and opsins. Specifically, we found that white light guides *C. elegans* foraging decisions away from a blue-pigment toxin secreted by harmful bacteria. These foraging decisions are guided by specific blue-to-amber ratios of light. The color specificity of color-dependent foraging varies notably among wild *C. elegans* strains, which indicates that color discrimination is ecologically important. We identified two evolutionarily conserved cellular stress response genes required for opsin-independent, color-dependent foraging by *C. elegans*, and we speculate that cellular stress response pathways can mediate spectral discrimination by photosensitive cells and organisms—even by those lacking opsins.

**T**he roundworm *C. elegans* lives in decomposing organic matter such as compost heaps, where it feeds on microorganisms (1, 2), some of which secrete colorful pigments (3–5). *C. elegans* lacks the specialized eyes, photoreceptor cells, and opsin genes that underlie canonical visual-system functions (6–8). Nevertheless, *C. elegans* can

detect and respond to short-wavelength light, including blue light, using the LITE-1 and GUR-3 proteins, which are similar to insect gustatory chemoreceptors (9–14). Although it has been shown that visible light can influence *C. elegans* physiology (15) and behavior (9–14), whether microbial pigments affect *C. elegans* foraging has not been previously addressed.

We investigated whether white light alters *C. elegans* strain N2's avoidance of pathogenic *Pseudomonas aeruginosa* PA14 bacterial lawns secreting the blue pigment pyocyanin, a reactive oxygen species (ROS)-generating toxin (Fig. 1A and fig. S1A) (16–23). White light markedly potentiated the gradual avoidance of PA14 but not of nontoxic *Escherichia coli* strain OP50 (Fig. 1B). *lite-1* null-mutant worms

<sup>1</sup>Department of Cellular and Molecular Physiology, Yale University, New Haven, CT, USA. <sup>2</sup>Howard Hughes Medical Institute, Department of Biology, Massachusetts Institute of Technology, Cambridge, MA, USA. <sup>3</sup>Department of Genetics, Yale University, New Haven, CT, USA. <sup>4</sup>Department of Neuroscience, Yale University, New Haven, CT, USA.  
**\*Corresponding author. Email:** [dipon@mit.edu](mailto:dipon@mit.edu) (D.D.G.); [michael.nitabach@yale.edu](mailto:michael.nitabach@yale.edu) (M.N.N.) <sup>†</sup>Present address: School of Medicine, Nankai University, Tianjin, China.

also avoided PA14, but their avoidance was unaffected by white light (fig. S1B). We also examined the worms' avoidance of a *P. aeruginosa* mutant strain, PA14 $\Delta$ phzM, that cannot synthesize pyocyanin but still synthesizes other nonblue ROS-generating toxins (19). PA14 $\Delta$ phzM cultures were not blue (Fig. 1C), and light only minimally affected the avoidance of PA14 $\Delta$ phzM by wild-type or *lite-1* null-mutant worms (Fig. 1D and fig. S1C). These results demonstrate that light-dependent potentiation of PA14 avoidance requires both *lite-1* and pyocyanin.

By supplementing lawns of nontoxic OP50 with pyocyanin (Fig. 1E), we found that pyocyanin is sufficient to confer light- and *lite-1*-dependent avoidance on otherwise innocuous bacteria (Fig. 1, F and G). We tested whether a chemically inert blue dye, spectrally matched (fig. S2A) to pyocyanin, coupled with the colorless ROS-generating toxin paraquat (fig. S2B)

would support light-potentiated avoidance. Light potentiated wild-type but not *lite-1* avoidance of OP50 supplemented with both blue dye and paraquat, but not with either independently (Fig. 2, A to D, and fig. S2, C to F). This observation indicates that avoidance of pyocyanin-containing lawns relies on both pyocyanin's chemical and spectral properties.

Using optical filters (fig. S3, A and B), we found that eliminating short-wavelength blue or long-wavelength amber light disrupted light-potentiated avoidance (fig. S3C). By contrast, directly filtering incident white light through a blue vinyl filter that increased the blue-to-amber ratio to match the spectral properties of pyocyanin potentiated avoidance of OP50 supplemented with paraquat without blue pigment (Fig. 2, E to G). These results indicate that blue pigments enhance avoidance by changing the spectrum of light in the worm's

environment (fig. S4). Blue vinyl-filtered light also potentiated avoidance of OP50 lawns in the presence of the aversive odorant 1-octanol (24), which suggests that color might generally influence the avoidance of aversive stimuli (Fig. 3, A and B, and fig. S5A).

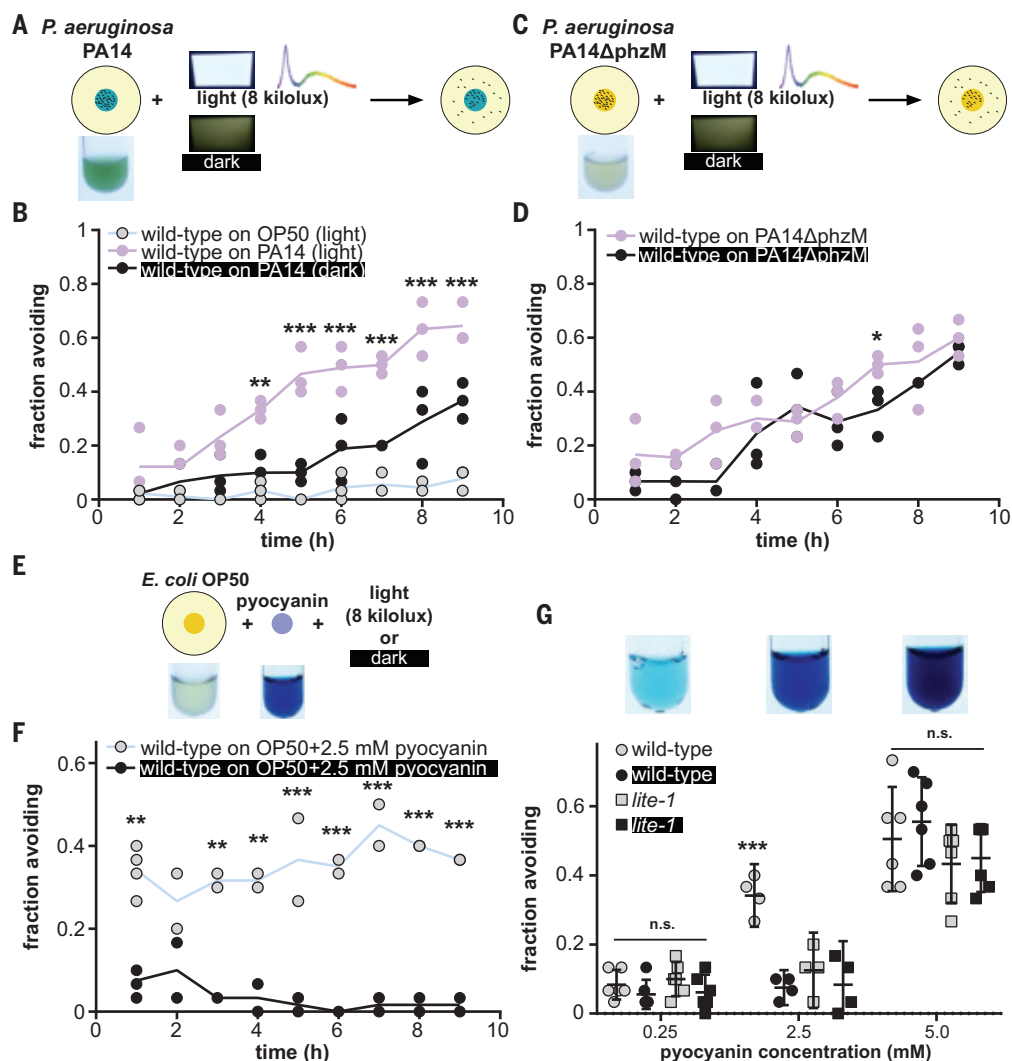
To analyze spectral influences on foraging, we tested combinations of monochromatic blue and amber light sources for potentiation of OP50-lawn avoidance in the presence of 1-octanol (Fig. 3C). Although neither pure blue nor pure amber light potentiated lawn avoidance, mixed colors differentially potentiated avoidance depending on the blue-to-amber ratio (Fig. 3D). This observation indicates that the relative intensities of blue and amber visible light guide foraging decisions and establishes that *C. elegans* can discriminate colors.

Next, we investigated whether *C. elegans* strains that are independently isolated from

**Fig. 1. Blue-pigment toxin pyocyanin underlies light-potentiated avoidance of *P. aeruginosa*.**

(A) Schematic depicting worms ( $n = 30$  per assay) on a lawn of *P. aeruginosa* strain PA14 in the absence (dark) or presence (light) of 8 kilolux of white light. All photographs shown in this and the following figures are of example liquid cultures or test solutions used in the experiment and of lights, modified as indicated, shining on a white background. (B) Time course of wild-type worm avoidance of lawns of PA14 in the light (purple) and dark (black) or of *E. coli* OP50 in the light (gray). Lines represent the average of assays individually depicted by data points.  $n = 3$  lawn avoidance assays. (C and D) Time course of wild-type worm avoidance of PA14 $\Delta$ phzM lawns in light (purple) and dark (black). PA14 $\Delta$ phzM is incapable of synthesizing pyocyanin (note, these cultures are not blue).  $n = 3$ . (E and F) Time course of avoidance by wild-type worms of *E. coli* OP50 lawns supplemented with 2.5 mM pyocyanin in the presence (gray) or absence (black) of light.  $n = 4$  for measurement at 1 hour;  $n = 2$  for measurements at 2 to 9 hours. (G) One-hour avoidance of OP50 lawns supplemented with 0.25, 2.5, or 5 mM pyocyanin by wild-type (circles) and *lite-1* null-mutant (squares) worms in either the presence (gray) or absence (black) of light. Data for wild-type avoidance of lawns supplemented with 2.5 mM pyocyanin in (F) and (G) were from the same experiments. All statistical comparisons for time course experiments

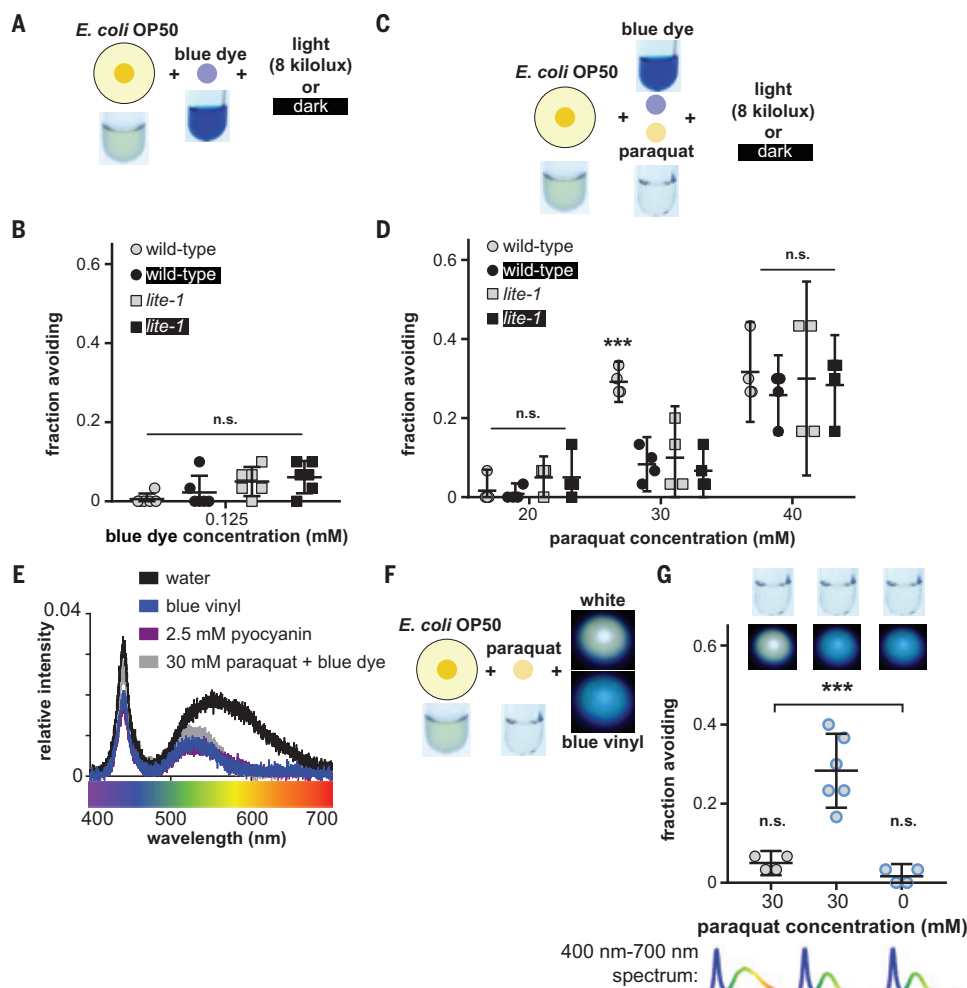
were by two-way analysis of variance (ANOVA) with time as a repeated measure and post-hoc Bonferroni tests. For *P* and *F* values, see table S1. Experiments are single time points (1 hour) unless otherwise indicated. Statistical analyses were performed by one-way ANOVA with post-hoc Tukey-Kramer tests for pairwise comparisons or Dunnett or Bonferroni tests, as appropriate, for comparisons with control. Error bars denote 95% confidence intervals.  $*P \leq 0.05$ ;  $**P \leq 0.01$ ;  $***P \leq 0.001$ ; n.s., not significant.





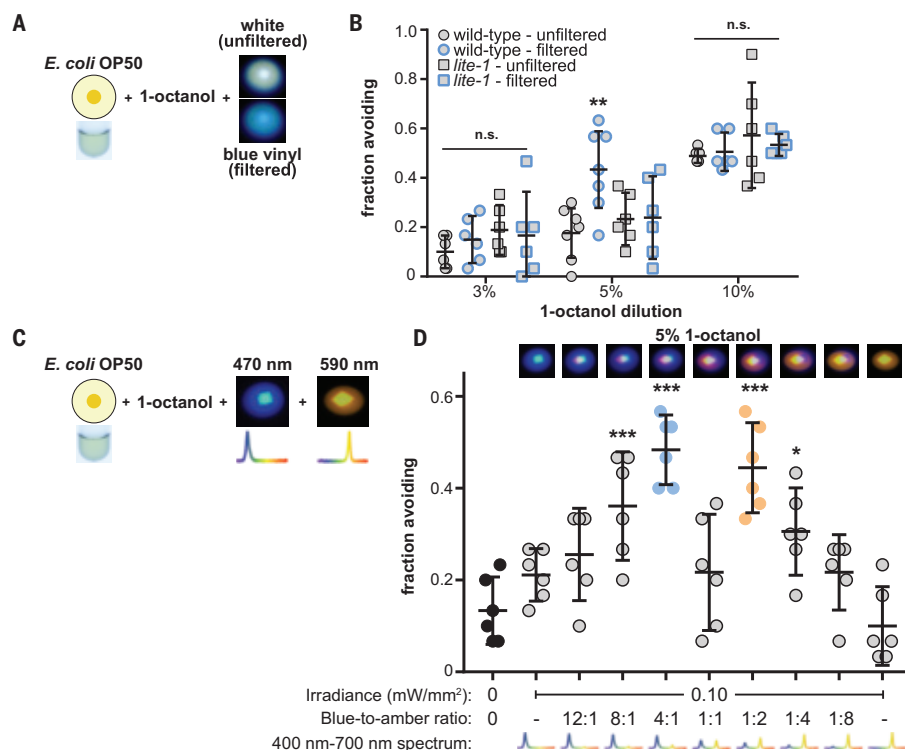
**Fig. 2. Spectral content potentiates avoidance of toxic bacterial lawns.**

(A and B) Avoidance of OP50 lawns supplemented with 0.125 mM blue dye. (C and D) Avoidance of OP50 lawns supplemented with 0.125 mM blue dye and specified concentrations of paraquat (20, 30, and 40 mM). (E) Comparison of the spectra of white light filtered with water (black), blue vinyl filter (blue), 2.5 mM pyocyanin solution (purple), or 30 mM paraquat and blue dye solution (gray). (F and G) Avoidance of OP50 lawns supplemented with or without paraquat in the presence (gray with blue borders) or absence (gray) of a blue vinyl filter modifying the color of the white light.



**Fig. 3. Foraging is guided by the relative intensities of blue and amber light.**

(A and B) Avoidance of OP50 lawns in the presence of the specified dilutions of 1-octanol (3, 5, and 10%) and in the presence (gray with blue borders) or absence (gray) of the blue vinyl filter. (C and D) Avoidance of OP50 lawns in the presence of 5% 1-octanol and incident light of different colors composed of the specified ratios of narrow-band blue and amber light.



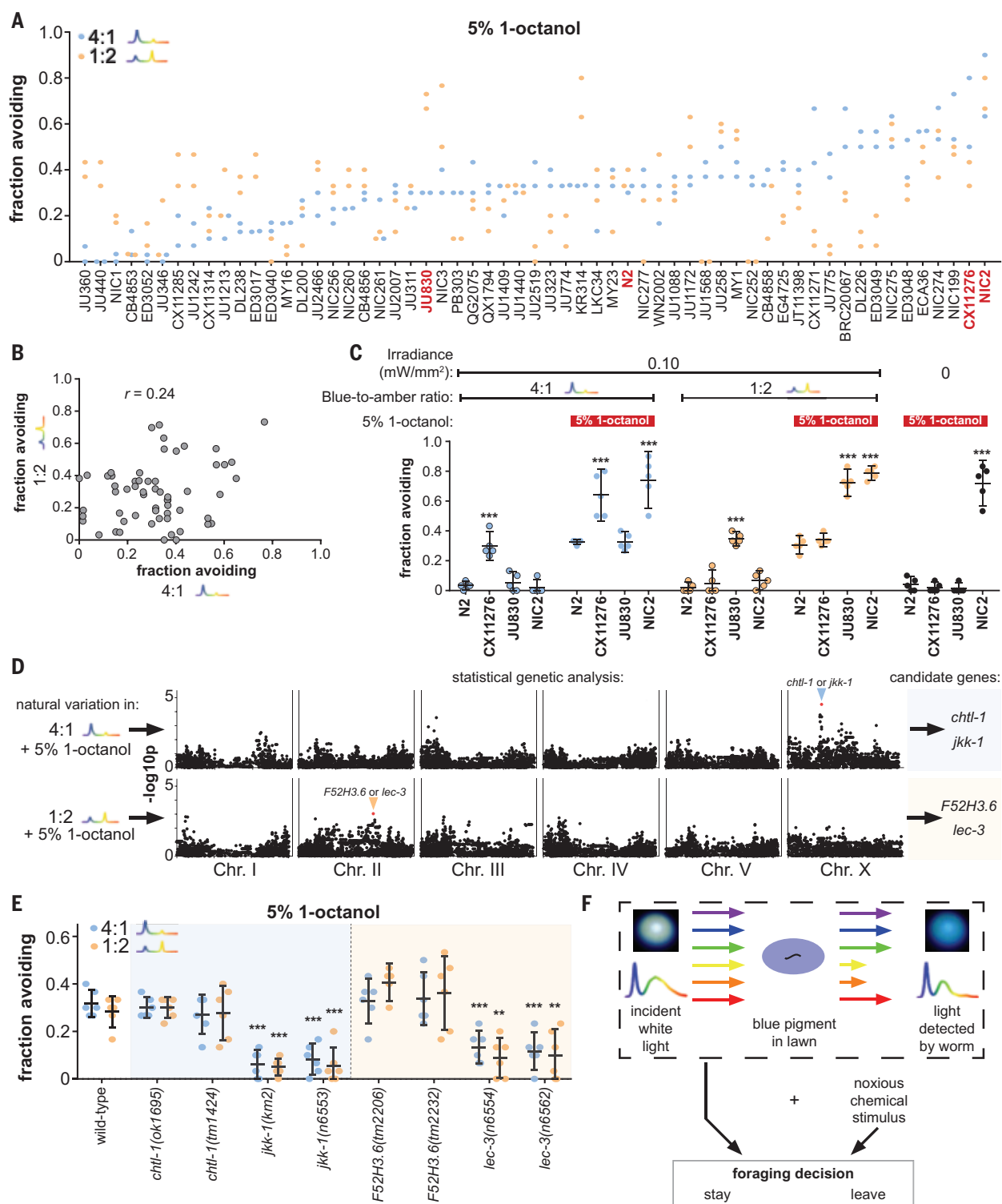


**Fig. 4. Evolutionarily conserved genes *jkk-1* and *lec-3* are required for naturally varying color-dependent foraging.** (A) Avoidance of OP50 lawns by 59 wild *C. elegans* strains in the presence of 5% 1-octanol and 4:1 or 1:2 blue-to-amber light. N2, CX11276, JU830, and NIC2 strains are indicated in red.  $n = 2$ . (B) Correlation of lawn avoidance in the presence of 5% 1-octanol and 4:1 and 1:2 blue-to-amber light by each wild strain. Pearson's correlation coefficient  $r(57) = 0.24$ ;  $P = 0.063$ . (C) Avoidance of OP50 lawns by N2, CX11276, JU830, and NIC2 strains with or without 5% 1-octanol and 4:1 or 1:2 blue-to-amber light, as specified. (D) Statistical genetics analysis with

highest-scoring polymorphisms (indicated by red dots) and neighboring high-confidence polymorphisms that suggested the candidate genes *chtl-1* and *jkk-1* [blue arrowhead and blue box in (E)] and *F52H3.6* and *lec-3* [orange arrowhead and orange box in (E)]. (E) Avoidance of OP50 lawns in the presence of 5% 1-octanol and 4:1 or 1:2 blue-to-amber light by *chtl-1*, *jkk-1*, *F52H3.6*, and *lec-3* null-mutant worms. (F) Blue pigment absorbs long-wavelength light and thereby alters the spectral composition of light detected. The integration of color and chemical information guides worms' foraging decision to stay on or leave bacterial lawns.



the wild, and presumably adapted to diverse ecological niches (25–27), exhibit variation in color-dependent foraging. We detected substantial variation in 4:1 and 1:2 blue-to-amber spectrum-dependent foraging among 59 wild strains (Fig. 4A). Notably, 4:1 and 1:2 blue-to-amber ratio sensitivities were uncorrelated (Fig. 4B), which suggests that complex, potentially distinct mechanisms underlie color-specific sensitivities. For example, compared with N2, strains CX11276 and JU830 exhibited relatively heightened sensitivities to 4:1 blue-to-amber light and 1:2 blue-to-amber light, respectively, whereas NIC2 maximally avoided the lawn regardless of color (Fig. 4A). To dissect how spectral discrimination and 1-octanol avoidance contribute to color-dependent foraging, we tested the avoidance of lawns illuminated with 4:1 and 1:2 blue-to-amber light, with and without octanol, by these strains. CX11276 and JU830 were sensitive to specific colors even without 1-octanol, whereas NIC2 avoided lawns with 1-octanol even without light (Fig. 4C). Thus, whereas color-dependent lawn avoidance by N2, which is relatively insensitive to colors, requires the presence of an additional aversive stimulus, for more color-sensitive strains like CX11276, color-specific illumination is sufficient. These results demonstrate that naturally varying color and odorant sensitivities drive strain differences in foraging.

Using approaches adapted from statistical genetics (27), we determined that no single genomic polymorphism could causally account for the observed variation in color-dependent foraging (Fig. 4D). However, by considering multiple neighboring single-nucleotide polymorphism (SNPs) within a given genomic region (28), we identified two sets of two genes—*chtl-1* and *jkk-1* as well as *F52H3.6* and *lec-3*—in the regions of the two highest-scoring polymorphisms that contribute to variation in the avoidance of lawns under 4:1 and 1:2 blue-to-amber light, respectively (Fig. 4E and fig. S6). Color-dependent avoidance was abolished in two independent null-mutant strains of *jkk-1* and in two independent null-mutant strains of *lec-3*, whereas color-dependent foraging by *chtl-1* and *F52H3.6* null-mutant worms was

unaffected (Fig. 4E). Loss of *jkk-1* or *lec-3* function did not impair avoidance responses to brighter blue light or higher 1-octanol concentrations (fig. S7). These results revealed that *jkk-1* and *lec-3* contribute to color-dependent foraging.

We established that *C. elegans* discriminates colors, and we identified two genes required for color-dependent foraging. Mammalian homologs of *jkk-1* and *lec-3*—MKK7, an activator of c-Jun N-terminal kinases (JNKs) (29), and galectin, a member of a protein family that binds beta-galactoside sugars (30), respectively—can interact in mediating cellular responses to stressors, including ultraviolet light (31–37). Genes like *jkk-1* and *lec-3* might function in opsin-independent, spectrally sensitive stress response pathways to guide *C. elegans* foraging decisions on food sources that vary in color and toxicity (Fig. 4F). The functions of microbial pigmentation are poorly understood (38). We suggest that pigmentation contributes to evolving interactions between pathways underlying the synthesis and secretion of pigmented factors by microbes and the responses to these pigments by foraging hosts like *C. elegans*.

## REFERENCES AND NOTES

1. L. Frézal, M.-A. Félix, *eLife* **4**, e05849 (2015).
2. B. S. Samuel, H. Rowedder, C. Braendle, M.-A. Félix, G. Ruvkun, *Proc. Natl. Acad. Sci. U.S.A.* **113**, E3941–E3949 (2016).
3. E. Pradel et al., *Proc. Natl. Acad. Sci. U.S.A.* **104**, 2295–2300 (2007).
4. P. Burlinson et al., *ISME J.* **7**, 1126–1138 (2013).
5. A. P. Page et al., *BMC Biol.* **17**, 10 (2019).
6. F. Pichaud, A. Briscoe, C. Desplan, *Curr. Opin. Neurobiol.* **9**, 622–627 (1999).
7. K. D. Longden, *Curr. Biol.* **26**, R981–R988 (2016).
8. I. C. Cuthill et al., *Science* **357**, eaan0221 (2017).
9. S. L. Edwards et al., *PLOS Biol.* **6**, e198 (2008).
10. A. Ward, J. Liu, Z. Feng, X. Z. Xu, *Nat. Neurosci.* **11**, 916–922 (2008).
11. J. Liu et al., *Nat. Neurosci.* **13**, 715–722 (2010).
12. N. Bhatla, H. R. Horvitz, *Neuron* **85**, 804–818 (2015).
13. N. Bhatla, R. Droste, S. R. Sando, A. Huang, H. R. Horvitz, *Curr. Biol.* **25**, 2075–2089 (2015).
14. J. Gong et al., *Cell* **167**, 1252–1263.e10 (2016).
15. C. D. De Magalhães Filho et al., *Nat. Commun.* **9**, 927 (2018).
16. S. Mahajan-Miklos, M. W. Tan, L. G. Rahme, F. M. Ausubel, *Cell* **96**, 47–56 (1999).
17. M. W. Tan, S. Mahajan-Miklos, F. M. Ausubel, *Proc. Natl. Acad. Sci. U.S.A.* **96**, 715–720 (1999).

18. M. W. Tan, L. G. Rahme, J. A. Sternberg, R. G. Tompkins, F. M. Ausubel, *Proc. Natl. Acad. Sci. U.S.A.* **96**, 2408–2413 (1999).
19. B. Cezairliyan et al., *PLOS Pathog.* **9**, e1003101 (2013).
20. Y. Zhang, H. Lu, C. I. Bargmann, *Nature* **438**, 179–184 (2005).
21. J. D. Meisel, D. H. Kim, *Trends Immunol.* **35**, 465–470 (2014).
22. J. D. Meisel, O. Panda, P. Mahanti, F. C. Schroeder, D. H. Kim, *Cell* **159**, 267–280 (2014).
23. J. Singh, A. Aballay, *eLife* **8**, e50033 (2019).
24. C. I. Bargmann, E. Hartwig, H. R. Horvitz, *Cell* **74**, 515–527 (1993).
25. A. Barrière, M.-A. Félix, *WormBook* **2005**, 1–19 (2005).
26. K. S. Evans et al., *G3* **7**, 289–298 (2017).
27. D. E. Cook, S. Zdravljek, J. P. Roberts, E. C. Andersen, *Nucleic Acids Res.* **45**, D650–D657 (2017).
28. J. Yang et al., *Nat. Genet.* **44**, 369–375 (2012).
29. M. Kawasaki et al., *EMBO J.* **18**, 3604–3615 (1999).
30. Y. Nemoto-Sasaki et al., *Biochim. Biophys. Acta* **1780**, 1131–1142 (2008).
31. I. N. Foltz et al., *J. Biol. Chem.* **273**, 9344–9351 (1998).
32. F. Berner, A. Sarasin, T. Magnaldo, *Proc. Natl. Acad. Sci. U.S.A.* **96**, 11329–11334 (1999).
33. C. Tournier et al., *Science* **288**, 870–874 (2000).
34. C. Tournier et al., *Genes Dev.* **15**, 1419–1426 (2001).
35. I. Kuwabara et al., *J. Biol. Chem.* **277**, 3487–3497 (2002).
36. J. Saegusa et al., *J. Invest. Dermatol.* **128**, 2403–2411 (2008).
37. B. Brandt, E. F. Abou-Eladab, M. Tiedge, H. Walzel, *Cell Death Dis.* **1**, e23 (2010).
38. G. Y. Liu, V. Nizet, *Trends Microbiol.* **17**, 406–413 (2009).

## ACKNOWLEDGMENTS

We thank S. Xu, E. Andersen, S. Mitani, and the Caenorhabditis Genetics Center for *C. elegans* strains; F. Ausubel and L. Dietrich for *P. aeruginosa* strains; and members of the Nitabach, Horvitz, and Kazmierczak laboratories for technical support, advice, and comments. **Funding:** D.D.G. is a Howard Hughes Medical Institute Fellow of the Life Sciences Research Foundation. Work in the laboratory of H.R.H. was supported by the National Institute of General Medical Sciences (NIGMS), NIH (R01GM024663). H.R.H. is an investigator of the Howard Hughes Medical Institute. Work in the laboratory of M.N.N. is supported in part by NIGMS, NIH (R01GM098931). **Author contributions:** D.D.G. initiated the study. D.D.G., D.L., and X.J. performed experiments. D.D.G., D.L., X.J., H.R.H., and M.N.N. designed experiments and analyzed data. D.D.G., H.R.H., and M.N.N. wrote the paper with input from the other authors. **Competing interests:** The authors declare no competing interests. **Data and materials availability:** All data are available in the manuscript or the supplementary materials.

## SUPPLEMENTARY MATERIALS

science.sciencemag.org/content/371/6533/1059/suppl/DC1  
Materials and Methods  
Figs. S1 to S7  
Table S1  
References (39, 40)  
MDAR Reproducibility Checklist

12 June 2020; accepted 8 January 2021  
10.1126/science.abd3010



### Ultrasonic Cleaners

Control the ultrasonic power to clean a wide range of instruments with Cole-Parmer Ultrasonic Cleaners. Available in digital and analog series, both feature a pulse function for 20% increase in ultrasonic power for hard-to-remove soil and pastes and an adjustable temperature range

from 30°C to 80°C in 5°C increments to accommodate sensitive items and instruments. A sweep function ensures uniform sound and power throughout the entire bath. With the latest in ultrasonic cleaning technology, these are ideal for the lab or the process floor. Along with the above features, the digital series comes in six different sizes and features seven convenient operating modes. Use the normal mode for mixing, dissolving, and dispersing samples, and the degas mode to quickly remove air from HPLC samples and solvents. The dual-selection power control allows the user to choose 37-kHz operation for standard and industrial applications or 80 kHz for smaller or more delicate cleaning needs. The pause function allows for temporary operation interruption, and autostart mode will begin operation once the preselected temperature is reached. The cleaners can be set to operate continuously or in timed runs, from 1 min to 30 min.

#### Cole-Parmer

For info: 800-323-4340

[www.coleparmer.com](http://www.coleparmer.com)

### Zeta Potential Instrument

The Stabino II from Analytik is a fast, easy-to-operate zeta potential instrument for analyzing and optimizing the stability of colloids and dispersions, based on measurement of streaming potential. Many analytical systems for determining stability are based on electrophoresis techniques that rely on a limited number of low-resolution measurements of the zeta potential. These systems can be slow and imprecise, leading to inconclusive analysis of the colloid/dispersion stability and incorrectly formulated products. Based upon rapid pH and polyelectrolyte titrations, the unit enables rapid, precise, reproducible measurement of the surface charge of particles in the range of 0.3 nm to 300 µm in just minutes. With each measuring point, the Stabino II provides valuable information about the conductivity, zeta potential, streaming potential, temperature, and pH of your sample.

#### Analytik

For info: +44-(0)-1954-232-776

[analytik.co.uk](http://analytik.co.uk)

### Extended-Range Non-Browning Zoom Lens

Resolve Optics new Model 192-001 non-browning 6x zoom lens offers high performance over an extended 24 mm–144 mm focal-length range, making it perfect for remote monitoring tasks in nuclear reprocessing and power plants. The compact lens's speciality glass components can withstand long-term exposure to radiation—up to a dose of 100 million RAD—without loss of transmission and minimal color change. Operating at f/3.6, the lens provides good image resolution and minimum geometric distortion from 400 nm–750 nm. When focused at infinity, it maintains focus throughout the zoom range without the need to refocus. Available in 1/2-in. and 2/3-in. image formats, the C-mounted Model 192-001 can be simply mounted on Newwicon tubes, Chalnicon tubes, and charge-coupled devices.

#### Resolve Optics

For info: +44-(0)-1494-777100

[www.resolveoptics.com](http://www.resolveoptics.com)

### Cell-Free Nucleic Acid Extraction

The cfPure Cell Free DNA Extraction Kit from AMS Biotechnology is a magnetic bead-based DNA extraction kit designed to isolate circulating cell-free DNA (cfDNA) from human plasma or serum samples. Using a simple, automation-friendly protocol, the kit allows users to quickly extract high-quality cfDNA that is ready for use in downstream applications, including next-generation sequencing, bisulfite sequencing, PCR, quantitative PCR, droplet digital PCR, and other demanding applications. This optimized protocol gives highly reproducible results and higher yields relative to other magnetic bead-based methods. Using silica-coated paramagnetic particles, cfPure kits were developed to ensure efficient recovery of 100 bp–500 bp DNA fragments, in order to maximize recovery of low-molecular-weight cfDNA. Designed for scalability (100 µl–10 mL of serum or plasma), cfPure kits enable you to use just the number of beads and amount of reagent you need for your cfDNA extraction.

#### AMS Biotechnology

For info: 617-945-5033

[www.amsbio.com/cfpure-cell-free-dna-extraction-kit](http://www.amsbio.com/cfpure-cell-free-dna-extraction-kit)

### Single-Photon Source

Thorlabs announces its latest addition to their product lineup for the rapidly growing field of quantum photonics, a correlated photon-pair source. The availability of a robust, high-brightness photon source is critical to the quantum photonics community for any number of applications spanning from fundamental photon-matter interaction to device characterization. The design features a user-adjustable, fully integrated 405-nm pump source on the front end of a spontaneous parametric down-conversion (SPDC) device to produce greater than 450-kHz photon pairs at 810 nm. Various design considerations were evaluated to produce a best-in-class (>0.45) heralding ratio for use as a heralded single-photon source without sacrificing pair-production rates. The photon pair (signal and idler) produced in the SPDC process is conveniently fiber-coupled out of the compact room-temperature housing for plug-and-play usage.

#### Thorlabs

For info: 973-300-3000

[www.thorlabs.com](http://www.thorlabs.com)

### Confocal Imaging Reader

Cytation C10 Confocal Imaging Reader combines automated digital confocal and widefield microscopy with conventional multimode microplate reading in a unique, patented design. The spinning-disk confocal module provides exquisite resolution and optical sectioning capabilities in a wide variety of sample types. High-quality components, including a Hamamatsu sCMOS camera, Olympus objectives, and laser-based illumination, deliver excellent image quality at a significantly lower price than other models. Cytation C10 also includes widefield fluorescence, brightfield, and phase-contrast optics. Its variable-bandwidth, monochromator-based multimode plate reading is based on the proven design of our market-leading Synergy products. Environmental controls enable live-cell assays, and Gen5 software makes sample detection and image capture quick and effortless. The new 3D viewer provides users with 3D reconstruction of their thicker samples captured with the confocal microscope. Cytation C10 brings affordable confocal to every laboratory.

#### BioTek

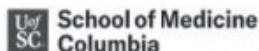
For info: 888-451-5171

[www.biotek.com](http://www.biotek.com)

Electronically submit your new product description or product literature information! Go to [www.sciencemag.org/about/new-products-section](http://www.sciencemag.org/about/new-products-section) for more information.

Newly offered instrumentation, apparatus, and laboratory materials of interest to researchers in all disciplines in academic, industrial, and governmental organizations are featured in this space. Emphasis is given to purpose, chief characteristics, and availability of products and materials. Endorsement by *Science* or AAAS of any products or materials mentioned is not implied. Additional information may be obtained from the manufacturer or supplier.





## UNIVERSITY OF SOUTH CAROLINA TENURE-TRACK ASSISTANT PROFESSOR

The NIH Center for Dietary Supplements and Inflammation (CDSI) at the University of South Carolina (UofSC) invites applications for **two tenure-track ASSISTANT PROFESSOR** positions with research expertise in Inflammation. The phase-2 Center of Biomedical Research Excellence (COBRE) will provide NIH research support and mentoring to junior faculty who have not received NIH R01 or similar grants as a PI, to become successful independent investigators. More information is available at: [https://sc.edu/study/colleges\\_schools/medicine/centers\\_and\\_institutes\\_new/center\\_for\\_dietary\\_supplements\\_and\\_inflammation/index.php](https://sc.edu/study/colleges_schools/medicine/centers_and_institutes_new/center_for_dietary_supplements_and_inflammation/index.php)

Candidates must have a PhD or equivalent, and at least 3 years of postdoctoral research experience. Competitive salary and startup funds are available. Please submit CV and a statement of research and teaching interests with names of 3 references online at <https://uscjobs.sc.edu/postings/93373>. The search will start immediately and will continue until the position is filled.

*The University of South Carolina does not discriminate in educational or employment opportunities on the basis of race, sex, gender, gender identity, transgender status, age, color, religion, national origin, disability, sexual orientation, genetics, protected veteran status, pregnancy, childbirth or related medical conditions.*



The Department of Molecular Medicine in the Joe R and Teresa Lozano Long School of Medicine at UT Health San Antonio invites applications from exceptional scientists/physician scientists to fill a faculty position (**Assistant/Associate/Professor**). The position will be commensurate with experience. Qualified candidates must be working in the area of tumor microenvironment, microbiome, oncogenic signaling, cell metabolism, integrative (synthetic) biology, genomics/epigenomics or any combination thereof. Competitive candidates will have an outstanding history of novel contributions to the field, and a record of current and sustained extramural funding. The successful candidate will be provided with a generous start-up package, space in a modern, open lab setting and fully equipped research facility that is conducive to multidisciplinary research. In addition, the candidate will be eligible for an application of the Cancer Prevention & Research Institute of Texas (CPRIT) recruitment award ([www.cprit.state.tx.us/funding-opportunities](http://www.cprit.state.tx.us/funding-opportunities)). Well qualified senior or mid-career investigator may be considered for the appointment of Zachry Distinguished University Chair in the Department.

For full consideration, an application package consisting of a cover letter, curriculum vitae, summary of research accomplishments, outline of future plans, names and contact information of at least 3 professional references must be submitted to <https://uthscsa.referrals.selectminds.com/faculty> with a cover letter, curriculum vitae, a summary of research accomplishments and outline of future plans, and contact information for at least three professional references.

Pratap Kumar, Ph.D., Chair  
Faculty Search Committee  
UT Health San Antonio  
Department of Molecular Medicine  
Joe R. & Teresa Lozano Long School of Medicine

*UT Health San Antonio is an Equal Employment Opportunity/Affirmative Action Employer including protected veterans and persons with disabilities. All faculty appointments are designated as security sensitive positions.*

## SIMONS FOUNDATION

The Simons Foundation is pleased to announce the appointment of our new class of Junior Fellows of the Simons Society of Fellows, a community of scholars created to encourage intellectual interactions across disciplines and research centers in New York City.

### Abigail Bodner

New York University  
Climate Dynamics, Geophysical  
Fluid Dynamics and Turbulence

### Ashley Chui

New York University  
Molecular Pharmacology

### Benem-Orom Davids

Columbia University  
Biochemistry and Molecular  
Biophysics

### Aravind Devarakonda

Columbia University  
Experimental Condensed  
Matter Physics

### Robert Fernandez

Columbia University  
Molecular and Developmental  
Neuroscience

### Emanuele Galiffi

Advanced Science Research Center at  
the Graduate Center of the City  
University of New York  
Plasmonics and Metamaterials

### Carla Golden

Columbia University  
Neuroscience

### Tim Large

Columbia University  
Symplectic topology/Floer  
homotopy theory

### Jennifer Merritt

Columbia University  
Behavioral Neuroscience  
Ecology and Evolution

### Fedor Popov

New York University  
Quantum Field Theory, Large  
N models and Applications

### Joan Pulupa

Columbia University  
Neuronal Cell Biology

### Sebastian Wolff

New York University  
Theoretical Computer science  
formal methods

For more information:

@Simons\_SOF • <https://www.simonsfoundation.org/simons-society-of-fellows>



## TENURE-TRACK ASSISTANT PROFESSOR IN MICROBIOME BIOINFORMATICS

The Center for Advanced Biotechnology and Medicine (CABM) seeks an outstanding candidate for a **Tenure-Track Assistant Professor** position with expertise in Microbiome Bioinformatics. This position can have a tenure home in one of many departments in the Schools comprising Rutgers Biomedical and Health Sciences (RBHS).

Our faculty members drive federally funded research programs in broad areas of biomedical science. We seek individuals with research interests in Microbiome Bioinformatics that will complement and/or expand our existing strengths. The successful candidate will be expected to develop a strong, externally funded research program to conduct microbiome studies, including those related to human health, development, and disease. Applicants with translational research interests relevant to metabolic disorders, cancer, or neurological disease, and microbiome-derived drug discovery, are encouraged to apply. Related computational research for systems biology and/or network modeling also is of interest. The successful candidate will be expected to support the educational goals of Rutgers University through teaching and service.

Qualified candidates must have a Ph.D. or equivalent graduate degree in Computational Biology, Mathematics, Evolutionary Biology, Molecular Biology, or a related discipline with at least 3 years postdoctoral research experience related to the microbiome or related field, a record of significant research, potential to make substantial contributions as an independent investigator, and commitment to teaching undergraduate and graduate students. Candidates with current funding or grants under review are preferred. The successful candidate will be provided with access to computing clusters and laboratory space at CABM, and full access to graduate training programs and research resources. Salary will be commensurate with experience; excellent benefits and competitive start-up package are offered. Research programs utilizing interdisciplinary and translational approaches that develop interactions with other RBHS institutes and clinical departments are encouraged. Interested candidates should apply online at: <https://jobs.rutgers.edu/postings/125973>.

*Rutgers University is an equal employment opportunity and affirmative action employer. We are deeply committed to increasing diversity and encourage applications from persons with disabilities, women, veterans, and minority scholars.*



# Peking University First Hospital——

**Healthcare, Education and  
Innovation for 106 years**



**北京大学第一医院建院106周年**  
106<sup>th</sup> Anniversary of Peking University First Hospital  
1915-2021

## **Professor Xinmin Liu, MD.**

Director of Peking University First Hospital

Founded in 1915, Peking University First Hospital (PUFH) is the first state-owned hospital and one of the earliest clinical medical schools. It was initially the affiliated clinic of Beijing Medical School approved by the Ministry of Education(MOE) of the Republic of China. In 1946, it merged with Peking University, hence it is also known as Beida Hospital.

For over a century, PUFH has boasted a number of pioneering medical disciplines as well as diagnosis and treatment technologies that were later established or applied in other parts of China. With 5 sub-campuses, it currently has over 3,600 faculty and staff members with a daily average of 10,000 outpatient visits, an annual average of 86,000 inpatients and 44,000 surgeries. As a top-notch hospital in Beijing, it provides the best services to patients, one third of whom are from all over the country and suffer from intractable diseases.

In pursuit of academic excellence, PUFH has been striving to build world-class disciplines and research platforms, boasting one national clinical research center, two Ministry-level key laboratories, and over 6,000 square meters for public laboratory service. In the past decade, it has conducted several large-scale multicenter clinical trials, with some research findings cited by international guidelines. Many of its alumni have become scientists with national and international reputations.

With a strong sense of social responsibility, PUFH has been actively engaged in China's public hospital reform. In recent years, it has undertaken many key national projects, with research findings widely adopted by government sectors. With improved management, it has played an exemplary role in clinical pathway, nursing services, pairing assistance, and the Aid Program for Tibet and Xinjiang. Meanwhile, it has also provided medical services in times of crucial or critical events, such as the 70th anniversary celebrations of the PRC and COVID-19.

Adhering to the core values of virtue and commitment, PUFH aspires to set the benchmark of medical service and endeavors to become a supportive community for its employees, a nurturing incubator for talent cultivation, a holy land for medical research, a perfect place for medical treatment and a hub for international communication.

## **The Department of Neurology**

The Department of Neurology, also called Peking University Institute of Nephrology, was established in the 1950s as the first kidney institute in China by the late Professor Shuxian Wang, founder of China's modern nephrology. From the 1980s, under the leadership of the late Professor Haiyan Wang, Mother of Chinese Nephrology, and Professor Minghui Zhao, a Key Laboratory of Renal Disease was established with the approval of both the Ministry of Health(MOH) and the Ministry of Education(MOE). With over 50 articles published annually in SCI journals, such as The New England Journal of Medicine and The Lancet, the department has consistently ranked No.1 in academic achievements nationwide for the past 10 years.

As a training center for the International Society of Nephrology (ISN) in North East Asia, the department provides many opportunities for academic research in both clinical and bench studies. A total of 50 physicians and researchers are devoting themselves to various research projects on kidney diseases, ready to cooperate with specialists all over the world on big data and artificial intelligence, advanced diagnosis and therapy in grave and extremely critical diseases, translational medicine and continuing medical education.

## **The Department of Urology**

The Department of Urology, together with the Institute of Urology (Peking University), is the birthplace and pioneer of urology in China. Both the department and the institute were established by Jieping Wu in 1946 and in 1978, respectively. Since 1989, the discipline has been evaluated as a key discipline by the Ministry of Education(MOE). In 2012, it was rated as a Ministry of Health(MOH) key clinical discipline and a Beijing key laboratory. Since 2010, the department has ranked No.1 in the list of "The Best Hospitals in China" issued by Fudan University for ten consecutive years. It has integrated a number of platforms, including the National Urological & Male Reproductive Cancer Research Center, Ministry of Health(MOH) Urological & Male Reproductive Cancer Medical Treatment Center, the Andrology Center of Peking University, Peking University Training School of Urologists and Beijing Guo Yinglu Urological Development Foundation. There are six main professional subspecialties, namely urological & male reproductive





Ward Round



Operating Theatre



Fight Against COVID-19

cancer, prostatic disease, urinary incontinence, male reproductive disease, urinary stone and kidney transplantation. Featuring standardization, professionalization, academicization and internationalization, the department tries to integrate new technologies such as endoscopy, minimally invasive surgery, intervention, microsurgery, novel biomaterials, innovative drugs, cellular and molecular biology, in order to achieve the goal of saving lives, protecting and restoring organ structure and function, and improving patients' quality of life.

### The Department of Dermatology

Founded in 1915, the Department of Dermatology is the most renowned in China as the only national clinical research center for skin diseases as well as a founding member of the Chinese Society of Dermatology. In the past 5 years, it has published many research papers in top medical journals, such as NEJM and Nat Genet. It is also the recipient of several provincial-level awards and national-level patents. Many of its faculty members hold important positions in domestic and international academic associations.

Up till now, the department has developed more than 10 sub-professional directions. The average number of outpatient visits is about 1,000 per day. The department boasts one of the largest domestic biological specimen and clinical big data banks, mainly of skin tumors, autoimmune bullous diseases and genodermatoses, and the largest fungal strains. As the national platform for dermatology, it has also established a cooperation network with more than 100 hospitals in China in partnership with many foreign hospitals and organizations.

### The Department of Pediatrics

As one of the earliest contemporary pediatrics China, the department of pediatrics was founded in 1926 and has gradually developed into an integrated center for patient care, medical education and cutting-edge scientific research. As a National Key Discipline, the department is a pioneering Chinese Training Base of Doctoral Training Program, a National Base for Continuing Medical Education, National Key Clinical Discipline (Pediatric Critical Care Medicine) approved by the Ministry of Health(MOH), National Demonstration Base for Pediatric Residency Program and Beijing Key Laboratory of Molecular Diagnosis and Research of Pediatric Genetic Diseases.

The department now has 225 faculty and staff members, with Professor Yuwu Jiang as department chair. Many of the pediatric experts hold leading positions in major academic societies and editorial boards of professional journals in China. Equipped with 203 beds, the department has all major divisions of pediatrics, such

as pediatric neurology & EEG monitoring center, cardiology, nephrology, hematology/oncology, neonatology, PICU, NICU, pulmonology, gastroenterology, endocrinology, genetic metabolic diseases, and development and behavior pediatrics. The research in pediatric neurological diseases, cardiovascular diseases, kidney diseases, and genetic diseases is academically competitive and internationally reputable. In the past decade, the doctors of the department have won 388 research grants, participated in 11 international multi-center clinical research projects, and developed 26 national and international consensus or guidelines for pediatric diseases.

### The Department of Cardiology

Founded on November 11, 1983, the Department of Cardiology is among the earliest ones established in China's general hospitals. As a national key clinical and educational unit, it has comprehensive capabilities for diagnosing and treating various kinds of cardiovascular diseases. Currently it has 5 sub-specialties: coronary artery disease and atherosclerosis, arrhythmia, heart failure and cardiomyopathy, structural heart disease and hypertension.

With fast development over several decades, a professional team composed of clinical experts, researchers and administrators has been formed. As the national center for quality control of coronary intervention, our department has pioneered the interventional therapy nationwide for patients with coronary artery disease and arrhythmia, accumulated rich experience in complex and higher-risk interventional therapy, and made huge contributions to the popularization, regulation and improvement of coronary intervention therapy.

The department also conducts cardiovascular research, having led and implemented a large amount of clinical and basic research at national and provincial levels, engaged in several key nationally funded projects and won a dozen of national- and provincial-level awards, with many research findings widely adopted by clinical guidelines.

PUFH cordially welcomes job applicants and visiting scholars with expertise in related areas. Feel free to contact us:


Website: <http://www.pkufh.com>

Email: [kyc@pkufh.com](mailto:kyc@pkufh.com); [kyc@bjmu.edu.cn](mailto:kyc@bjmu.edu.cn)

Tel: +86-10-83572075

Fax: +86-10-66551211

Address: Peking University First Hospital, 8 Xishiku Road, Beijing, China.100034

A smiling man with short dark hair, wearing a white lab coat over a light blue button-down shirt, and clear safety goggles. He is standing in a laboratory with shelves of various bottles and equipment in the background. His arms are crossed, and he is wearing a blue nitrile glove on his left hand.

# YOU'D SMILE TOO IF YOU JUST ADVANCED YOUR CAREER.



**Find your next job at [ScienceCareers.org](https://www.sciencecareers.org)**

There's scientific proof that when you're happy with what you do, you're better at what you do. Access career opportunities, see who's hiring and take advantage of our proprietary career-search tools. Get tailored job alerts, post your resume and manage your applications all in one place: [sciencecareers.org](https://www.sciencecareers.org)

**ScienceCareers**

FROM THE JOURNAL SCIENCE  AAAS



## FACULTY POSITION IN MOLECULAR & CELL BIOLOGY

The Department of Anatomy in the Howard University College of Medicine in Washington, D.C., is seeking applicants for a **full-time Assistant Professor** tenure-track position to start in the summer of 2021. Applicants must possess a Ph.D. and have postdoctoral experience. Within the context of molecular and cell biology, the candidate may be involved in neuroscience, developmental, genomic, or other innovative molecular and cell biology research. Highest priority will be given to candidates with a strong history of scholarly activity with either an established research program or the potential to develop an externally funded research program. Preference will be given to candidates with a record of teaching competency in the anatomical sciences.

The College of Medicine is currently expanding its basic science faculty and offers a competitive start-up package. There are abundant opportunities for collaborations within the College of Medicine and at nearby institutions (NIH, FDA, USDA). Applicants should email a single PDF file that includes a comprehensive curriculum vitae, research interests and goals, and the names and contact information for 3 references to Dr. Antonei Csoka, Chair of Search Committee ([antonei.csoka@howard.edu](mailto:antonei.csoka@howard.edu)).

*Howard University is a private, federally chartered historically black university (HBCU), an equal opportunity/affirmative action employer of minorities, females, individuals with disabilities and protected veterans, and a drug and tobacco free workplace.*

## DESTINATION VANDERBILT – BIOMEDICAL DISCOVERY

Destination Vanderbilt is a \$100 M investment to recruit the next generation of exceptionally creative faculty who are pushing their fields forward with excellence. Applications are invited from **early-to-mid career faculty in the biomedical sciences for positions** in the School of Medicine Basic Sciences. Opportunities are available in all four departments - Biochemistry, Cell and Developmental Biology, Molecular Physiology and Biophysics and Pharmacology. Candidates should have a sustained record of publications yielding novel insights into fundamental biomedical questions and promise of future innovative accomplishments; research funding; and an excellent training and mentoring record.

Vanderbilt University provides a rich, diverse research environment that strongly supports further career development and fosters opportunities for multidisciplinary collaborations with faculty across the School of Medicine, Vanderbilt University Medical Center, the School of Engineering, and the College of Arts & Science. This culture is enhanced by the activities of several trans-institutional centers and institutes (<https://www.vumc.org/oor/departments-and-centers>). Vanderbilt also has developed a wonderful suite of state-of-the-art core facilities (<https://medschool.vanderbilt.edu/basic-sciences/core-facilities/>) including large investments in cryo-electron microscopy/tomography and genomics.

Vanderbilt University is located in Nashville, a rapidly growing cosmopolitan city rich in cultural activities with easy access to a multitude of outdoor recreational opportunities.

Interested individuals should submit a curriculum vitae and a cover letter that includes statements about mentoring, promotion of diversity and inclusion and current research directions not reflected in the cv. Please send material to (<https://apply.interfolio.com/83909>).

*Vanderbilt University is an affirmative action/equal opportunity employer committed to recruiting and retaining an academically and culturally diverse community of faculty. The university has a strong institutional commitment to diversity in all areas, and particularly encourages applications from minorities, women, individuals with disabilities, and members of other underrepresented groups.*

# ScienceCareers

FROM THE JOURNAL SCIENCE  AAAS

## Confused about your next career move?



**Download Free Career  
Advice Booklets!**

[ScienceCareers.org/booklets](https://ScienceCareers.org/booklets)



By Samuel Peña-Llopis

# Leadership challenges defused

**B**oom! The bomb exploded. But don't worry—it was a virtual bomb, part of a game I started to play with my research group through teleconferencing in the early days of the pandemic. Called *Keep Talking and Nobody Explodes (KTANE)*, the game consists of a “defuser”—me—who has the bomb but no idea how to defuse it, and a group of “experts”—the members of my team—who have an instruction manual but cannot see the bomb. I have to describe the components of the bomb to them. They have to identify each component in their manual, figure out how to defuse it, and explain the solution to me. Then I have to execute based on their instructions. If we make too many mistakes or run out of time—boom!—the bomb explodes and the game is over. For our group, playing offered excitement and camaraderie—and for me, a lesson in how games can hone leadership skills.

I learned about *KTANE* from my older son, who organized a game for our family. He was the defuser, describing to his younger brother, my wife, and me each of the bomb's modules—for example, a set of colored wires that need to be “cut” a certain way and a set of buttons labeled with symbols that need to be pushed in a certain order, among hundreds of much more complex puzzles. It was a roller coaster of joy and desperation. We were hooked.

I was especially captivated by the role of the defuser, who controls the flow of tasks and information to keep everyone busy, productive, and efficient—just as I try to do as lab head. Maybe bringing this game to my research group, with me as the defuser, would be good practice for me while also helping our lab stay connected and maintain morale during the COVID-19 shutdown.

After an initial round to get our bearings, we hit our groove. Our communication flowed smoothly, the experts solved their puzzles efficiently, and we had some laughs along the way. I thought we were ready to increase the complexity of the modules—but I pushed us too far, too fast. Frustration skyrocketed as our bombs exploded again and again. The worst part was that we weren't identifying or learning from our mistakes.

This reminded me of my experience struggling to mentor some students who didn't acknowledge their mistakes, and as a result weren't growing as scientists. I tried to convey to them that we all make mistakes; certain errors are beyond our control and we might not even be aware of them. The most important thing is to take responsibility for our mistakes and move forward, not pretend they never happened.



**“Maybe bringing this game to my research group ... would be good practice for me.”**

But that message rarely seemed to get through.

So after each explosion, I began to lead the group through the game's logfile analyzer, which included information about the correct solutions to each module. Talking about research mistakes can be delicate and uncomfortable, but within a game the stakes are low. I practiced offering constructive, supportive feedback—and my students became more comfortable receiving and acting on my input. Within a few rounds, our bombs rarely exploded. I realized that cooperative games like *KTANE*—and we've gone on to play others, too—offer a fun, non-threatening environment to practice effective communication and dealing with mistakes.

In real life, we don't have a logfile analyzer to show where we've gone wrong. Still, the game has given us a foundation to build on. Recently, one of my students inadvertently provided the wrong cells to another student, affecting a lengthy and expensive experiment. This could have been a sensitive situation to navigate. But I reminded my group of the lessons we learned from *KTANE*. I emphasized the importance of communication, the humbling experience of realizing that everybody makes mistakes, and the crucial value of identifying and learning from these errors so we can minimize repeating them. I felt like a pilot who, after many hours training with a flight simulator, was confidently flying a real plane. ■

Samuel Peña-Llopis is a junior group leader and coordinator of the School of Oncology in the German Cancer Consortium (DKTK) at the University Hospital Essen. Send your career story to [SciCareerEditor@aaas.org](mailto:SciCareerEditor@aaas.org).



CALL FOR PAPERS



# Plant Phenomics

 OPEN ACCESS

*Plant Phenomics* is a Science Partner Journal published in affiliation with the State Key Laboratory of Crop Genetics & Germplasm Enhancement, Nanjing Agricultural University (NAU) and distributed by the American Association for the Advancement of Science (AAAS). *Plant Phenomics* publishes novel research that advances both in field and indoor plant phenotyping, with focus on data acquisition systems, data management, data interpretation into structural or functional traits, integration into process based or machine learning based models, and connects phenomics to applications and other research domains.

**Submit your research to *Plant Phenomics* today!**

Learn more: [spj.sciencemag.org/plantphenomics](http://spj.sciencemag.org/plantphenomics)

The Science Partner Journals (SPJ) program was established by the American Association for the Advancement of Science (AAAS), the non-profit publisher of the *Science* family of journals. The SPJ program features high-quality, online-only, Open-Access publications produced in collaboration with international research institutions, foundations, funders, and societies. Through these collaborations, AAAS furthers its mission to communicate science broadly and for the benefit of all people by providing top-tier international research organizations with the technology, visibility, and publishing expertise that AAAS is uniquely positioned to offer as the world's largest general science membership society.

Learn more at [spj.sciencemag.org](http://spj.sciencemag.org)



@SPJournals



@SPJournals

ARTICLE PROCESSING CHARGES WAIVED UNTIL 2022



Apply for our exciting research Prize!



**\$25, 000 Grand Prize!**  
**Get published in *Science*!**

The *Science*-PINS Prize is a highly competitive international prize that honors scientists for their excellent contributions to neuromodulation research. For purposes of the Prize, neuromodulation is any form of alteration of nerve activity through the delivery of physical (electrical, magnetic, or optical) stimulation to targeted sites of the nervous system with implications for translational medicine.

For full details, judging criteria and eligibility requirements, visit:

**[www.sciencemag.org/prizes/pins](http://www.sciencemag.org/prizes/pins)**

**Submission Deadline: 15 March 2021**

**Science**  
AAAS



**Science**  
**Translational**  
**Medicine**  
AAAS